NOVEL METAL OXIDE NANOSTRUCTURES FOR ADSORPTION AND PHOTOCATALYTIC DEGRADATION OF ORGANIC DYES FROM AQUEOUS STREAM

Jyoti Prakash Dhal

DEPARTMENT OF CHEMISTRY
NATIONAL INSTITUTE OF TECHNOLOGY
ROURKELA-769008, ODISHA, INDIA

August 2015

NOVEL METAL OXIDE NANOSTRUCTURES FOR ADSORPTION AND PHOTOCATALYTIC DEGRADATION OF ORGANIC DYES FROM AQUEOUS STREAM

Thesis submitted in partial fulfilment of the requirements for the degree of

DOCTOR OF PHILOSOPHY

By

Jyoti Prakash Dhal

Roll No: 511CY101

Under the supervision of

Dr. Garudadhwaj Hota

&

Dr. Braja Gopal Mishra

DEPARTMENT OF CHEMISTRY
NATIONAL INSTITUTE OF TECHNOLOGY
ROURKELA-769008, ODISHA, INDIA

August 2015

CERTIFICATE

This is to certify that the thesis entitled “**Novel Metal oxide Nanostructures for Adsorption and Photocatalytic degradation of Organic Dyes from Aqueous Stream**” being submitted by **Sri Jyoti Prakash Dhal** to the National Institute of Technology, Rourkela, India, for the award of the degree of **Doctor of Philosophy** is a record of bonafide research work carried out by him under my supervision and guidance. I am satisfied that the thesis has reached the standard for fulfilling the requirements of the regulations relating to the nature of the degree. To the best of my knowledge, the matter embodied in the thesis has not been submitted to any other University/Institute for the award of any Degree or Diploma.

Supervisor

Place: Rourkela
Date: 28-03-2016

Dr. Garudadhwaj Hota
Department of Chemistry
National Institute of Technology
Rourkela-769008

Co-Supervisor

Dr. Braja Gopal Mishra
Department of Chemistry
National Institute of Technology
Rourkela- 769008

Acknowledgement

I take this opportunity to express my deep sense of gratitude and indebtedness to my research supervisor **Prof. Garudadhwaj Hota**, for providing his excellent guidance, support, encouragement and inspiration throughout my research work. It has been a great opportunity to work with him with his vast scientific knowledge and analytical approach. I greatly feel fortunate enough for his patience to assist me, which he devoted from his busy schedule. Without his expertise and guidance, this work would not have been accomplished. I feel so lucky to have spent my research work under the guidance of an intelligent, forgiving, open minded, honest and beloved person like him. I am also very much thankful to his family members for their hospitality, love and encouragement.

I would also like to acknowledge **Prof. Braja Gopal Mishra**, my co-supervisor for providing his outstanding technical support, caring and valuable suggestions, which helped me making this research work a success.

I am extremely grateful to our honorable director sir **Prof. Sunil Kumar Sarangi**, a visionary personality, who encouraged and inspired through his motivating speech to carry out the research programme.

I am thankful to all my Doctoral Scrutiny Committee members **Prof. S. Paria**, **Prof. S. Mohapatra** and **Prof. S. Patel** for their valuable suggestions throughout my research career.

I would also like to express my deep sense of gratitude to **Prof. N. Panda**, HOD, Department of Chemistry, NIT Rourkela for allowing me to avail the experimental facilities.

I wish to express my sincere thanks to **Prof. R. K. Patel** (Ex-HOD), **Prof U. Subbudhi** and **Prof A. Mandal**, Department of Chemistry, NIT, Rourkela for good suggestions and useful discussions during my research work.

Above all, I am very much thankful and indebted to the **National Institute of Technology, Rourkela** for selecting me as a Ph. D. scholar and sponsored me financially throughout the research programme.

I would like to thank all the faculty and staff members, Department of Chemistry, NIT Rourkela for their help and inspirations.

I am very much grateful to Department of Physics, Ceramic and Metallurgical Engineering, NIT Rourkela, for providing various characterization techniques.

I wish to thank my lab mates Abhipsa, Shabna, Srabana, Bappaditya, Amar and Tapaswini for their immense help, timeless effort and cooperation throughout my work in laboratory. I would also like to thank all of my friends and seniors Rakesh bhai, Subrat bhai, Tapan, Ranjit, Achyut and Ranjit baba who supported me in writing, and incented me to strive towards my goal. My special thanks to Prakash, Smruti Snigdha, Subhraseema, Purabi, Uttam, Manoj, Kishore and Yagna for their companionship, emotional support and entertainment, which helped me a lot to get through the difficult times during my work.

Words cannot express how grateful I am to my mother (Bou) and father (Bapa) for all of their sacrifices that they have made on my behalf. I would like express appreciation to my grandmother, elder brothers (Bhai and Tikila Bhai), loving sister Lucky, younger brother Papa and Bhauja for their love inspiration, mental support and encouragement.

August 2015 **Jyoti Prakash Dhal**

CONTENT

ABBREVIATIONS

XRD	:	X-Ray Diffraction
SEM	:	Scanning Electron Microscopy
FESEM	:	Field Emission Scanning Electron Microscopy
TEM	:	Transmission Electron Microscopy
XPS	:	X-ray Photoelectron Spectroscopy
UV-Vis-DRS	:	Ultra-visible Diffuse reflectance Spectroscopy
FTIR	:	Fourier Transform Infrared Spectroscopy
BET	:	Brunauer-Emmett-Teller
BJH	:	Barrett-Joyner-Halenda
IUPAC	:	International Union of Pure and Applied Chemistry
JCPDS	:	Joint Committee for Powder Diffraction Standards
CR	:	Congo red dye
MB	:	Methylene blue dye
MG	:	Malachite green dye
MO	:	Methyl orange dye

NOTATION

eV : electronvolt

m^2/g : square meter per gram

g : gram

nm : nanometer

Hz : Hertz

Å : Angstrong

cm : centimetre

KJ : kilo Joule

h : hour

θ : Bragg angle

ν : frequency

KHz : kilo Hertz

min : minute

L/g : litre per gram

M : Molar

$mg\ L^{-1}$: milligram per litre

List of Figures

List of Tables

Abstract

Recent research focused on the applications of nanomaterials in environmental remediation especially the treatment of natural waters, industrial and domestic waste water and the polluted underground water. Providing clean water and a clean environment for the world growing population is a challenging task. The present thesis represents an extensive view of the use of nanomaterials in environmental remediation such as water purification using single and composite metal oxide nanomaterials by sorption and photocatalysis of toxic organic dyes.

In the present study, we have synthesized 1D iron oxide nanomaterials and iron oxide based nanocomposites such as Fe_2O_3-SnO_2, Fe_2O_3-CuO, $Fe_2O_3/ZnFe_2O_4$/ZnO, and $MgFe_2O_4$-Fe_2O_3 of different morphology using precipitation, hydrothermal and reflux methods. Apart from this we have also synthesized MgO nanomaterials and iron oxide impregnated mesoporous MCM-41 by wet chemical impregnation method. The obtained metal oxide nanomaterials and their nanocomposites were characterized using XRD, SEM, TEM, EDAX, XPS, Raman, FTIR, UV-Vis-DRS and BET surface area analytical techniques and were used as adsorbents and photocatalysts for decontamination of organic dyes from aqueous solutions.

We have synthesized ferrous oxalate, hematite and maghemite nanorods by precipitation method. The XRD patterns indicate the formation of different crystalline phases of ferrous oxalate ($FeC_2O_4.2H_2O$), hematite (α-Fe_2O_3) and maghemite (γ-Fe_2O_3). The SEM and TEM images confirm the formation of rod shaped morphology with diameter in the range of 100-200 nm and length up to micrometers. The prepared nanorods were used as adsorbents for removal of carcinogenic Congo red dye from aqueous solution. After the batch adsorption study, the maximum adsorption capacities of the adsorbents were found to be 103, 232 and 78 mg/g for $FeC_2O_4.2H_2O$, γ-Fe_2O_3 and α-Fe_2O_3 nanorods, respectively. We have also prepared Fe_2O_3-SnO_2 composite nanorods by using same precipitation method. XRD study revealed the presence of magnetic γ-Fe_2O_3 phase along with SnO_2 in Fe_2O_3–SnO_2 composite. The Fe_2O_3–SnO_2 composite nanorods were used as adsorbents for removal of Congo red dye from aqueous solution. Among different compositions, Fe_2O_3–SnO_2 (Fe:Sn=8:2)

composite nanorod showed highest percentage adsorption with sorption capacity of 182 mg/g.

Mesoporous MCM-41 and MCM-41 impregnated with iron oxide nanomaterials (Fe-MCM-41) were prepared by a facile surfactant based wet chemical method. The experimental results indicate the formation of porous nanostructure with high surface area (>800 m^2/g) and particle size in the range of 200-400 nm. The mesoporous materials were used as adsorbents for the removal of Methylene blue from aqueous media. The maximum adsorption capacity of Fe-MCM-41 was found to be 194 mg/g and was higher than that of MCM-41.

MgO nanomaterials with different morphologies such as: nanorods, hierarchical nanostructures and nanoflakes were synthesized by precipitation, reflux and hydrothermal methods, respectively. The prepared nanomaterials were used as adsorbents to remove as Malachite green and Congo red from aqueous media. The hierarchical MgO nanostructure exhibited excellent adsorption performance for removal of Malachite green and Congo red with maximum sorption capacities of 1205 and 1051 mg/g, respectively. Using same synthesis methods we have used iron salt precursor along magnesium to prepare $MgFe_2O_4$ and $MgFe_2O_4$-Fe_2O_3 composite nanostructures. The $MgFe_2O_4$-Fe_2O_3 nanocomposite prepared by precipitation method was regarded as a superb photocatalyst for 99.9 % methylene blue degradation.

We have also synthesized Fe_2O_3-CuO composite nanorod by same precipitation method. From FESEM and TEM analysis it was observed that the spherical CuO nanoparticles are decorated uniformly onto the α-Fe_2O_3 nanorod surface forming a one-dimensional heteronanostructure. The obtained 1D Fe_2O_3-CuO nanocomposite exhibited higher photocatalytic activity than individual α-Fe_2O_3 nanorods and CuO nanoparticles for degradation of Methyl orange from aqueous media under solar light irradiation.

Furthermore, we have synthesized α-Fe_2O_3 nanoparticle and $Fe_2O_3/ZnFe_2O_4$, $Fe_2O_3/ZnFe_2O_4/ZnO$ and $ZnFe_2O_4/ZnO$ mixed oxide nanocomposites by varying different molar ratio of Fe and Zn using hydrothermal method. The nanocomposite with Fe:Zn=70:30 and 60:40 contains ternary $Fe_2O_3/ZnFe_2O_4/ZnO$ phase. The nanomaterials have been used for photocatalytic degradation of Malachite green from aqueous media using solar light irradiation. The ternary $Fe_2O_3/ZnFe_2O_4/ZnO$ (Fe:Zn=70:30) nanocomposite exhibits highest photocatalytic activity among all the prepared nanomaterials. The enhanced activity could be

attributed to the cascade electron transfer from $ZnFe_2O_4$ to ZnO to Fe_2O_3through the interfacial potential gradient in the ternary nanostructure.

Kew Words: Nanomaterial; One dimensional nanomaterial; Nanocomposite; Metal oxide nanomaterials; Adsorption; Photocatalysis; Organic dye

CHAPTER 1

INTRODUCTION AND MOTIVATION

1. Background on Nanomaterials

Nano (like micro, pico, and so on) is a prefix used in front of a macroscopic unit to change its value by orders of magnitude. Nano means one billionth, or 10^{-9}. Thus, one nanometer is one billionth of a meter (Balzani, 2005). Nanomaterials include the study of objects and systems with sizes in the range of 1-100 nm (Zhu et al., 2011). The nanosized materials are intermediate in size between atoms or small molecules and that of bulk structures. The dimensions of these systems are often equal to or smaller than the characteristic length scales that define the physical properties of materials. At these sizes, nanosystems can exhibit interesting and useful physical behaviors based on quantum phenomena (electron confinement, near-field optical effects, quantum entanglement, electron tunneling, and ballistic transport) or subdomain phenomena (superparamagnetism, overlapping double layers in fluids) (Love et al., 2005; Whitesides, 2005).

Nanocrystalline materials are the solids composed of nanometer sized particles, or grains, or crystallites (Valiev, 2002). Recent progress in nanomaterials research is regarded as one of the most advanced and interdisciplinary area of research in chemistry, physics, bioscience and engineering (Edelstein and Cammaratra, 1998). The application of nanomaterials permits the alteration of the fundamental physical and chemical properties of conventional materials as their size is reduced to the nanoscale, offering new materials with unique electrical, optical and mechanical properties. Nanomaterials are being increasingly used for commercial purposes such as adsorbents, fillers, catalysts, semiconductors, photocatalysts, cosmetics, microelectronics, pharmaceuticals, drug carriers, energy storage and antifriction coatings (Farre et al., 2009; Yoshimatsu et al., 2008). The unique properties of nanomaterials, which arise due to the domination of surface effects over interior volume effect due to their nano dimension, can be used to design novel technologies or to improve the performance of existing processes. Nanomaterials have found multiple applications in water treatment, energy production, and contaminant sensing. In addition, a growing number of literatures also describe how novel nanomaterials can be used to address major environmental challenges (Perreault et al., 2015).

Water pollution is a major global problem threatening the life system which accounts for a large number of diseases and death by consuming contaminated water. There are various types of water contaminants such as inorganic pollutants like antimony, arsenic, barium, cadmium, chromium, fluoride, lead, mercury etc. and organic contaminants like acrylamide, phenol, benzene hexachloride, carbon tetrachloride and different organic dyes like congo red dye, methyl blue, methyl orange etc. (Chowdhury and Yanful, 2010; Bhoumik et al., 2011; Yang and He, 2011; Cao et al., 2010). Dyes and pigments are widely using in paper, plastics, lathers, food and cosmetic industries as colour products. The toxic nature of dye is that on decomposition it gives hazardous products such as Carbon dioxide, carbon monoxide, nitrogen oxide and hydrogen chloride. These products are toxic and causes severe health problem to living beings (Iram et al., 2010; Kerkez and Bayazit, 2014). The various contaminants removal processes from wastewater sources include reverse osmosis, activated carbon filter, precipitation, membrane separation, ion exchange, adsorption, photocatalysis, solvent extraction, nanofiltration etc. Recent research focused on the use of nanotechnology for environmental clean-up/remediation. Arising out of their ultrafine size, large surface area & interface dominated properties nano-sized materials can be used to decontaminate the toxic organic and inorganic chemical from the environments.

In the past two decades, worldwide research efforts have been made both on theoretical and the experimental investigation of synthesis, growth, characterization and applications of inorganic nanostructures including metal oxides, ceramics and composites that have resulted in a mature, multidisciplinary field. Among the various classes of inorganic nanoparticles, metal oxide nanoparticles are particularly attractive from both the scientific and technological point of view. Metal oxide nanomaterials can exhibit unique physical and chemical properties due to their limited size and a high density of corner or edge surface sites (Fernández-García et al., 2004). Metal oxide nanomaterials have attracted a great deal of attention because of their large applications in various fields like catalysis, sensors and environmental remediation like adsorption and degradation of various contaminants from aqueous media (Oskam, 2006).

1.1. Nanorods/Nanofibers materials

One dimensional (1D) nanomaterial, including nanotubes, nanowires, nanofibers and nanorods have attracted a great deal of attention due to their combination of superior properties like small dimension structure, high aspect ratio and unique device function that lead to a large range of promising applications in electronics, photonics, chemical sensors, field emission devices, solar cells, lithium ion battery, hydrogen storage, and drug delivery (Zhao et al., 2011; Li et al., 2011; Mahapatra et al., 2011). One dimensional nanostructure possesses two quantum confined directions with one unconfined direction for electrical conduction; which allow these materials for electrical conduction rather than tunnelling transport. Besides that, the unique density of electronic states in the limit of small diameters is expected to exhibit significantly different optical, electrical and magnetic properties from their bulk 3D crystalline counterparts. Again, incorporation of functional heterostructures is a potential application of one-dimensional material which is very difficult or impossible in case of two-dimensional systems (Shankar and Raychaudhuri, 2005; Dick, 2008; Li et al., 2011; Zhanj and Zhu, 2002). Furthermore, one-dimensional nanostructures, such as nanowires, nanobelts, nanoribbons, nanorods and nanotubes, represent the smallest dimension for efficient transport of electrons and excitons and thus are ideal building blocks for hierarchical assembly of functional nanoscale electronic and photonic structures. Depending on the nature of materials, a nanowire obtained can have shown the properties of an insulator, a semiconductor or a conductor (Singh and Ali, 2010). Recently, well-defined 1-D nanostructures and/or 1-D arrays have been used for the establishment of many new and promising fields, including nanofabrication, nanodevices, nanobiology, nano-catalysis, etc. (Wang and Li, 2006).

In nanotechnology, one-dimensional (1-D) metal oxide nanostructures are the most important nanomaterials and current researchers are giving more focus towards these materials since they are the commonest minerals in the earth. They have gained great attention as a key component in ceramics, catalysis, sensors, transparent conductive films, electro-optical and electro-chromic devices. Intensive studies have been carried out on the synthesis of metal oxide nanowires as well as the exploration of their novel properties (Shen et al., 2009; Li et al., 2010; Comini et al., 2009). Over the past decade, one-dimensional (1D) semiconducting metal oxide nano-structures such as nanotubes (NTs), nanobelts (NBs), nanowires (NWs) and nanorods (NRs) have attracted extraordinary attention due largely to the unique physical and chemical properties associated with the 1D structural confinement at this scale (Zhou et al., 2010).

1.2. Mesoporous Materials

Mesoporous materials are materials having pore sizes in the range of 2–50 nm. Due to combination of porous structure and high surface area these materials are expected to have unique properties for applications in the field of adsorption, catalysis, membrane separation, fixing agent for biomolecule and semiconductor cluster, functional electronics and photonic applications (Nagata et al., 2006). MCM-41 (Mobil Composition of Matter) is the first ever synthesized mesoporous solid that showed a regularly ordered pore arrangement and a very narrow pore-size distribution (Ciesla and Schuth, 1999). It is a member of M41S family, contains of a hexagonal array of tubular pores possessing a high surface area i.e. more than 1000 m^2/g and uniform pore size distribution. MCM-41 material exhibits a regular, hexagonal arrangement of pores with one-dimensional parallel channels, formed a liquid crystal tinplating. It was synthesized with a self-assembly mechanism for the silicate source and surfactants with a long chain length as the template, and the structure of MCM-41 can be included with a metal atom to substitute Si^{4+} atom in the framework (Jehng et al., 2007). The presence of large internal surface area and favorable uniformity with easily controlled size of the pore enables the material (MCM-41) for applications of various fields in physics, chemistry, materials science, and other relevant areas such as: shape/size selective adsorbents, hosts for quantum structures, catalysts, and catalyst supports (Yu et al., 2001).

1.3. Nanocomposite materials

A composite is considered to be any multiphase material that exhibits a significant proportion of the properties of all constituent phases such that a better combination of properties is realized. According to the principle of combined action, better property combinations are fashioned by the judicious combination of two or more distinct materials (Callister, 2007). Nanocomposites are composites in which at least one of the phases shows dimensions in the nanometre range ($1\ nm = 10^{-9}\ m$). Nanocomposite materials have emerged as suitable alternatives to overcome limitations of microcomposites and monolithics, while posing preparation challenges related to the control of elemental composition and stoichiometry in the nanocluster phase (Camargo et al., 2009). Nanocomposites are reported to be the materials of 21st century in the view of possessing design uniqueness and property combinations that are not found in conventional composites.

1.4. Importance of Metal oxide Nanomaterials

Metal oxides nanomaterials are the common, most diverse, and important class of materials which attract research attention due to their unique physical, chemical, and structural properties. Metal elements are able to form different types of oxide compounds, which can adopt a vast number of structural geometries with an electronic structure with metallic, semiconductor or insulator character. They include optical, optoelectronic, magnetic, electrical, thermal, electrochemical, photoelectrochemical, mechanical, and catalytic properties (Vayssieres, 2004). The efficiency of the aforesaid properties of metal oxides largely varies with the reduction of particle size into nano scale and which is either enhanced or completely novel properties compared to their bulk materials (Zhang, 2008).

1.4.1. Iron Oxides

Iron oxide nanoparticles have been attracting much attention of researchers for its environmental benignity, multivalent oxidation states, abundant polymorphism, mutual polymorphous changes in nanophase, nontoxicity and low cost (Zhu et al., 2014). Iron oxides exist in different phases in nature including oxides, hydroxides and oxy-hydroxides. Some of them are: FeO, Fe_3O_4, Fe_4O_5, Fe_4O_3, polymorphs of Fe_2O_3 (α-Fe_2O_3, and γ-Fe_2O_3), $Fe(OH)_3$, FeOOH and so on. Among different phases of iron oxide, the magnetite (Fe_3O_4), the maghemite (γ-Fe_2O_3), and the hematite (α-Fe_2O_3) are probably the most common for fundamental study and also very important in technologically and hence therefore, the subject of discussion. Hematite (α-Fe_2O_3) is the most stable iron oxide under the ambient conditions and has a great scientific and technological importance because of its n-type semiconducting properties due to its narrow band gap of 2.2 eV, chemical and thermal stability and nontoxicity. This compound possesses rhombohedral, corundum (α-Al_2O_3) structure which is the most common form. It shows antiferromagnetic behaviour below ~260 K (Morin transition temperature), and exhibits weak ferromagnetism between 260 K and 950 K (Neel temperature). Apart from this, Hematite (α-Fe_2O_3) is a potential photocatalyst which can be driven by visible light up to 600 nm (Zhang et al., 2012; Chen et al., 2006). But, Magnetite (Fe_3O_4) assumes inverse cubic spinel structure in which iron cation exists in two oxidation states of Fe^{2+} and Fe^{3+} and hence shows very interesting properties. Magnetic properties of magnetite nanoparticles have been widely studied because of their relevance to magnetic recording, biomedical applications and so on (Daou et al., 2006). Maghemite (γ-Fe_2O_3) is a ferrimagnetic spinel in which the magnetic Fe^{3+} ions with spin S=5/2 are disposed in two sub-lattices with different coordination with the O^{2-} ions. At ambient conditions, these phases are thermodynamically less stable than hematite. Maghemite is used in large number of applications i.e. magnetic resonance imaging, magnetic recording media, fabrication of biocompatible magnetic fluids and electronic devices. Nanoparticles of maghemite (γ-Fe_2O_3) have many advantages as an adsorbent, such as high adsorptive capacity, easy and fast production, rapid uptake, and easy separation of the metal loaded magnetic adsorbent from treated water via an external magnetic field (Akhbarizadeh et al., 2014).

1.4.2. Iron oxide based composite nanomaterials

Metal oxide composite nanomaterials have been emerging as alternative adsorbents for the scavenging of toxic organic dyes from wastewater. The hybrid nanostructured materials show unusual mechanical, thermal, physical, and chemical properties. They also have a large surface area, which makes the composite materials quite promising as good adsorbents and photocatalysts (Ahmad and Kumar, 2010). Iron oxide based nanocomposite materials have been found to exhibit interesting physicochemical properties suitable for many advanced technological applications such as catalysts, adsorbents for removal of toxic ions and organic dyes, sensors, magnetic-optical materials, and many more applications. The coupling or incorporation of some other metal ion into the lattice structure of Fe_2O_3 form iron oxide based mixed oxide nanocomposites. They are very good materials for the sorption and photocatalytic studies, because combination of other metal oxides with Fe_2O_3 lattice structure enhanced the material properties namely surface sorption, photo-induced catalysis, etc. The improved physicochemical properties of these complex oxides is due to incorporation of additive metal oxides which changes the surface characteristics and micro-structure (Gupta and Ghosh, 2009; Wu at al., 2012). Compare to single iron oxide, iron oxide based nanocomposites offer a potential material as a result of the synergic effect that is possible among the components. Although iron oxide (Fe_2O_3) is a low cost, non toxic, high chemical stability and visible-light-driven photocatalyst, the single component semiconductor (α-Fe_2O_3) has a number of disadvantageous features including low light harvesting, high recombination rate of electron−hole pairs, and hardly being able to be separated and recycled. Therefore, in recent years, more attention have been paid to combine a variety of different semiconductor metal oxides components and ion doping or introduce noble metals in order to precisely control nanostructures and the corresponding properties (Sun et al., 2014). Iron oxide (Fe_2O_3)-based nanocomposites have been proved to be effective adsorbent materials and photocatalysts with improved sorption properties as well separation efficiency of photogenerated electron-hole pairs.

1.5. Synthetic Techniques of Metal Oxide Nanomaterials

Several synthetic approaches have been developed for synthesizing metal oxide nanomaterials over the past few decades. But the synthesis of nanomaterials with controlled size, shape and morphology has long been of scientific and technological interest. Up to now, many techniques have been developed in the synthesis of metal oxide nanomaterials. Basically, they can be described as two different types: the ‘‘top-down’’ approaches and the “bottom-up’’ approaches. Top-down methods use bulk materials of desired composition, and achieve nanoscale dimensions by lithographic techniques (UV, electron or ion beam, scanning probe, optical near field), laser-beam processing, and mechanical techniques (machining, grinding, and polishing) that essentially carve the desired structure out of the material. However, there are many practical problems in the methods such as: techniques to carve out ever-smaller structures are difficult to find. More importantly, uniformity of bulk crystals on nanometer length scales is not very high, and quality of structures becomes difficult to control (Dick, 2008). “Bottom-up” approaches, on the other hand, exploit the chemical properties of the molecules to cause self-assembling atoms to form increasingly larger structures. Such techniques involve controlled crystallization of materials from vapour or liquid sources, typically yielding uniform and highly ordered nanometer scale structures. The most common bottom-up approaches are chemical synthesis, chemical vapor deposition, laser-induced assembly, self-assembly, colloidal aggregation, film deposition and growth. The bottom-up approach can produce much smaller sized particles and has the potential to be more cost-effective in the future because of the advantages of absolute precision, control over the process, and minimum energy loss compared with that of a top-down approach (Chaudhuri and Paria, 2012). Significant progress has been made over the last decade in understanding fundamental aspects of the synthesis of nanoparticles, nanorods, nanofibers, nanowires, nanotubes, nanoflakes and hierarchical nanostructures. Metal oxides can be prepared using a number of synthetic techniques, which are broadly classified into two categories, namely, physical methods and chemical methods.

1.5.1. Physical Methods

The methods of generation of nanomaterials in the gas or solid phase using high-energy treatment of the material are usually called physical methods. The various physical methods include laser ablation, sputtering, high energy ball milling, vapor deposition, electro-deposition and so on. In our research work we have used chemical methods for synthesis of metal oxide nanomaterials.

1.5.2. Chemical Methods

Chemical synthesis methods are the most promising strategy to exploit science and technology at the nanometer scale, in which the building of materials occur from the bottom i.e. atom by atom, molecule by molecule or cluster by cluster. Various synthesis methods can be grouped into two categories: thermodynamic approach or kinetic approach. In the thermodynamic approach, synthesis process consists of (i) generation of super saturation, (ii) nucleation, and (iii) subsequent growth. In kinetic approach, formation of nanoparticles is achieved by either limiting the amount of precursors available for the growth or confining the process in a limited space. Chemical methods have been playing a major role in developing nanomaterials with desired shapes, morphologies and sizes such as: nanorods, nanofibers, nanowires, nanotubes, nanoplates, nanoflakes, spherical, cubical, elliptical nanoparticles, and nanocomposites with novel and technological important properties. In our study we have followed three chemical methods namely chemical precipitation, reflux and hydrothermal methods for preparation of iron oxide and iron based composite nanomaterials. Brief description of precipitation, reflux and hydrothermal methods for metal oxide nanomaterial synthesis are as follows:

Hydrothermal Method

Hydrothermal method is a chemical method where heterogeneous reaction takes place in the presence of aqueous solvents or mineralizers under high pressure and temperature conditions. This is a process that utilizes single or heterogeneous phase reactions in aqueous media at elevated temperature ($T>25$ ºC) and pressure ($P>100$ kPa) to crystallize metal oxide materials directly from solution. Since ionic product of water (K_w) has a maximum value of around 250-300 °C, hydrothermal synthesis is usually carried out below 300 °C. The crystal growth is performed in an apparatus consisting of a steel pressure vessel called autoclave, which is hermetically sealed in order to withstand high temperatures and pressures for prolonged periods of time. The contribution of the dielectric constant to the reaction rates becomes remarkable based on the electrostatic theory. The main advantages of hydrothermal synthesis over conventional and non-conventional methods is that all forms of metal oxides can be prepared with hydrothermal synthesis, namely powders, fibers, rods, wires, tubes, cubes, spheres, flakes, ellipses and single crystals, monolithic ceramic bodies, and coatings on metals, polymers, and ceramics (Byrappa and Adschiri, 2007; Wojciech et al., 2006). In addition, powders prepared by hydrothermal route are known to produce pure and crystalline oxide powders with relatively narrow size distribution (Panda et al., 2006). For synthesis of metal oxide nanomaterials, first hydrated metal ions are hydrolyzed to metal hydroxide. Then, metal hydroxides proceed to precipitate as metal oxides through dehydration. Hydrolysis is regarded as an electrostatic reaction between metal ions and hydroxyl ions.

Hematite (α-Fe_2O_3) nanotubes have been prepared by hydrothermal method and their catalytic performance for thermal decomposition of ammonium perchlorate was studied (Song et al., 2010). Similarly, SnO_2/graphene (GN) composite was fabricated via a simple one-pot hydrothermal method with graphene oxide (GO) and $SnCl_2$ as the precursors (Lin et al., 2012).

Solvothermal synthesis is a method of producing nanomaterials, which is very similar to the hydrothermal route, the only difference being that the precursor solution is usually different organic solvents rather than aqueous. Zhou et al. (2015) have synthesized ZnO/α-Fe_2O_3 composites in which plenty of ZnO nanoparticles decorated on the surfaces of uniform round-edged α-Fe_2O_3 hexahedrons via a facile solvothermal method using ethylene glycol solvent.

Precipitation Method

Precipitation method is a facile way of synthesis of metal oxide nanomaterials, which attracts considerable interest in industries because of low energy and temperature, inexpensive and cost-effective approach for large scale production and good yield. In this method, precipitation of solids from a solution with metal ions occurs by pH adjustment. In supersaturated solutions, particles are formed via homogeneous or heterogeneous nucleation. The growth of particles usually occurs via diffusion or Ostwald ripening concentration and temperature has a big influence on the growth rate. Particle size and particle size distribution, crystallinity as well as morphology of the nanomaterials are controlled by applying reaction kinetics. The important parameters involve in precipitation method are the concentration, the temperature, the pH of the solution, the order of adding the reactants and mixing processes (Rao and Müller, 2005). Hexagonal zinc oxide (ZnO) nanoparticles have been synthesized by precipitation method using zinc nitrate as a precursor and NaOH starch as a stabilizing agent (Lanje et al., 2013). Co-precipitation method is similar to this method, where two or more precipitants are have been used and usually reaction proceeded at temperature below 100 °C. Pure maghemite (γ-Fe_2O_3) nanoparticles were prepared via co-precipitation method using urea and ammonia as precipitation agent for ferrous and ferric ions at ambient temperature (Wu and Gao, 2013). Superparamagnetic ferrite nanoparticles (MFe_2O_4, where M = Fe, Co, Mn) were synthesized through one-step aqueous co-precipitation method by using alkaline agent, alkanolamines isopropanolamine and diisopropanolamine (Pereira et al., 2012).

Reflux Method

Reflux synthesis methods in wet chemistry include techniques that normally involve relatively lower reaction temperatures compared with hydrothermal synthesis, a very positive aspect in the fabrication of metal oxide nanomaterials. The reflux condensation method can be used when the solvent has boiling point lower (example 50-60 °C) to avoid any loss amount and at same time the temperature of refluxing depends on the dissolve of starting materiel that can produce the final nano-particle. The reflux condensation technique can be used in sol gel or precipitation or any methods. CuO with urchin-like morphologies has been synthesized via a simple reflux method using $Cu(NO_3)_2 \cdot 3H_2O$ and urea precursors dissolved in the solvent of distilled deionized water and ethylene glycol monomethyl ether in a round-bottom flask kept in an oil bath at 100 °C for 6 h (Xu et al., 2009).

1.6. Applications of Metal Oxide Nanomaterials

Metal oxide nanomaterials can exhibit unique physical and chemical properties due to their limited size and a high density of corner or edge surface sites. They have attracted a great deal of attention recent research because of their applications in various fields like catalysis, sensors, optical, electronic, magnetic, biological and environmental remediation like photocatalytic degradation and adsorption of various contaminants from water. In this research work we have focoused on environmental applications of metal oxide nanomaterials specifically adsorptive removal and photocatalytic degradation of organic dyes from aqueous media.

1.6.1. Environmental Applications

Due to worldwide population growth, rapid development of industrialization and use of pesticides, insecticides etc. in agriculture fields, a wide range of organic and inorganic pollutants contaminant the surface and ground water which deteriorates the environment and affects the living organism. Thus, the prevention of the harmful effects of contaminants is necessary to keep the environment safe and improve the human living conditions. The various contaminants persisting in wastewater include heavy metals, inorganic compounds, organic dyes, chlorinated hydrocarbons and many other complex compounds. Organic dyes imparts colour to substances such as textile fibers, leather, plastic materials, papers, or wax either in solution or dispersion. Among industrial wastewater, organic dyes distrached from the textile, lether, plastics and paper industries are major source of organic pollutants. They are very hazardous to living beings and ecological environments. Dye molecules include of two key components: the chromophores, responsible for producing the colour, and the auxochromes, which can not only supplement the chromophore but also render the molecule soluble in water and give enhanced affinity toward the fibers. This is because organic dyes usually have a synthetic origin and complex aromatic structures which make them stable and more difficult to be biodegrade (Gupta and Suhas, 2009). These organic dye contaminants are releasing into the environment through wastewater. Even just 1.0 mg/L of dye concentration in drinking water could impart a significant color, making it unhealthy for human consumption. Furthermore organic dyes can affect aquatic plants because they reduce sunlight penetration into water there by decreasing the efficiency of photosynthesis and hence having adverse effect on their growth. Also dyes molecules may impart toxicity to aquatic life and may be mutagenic, carcinogenic and may cause severe damage to human beings, such as dysfunction of the kidneys, reproductive system, liver, brain and central nervous system. Generally, the organic dyes used in the textile industries are basic dyes, acid dyes, reactive dyes, azo dyes, disperse dyes and sulfur dyes. The organic dyes can be classified as cationic, anionic and nonionic dyes. Cationic dyes are basic dyes while the anionic dyes include acid and reactive dyes (Salleh et al., 2011). Nowadays, there is an increasing concern over worldwide for the development of dye wastewater treatment technologies (Xu et al., 2012). The different processes of removing the dye contaminants present in water to clean the environment by using nanotechnologies are nanofiltration, bioremediation, adsorption by nanomatrerials, photocatalysis by semiconductor metal oxide nanomaterials and so on. Keeping the hazardous nature and harmful environmental effects in view, we have made systematic efforts for complete removal of different organic dyes pollutants from wastewaters by using novel iron oxide based other metal oxide composite nanomaterials adsorbents and photoctalysts.

Adsorption

Adsorption is commonly employed as a polishing step to remove organic and inorganic contaminants in water and wastewater treatment. Efficiency of conventional adsorbents is usually limited by the surface area or active sites, the lack of selectivity, and the adsorption kinetics. Nowadays, nanoadsorbents have been appeared as an alternate source for conventional adsorbents. Metal oxide nanoadsorbents are widely studied due to their unique properties compared to their bulk counterpart (Nassar, 2012). Arising out of their ultrafine size, large surface area, associated sorption sites, short intra-particle diffusion, high density of corner or edge surface sites, tunable pore size, chemical stability and nontoxicity, metal oxide nano-adsorbents offer significant improvement in the field of adsorption (Qu et al., 2013). Chaudhary et al. (2013) have synthesized γ-Fe_2O_3 nanoparticles with controlled morphology using chemical precipitation method and studied adsorptive removal of hazardous azo dye such as Congo red by using the γ-Fe_2O_3 nanoparticles. They reported that 98 % of the dye was effectively removed from water. Hematite (α-Fe_2O_3) nanofibers synthesized by hydrothermal method was found to be a potential adsorbent for removal and recovery of noxious Cr(VI) from wastewater (Ren et al., 2013). Mesoporous γ-Fe_2O_3/SiO_2 nanocomposite prepared by sol-gel method was found to be a superb adsorbent for removal of methyl orange dye from aqueous media with maximum adsorption capacity of 476 mg/g (Deligeer et al., 2011).

Photocatalysis

Photocatalytic oxidation is an advanced oxidation process for degradation of organic dyes and other toxic organic compounds. It is a useful pretreatment for hazardous and non-biodegradable contaminants to enhance their biodegradability. In photogenerated catalysis, the photocatalytic activity (PCA) depends on the ability of the catalyst to create the electron–hole pairs, which generate free radicals (e.g. hydroxyl radicals: $^{\bullet}OH$) which are able to undergo secondary reactions. In recent years, degradation of organic pollutants in waste water is one of the most active areas in heterogeneous photocatalysis. In a heterogeneous photocatalysis system, photoinduced molecular transformations or reactions take place at the surface of a catalyst. Recently, Madrakian et al. (2014) have synthesized γ-Fe_2O_3/TiO_2 nanocomposite by wet chemical method and found that the nanocomposite can efficiently degrade Janus Green B, a cationic dye, and Congo red, an anionic dye under solar light irradiation with better performance than bare TiO_2 nanoparticles. Ahmed et al. (2015) have synthesized nanocrystalline ZnO, α-Fe_2O_3 and $ZnFe_2O_4/ZnO$ by solution combustion method and studied the photocatalytic degradation of Brilliant yellow dye from aqueous solution using the nanomaterials. They reported that $ZnFe_2O_4/ZnO$ showed better photocatalytic activity for the degradation of Brilliant yellow dye than ZnO and α-Fe_2O_3.

1.7. Organization of the thesis

The present thesis is organized into seven chapters. The present chapter (Chapter-1) represents the introduction to nanomaterials, one dimensional nanomaterial, composite nanomaterials, metal oxide nanomaterials, their synthesis and applications. Chapter-2 contains an extensive literature review on metal oxide nanomaterials synthesis by wet chemical methods and their environmental application towards adsorption and photocatalysis of organic dyes from aqueous media. Chapter-3 contains two parts. Both the first and second parts describes the synthesis of $FeC_2O_4.2H_2O$, γ-Fe_2O_3 and α-Fe_2O_3 nanorods and Fe_2O_3-SnO_2 composite nanorods by precipitation method and their application towards adsorption of Congo red dye from aqueous media. Chapter-4 describes synthesis of mesoporous MCM-41 and iron oxide dispersed mesoporous MCM-41 and their application towards adsorptive removal of Methylene blue dye from aqueous solution. Chapter-5 contains two parts. The first part represents the synthesis and high adsorption properties of MgO nanomaterials with three different morphology for removal of malachite green and Congo red dyes. The second part describes the synthesis of magnesium ferrite nanocomposites by three different wet chemical methods for photocatalytic degradation of Methylene blue dye form aqueous solution under solar light irradiation. In Chapter-6, the synthesis of one dimensional Fe_2O_3-CuO nanocomposites and their photocatalytic activity towards degradation of Methyl orange dye have been discussed. Chapter-7 is about the synthesis of ternary $Fe_2O_3/ZnFe_2O_4/ZnO$ nanocomposites and their enhanced photocatalytical activity for degradation of Malachite green dye under solar light irradiation. Finally, Chapter-8 concludes our research works and highlights our contribution.

CHAPTER 2

REVIEW OF BACKGROUND LITRATURE

In this chapter, we have reported a review of the current developments in the area of synthesis and characterization of iron oxide and iron oxide based nanocomposites, ferrites, and mesoporous MCM-41 nanomaterials using different chemical methods such as: precipitation, hydrothermal and reflux methods. Apart from this the basic principles of formation along with the advantages and disadvanges using these synthetic techniques have been briefly presented. Again, the environmental applications of these metal oxide nanomaterials such as: adsorption and photocatalytic degradation of organic dyes have also been discussed.

2.1. Precipitation Method

Precipitation method is a simple and well established wet chemical processes in which solutions of the different ions are mixed under controlled temperature, concentration and pH to form insoluble precipitates. Precipitation approach in comparision to with other traditional methods provides a facile way for low cost and large-scale production, which does not need expensive raw materials and complicated equipments. In this method, particle growth takes place by interaction between different ions present in the solutions and therefore very small particles are formed via diffusion or Ostwald ripening concentration and temperature. Tiny size particles with lower solubility product dissolve and re-precipitate on the surface of larger particles in solution; consequently agglomeration takes place in solution as the particles clog together to minimize surface energy (Bagheri et al., 2013). In this method the particles size, size-distribution, crystallinity as well as morphology of the prepared nanomaterials are controlled by applying reaction kinetics.

Advantages: The precipitation method is the simplest, most efficient, environment friendly and rapid preparative chemical pathway to obtain metal oxide nanomaterials. The main advantage of the precipitation method is that a large scale production of nanomaterials can be achieved within a short time interval. Easy control of composition with better homogeneity can be made in this method and also, there are various possibilities to modify the particle surface. Moreover the precipitation reaction can be carried out mostly in aqueous or greener solvent media, which are environment friendly (Nazari et al., 2014; Mohapatra and Anand, 2010; Kumar et al., 2013; Vivekanandhan, 2010).

Disadvantages: The control of particle size distribution is limited, because only kinetic factors are controlling the growth of the crystal. Universal experimental condition for the synthesis of various types of metal oxides is not possible by this method. It is not a suitable method for the reactants having different solubility as well as different precipitate rate (Mohapatra and Anand, 2010; Vivekanandhan, 2010).

2.1.1. Metal oxide nanomaterials by precipitation method

Nanorods as one-dimensional nanomaterials have attracted much attention due to their peculiar properties, which is due to their high surface area and low dimensionality. One-dimensional (1-D) metal oxide nanostructures are the most important nanostructures and recent research on the synthesis and application of 1D nanomaterial in various fields. They have gained great attention as a key component in ceramics, catalysis, sensors, transparent conductive films, electro-optical and electro-chromic devices. Intensive studies have been carried out on the synthesis of metal oxide nanowires as well as the exploration of their novel properties (Shen at al., 2009; Li et al., 2010; Comini et al., 2009). Yao et al. (2011) have prepared porous hematite (α-Fe_2O_3) nanorods, having diameters of 30-60 nm (figure 2.1), through thermal decomposition of $FeC_2O_4{\cdot}2H_2O$ nanorods which were readily synthesized through poly(vinyl alcohol)-assisted precipitation process. They have reported that the formation of porous structure of the nanorod due to the release of CO_2 during the decomposition of $FeC_2O_4{\cdot}2H_2O$. Compared to the commercial α-Fe_2O_3 submicrometer powders, the porous α-Fe_2O_3 nanorods are revealed as a superior electrode material in lithium-ion batteries, due to their nanorod shape and porous structure.

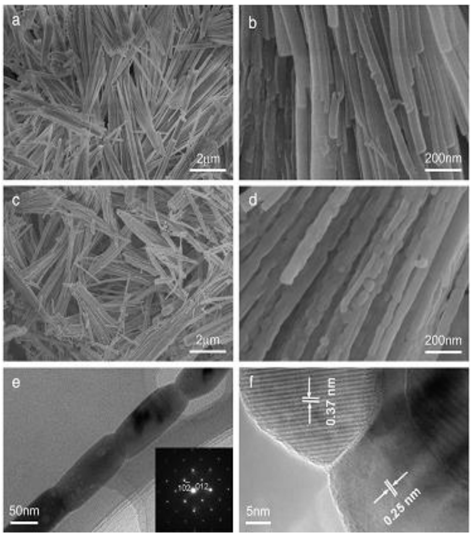

Figure 2.1 (a, b) SEM images of $FeC_2O_4{\cdot}2H_2O$ nanorods; (c, d) SEM images of α-Fe_2O_3 nanorods, (e) TEM image of a individual α-Fe_2O_3 nanorod, the inset is the corresponding SAED pattern, (f) HRTEM image of the α-Fe_2O_3 nanorod (Yao et al., 2011).

Qiaoling et al. (2009) have synthesized one dimensional (1D) hematite (α-Fe_2O_3) nanorods with average diameter 60 nm and length up to 800 nm by simple chemical precipitation method. During preparation of α-Fe_2O_3, the length of α-Fe_2O_3 was found to be increased by the addition of polyethylene glycol (PEG) and the diameter was found to be decreased by addition of Zn^{2+}. MgO nano-rods of several microns in length and 50-100 nm in width were prepared by Sutradhar et al. (2011) by calcining nesquehonite phase, which was obtained by simple precipitation using $(NH_4)_2CO_3$ under ambient condition. The preparation method was flexible and easily scalable which avoids extreme reaction conditions, high pressure treatment and longer processing time. It was based on controlled growth of nesquehonite phase in unique rod morphology using cheap and abundant chemicals. The synthesized MgO nano-rod exhibited strong activity in solvent-free base catalyzed Claisen-Schmidt condensation giving 99 % conversion in 2 h and was easily recyclable with no significant change in catalytic activity. Sangari and Devi (2013) have synthesized ZnO nano rods by reacting zinc nitrate and potassium hydroxide via microwave assisted chemical precipitation method. The amount of potassium hydroxide was adjusted for three different pHs to achieve ZnO nano rods with varying aspect ratio. From figure 2.2, it is observed that at pH 9 and 11, ZnO powder exhibited well separated rods with few tetrapod and flower-like structures with each petal having the single hexagonal rod shape respectively.

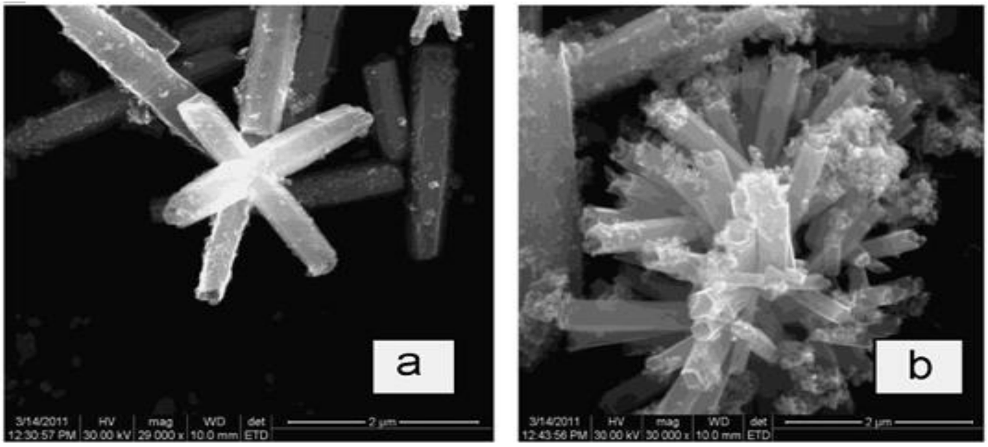

Figure 2.2 SEM images of synthesized ZnO rods obtained at (a) pH 9 and (b) pH 11 (Sangari and Devi, 2013).

Very fine, single crystalline hexagonal nano crystals of γ-Fe_2O_3 (maghemite) with particle size of ~70-100 nm were synthesized by emulsion precipitation method using kerosene as oil phase, SPAN-80 (sorbitane monooleate) as the surfactant and sodium hydroxide as the precipitating agent. When the γ-Fe_2O_3 was calcined in the temperature range of 500 to 850 °C, the γ-Fe_2O_3 was transferred to α-Fe_2O_3 (hematite) nanoparticles (Sahoo et al., 2010). Sarangi et al. (2009) have synthesized single-phase α-Fe_2O_3 nano-powders with particle size~20–30 nm using two simple chemical precipitation methods. In method 1, an aqueous solution of ferric nitrate was mixed with aqueous solution of PVA by vigorously stirring. Then, a dark brown colored fluffy precursor was formed when this mixture was dried and calcined in air for 2.30 h at 250 to 450 °C to form α-Fe_2O_3 nanoparticles. In method 2, they have followed the first method by using EDTA solution instead of PVP solution. BET surface area of calcined powders, prepared from method-1 and method-2, was found to be 35 and 20 m^2/gm, respectively. In 2013 Naje et al. have synthesized nanocrystalline tetragonal rutile SnO_2 with crystalline size in the range of 8-10 nm by a chemical precipitation method. In a typical synthesis procedure, they added ammonia solution to stannous chloride dehydrate ($SnCl_2.2H_2O$) solution drop wise under stirring to form gels, which was dried and calcined at 550 ºC for 2h to form SnO_2 nanopowder. Bakhtiari et al. (2011) have synthesized CuO nanoparticles by the direct thermal-decomposition of brochantite ($Cu_4(SO_4)$ $(OH)_6$) at 750 °C for 2 h. The brochantite was synthesized by precipitation method in which Na_2CO_3 solution was added drop wise to copper (II) sulfate solution with vigorous stirring to form green precipitate. The green precipitate was then filtered and dried at 70 °C for several hours to form brochantite. Similarly, semiconductor CuO nanoparticles were synthesis by a simple precipitate method using copper acetate and glacial acetic acid precursor. In a typical procedure, copper acetate aqueous solution was mixed with glacial acetic acid and aqueous NaOH solution was added to the mixture at different temperatures until the pH value of the mixture reached to 6.5. A large amount of the black CuO precipitate was produced which was stirred for 30 min at different temperatures (10, 20, 60 and 115 °C) to form CuO nanoparticles. It is observed that in the absence of ultrasonic irradiation needle-like CuO nanostructures with an average diameter of 16–27 nm were formed and under ultrasonic condition uniform CuO spherical nanoparticles with particle size distribution in the range of 12–15 nm were obtained. The band gap of samples was estimated to be in the range of 1.9–2.9 eV that is larger than the reported value for the bulk CuO (1.85 eV). Wang and co-workers (2007) have synthesized MgO nanoplates via chemical precipitation using ammonia hydroxide as precipitator in the presence of a nonionic surfactant polyethylene glycol (PEG 400). It is observed that the particles have a plate-like shape with thickness is in the range of 10–20 nm and length is up to 100 nm when less amount of ammonium hydroxide is used and the MgO particles aggregate into large flocks, which could be attributed to the relative deficiency of PEG 400 to cap the precursor with the increase of the nuclei, when high of $NH_3 \cdot H_2O$ is used. In 2012, Veldurthi et al. have synthesized single crystals of mesoporous plate-like MgO nanoparticles using a simple precipitation method without using any templates. Initially, $Mg(OH)_2$ was synthesized by the precipitation of magnesium nitrate solution and then the $Mg(OH)_2$ was calcined to form plate-like MgO nanocrystals. Yadav et al. (2008) have synthesized ZnO nanomaterial through pyrolysis of the oxalate, which was produced by a conventional precipitation method. In the method, a sodium oxalate solution was mixed with a zinc sulphate solution at room temperature in the molar ratio 1:1 to yield a precipitate of zinc oxalate. This precipitate was filtered out and washed, dried and calcined at 450 °C for 15 min to form zinc oxide nanopowder. The prepared ZnO nanoparticles have good sensing properties for water vapour. Chen and co-workers (2008) have synthesized ZnO nanoparticles by direct precipitation method via the reaction between Zinc nitrate ($Zn(NO_3)_2$) and ammonium carbonate ($(NH_4)_2CO_3$) in aqueous solutions. The SEM morphology (figure 2.3) of the nano-sized ZnO particles suggested that the particles are pseudo-spherical in shape. Moharram et al. (2014) have synthesized ZnO nanoparticles with crystalline size about 22.4±0.6 nm through hydrolysis and condensation of zinc acetate dihydrate by potassium hydroxide in alcoholic medium at low temperatures. Similarly, Gao et al. (2013) have synthesized hierarchically structured ZnO nanocrystallite aggregates through an interface precipitation method by taking zinc acetate dihydrate and NaOH precursor in water and ethanol medium and Raoufi (2013) has prepared zinc oxide (ZnO) nanoparticles by precipitation method from zinc nitrate and ammonium carbonate in aqueous solutions.

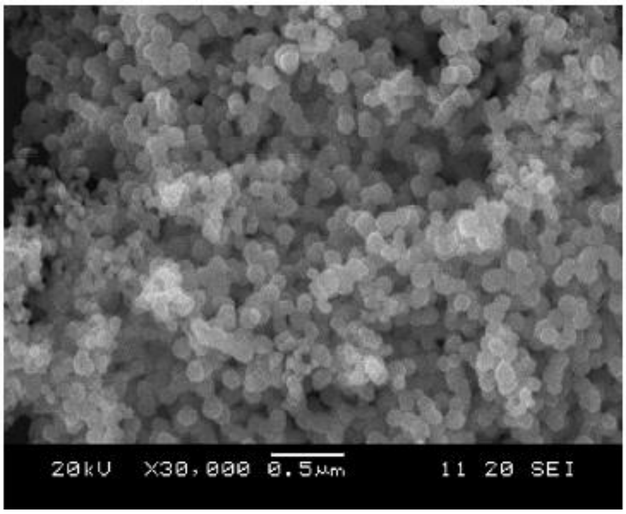

Figure 2.3 SEM photograph of the nano-sized ZnO powders (Chen et al., 2008).

2.1.2. Mixed metal oxide nanocomposites by precipitation method

Nowadays, the synthesis of mixed metal oxide nanocomposites has attracted much interest of researchers. These mixed oxides are attractive with respect to applications in catalysis, sensing, adsorption, energy storage, electronics and many more. The combination of 2 metals in an oxide matrix can produce materials with novel structural and/or electronic properties.

The unique properties arise due to metal-metal or metal-oxygen- metal interactions in mixed metal oxides may not be seen in single-metal oxides (Park et al., 2009).

Azhari et al. (2010) synthesized Fe_2O_3/MgO nanocomposite via a simple precipitation route in which a dispersed system containing nano-MgO flakes and nano-Fe_2O_3 particles was obtained. In a typical synthesis procedure, suspension of iron oxide was added to magnesium sulfate solution and then ammonia (NH_4OH, 25 wt. %) as the alkaline agent was added drop wise to the suspension with vigorous stirring to adjust pH to 11. Then, the product was washed, dried and heated at 475 °C for 1h to convert magnesium hydroxide to magnesium oxide and finally calcined at 600 °C to form Fe_2O_3/MgO nanocomposite. Chu et al. (2009) have synthesized In_2O_3–SnO_2 nanocomposites with controllable morphologies via a precipitation method. In a typical procedure, tin (II or IV) chloride and different molars of indium (III) nitrate were dissolved in 40 mL absolute ethanol at room temperature and 40 ml of ethanol solution that contains 1.2 g KOH were slowly dripped into the mixed metal salt solution under stirring to form a precipitate. Then, the precipitate was washed, dried and calcined at 600 °C to form of In_2O_3–SnO_2 nanocomposite. They have found that variation of In/Sn ratios facilitated the modification of In_2O_3–SnO_2 morphology from nanoparticles to nano-toasts and nanorods that possess ultrahigh response and selectivity to ethanol. Narkiewicz and co-workers (2008) have synthesized series of ZnO nanosized samples doped with wide range of Fe_2O_3 concentration (5-95 wt. %) by precipitation from nitrate solutions using ammonia. Initially, mixture of iron and zinc hydroxides were obtained by addition of ammonia solution, proper amount of $Zn(NO_3)$. $6H_2O$ and $Fe(NO_3)_3.4H_2O$ in water. Then, the obtained hydroxides were filtered, dried and calcined at300 °C for 1 h. A series of samples containing from 5- 95 wt % of Fe_2O_3 was obtained using this method. From XRD result it was observed that, different phases are formed with respect to Fe_2O_3 concentration such as: $ZnFe_2O_4$ phase for 5-10 wt % Fe_2O_3 concentration, composite ZnO-$ZnFe_2O_4$ for 30 & 40 wt % Fe_2O_3 concentration, again $ZnFe_2O_4$ phase for 50-80 wt % Fe_2O_3 concentration and Fe_2O_3 phase for 90 & 95 wt % Fe_2O_3 concentration. Uniform MgO/CNT nanorods were fabricated by Taleshi and Hosseini (2012) using precipitation method. In this work, they used carbon nanotubes (CNTs) as a support for synthesis, size control, and morphology of magnesium oxide. The morphology of MgO nanoparticles were varying by changing the weight percent of CNTs in the solution. Basu and Ghosh (2013) synthesized nano-structured iron(III)–cerium(IV) mixed oxide by a facile precipitation method. In a typical procedure, NaOH solution was added drop wise to ammonium cerium (IV) nitrate and ferric chloride solutions with continuous stirring to raise pH 9.3 (±0.3). The obtained gel-like precipitate was allowed to stand for two days, then washed and dried at 100 °C in an air oven. The dried product was grinded using mortar and pestle followed by sieving to separate the agglomerates. From figure 2.4 TEM image, it is observed that the bimetal mixed oxide contained agglomerated crystalline nano-particles of dimension 10-20 nm. The synthesized iron(III)–cerium(IV) mixed oxide nanomaterial was regarded as an excellent adsorbent for removal of carcinogenic arsenic ion from aqueous solution.

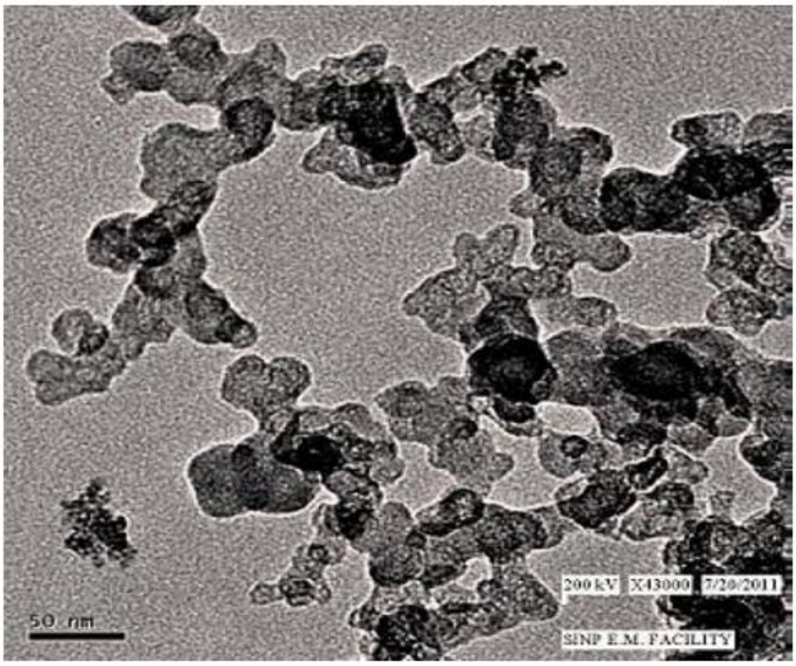

Figure 2.4 TEM image of nano-structured iron(III)–cerium(IV) mixed oxide (Basu and Ghosh, 2013).

Cao et al. (2014) have fabricated Fe_3O_4/chitosan nanoparticles with quasi-spherical or ellipsoidal in shape and about 7 nm in average diameter by a simple reduction–precipitation method through partial reduction of Fe^{3+} before the formation of Fe_3O_4 nanoparticles. Typically, $FeCl_3$ solution was added into chitosan solution under continuous stirring for 1 h. Then, Na_2SO_3 solution was added into the yellow colloidal solution of chitosan, and the color of the mixed solution immediately changed from yellow to red and again from red to yellow. Then mixed solution was poured quickly into ammonia solution under vigorous stirring at room temperature to form black precipitate suspension. After that, cross-linking agent epoxy chloropropane was added to the black suspension solution in order to stabilize Fe_3O_4/CS NPs in acid solution. The prepared MFe_3O_4/CS NPs exhibited high adsorption capacity and removal rate for brilliant red X-3B dye. Again in 2015, Cao et al. have synthesized Cu_2O/chitosan–Fe_3O_4 nanocomposite (Cu_2O/CS–Fe_3O_4 NC) with large specific surface areas and special dimodal pore structure via a facile one-step precipitation-reduction process by using magnetic chitosan chelating copper ions as precursor. Initially, they have prepared CS–Fe_3O_4 by using their previous method. The as-prepared CS–Fe_3O_4 NPs were dissolved acid solution and $CuSO_4·5H_2O$ and glucose were added into above colloidal solution under continuous stirring until they fully dissolved. The obtained mixture was then kept in water bath at 54 °C and pH value was adjusted to 10. Then, cross-linking agent epoxy chloropropane was added to stabilize Cu_2O/CS–Fe_3O_4 NCs in acid solution. The prepared Cu_2O/CS–Fe_3O_4 NCs were used as an effective photocatalyst for decolorization of reactive brilliant red X-3B (X-3B) under visible light irradiation and it was observed that the decolorization rates of X-3B were still above 87 % after five reaction cycles. Synthesis of mixed metal ferrites is also possible through precipitation method. Shinde et al. (2008) have prepared polycrystalline cubic spinel structured ferrites with general formula $Ni_{1-x}Zn_xFe_2O_4$ (x=0, 0.2, 0.4, 0.6, 0.8, and 1.0) using oxalate precipitation method. They observed that the average crystallite size of the ferrites were in the range 27.59–31.49 nm.

2.2. Hydrothermal Method

In this method heterogeneous reaction is carried out in the presence of aqueous solvents under high pressure and temperature conditions using a hydrothermal vessel. Hydrothermal reaction is normally accompanied in steel pressure vessels called autoclaves (hydrothermal vessel) with or without Teflon liners under controlled temperature and/or pressure in aqueous solutions. The process involves elevation of temperature above the boiling point of water at the pressure of vapour saturation. This method is cost-effective and easy route for preparing various metal hydroxides and oxy-hydroxides at low temperature and in a short reaction time and widely used for the production of small particles in the ceramics industry (Sahin, 2004; Chen et al., 2006).

Advantages of hydrothermal method: The method is useful for synthesis of low temperature phases and metastable compounds. Compounds having elements with an unusual oxidation state can be synthesized by this method. Nanopowders are formed directly from the solution. It is possible to control particle size and shapes by using different starting materials and hydrothermal conditions. Monodispersed and highly homogeneous metal oxide nanomaterials (Nanoparticles/nanorods) can be prepared by this method. The method acts as one of the most attractive techniques for processing nanocomposite and nano-hybrid materials. Less time consumption, rapid growth rates (because of the rapid diffusion processes), low cost, high product purity, environment friendly and the ability to control the particle size are the other strengths of this method (Byrappa and Adschiri; 2007; Sahin, 2004; Wojciech et al., 2006; Vivekanandhan, 2010).

Disadvantages of hydrothermal method: The method includes the need of expensive autoclaves. Observing the crystal as it grows is not possible. Hydrothermal slurries are potentially corrosive. Accidental explosion of the high pressure vessel cannot be ruled out (Vivekanandhan, 2010; Byrappa and Adschiri; 2007).

2.2.1. Metal oxide nanomaterials by hydrothermal method

Properties of metal oxide nanomaterials are widely depend on their size, shape and morphologies. Nowadays, synthesis of metal oxide nanomaterials with controlled shape and methodologies and surface modification has attracted increasing attention in biological, electronics, and environmental applications including chemical sensing, photocatalytic degradation, separation, and purification of toxic molecules from the matrices. Development simple and reliable synthetic techniques for low-dimensional metal oxide nanostructures with designed chemical components and well-ordered morphologies can easily achieved by hydrothermal method.

Li et al. (2008) have synthesised Uniform α-Fe_2O_3 nanorods with high aspect ratios in large scale by a simple and direct 1, 2-propanediamine-assisted hydrothermal method. In this method, they mixed $FeCl_3$ solution and 1, 2-propanediamine with vigorous stirring and then transferred the above solution into Teflon-lined stainless-steel autoclave for hydrothermal treatment at 180 °C for 16 h. They have reported the formation of α-Fe_2O_3 nanorods by varying the 1, 2-propanediamine content, pH value, concentration of $FeCl_3$ and reaction temperature. By this method they found high yield rod like products with a diameter of 30–40 nm and length of 400–600 nm (figure 2.5). Pradhan and Parida (2011) have synthesized α-Fe_2O_3 nanorods and nano-hexagons by facile hydrothermal method. In a typical experiment, stoichiometric amounts of $(NH_4)_2HPO_4$ were added to aqueous solution of $FeCl_3.6H_2O$, under vigorous stirring to form a yellow homogeneous solution. Then the solution was then sealed into a Teflon-lined autoclave, followed by hydrothermal treatment at 220 °C for 12, 24 and 36 h. They also prepared α-Fe_2O_3 nanostructures by adding surfactant SDS and PEG following the same method. It is observed that addition of SDS doesn’t affect the surface structure of the nanorod. On the other hand, when the system was added with PEG, hexagonal-shaped nanoparticles were obtained.

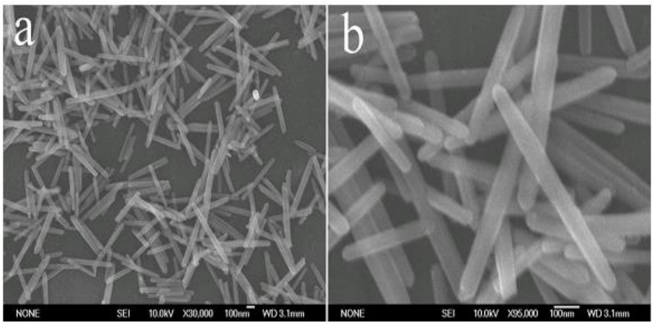

Figure 2.5 SEM images of the α-Fe_2O_3 nanorods: (a) low-magnification SEM image and (b) high-magnification SEM image (Li et al., 2008).

Xiao and co-workers (2012) have successfully synthesized single-crystalline α-FeOOH nanorods with a length of 400–700 nm and a diameter of 20–80 nm via a facile template-free hydrothermal method using $Fe(NO_3)_3.9H_2O$ and KOH as the starting materials. The α-FeOOH precursors were calcined at 350 °C in air and at 500 °C in nitrogen, respectively to form single-crystalline mesoporous α-Fe_2O_3 and Fe_3O_4 nanorods, with large specific surface area and porosity. Similarly, α-Fe_2O_3 nanorods of average ∼40 nm in diameter and ∼400 nm in length were successfully fabricated by Lin and co-workers in 2011 through hydrothermal method. They have added iron chloride hexahydrate ($FeCl_3.6H_2O$) solution to 1, 2-diaminopropane ($C_3H_{10}N_2$) at a 1:1 volume ratio with continuous stirring 15 min. Then the solution was transferred to a Teflon-lined stainless steel autoclave and heated to 220 °C for 20 h. TEM image of the prepared nanorod hydrothermal method is shown in figure 2.6. This indicates the periodic lattice fringes across the entire nanorod and each of the nanorods is a monocrystal and the calculated lattice spacing is 3.65 Å, corresponding to the (012) plane of α-Fe_2O_3.

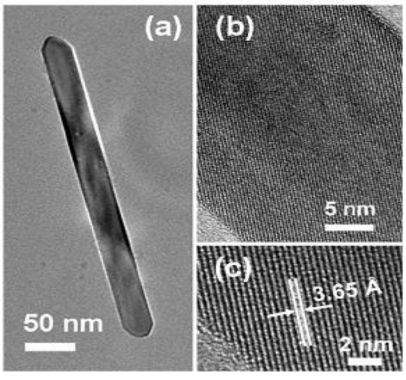

Figure 2.6 TEM images of a single α-Fe_2O_3 nanorod (a) at a low magnification (b) at a medium magnification, and (c) at a high magnification. The white arrows and solid lines in panel c indicate two consecutive lattice fringes (Lin et al., 2011)

Other 1D metal oxide nanostructures such as; MgO, CuO, SnO_2, ZnO were also synthesized by hydrothermal method. Wen et al. (2013) have synthesized mesoporous rhombic ZnO nanorod arrays by a facile fluorine-mediated hydrothermal method. In a typical procedure, 4 mmol $Zn(NO_3)_2 \cdot 6H_2O$, 16 mmol NH_4F and 8 mmol hexamethylenetetramine ($C_6H_{12}N_4$) were dis-solved in 40 ml water. After stirring, the homogeneous solution was transferred into a 50 ml Teflon-lined stainless steel autoclave and then a piece of titanium foil was immersed. The autoclave was maintained at 95 °C for 24 h and obtain the precursor Zn(OH)F were converted to ZnO via thermal decomposition at 450 °C in air for 4 h. From SEM images (figure 2.7), It is observed that in the absence of NH_4F, the surface of the substrate is covered with hexagon-shaped nano-rods of diameter more than 500 nm; for 4 mmol NH_4F, hexagon-shaped nanorods and rhombic nano-wires coexist in the product and for 8 mmol, rhombic nanowires are the only morphology while the hexagon-shaped NRs disappear entirely; again for 16 mmol of NH_4F, the morphology retains a rhombus-shaped architecture, and shows complete nanorods. The prepared ZnO nanorod array based gas sensor showed high performance for ethanol detection.

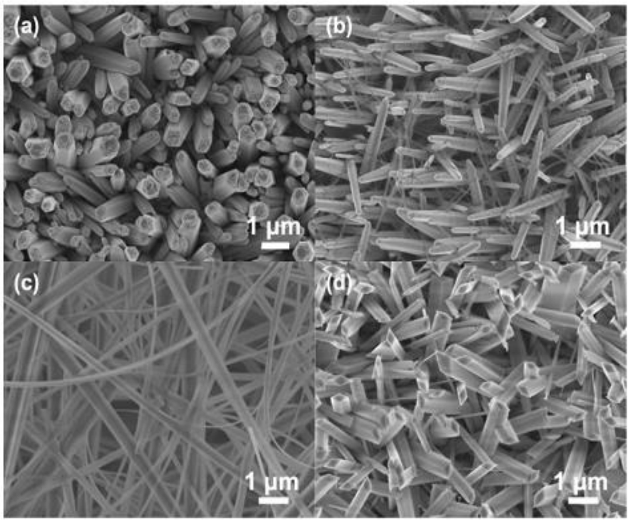

Figure 2.7 SEM images of ZnO nanostructures with different concentrations of NH_4F: (a) 0 mmol, (b) 4 mmol, (c) 8 mmol and (d) 16 mmol (Wen et al., 2013)

Jiang and co-workers (2013) have synthesized SnO_2 nanorods with the diameter of 25 nm and the length of 200-300 nm by a facile one-step hydrothermal route. NaOH solution was added into $Na_2SnO_3.3H_2O$ aqueous solution with continuous stirring, and then absolute ethanol was slowly added into the mixed solution followed by transformation into a Teflon-lined auto-clave and kept at 210 °C for 48 h. After cooling to room temperature, the resulting precipitates were collected and washed and dried to form SnO_2 nanorod. Dhaouadi et al. (2011) have synthesized Magnesium hydroxide ($Mg(OH)_2$) nanorods with a diameter between 10 and 40 nm and a length of up to 300 nm by a simple and facile hydrothermal method in the presence of cetyltetramethylammonium bromide (CTAB) as a surfactant. In a typical procedure, they have dispersed commercial MgO powder in aqueous solution of CTAB with sufficient stirring and the solution was transferred into a Teflon-lined stainless steel autoclave and maintained at 200 ℃ for 24 h. The resulted powders were filtered, washed and dried in vacuum at 80 ℃ for 2h to form $Mg(OH)_2$ nanorod. The $Mg(OH)_2$ nanorods were found to exhibit higher antibacterial efficiency against several tested bacterial strains such as: Staphylococcus aureus ATCC 6538, Enterococcus faecalis ATCC 29212, Enterococcus faecium ATCC 19434, Bacillus cereus, Bacillus subtilis, Staphylococcus feacalis and Streptocoque B (Streptococcus agalactiae).

Similarly, CuO nanoneedles were synthesized by Dar et al. (2008) using hydrothermal method. They have mixed NaOH solution with $Cu(NO_3)_2.3H_2O$ solution and then the mixed solution was transferred into a Teflon-lined stainless steel autoclave maintained at a temperature of 120-180 °C for 20-60 h followed by cooling to room temperature. The obtained black precipitate was washed and dried at 75 °C for 6 h to form CuO nanoneedles with typical diameters of the stem part and the sharp ultrathin nanotip that range between 70±10 and 15±5 nm, respectively, and the whole length of nanoneedle appears to be 500 nm to 1 µm. The authors have studied the magnetic properties of CuO nanoneedles using a superconductor quantum interference device (SQUID) magnetometer, and found a ferromagnetic behavior of the CuO nanoneedles with coercivity of 42 Oe at 3 K. The synthesized CuO nanoneedles may be implicated to various applications such as drug delivery, magnetic resonance imaging and field emission devices.

Recently, porous α-Fe_2O_3 nanospheres with diameter about 50 nm have been successfully prepared by Deng et al. (2013) using a microwave-assisted hydrothermal method. In a typical synthesis, 0.5 mmol of $FeCl_2 \cdot 4H_2O$ and 1.5 mmol of sodium acetate were dissolved into 40 ml of distilled water, and then heated by microwave method with power of 800 W for 10 min. Finally, the product was cooled, washed, dried and annealed at 500 °C for 2h. The porous α-Fe_2O_3 nanosphere-based sensor offered a fast response, superior sensitivity and outstanding selectivity towards H_2S due to its intrinsic characteristics, porous structure and nanoscale size. Hu et al. (2007) have developed a fast and economical route based on an efficient microwave-assisted hydrothermal process to synthesize self-assembled hierarchical α-Fe_2O_3 nanoarchitectures on a large scale. 30 mL of an aqueous $K_3[Fe(CN)_6]$ solution was sealed in a Teflon-lined double-walled digestion vessel and treated at a controllable temperature for 10 min in a microwave digestion system, thereafter the product was collected, washed with deionized water and absolute ethanol, and dried in a vacuum at 80°C for 4 h. Figure 2.8 clearly reveals that the product is composed of a large quantity of uniform dendritic architectures with many hierarchical fractals with six symmetric trunks, forming “star-like” architectures.

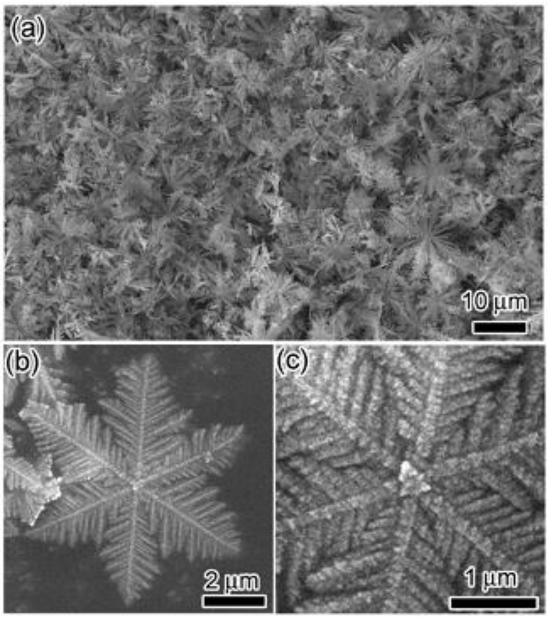

Figure 2.8 (a) Low-magnification and (b, c) high-magnification SEM images of the hierarchical α-Fe_2O_3 nanoarchitectures (Hu et al., 2007)

Single-crystalline α-Fe_2O_3 hollow nanocrystals from nanotube to nanoring have been successfully synthesized by Fan et al. (2009) using a facile hydrothermal method. They have used $FeCl_3$ and $NH_4H_2PO_4$ precursors as solutions followed by hydrothermal treatment at 220 °C for 60 h. The red precipitate obtained was centrifuged, washed and dried under vacuum at 80 °C to form the hollow α-Fe_2O_3 nanocrystals. They have also studied the size- and shape-dependent optical response of these hollow nanocrystals using steady absorption and femtosecond OHD-OKE measurements. Ma et al. (2010) have reported size- and shape-controlled fabrication of α-Fe_2O_3 via a facile template-free hydrothermal route by simply changing only reaction time and solvent. In this report, $FeCl_3 \cdot 6H_2O$ was dissolved in ammonia-water under mild stirring and the brown precipitate floccules immediately formed were transferred into a Teflon-lined stainless steel autoclave followed by heating to 180 °C for 8 h to form red precipitate of α-Fe_2O_3 nanoparticles of 80 nm in diameter. While the reaction time was continued to 24 h, nanoparticles-aggregated α-Fe_2O_3 microcubes with edge about 1µm could be obtained. The SEM, TEM, and HR-TEM images of the prepared nanoparticles and microcubes were given in figure 2.9. They have also done magnetic measurement of the prepared nanostructutrs. The magnetic hysteresis measurements demonstrated that the as-obtained α-Fe_2O_3 nanostructures show structure-dependent magnetic properties.

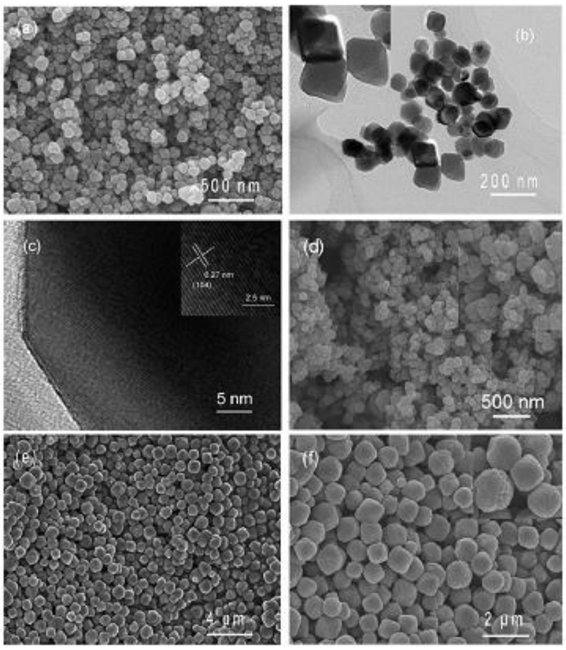

Figure 2.9 (a) SEM, (b) TEM, and (c) HRTEM images of α-Fe_2O_3 nanopolyhedra; (d) SEM image of α-Fe_2O_3 nanoparticles; (e and f) SEM images of nanoparticles-aggregated α-Fe_2O_3 microcubes (Ma et al., 2010).

Other metal oxide nanostructure such as: MgO, ZnO and CuO with different morphologies also have been synthesized by hydrothermal method. Li et al. (2012) have synthesized mesoporous MgO nanoplate adsorbent with mesopore diameter of 10-20 nm by hydrothermal method using Dioctylsulfosuccinate sodium surfactant (AOT) as a structure-directing agent. In a typical synthesis, MgO was added into deionized water containing different concentrations of AOT surfactant with ultrasonically stirred for 10 min followed by hydrothermal treatment for 24 h at 160 °C. The white $Mg(OH)_2$ precipitate was calcined at 600 °C for 3 h in air to produce porous MgO samples. The prepared MgO nanomaterials were used as adsorbents for removal of three typical azo dye pollutants, Congo red, Methyl orange and Sudan III. Because of their higher specific surface area and porous structure, the MgO materials exhibited a satisfactory adsorptive property with maximum adsorption capacities of 588, 370 and 180 mg/g for Congo red, Methyl orange and Sudan III, respectively.

In 2011 Xie and co-workers have successfully synthesized flower-like and sheet-like ZnO structures by hydrothermal method. First aqueous precursor was prepared by zinc nitrate hexahydrate ($Zn(NO_3)_2\cdot 6H_2O$) and hexamethylenetetramine (HMT) and was transferred into a teflon-lined stainless steel autoclave. A piece of substrate, coated with pre synthesized ZnO seeds, was placed in the bottom of the autoclave. The reaction pressure was 5 MPa and the temperature was 150 °C. Finally, the substrate was thoroughly washed with deionized water to eliminate residual salts, and dried in air. The obtained ZnO nanostructure was consisting of numerous flower-like aggregates made up of many thin nanosheets with an average about 80 nm in thickness and 500 nm in length. The obtained nanomaterials were applied as photocatalyst for degradation of Methyl orange from aqueous solution under UV light irradiation. The results indicated that the sheet-like ZnO nanostructures exhibited higher photodegradation efficiencies under UV light irradiation than flower-like ZnO structures due to the blue shift of the bandgap.

2.2.2. Mixed metal oxide nanocomposites by hydrothermal method

Metal oxide nanocomposite cannot be considered as a simple superposition of the properties of individual components due to the strong surface interactions between the closely packed nanoparticles in the multiple metal oxide systems. Here mixing of two or more metal oxide phases can be controlled on both the molecular and the nanoscale. These metal oxides are attractive with respect to applications in catalysis, adsorption, sensing, energy storage, electronics and many more. Numerous investigations are being carried out for production of mixed metal oxide nanocomposite in recent past few years.

Hierarchical α-Fe_2O_3/SnO_2 composites were synthesized by a low-cost and environmentally friendly hydrothermal strategy by Sun et al. (2013). Initially, they have synthesized SnO_2 hierarchical nanostructures by using $SnSO_4$ and $Na_3C_6H_5O_7 \cdot 2H_2O$ in alcohol-water solution followed by hydrothermal treatment at 80 °C for 12 h. For synthesis of α-Fe_2O_3/SnO_2 composites, the above prepared SnO_2 powder was dispersed in deionized water under magnetic stirring and $FeCl_3 \cdot 6H_2O$ and $Na_2SO_4 \cdot 10H_2O$ were added into the above solution. After that, the formed suspension was transferred into a Teflon-lined stainless-steel autoclave and heated at 120 °C for 8 h. The resulting product was centrifuged, washed, dried and finally annealed at 500 °C for 2 h to form hierarchical α-Fe_2O_3/SnO_2 composites. The FESEM and TEM results revealed that the α-Fe_2O_3 nanorods grew epitaxially on the surface of SnO_2 nanosheets. The diameter and length of the α-Fe_2O_3 nanorods were about 10 and 80 nm, respectively, and the thickness of the SnO_2 nanosheets was about 15 nm. They have studied the acetone sensing properties of the prepared nanocomposite and have reported that hierarchical α-Fe_2O_3/SnO_2 nanostructures exhibited an enhanced acetone sensing properties compared with the primary SnO_2 nanostructures. Wang et al. (2012) have synthesized a novel hierarchical SnO_2-Fe_2O_3 heterostructure, consisting of a micron-sized primary SnO_2 nanosheet base and sub-10 nm diameter Fe_2O_3 nanorod branches grown on the nanosheet surface by a facile two-step hydrothermal growth method. Initially, SnO_2 nanosheets were synthesized by a modified hydrothermal method using $SnCl_2.2H_2O$ and NaOH precursor solutions at 160 °C for 14 h. For synthesis of SnO_2-Fe_2O_3 heterostructures, the previously prepared SnO_2 nanosheet powder was placed in a Teflon-lined autoclave containing a solution consisting of $FeCl_3$ and Na_2SO_4 and incubated in an oven at 120 °C for 8 h. Then the products obtained were centrifuged, washed and further heated in air at 450 °C for 2 h. From SEM images, it is observed that SnO_2 nanosheets have an average edge length of 500 nm to 1 µm and a uniform thickness of 5 nm, and are assembled into flower-like aggregates (figure 2.10). It is observed from the figure that a layer of short nanorod branches were grown on each basal surface of composite nanosheets (given in Figure 2.10 c and d). These nanorod branches have a relatively uniform length of 50-100 nm. The hierarchical SnO_2–Fe_2O_3 heterostructures can be used as lithium-ion battery anodes made with high initial discharge capacity of 1632 mA h g^{-1} at 400 mA g^{-1}, which will retain at 325 mA h g^{-1} after 50 cycles.

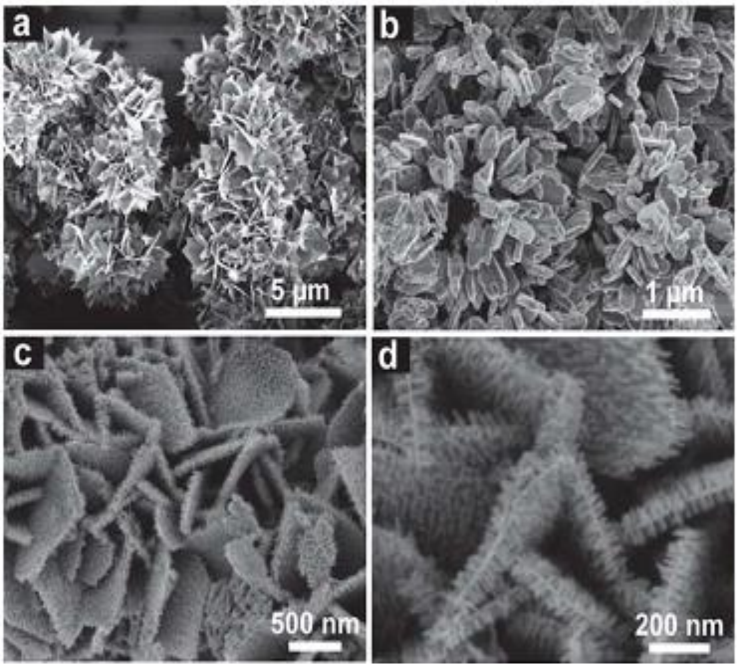

Figure 2.10 SEM images of (a) pristine SnO_2 nanosheets; (b) undecorated α-Fe_2O_3 nanorods; and (c and d) hierarchical SnO_2–Fe_2O_3 heterostructures (Wang et al., 2012).

More recently, Kaneti et al. (2015) have reported a facile hydrothermal strategy for the synthesis of novel ternary α-Fe_2O_3-ZnO-Au nanocomposites under mild conditions, through surface coating of ZnO and Au nanoparticles (NPs) on α-Fe_2O_3 nanorods. They have schematically described the three steps in figure 2.11. According to them, porous α-Fe_2O_3

nanorods achieved by the calcination of α-FeOOH nanorods were used as a template to deposit ZnO NPs using hydrothermal technique. Then, an in situ reduction of $HAuCl_4$ was done to decorate Au NPs on the surfaces of the deposited ZnO NPs and on the inner and outer parts of the α-Fe_2O_3 nanorods. The ternary α-Fe_2O_3-ZnO-Au nanocomposites were found to show higher sensitivity/responses with lower optimum operating temperature towards n-butanol and acetone compared to single α-Fe_2O_3 and binary α-Fe_2O_3-ZnO.

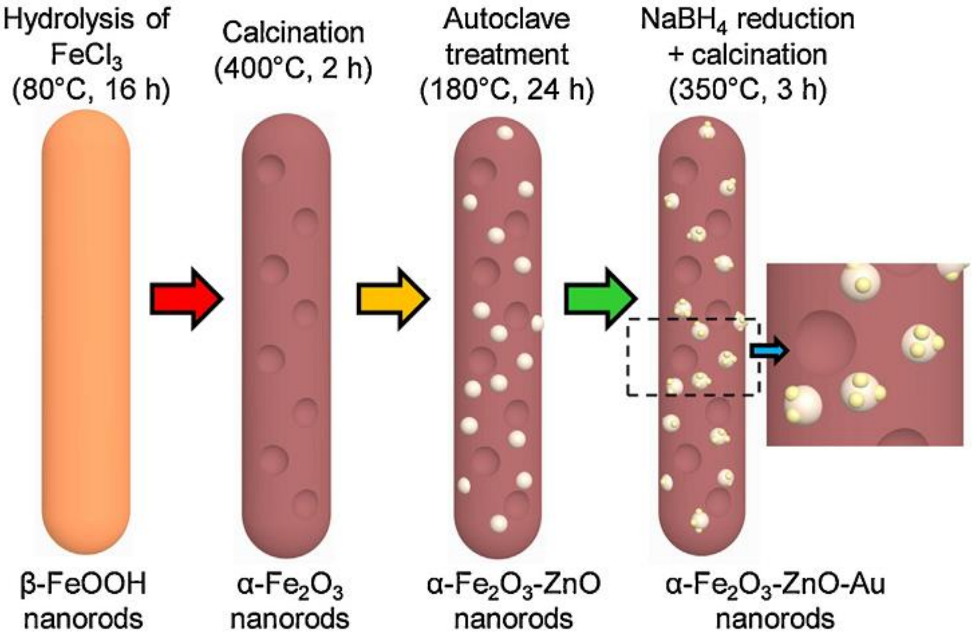

Figure 2.11 Schematic diagram of the preparation of ternary α-Fe_2O_3-ZnO-Au nanocomposites (Kaneti et al., 2015).

Niu et al. (2010) have synthesized branched SnO_2/α-Fe_2O_3 composite nanoheterostructures by a low-cost and environmentally friendly hydrothermal strategy, through crystallographic-oriented epitaxial growth of the SnO_2 nanorods onto the α-Fe_2O_3 nanospindles and nanocubes, respectively. Initially, they have prepared α-Fe_2O_3 precursors of nanospindles and nanocubes by hydrothermal method. For SnO_2/α-Fe_2O_3, the α-Fe_2O_3 precursors were dispersed in the $Sn(OH)_6$ dilute aqueous solution with ultrasonication for 10 min followed by hydrothermal treatment at 220 °C for various durations. The resulting products were centrifuged, washed and dried in vacuum. The SnO_2/α-Fe_2O_3 semiconductor nanoheterostructures exhibited excellent visible light or UV photocatalytic abilities; which was superior to α-Fe_2O_3 precursors, due to the effective electron-hole separation at the SnO_2/α-Fe_2O_3 interfaces. Similarly, El-Molla and co-workers (2015) have synthesized Fe_2O_3/MgO systems by the incipient impregnation, co-precipitation, and hydrothermal techniques. In the wet impregnation method, $Mg(OH)_2$ was impregnated into iron nitrate and dissolved in smallest possible volume of double-distilled water. Then co-precipitation of iron and magnesium was achieved by addition of aqueous ammonia solution (NH_4OH) to iron and magnesium nitrates at 25 °C and pH 8. The obtained precipitate was washed and dried at 110 °C. Then a suspension of the obtained precipitate was taken in a Teflon-lined autoclave and treated at 200 °C for 1 h. The solids obtained were calcined at 500-900 °C to form Fe_2O_3/MgO nanocomposite. The nanocomposite contained the nanosized MgO phase in addition to the $MgFe_2O_4$ phase. The prepared nanocomposite was used as an efficient catalyst for decomposition of H_2O_2. Mahapatra et al. (2013) have synthesized mixed iron and aluminium oxide (Fe_2O_3-Al_2O_3) nanocomposites by hydrothermal method, and studied their adsorption behavior towards decolorization of Congo red dye from an aqueous system. In their work, $Al(NO_3)_3.9H_2O$ and $FeSO_4.7H_2O$ salts were taken in a molar ratio of 1:1 and were mixed in distilled water. They have added a mixed solution of NaOH and NH_4OH drop wise to the above salt solution up to pH 5.6. Then the obtained green precipitate was transferred into a Teflon cupped pressure pot and treated 180 °C for 6 h. The obtained deep yellow powder was further calcined at 500 °C and 1000 °C, to form mixed Fe_2O_3-Al_2O_3 nanocomposites. From XRD results they have observed the formation of mixed γ-Fe_2O_3–Al_2O_3 phase and α-Fe_2O_3–Al_2O_3 phase for calcination temperatures 500 and 1000 °C, respectively. They have used the three different nanocomposites as adsorbents for removal of Congo red dye molecules and found that the γ-Fe_2O_3–Al_2O_3 exhibited superb adsorption efficiency with maximum adsorption capacity of 498 mg/g.

Chang et al. (2013) have demonstrated a facile and low-cost synthesis of the ZnO/CuO nanocomposites by two-step hydrothermal methods. Initially they have synthesized pure ZnO nanostructures by hydrothermal method using $ZnCl_2$ solution in water and isopropanol. The pH of the solution was maintained to 11 using KOH and the hydrothermal temperature was 120 °C for 10 h. For synthesis of ZnO/CuO nanocomposites, they have redispersed the as-prepared ZnO nanostructures into water and added copper(II) acetate with the solution under ultra-sonication. Then, hydrothermal reaction was carried out at 120°C for 8 h and the ZnO/CuO nanocomposites were synthesized and collected through washing, centrifugation and drying. The prepared ZnO nanoplates have smooth surface and high crystallinity with sizes in the range 100~300 nm and the thicknesses in the range 40~50 nm. In ZnO/CuO nanocomposites, it is found that the CuO nanopariticles with 300~500 nm are well-mixed with ZnO uniformly in the nanocomposites. The photocatalytic properties of the as-synthesized ZnO/CuO nanocomposites for degradation of methylene blue dye have been investigated under UV irradiation and the experimental results showed that MB can be degraded completely within 15 min and its photodegradation efficiency was six times faster than that of pure ZnO.

Wang et al. (2014) have synthesized hierarchically structured magnetic $MnO_2/ZnFe_2O_4$ hybrid materials and studied their performance in heterogeneous activation of peroxymonosulfate. Initially, they have synthesized $ZnFe_2O_4$ nanoparticles via a modified hydrothermal method. For synthesis of $ZnFe_2O_4/MnO_2$ hybrid structures, they have dispersed the prepared $ZnFe_2O_4$ in water by sonication followed by addition of $KMnO_4$ and HCl to the suspension under vigorous stirring. Then the solution was transferred into a Teflon-lined stainless steel autoclave and treated at 100 and 140 °C for 12 h. The SEM images (figure 2.12) of the sample prepared at 100 °C suggested a uniform corolla-like structure consisting of microsphere/nanosheet hierarchical nanostructures with an average diameter around 2 μm, on the other hand the sample prepared at 140 °C contained hierarchical sea-urchin shaped microstructure with a diameter of 3-4 μm, made of straight tetragonal nanorods with a uniform diameter of 30-40 nm. The $ZnFe_2O_4/MnO_2$ nanocomposites prepared at 140 °C have shown enhanced photocatalytic efficiency towards degradation phenol than $ZnFe_2O_4/MnO_2$ nanocomposites prepared at 100 °C, $ZnFe_2O_4$ nanoparticles and commercial MnO_2. Hu et al. (2015) have synthesized novel starfish- shaped porous $Co_3O_4/ZnFe_2O_4$ hollow nanocomposite by a facile and stepwise hydrothermal approach, utilizing metal−organic frameworks as precursors and sacrificial templates. Previously prepared porous Co_3O_4 nanocages were dissolved in DMF-ethanol mixture solution and sonicated for 30 min at room temperature. Then, $Fe(acac)_3$, $Zn(NO_3)_2{\cdot}6H_2O$ and H_2BDC were added to the above solution under sonication. The mixed solution was transferred to a 50 mL Teflon autoclave and was heated at 100 °C for 6 h to form starfish-shaped Co_3O_4/Fe^{III}-MOF-5 hollow nano-composites. The starfish-shaped $Co_3O_4/ZnFe_2O_4$ hollow nanocomposite was synthesized by heating the as-synthesized Co_3O_4/Fe^{III}-MOF-5 in the tube furnace in air at 500 °C for 2 h. From TEM image (figure 2.13), they have observed that the $Co_3O_4/ZnFe_2O_4$ nanocomposite was starfish-shaped hollow structure, while the nanotubes become highly porous, consisting of numerous $ZnFe_2O_4$ nanocrystals of 10 nm. Magnetic measurements show that the system presents a large coercivity and high squareness (at 1.8 K, Hc = 884 Oe and Mr/Ms = 0.52) with respect to the individual components.

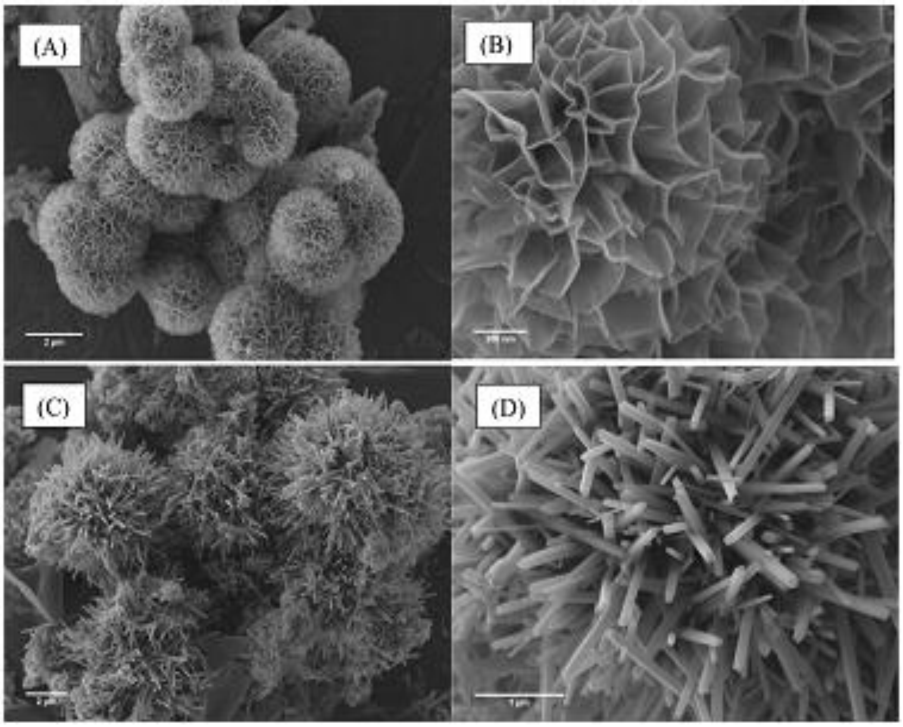

Figure 2.12 SEM images of $ZnFe_2O_4/MnO_2$ samples prepared at (A) and (B 100 °C, (C) and (D) 140 °C (Wang et al., 2014).

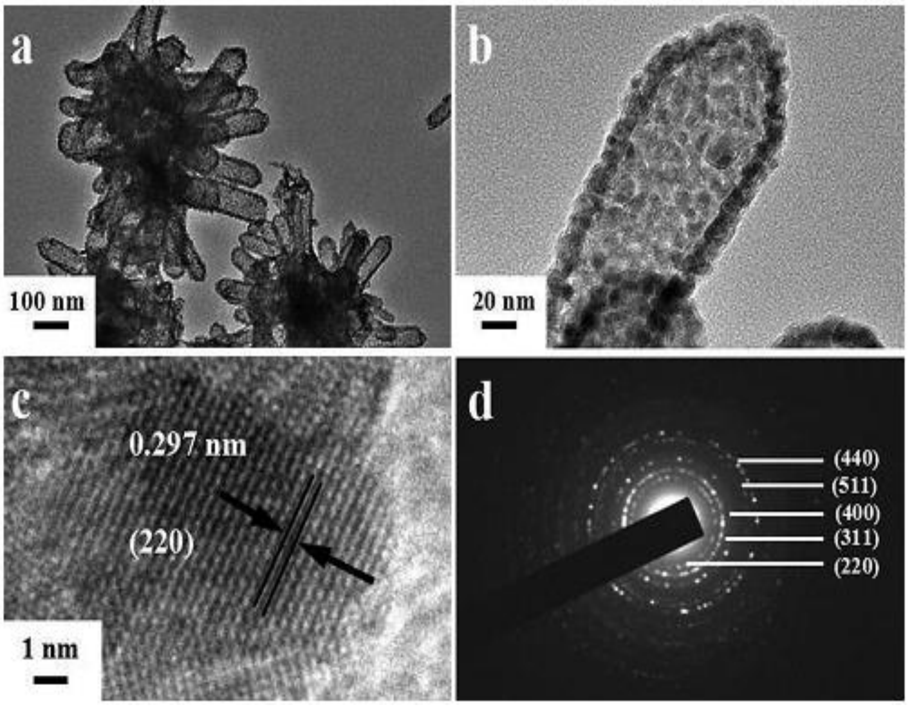

Figure 2.13 TEM images of (a) $Co_3O_4/ZnFe_2O_4$ hollow nanocomposites, (b) a single $ZnFe_2O_4$ nanotube, (c) High resolution TEM lattice image of a $ZnFe_2O_4$ nanoparticle, and (d) SAED patterns of the $ZnFe_2O_4$ nanotube (Hu et al. 2015).

Similarly, Fu et al. (2014) have reported Ti-doped α-Fe_2O_3 nanorod arrays prepared by a facile approach and implemented them as photoanodes for photoelectrochemical water splitting. They have sealed an aqueous solution of ferric chloride and sodium nitrate in a teflon-lined autoclave. Again, fluorine doped tin oxide (FTO)-coated glass of 1 × 2.5 cm was cleaned with deionized water, ethanol, acetone, ethyl acetate and was placed in the liner with the FTO side facing the wall of the liner. Then, different volume percentage of titanium tetrachloride ($TiCl_4$) with ethanol solution was added to teflon-lined. After hydrothermal treatment at 100 °C for 12 h, the yellow films formed on the FTO substrates were thoroughly rinsed with deionized water and transferred to a furnace and were annealed at 550 °C. The Ti-doped α-Fe_2O_3 nanorod arrays showed enhanced photoelectrochemical activity for water splitting due to the improved donor density and reduced recombination of the electron-hole pairs. Ang et al. (2013) have synthesized ZnO-CuO corn-like composites via a simple two step solution-based method. First, they have synthesized ZnO nanorods on a glass substrate by the hydrothermal method and then they have deposited CuO on ZnO NRs photochemically using ultraviolet (UV) light irradiation at room temperature. They have reported that ZnO–CuO nanocomposites show an excellent improvement in photocatalytic characteristics compared to bare ZnO NRs for degradation of Methyl orange under UV and solar light irradiation.

2.3. Reflux Method

Reflux method is also another important wet chemical method used for the synthesis of metal oxide nanomaterials. In this method, generally a condenser is fitted to the boiling flask and is clamped in an upright position (called as reflux position) and cooling water is circulated to cause the vapours to condense as they rise up the condenser. Hence the solvent or reagent loss due to evaporation is prevented. This reaction follows the hydrolysis and condensation reaction of metal salt precursors to from the corresponding metal oxides nanomaterials.

Advantages of reflux method: This technique normally involves relatively lower reaction temperatures as compared to hydrothermal method with simpler operations, higher yield, lower cost, environment friendly and can be easily controlled (Genuino et al., 2012; Qiu et al., 2011). The method is efficient to achieve crystalline phase at a lower temperature with low aggregation (Bandgar et al., 2011).

Disadvantages of reflux method: Nanomaterials with **r**ather large and non-uniform particle size and shapes are formed by this method, which restrict further improvement in the performance of the products (Genuino et al., 2012; Qiu et al., 2011).

2.3.1. Metal oxide nanomaterials by Reflux method

The reflux method is an economical and environment friendly, which can be performed at relatively low temperature (<100 °C) without the use of any expensive equipment. Large scale production of metal oxide nanomaterials with well-defined size and shape is feasible by this method. Mageshwari et al. (2015) have synthesized flower-shaped hierarchical CuO microspheres consisting of interpenetrating nanosheets by reflux condensation method without using any surfactant or templates. In a typical synthesis procedure, NH_4OH solution was injected to a homogeneous blue color solution of $Cu(NO)_3.3H_2O$ and then refluxed at 100 °C for 12 h. The resulting black precipitate was centrifuged, washed and dried in air at 100 °C for 2 h to form single phase CuO with monoclinic crystal structure. They have applied the CuO microspheres for photodegradation of methyl orange (MO) and methylene blue (MB) dyes in the presence of hydrogen peroxide under UV light irradiation and found that the CuO hierarchical architecture possesses good photocatalytic activity towards MO and MB dyes. Ahmad et al. (2013) have reported the synthesis of copper oxide nanoparticles by reflux method. In a typical synthesis process, copper acetate solution was mixed with acetic acid and then slowly heated in a three-necked refluxing pot under stirring. When the temperature reached at 90°C, NaOH was added to form black coloured precipitates of CuO nanoparticles with average crystalline size of 5 nm. In 2004, Woo et al. have reported the synthesis of maghemite (γ-Fe_2O_3) and magnetite (Fe_3O_4) nanoparticles by thermal decomposition of $Fe(CO)_5$ using reflux method. They have injected $Fe(CO)_5$ into a mixture of octyl ether and oleic acid at 100 °C. The resulting mixture was slowly heated and refluxed for 2 h, followed by cooling to room temperature, aerated for 14 h at 80 °C, and then refluxed for 2 h to form γ-Fe_2O_3 nanoparticles. Similarly, by varying molar ratio of $Fe(CO)_5$ to oleic acid, they have also synthesized Fe_3O_4 nanoparticles. Bose et al. (2002) have reported on the synthesisi of nanocrystalline tin oxide (SnO_2) materials with average grain size in the range of 20 nm by using reflux condensation technique. Tin chloride solution was hydrolyzed for 144 h and then neutralized with ammonia solution in a flask fitted with a reflux condenser. After that the resulting precipitates were washed, dried and annealed at 600 and 900 °C to form nanocrystalline SnO_2 materials and was used for fabrication of lithium cell. Goswami et al. (2012) have synthesized cylindrical shaped CuO nanoparticles by thermal refluxing technique and used as an adsorbent for arsenic removal from water. They have mixed $CuCl_2$, NaOH and capping solvent with ethanol in a round bottom flask fitted with reflux condenser and heated the mixture or 16 h at 75 °C. Then, the dark precipitate obtained was centrifuged, washed and heated at 110 °C to form the nanoparticles. They have observed that the prepared CuO followed Langmuir isotherm with an adsorption capacity of 1086.2µg/g for removal of arsenic from water. Sathyamoorthy et al. (2013) have synthesized MgO nanoflakes by thermal decomposition of precursors, which are prepared by a reflux condensation approach using ethylenediamine (EDA), hexamethylediamine (HTMA) and triethanolamine (TEA) solvents separately. They have used the MgO nanoflakes for photocatalytic degradation of methyl orange (MO) dye and demonstrated that MgO nanoflakes possess appreciable photocatalytic activity for decomposing MO dye, when EDA is used as a capping agent. Zhong et al. (2006) have reported the synthesis of 3D flowerlike Iron oxides (α-Fe_2O_3, γ-Fe_2O_3 and Fe_3O_4) nanostructures (figure 2.14) by reflux condensation method. In a typical procedure, they have dissolved $FeCl_3 \cdot 6H_2O$, urea, and tetrabutylammonium bromide (TBAB) in EG and the solution was refluxed at 195 °C for 30 min to form iron alkoxide precursor. Then the precursor was calcined at 450 °C in air for 3 h to form α-Fe_2O_3 and at 450 °C under N_2 protection for 3 h to form Fe_3O_4. Then the resulting Fe_3O_4 was calcined in air at 250 °C to form γ-Fe_2O_3. The obtained iron oxide nanomaterials were used as adsorbents for removal of As(V) and Cr(VI) from water and observed that the nanomaterials showed an excellent ability to remove heavy metal ions and other pollutants in water treatment. The maximum adsorption capacity of α-Fe_2O_3, γ-Fe_2O_3 and Fe_3O_4 were found to be 5.31, 4.75 and 4.65 mg/g, respectively for removal of As(V) and 4.47, 3.86 and 4.38 mg/g, respectively for removal of Cr(VI) from water.

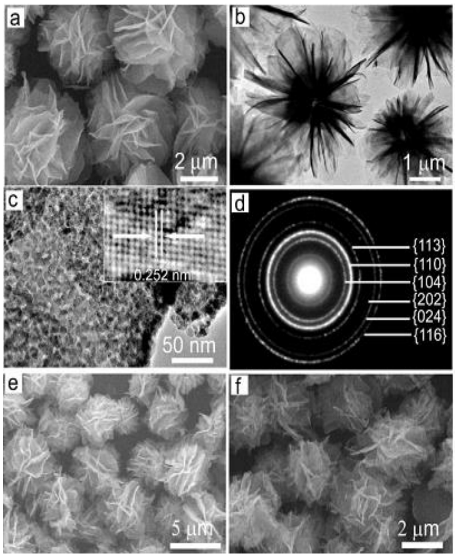

Figure 2.14 a) SEM and b) TEM images of the as-obtained α-Fe_2O_3. c) High-magnification TEM image of the petal of the flowerlike structure of the as-obtained α-Fe_2O_3. Inset: a high-resolution TEM (HRTEM) image taken from the as-obtaineda-Fe2O3nanoparticle. d) SAED pattern of the as-obtained α-Fe_2O_3. e) SEM image of the as-obtained Fe_3O_4. f) SEM image of the as-obtained γ-Fe_2O_3 (Zhong et al. 2006).

Similarly, Bharathi et al. (2010) have synthesized single-crystalline porous hematite nanorods with diameter ∼20 nm and length ∼125 nm by a low temperature reflux condensation method. In a typical experiment, precursor solution was prepared with $FeCl_3 \cdot 6H_2O$ and $(NH_2)_2CO$ and refluxed at a temperature slightly above the decomposition temperature of urea. Then the refluxing mixture was aged at 90-95 °C for 12 h to form akagenite nanorods. Then the akagenite nanostructures were transformed to porous hematite nanostructures upon calcination at 300 °C for 1 h. The prepared hematite nanorods showed excellent photocatalytic activity towards Rhodamine B from water.

2.3.2. Mixed metal oxide nanocomposites by Reflux method

Mageshwari et al. (2015) reported the synthesis of novel $CuO–CuCr_2O_4$ nanocomposite photocatalysts by reflux condensation method and evaluated their photocatalytic activity by monitoring the photodegradation of methyl orange (MO) and methylene blue dyes (MB) under UV light irradiation. In a typical synthesis, $Cu(NO)_3 \cdot 3H_2O$ and $Cr(NO_3)_3 \cdot 9H_2O$ was added in water to form a homogeneous blue color solution and refluxed at 100 °C for 12 h to form cluster-like $CuO–CuCr_2O_4$ nanocomposite microspheres. They have observed that, the $CuCr_2O_4$ loaded CuO showed enhanced photocatalytic activity for MO and MB dyes, and followed pseudo-first-order kinetics. Li et al. (2015) have synthesized 3D flower-like iron(III) oxide–indium(III) oxide ($Fe_2O_3–In_2O_3$) binary metal oxide nanocomposites by a simple and economical reflux method. In a typical synthesis procedure, they have refluxed a mixture solution of ferric chloride, indium nitrate, urea and tetrabutylammonium bromide in ethylene glycol at 220 °C for 4h followed by calcination at 450 °C for 3 h to form the $Fe_2O_3–In_2O_3$ nanocomposite. Shafiu et al. (2014) have reported the synthesis of Co_3O_4@ZnO nanocomposite by a two-step reflux method using pre-prepared Co_3O_4 nanoparticles. They have taken $Co(acac)_3$ and TEG in a three-neck round-bottomed flask equipped with a condenser with continuous stirring under argon. Then the mixture was refluxed at 280 °C for 45 min to form colloidal suspension containing Co_3O_4 nanoparticles. Then zinc acetate was added into the colloidal suspension obtained and the mixture was refluxed again at 270 °C for additional 45 min to form colloidal suspension containing Co_3O_4@ZnO nanocomposites. Then the products obtained were washed and dried at 300 °C for 3 h to form Co_3O_4@ZnO nanocomposites with average particle diameter 46 nm (figure 2.15). Mageshwari et al. (2015) have synthesized nanostructured CuO–ZnO nanocomposites taking different concentrations of Zn^{2+} (5%, 10%, 15%, 20% and 25%,) by reflux condensation method without using any surfactant and have studied their photocatalytic activity for methyl orange and methylene blue dyes under UV light irradiation. They have prepared an aqueous solution of $Cu(NO)_3.3H_2O$ and $Zn(CH_3COO)_2.2H_2O$ and injected NH_4OH solution to the above suspension. Then the mixture solution was refluxed at 100 °C for 12 h to form CuO–ZnO nanocomposites. They have observed that pure CuO contains 3D flower-like hierarchical architecture while CuO–ZnO nanocomposites contains flower-like CuO microspheres decorated with rod-like ZnO particles (figure 2.16). They have reported that photodegradation activity of CuO–ZnO nanocomposites increased with Zn^{2+} concentration due to the reduced recombination and efficient separation of photogenerated charge carriers.

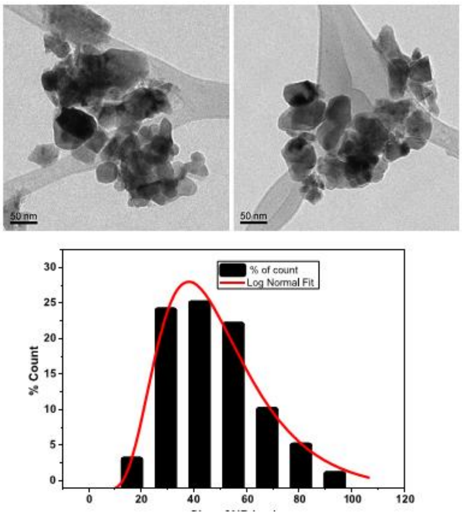

Figure 2.15 TEM micrographs of Co_3O_4@ZnO nanocomposite together with its particle size distribution diagram (Shafiu et al., 2014)

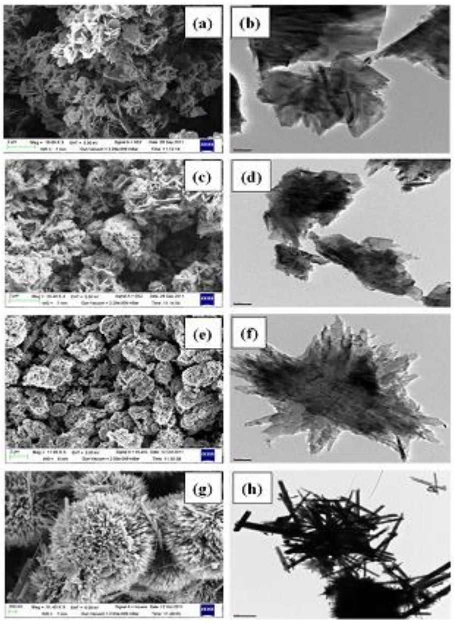

Figure 2.16 FESEM and TEM (scale bar is 0.2l m) images (a) and (b) pure CuO, (c) and (d) CuO-5% ZnO, (e) and (f) CuO-10% ZnO, (g) and (h) CuO-25% ZnO (Mageshwari et al. 2015).

2.4. Characterization Techniques

There are numerous analytical techniques used for characterizing metal oxide nanomaterials and mixed metal oxide nanocomposites. Here, we have deliberated the basic principles of few techniques that have been used in the experimental part of this research work. The various techniques included are X-ray Diffraction (XRD), Scanning electron microscopy (SEM), Transmission electron microscopy (TEM), absorption spectroscopy (UV-Vis), Infrared spectroscopy (FT-IR), Brunauer-Emmet-Teller (BET) surface area and X-ray photoelectron Spectroscopy (XPS).

2.4.1. X-ray diffraction

X-ray diffraction (XRD) is an essential structural technique for characterization of nanocrystalline materials. The main objective of this technique is to determine structural phase and crystallite size of nanomaterials. Diffraction patterns of the nanomaterials are recorded with a X-ray diffractometer using Cu Kα radiation (λ = 1.5418 Å). By investigative diffraction pattern, one can identify the crystalline phase of nanomaterial. X-Ray Diffraction is in accordance with the principle of Bragg's law:

$$\mathbf{n\lambda = 2d\sin\theta} \qquad \textbf{(2.1)}$$

here, d is interplaner distance between lattice planes of miller indices, λ is the wavelength of the incident X-ray and θ is Bragg angle. The widths of the diffraction peaks are closely related to the size, size distribution, defects and strain in the nanocrystals. For nanomaterials, as the size of the nanocrystals decreases, the peak width is broadened due to loss of long range order relative to bulk. The crystallite size of nanomaterials can be estimated from the peak width of the diffraction pattern corresponding to a particular (hkl) reflection plane using the Debye-Scherrer formula:

$$\mathbf{D = \frac{0.9\lambda}{\beta\cos\theta}} \qquad \textbf{(2.2)}$$

here, D is the mean crystallite size, which may be smaller or equal to the grain size, λ is the wavelength of the incident X-ray, θ is Bragg angle and β is the full width half at maximum (FWHM) of the peaks in radians.

Formation of $FeC_2O_4.2H_2O$ ((JCPDS: 72-1305) precursors and their conversion to α-Fe_2O_3 (rhombohedral phase, JCPDS: 33-0664) and Fe_3O_4 (cubic phase, JCPDS: 65-3107) during the annealing processes under different atmosphere was clearly demonstrated by XRD (Du et al.

2010). With increase in increasing calcination temperature from 700 to 800 °C, the increase in the peak intensity and hence improvement of crystallization of anatase and rutile phases of TiO_2 were clearly explained using XRD by Xiao et al. (2010). Phase identification of three different phases of face-centered cubic Ag (JCPDS No. 04-0783), cubic magnetite (JCPDS No. 36-1451) and cubic $ZnFe_2O_4$ (JCPDS No. 22-1012) of a mesoporous carbon fibers containing ternary nanocomposite $ZnFe_2O_4/Fe_3O_4/Ag$ was done by XRD (Xie et al., 2012).

2.4.2. Scanning electron microscopy (SEM)

Scanning electron microscopy (SEM) is a powerful and popular technique for imaging surface of a sample and detecting signals from the interaction of the incident electron with the sample surface. When incident electron beams interact with specimen surface, secondary electrons with energies typically smaller than 50 eV evolve from the surface. The emission efficiency of the secondary electron depends upon the surface geometry, surface chemical characteristics and bulk chemical composition. Thus SEM can provide information about the surface topology, morphology and chemical composition. The high resolution capability of SEM makes it useful for characterization of nanomaterials.

The shape and morphology of nanostructured materials can be preliminary determined by SEM. The rod shaped morphology of prepared α-FeOOH and α-Fe_2O_3 nanomaterials with diameter about 30 nm and length up to 400 nm was determined by Zeng et al. (2007) using FESEM. Deng et al. (2014) have described the growth of the CuO nanocubes (with diameters ranging from 40 nm to 80 nm) onto the TiO_2 nanofibers (with diameters of about 200 nm) surface to form hierarchical heterostructures using FESEM (Deng et al., 2014).

2.4.3. Transmission electron microscopy (TEM)

Transmission electron microscopy (TEM) is a high spatial resolution structural and chemical characterization instrument. An advanced TEM has capability to directly image atoms in crystalline specimens at resolution close to 0.1 nm, which is smaller than interatomic distance. An electron beam can also be focused to a diameter smaller than 0.3 nm, by which quantitative chemical analysis from a single crystal is possible. TEM can be used to characterize metal oxide nanomaterials to determine particle size, shape, crystallinity and interparticle interaction (Zhang, 2009).

Meng et al. (2010) have investigated the shape, size and morphology of uniform coalescent moniliforme-shape α-Fe_2O_3 straight nanochains built up of single crystal building blocks using TEM and found that the one-dimensional coalescent architectures were built up of single crystal building blocks with an average diameter of 19.8 nm. Starfish-shaped hollow structures of $Co_3O_4/ZnFe_2O_4$ nanocomposite were investigated using TEM. It has been observed that the nanotubes of the starfish-shaped materials are highly porous, consisting of numerous $ZnFe_2O_4$ nanocrystals of 10 nm (Hu et al., 2015).

2.4.4. UV-Vis spectroscopy

UV-visible spectroscopy is one of the simplest and useful optical characterization techniques for studying optical and electronic properties of nanomaterials. Measurement of light absorption due to electronic transitions in nanomaterials is the basic operating principles of the spectroscopic technique. The wavelength of light required for electronic transition is typically in the UV and visible region of the electromagnetic spectrum, hence electronic spectroscopy is called UV-visible spectroscopy.

The UV-vis spectrometer records the intensity of absorption (A) as a function of wavelength. Let I_0 and I_t are the intensities of incident and transmitted rays of light, respectively. Then, based upon Beer's law, the absorbance is related as:

$$\mathbf{A = \log\frac{I_0}{I_t}} \qquad \mathbf{(2.3)}$$

or,

$$\mathbf{A=\varepsilon c x} \qquad \mathbf{(2.4)}$$

here, x=sample path length, c=concentration and ε=molar extinction coefficient ($mol^{-1}cm^{-1}$). This characterization technique provides the preliminary concept of particle size, size distribution such as mono or polydispersity and band-gap of semiconductor metal oxide nanomaterials. Saha and Bhunia (2013) have studied the optical and electronic properties of Fe_2O_3 nanoparticles using UV-vis spectroscopy and calculated the band-gap from it. Xia et al. (2008) have measured the UV–Vis diffuse reflectance spectra of Fe_2O_3/SnO_2 nanocomposite photocatalyst for the determination of the shifting of absorption edges of the samples and also calculated the band-gap using this characterization.

2.4.5. Fourier transforms infrared spectroscopy (FT-IR)

Infrared is a common vibrational spectroscopy technique useful for characterizing structural properties such as vibrational frequencies of molecules and phonons for determination of functional groups of the sample.

IR spectroscopy is based on measurement of transmitted IR light through a sample. For molecules, the IR spectrum reflects their vibrational modes, determined by selection rule. For nanoparticles, IR spectrum measures the phonon mode with appropriate selection rules that are determined by their crystal symmetry properties. Interaction between the surface molecules or ions with nanoparticles usually cause change in the vibrational or phonon frequencies. Hence the changes in frequencies measured in IR spectrum can give information about the interaction between the nanoparticles and surface molecules. Nowadays researchers are using various commercial spectrometer including FTIR (Fourier transform IR) (Zhang, 2009).

FTIR spectroscopy has been applied to determine the broad band centered -OH groups (3430 cm^{-1}), characteristic absorption peak of Fe-O (735 cm^{-1}) and characteristics absorption peak of Zn-O (548 cm^{-1}) of $ZnFe_2O_4$ nanoparticles (Habibi and Habibi, 2013). Umare and Shambharkar (2012) used FTIR spectroscopy to determine characteristic absorption at 474 and 578 cm^{-1} correspond to the Fe-O vibrations in α-Fe_2O_3 and C=C stretching modes of benzenoid and quinoid ring (1504 and 1585 cm^{-1}), C-H deformation of aromatic rings (826 cm^{-1}), C-N stretching of secondary aromatic amine (1154 cm^{-1}), $C\text{-}N^{\bullet+}$ stretching vibration in protonic acid doped PANI from SDBS-PANI (1307 cm^{-1}) and SO_3H of SDBS (513 cm^{-1}) of Polyaniline (PANI)-α-Fe_2O_3 nanocomposites.

2.4.6. Brunauer-Emmett-Teller (BET) surface area

The specific surface area of nanoparticle powder is determined by physical adsorption of N_2 gas on the surface of the solid and by calculating the amount of adsorbate gas corresponding to monolayer coverage on the nanomaterials surface. The determination is typically carried out at liquid nitrogen temperature. The amount of N_2 gas adsorbed on the nanomaterials surface can be measured by a volumetric or continuous flow procedure.

Using BET surface area analytical technique, determination of surface area, pore volume, pore diameter, pore size distribution and pore density measurements is carried out. Using this technique, Zhang et al. (2013) have measured N_2 adsorption–desorption isotherms and pore size distribution (PSD) of α-Fe_2O_3 nanoparticles. They have observed that the nanoparticles are mesoporous nature, due to appearance of a distinct type IV hysteresis loop in the range of 0.5 to 1.0 P/P_0 and from PSD curve, the calculated the mesopores diameter about 3 and 20 nm. The surface area of the α-Fe_2O_3 nanoparticles was found to be 112 $m^2\ g^{-1}$. The BET surface area, pore diameter and mesoporous structure of Cr-MCM-41 and Al, Cr-MCM-41 catalyst have been measured by Lezanska et al. (2007). According to them the BET surface area of 3%Cr-MCM-41, 5%Cr-MCM-41, 6%Cr-MCM-41 and 0.7%Cr+2.9%Al-MCM-41 were found to be 1117, 1043, 1110 and 557 m^2/g, respectively and the pore diameters were found to be 1.7, 2.8, 3.1 and 4.3 nm, respectively.

2.4.7. X-ray photoelectron spectroscopy (XPS)

The XPS technique is essentially used for elemental surface chemical analysis. Hence, the technique is also known as ESCA. XPS is based on the principle of measurement of the kinetic energy of photoelectrons generated when sample is illuminated with soft X-ray radiation in the ultrahigh vacuum. The principle follows the equation based on total energy conversion:

$$\mathbf{h\nu + E_i = KE + E_f} \qquad \mathbf{(2.5)}$$

here, one X-ray photon with energy hν is used to excite an atom in its initial state with energy E_i and to eject an electron with kinetic energy, KE, with an atom resulting in final state of energy E_f (Zhang, 2009). The energy of the photoelectrons thus leaving the sample is determined and this gives a spectrum of intensity as a function of binding energy. The binding energies of the peaks are characteristics of each element. Hence, XPS can also provide chemical binding information.

Xia et al. (2013) have determined C-C, C-OH and C(O)O groups of graphene plane, Sn 3d3/2 (486.9 eV), Sn 3d3/2 (495.4 eV), Fe 2p3/2 (712.2 eV) and Fe 2p1/2 (725.6 eV) peaks in Graphene/Fe_2O_3/SnO_2 ternary nanocomposites using XPS. Similarly, Zhang et al. (2012) have shown Ti, Ag, O, and C elements with sharp photoelectron peaks at binding energies of 530 eV (O1s), 459 eV (Ti2p), 368 eV (Ag3d), and 285 eV (C1s) in Ag Cluster-Doped TiO_2 nanoparticles using XPS. They have also evaluated the element ratio of Ag to Ti as 0.87% using high-resolution spectra of Ti2p and Ag3d.

2.5. Concluding remarks

Metal oxide nanocomposites are extremely attractive since they exhibit surface bifunctional properties. In the nanosized regime, specific metal oxide interactions can indeed be responsible for the enhanced physicochemical properties. Coupling of one metal oxide with other has also been observed to increase the adsorption & photocatalytic performance. In this chapter, we have reviewed various literatures report on the preparation and environmental applications of different iron oxides and iron oxide based composite nanomaterials. A large number of literatures are available on the synthesis and environmental applications of Fe_2O_3, SnO_2, CuO, MgO, and ZnO nanomaterials. Fe_2O_3 is found to very important adsorbent and photocatalyst for decontamination of both organic and inorganic pollutants from aqueous media. There are also various literatures available on other metal oxides such as SnO_2, MgO, CuO and ZnO nanomaterials that have been used as adsorbents and photocatalysts. More recently, various groups have focoused their research on the synthesis of metal oxide hybrid or composite nanomaterials inorder to further improve the performance of individual metal oxide nanomaterials. Metal oxide nanocomposites are observed to be showing enhanced photocatalytic as well as surface adsorption properties and hence have been used for environmental appications. A large number of reports are available on environmental applications of iron oxide base polymer, graphene and graphene oxide nanocomposite materials. However, a very few reports are available on synthesis of Fe_2O_3 based metal oxide nanocomposites such as Fe_2O_3/SnO_2, Fe_2O_3/MgO, Fe_2O_3/CuO and Fe_2O_3/ZnO. So, inorder to carry out extensive studies on the synthesis, structural properties and crystalline phases as well as their applications towards adsorptive removal and photocatalytic degradation of organic dyes pollutants, we have studied the synthesis and application of Fe_2O_3 based SnO_2, MgO, CuO and ZnO nanocomposites for decontamination of organic dyes from aqueous media.

Four different organic dyes (Congo red, Methylene blue, Malachite green and Methyl orange) have been chosen as model organic pollutants to study the adsorptive removal and photocatalytic degradation performance of the prepared iron oxides and their nanocomposites. Among the four dyes two anionic and two cationic dyes have been choosen with different structure and functionality. Congo red and Methyl orange are anionic and azo dyes. Similarly, Methylene blue and Malachite green are cationic dyes. Congo red [1-naphthalene sulfonic acid, 3, 30-(4, 40-biphenylenebis (azo)) bis (4-amino-) disodium salt, CR] is a benzidine-based anionic diazo dye, i.e. a dye with two azo groups. It is toxic to many organisms and is a suspected carcinogen and mutagen. The dye has been known to cause an allergic reaction and to be metabolised to benzidine, a human carcinogen (Afkhami and Moosavi, 2010). Methylene blue [3,7-bis(Dimethylamino)-phenothiazin-5-ium chloride, MB] have various harmful effects such as nausea, abdominal and precordial pain, dizziness, headache, profuse sweating, hemolytic anemia, hyperbilirubinemia, acute renal failure and mental confusion. Contact with methylene blue may also cause photoirritant contact dermatitis (PICD). Methyl Orange [Sodium 4-[(4-dimethylamino) phenyldiazenyl] benzenesulfonate, MO] is an azo dye used in textile industries and is an orange-coloured anionic dye. Methyl Orange is a harmful compound that exists in textile waste waters and has various harmful effects on human beings. For example, it may cause eye or skin irritation, or inhalation may cause gastrointestinal irritation with nausea, vomiting, and diarrhea (Azami et al., 2012). Malachite green [4-{[4-(dimethylamino) phenyl] (phenyl) methylidene}-*N*, *N*-dimethylcyclohexa-2, 5-dien-1-iminium chloride, MG] also called Basic Green 4 is the most widely used dye for colouring purpose among all other dyes of its category. It is highly cytotoxic and carcinogenic to mammalian cells and acts as a liver tumor promoter. It decreases food intake capacity, growth and fertility rates; causes damage to liver, spleen, kidney and heart; inflicts lesions on skin, eyes, lungs and bones. MG is also environmentally persistent and acutely toxic to a wide range of aquatic and terrestrial animals (Saha et al., 2010). The functional groups present in organic molecule also play an important role in adsorption as well as the photocatalytic studies. So in order to study a wide range of applications of our synthesized nanocomposite materials we have selected the four different dyes having different charges, different functional groups as model organic pollutants in this thesis.

2.6. Research Objectives

The main objectives of this research work are as follows:

- To synthesize novel metal oxide nanomaterials especially iron oxides, iron oxide based nanocomposites such as Fe_2O_3/SnO_2, Fe_2O_3/CuO, Fe_2O_3/ZnO and Fe_2O_3/MgO nanocomposites and iron oxide impregnated mesoporous MCM-41 using facile low cost wet chemical synthetic methods.
- To study the formation, stability, existence of crystalline phases, porous structures and surface properties of the prepared metal oxide nanomaterials using different sorptometric, scattering, spectroscopic and microscopic analytical techniques.
- Environmental applications of the nanomaterials towards surface adsorption and photocatalytic degradation of organic dyes from aqueous media.
- To study the adsorption and photocatalysis efficacy of the prepared metal oxide nanomaterials for a wide range of toxic organic dyes having different charge, functionality and molecular size.
- Fundamental understanding and correlation of the surface properties of the material with their activity.

CHAPTER-3

ONE DIMENSIONAL (1D) IRON OXIDES AND IRON-TIN MIXED OXIDE NANOCOMPOSITES: SYNTHESIS AND SORPTION STUDIES

PART A: IRON OXIDE ($FeC_2O_4.2H_2O$, γ-Fe_2O_3 AND α-Fe_2O_3) NANORODS

3.1. Introduction

Water pollution is a major global problem which is the leading worldwide cause of deaths and diseases. Many synthetic chemicals are extremely resistant to biodegradation by native microorganisms and are major water pollutants, such as pesticides, organochlorines, polychlorinated biphenyls, polycyclic aromatic hydrocarbons, wood preservatives, synthetic polymers and synthetic dyes. Synthetic dyes are extensively used in different industries, including paper, plastic, leather, pharmaceutical, food, cosmetic, dyestuff, and textile industries (Ge et al., 2012; Haider et al., 2011). Dyeing is a fundamental operation during the textile fiber processing. This operation causes the production of colored waste waters, depending on the degree of fixation of the dyes on the substrates, which varies with the nature of the substances, the desired intensity of coloration, and the application method (Wawrzkiewicz, 2012). According to a recent study, approximately 700,000 tons of different dyes are produced annually in the world, and more than 60 % of the world dye production is consumed by textile industries (Hu et al., 2010). Due to the presence of hazardous wastes and toxic pollutants in the effluents from the textile industry, they are highly problematic to environment. Among them, organic dyes are one of the major groups of pollutants in waste waters. These toxic dyes have significant impact on the human health and the aquatic life. The used dyes may cause an eco-toxic hazard and induce the potential danger of bioaccumulation (Toor and Jin, 2012; Wang et al., 2012; Kumar and Bansal, 2012).

The toxic nature of dye is that on decomposition it gives hazardous products such as Carbon dioxide, carbon monoxide, nitrogen oxide and hydrogen chloride. These products are toxic and causes severe health problem to living beings (Irama et al., 2010). Congo Red [1-naphthalene sulfonic acid, 3, 30-(4, 40-biphenylenebis(azo))bis(4-amino-)disodium salt] an anionic dye has been known to cause an allergic reaction and to be metabolised to benzidine, a human carcinogen. Congo red mainly occurs in the effluents discharged from textile, paper, printing, leather industries, etc. Its molecular formula is $C_{32}H_{22}N_6Na_2O_6S_2$ (Yosef and Avnir, 2011; Chatterjee et al., 2010).

There are several methods for removal of organic dyes from aqueous solution such as: coagulation (Marechal et al., 1997), nanofiltration (Chakraborty et al., 2003), ozonation (Khadhraoui et al., 2009), ultrasound irradiation (Song et al., 2009), ion exchange (Wawrzkiewicz and Hubicki, 2010), activated carbon filter (Chan et al., 2009), oxidation (Lucas and Peres, 2006), membrane processes (Sachdeva and Kumar, 2009), micellar enhanced ultrafiltration (Purkait et al., 2004), adsorption (Wang et al., 2012) etc. Among all the processes, adsorption is a very effective separation technique. Now it is considered as superior to other techniques for water treatment in terms of effectiveness, initial cost, simplicity of design, and ease of operation. Similarly, this technique can handle fairly large flow rates, producing a high-quality effluent that does not result in the formation of harmful substances, such as ozone and free radicals. In this process the dye species are transferred from the water effluent to a solid phase that leads to decrease the effluent volume (Dawood and Sen, 2012; Toor and Jin, 2012; Wang et al., 2012; Zhu et al., 2012).

Many researchers used various adsorbents for removal of Congo red from aqueous solution such as: fly ash (Dizge et al., 2008), bentonite (Lian et al., 2009), montmorillonite (Wang and Wang, 2008), chitosan (Chatterjee et al., 2009), organo-attapulgite (Chen and Zhao, 2009), activated carbon (Lorenc-Grabowska and Gryglewicz, 2007; Namasivayam and Kavitha ,2002; Purkait et al., 2007), bottom ash and deoiled soya (Mittal et al., 2009), Azadirachta indica leaf powder (Bhattacharyya and Sharma, 2004), Trametes versicolor (Binupriya et al., 2008), jute stick powder (Panda et al., 2009), Aspergillus niger (Fu and Viraraghavan, 2002), cattail root (Hu et al., 2010), anilinepropylsilica xerogel (Pavan et al., 2008), perlite (Vijayakumar et al., 2009), sawdust (Jain and Sikarwar, 2008), rice husk ash (Chowdhury et al., 2009), mesoporous hematite (α-Fe_2O_3) (Yu et al., 2008), CNTs/β-FeOOH (Song et al., 2012) etc. However, some of these adsorbents do not have good adsorption capacities for anionic dyes. Nowadays, research focused on the use of nanotechnology for environmental clean-up/remediation. Arising out of their ultrafine size, large surface area & interface dominated properties nano-sized materials can be used to decontaminate the toxic organic and inorganic chemical from the environments. Recently, Afkhami and Moosavi (2010) used maghemite nanoparticle, prepared by co-precipitation method, for removal of Congo red from aqueous solution.

From the literature review we observed that iron oxide is an afficient adsorbent for removal of both organic and inorganic pollutant from the aqueous stream and is also a non toxic metal oxide. This oxide is easily prepared using both basic and acidic medium. Our objective is to prepare iron oxide based nanocomposite materials for environmental applications prior to this we have synthesized iron oxide nanomaterials via iron oxalate precipitation method at room temperature. The low temperature calcination product of iron oxalate leads to form different iron oxide nanomaterials. Therefore for the convenient, low cost a, easy preparation and to adopt environmental benign condition we have chosen the oxalate precipitation method for synthesis of iron oxide nanomaterials (Borel et al., 2014). In the present investigation, by using a modified wet chemical method, we have prepared different 1-dimensional nano-adsorbents such as: Ferrous oxalate ($FeC_2O_4.2H_2O$) nanorod, hematite (α-Fe_2O_3) nanorod and maghemite (γ-Fe_2O_3) nanorod. The prepared adsorbents were employed for removal of Congo red (CR) and a comparative study were carried out by evaluating equilibrium isotherms and kinetic data for selection of the most effective adsorbent among them.

3.2. Materials and Methods

3.2.1 Materials

Congo Red (CR, molecular formula $C_{32}H_{22}N_6Na_2O_6S_2$, molecular weight 696.66 g mol^{-1}, λ_{max} = 498 nm), an anionic azo dye, obtained from Merck (India) was selected as dye. All chemicals used it the investigation such as: Ferrous sulphate heptahydrate, Oxalic acid dihydrate, CTAB and Ethanol were of analytical grade and were used without further purification. The chemicals were obtained from Merck (India).

3.2.2. Synthesis of Adsorbent

Ferrous sulphate heptahydrate ($FeSO_4.7H_2O$) was dissolved in 10 ml of double distilled water with intensive stirring to form solution-A. Oxalic acid dihydrate ($H_2C_2O_4.2H_2O$) and CTAB (Cetyl trimethylammonium bromide) were dissolved in 25 ml of ethanol with intensive stirring to form solution-B. Then solution-A was added to solution-B with intensive stirring to form a yellow coloured homogeneous solution. After addition the stirring was carried out for another 5 hours. Then the yellow coloured precipitate obtained was centrifuged, washed thoroughly by ethanol and double distilled water and dried at 80 ^{o}C for 2 hours to form $FeC_2O_4.2H_2O$ nanorod. A part of this nanopowder was heated at 300 °C in moist condition to obtained γ-Fe_2O_3 nanorod and heated at 550 ^{o}C to obtained α-Fe_2O_3 nanorod.

3.2.3. Characterization of Adsorbent

Various characterization techniques were used to characterize the 1-D nanoadsorbents. The crystalline phases were identified by mean of X-ray diffraction (XRD) by a PANalytical X-ray diffractometer with Cu Kα radiation (λ) 1.54156 ^{o}A at a scan rate of 2^{o}/min. The surface morphology of the prepared adsorbent materials was characterized by a JEOL JSM-5300 scanning electron microscope (SEM) operated at an acceleration voltage of 15 and 20.0 kV. The size of the particle and selected area electron diffraction (SAED) pattern of the dried γ-Fe_2O_3 powder was observed using a high resolution transmission electron microscope (TEM) (JEM-2100 HRTEM, Make-JEOL, Japan) with an acceleration voltage of 200KV. Fourier transform infrared spectroscopy (FTIR) results were recorded using Perkin-Elmer FTIR (Spectrum RX-I) spectrophotometer. Specific surface area and pore size distribution (PSD) were determined by the Brunauer-Emmett-Teller (BET) and Barrett-Joyner-Halenda (BJH) methods, respectively by N_2 adsorption-desorption technique by automated surface area and porosity analyser (COULTER SA 3100 Series Surface Area and Pore Analyzers). Prior to the analysis, sample was degassed under a vacuum ($1X10^{-5}$ Torr) at 150 ^{o}C for 1.5 h.

3.2.4. Adsorption Experiment

For the removal of Congo red (CR) dye from water, the adsorption experiments were carried out using the three prepared adsorbents: $FeC_2O_4.2H_2O$, α-Fe_2O_3 and γ-Fe_2O_3 nanorods. A stock solution of CR (1 g L^{-1}) was prepared in double distilled water and desired concentrations of the dye were obtained by diluting the same with double distilled water. The calibration curve of CR was prepared by measuring the absorbance of different concentrations of the samples at maximum absorbance at wavelength, λ_{max} = 498 nm using UV–vis spectrophotometer. The amount of adsorption q_e is calculated by equation (Nethaji et al., 2012; Kumar et al., 2012):

$$q_e = \frac{C_0 - C_e}{w} V \qquad (3.1)$$

where q_e is the amount of adsorption at equilibrium in mg g^{-1}, C_0 & C_e are the initial and equilibrium concentration of the dye in mg L^{-1}, V is the volume of the dye solution taken in litre and w is the weight of the nanorod (adsorbent) in gram. All the adsorption experiments were carried out three times in replicates and the mean data obtained were taken in results and discussion section.

3.3. Results and Discussion

3.3.1. Surface morphology

Figure 3.1 shows the SEM micrographs of as synthesised $FeC_2O_4.2H_2O$ nanorod, γ-Fe_2O_3 nanorod and α-Fe_2O_3 nanorod. Figure 3.1a SEM micrograph suggests that the obtained $FeC_2O_4.2H_2O$ nanostructure exhibits the morphology of the nanorod with the diameter of about 100-200 nm and the length up to micrometres. Moreover, the surface of the $FeC_2O_4.2H_2O$ nanorods seems to be smooth, and no defects can be observed. When the $FeC_2O_4.2H_2O$ nanorods were annealed in air at 300 ^oC in moist condition, γ-Fe_2O_3 nanorods were formed. Figure 3.1b shows the SEM, image of the as-synthesized γ-Fe_2O_3 nanorods. It can be seen that the as-synthesized γ-Fe_2O_3 nanorods retain the morphology of the $FeC_2O_4.2H_2O$ nanorods. Similarly when, the $FeC_2O_4.2H_2O$ nanorods were annealed in air at 550 ^oC, α-Fe_2O_3 nanorods were formed. Figure 3.1c shows the SEM, image of the as-synthesized α-Fe_2O_3 nanorods. It can also be seen that the as-synthesized α-Fe_2O_3 nanorods retain the morphology of the $FeC_2O_4.2H_2O$ nanorods. Figure 3.1d shows the EDX analysis of as-synthesized γ-Fe_2O_3 nanorods, which confirms the presence of Fe and O elements.

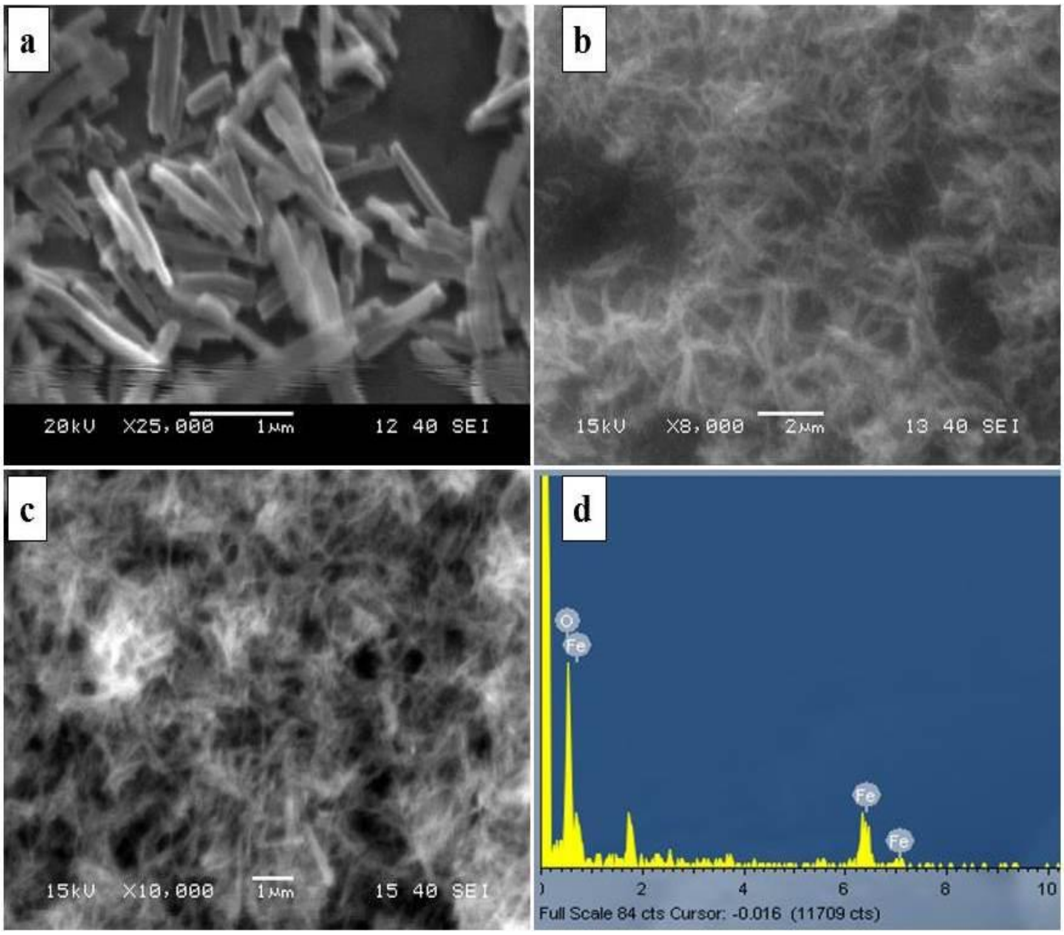

Figure 3.1 SEM micrographs of a) $FeC_2O_4.2H_2O$ nanorod, b) γ-Fe_2O_3 nanorod, c) α-Fe_2O_3 and d) EDX of γ-Fe_2O_3 nanorod.

A typical profile of TEM images of γ-Fe_2O_3 are shown in Figure 3.2a and 3.2b, which gives further evidence of the formation of high yield aligned nanorods. A typical TEM image of a single γ-Fe_2O_3 nanorod is given in figure 3.2c, which gives the average diameter of the rod is around 100 nm. The SAED pattern, taken from the same single nanorod (given in figure 3.2d), shows sharp bright rings which indicate the formation of polycrystalline spinel structure.

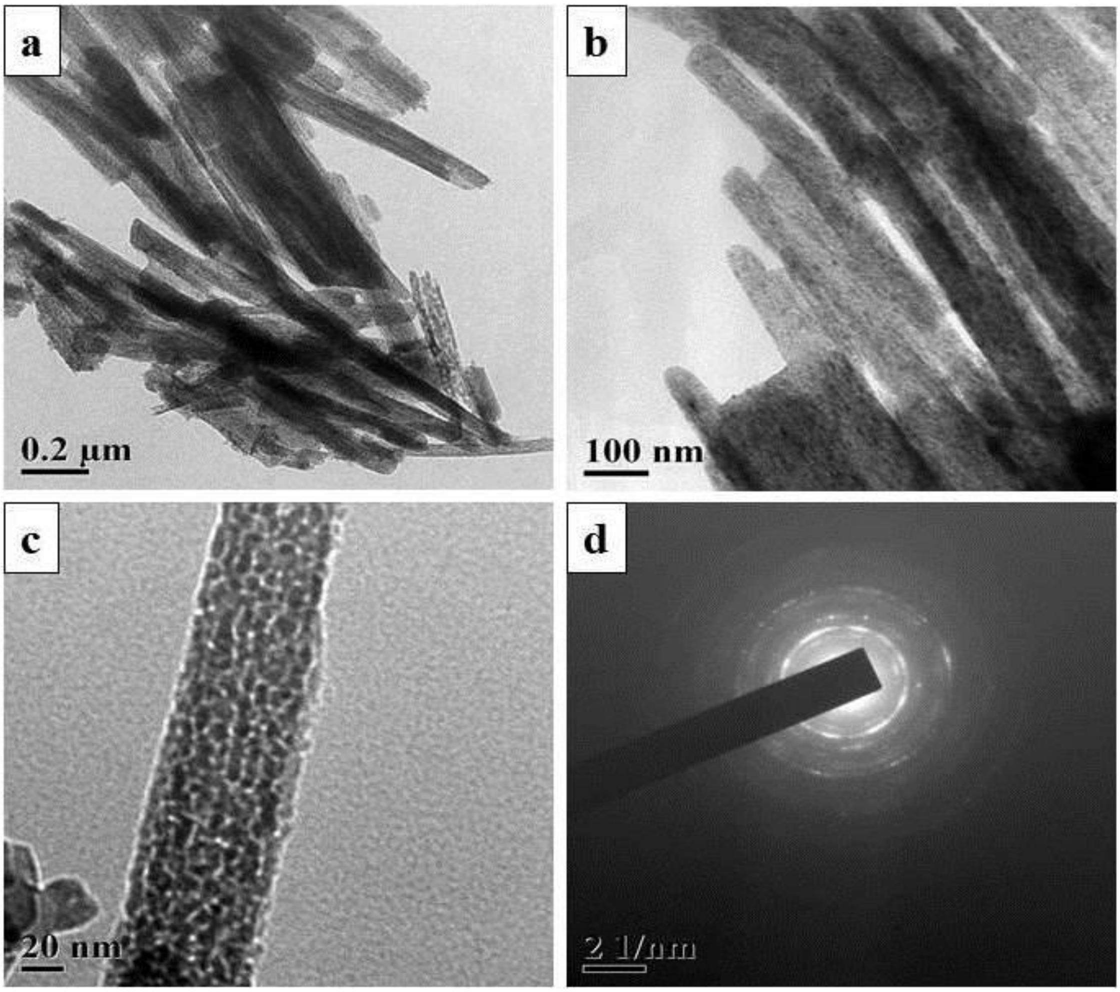

Figure 3.2 (a, b and c) TEM images and (d) SAED pattern of γ-Fe_2O_3 nanorod.

3.3.2. X-Ray diffraction analysis

The formation and phase analysis of the prepared nanomaterials were studied by XRD using Cu Kα radiation. Figure 3.3 shows the XRD patterns of as synthesized $FeC_2O_4.2H_2O$ nanorod, γ-Fe_2O_3 nanorod and α-Fe_2O_3 nanorod. Figure 3.3a represents the XRD pattern of $FeC_2O_4.2H_2O$ and contains the characteristics peaks and can be index to orthorhombic crystal structure according to JCPDS No: 22-0635. Figure 3.3b contains the characteristics peaks of γ-Fe_2O_3 and can be index to cubic crystal structure according to JCPDS No: 39-1346. The XRD pattern of figure 3.3c represents the characteristics peaks of α-Fe_2O_3 and can be index to rhombohedral crystal structure according to JCPDS No: 79-0007. The X-ray diffractograms reveal the crystalline nature of the compounds. The broadening of the peaks also indicates the decrease in the diameter and an increase in the surface to volume ratio of the compounds.

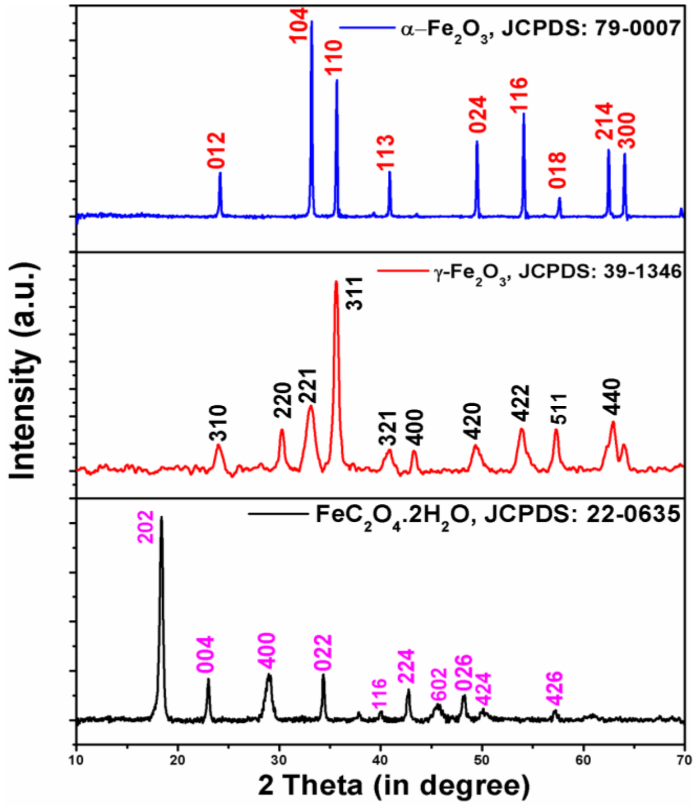

Figure 3.3 XRD patterns of a) $FeC_2O_4.2H_2O$ nanorod, b) γ-Fe_2O_3 nanorod and c) α-Fe_2O_3 nanorod.

Crystallite size and the lattice strain of the prepared samples are calculated from the X-ray diffractograms, by using the well-known Scherrer formula as follows:

$$L = \frac{K\lambda}{\beta Cos\theta} \tag{3.2}$$

Where L is average crystalline size, λ is the X-ray wavelength, θ is the diffraction angle, β is the line broadening at half the maximum intensity (FWHM) in radians resulting from small crystallite size, and K is a constant approximately equal to unity and related to crystallite shape. The crystallite size and lattice strain of ferrous oxalate was found to be 22.6 nm and 1.196 %, respectively. When it was heated to 300 °C form γ-Fe_2O_3 its crystallite size increased to 29.4 nm while lattice strain decreased to 0.5. Similarly, when the sample was further heated to higher temperature to form α-Fe_2O_3 its crystallite size still increases and lattice strain decreases. This phenomenon is also observed in the XRD patterns that for ferrous oxalate consists broadened peaks and γ-Fe_2O_3 consists less broadened peaks while α-

Fe_2O_3 contains comparatively sharp peaks. As the lattice strain of α-Fe_2O_3 is least, it is the most stable form among the three samples. The unit-cell dimension of the synthesized samples was measured to determine the crystal structure and given in table 3.1.

Table 3.1 Crystallographic information of the prepared nanorods.

Sample	**Crystal Structure**	**Lattice Parameters (^{o}A)**	**Crystallite Size (nm)**	**Lattice Strain (%)**
$FeC_2O_4.2H_2O$	Orthorhombic	a=12.26, b=5.57, c=15.48	22.6	1.196
γ-Fe_2O_3	Cubic	a=8.3515	29.4	0.5
α-Fe_2O_3	Rhombohedral	a=b=5.0285, c=13.736	39.1	0.433

3.3.3. FTIR study

To further confirm the formation and transformation from $FeC_2O_4.2H_2O$ to γ-Fe_2O_3 and α-Fe_2O_3, FTIR analysis was performed. In figure 3.4a pattern, the peaks at 3358, 1631, 1315 and 496 cm^{-1} are attributed to O-H, C=O, C-O and Fe-O functional groups, respectively, indicating the formation of $FeC_2O_4.2H_2O$. In figure 3.4b pattern, the peak at 632 cm^{-1} is due to Fe-O, which is characteristic peak of maghemite and at 1637 cm^{-1} is due to presence of water of crystallisation in the sample. In figure 3.4c pattern, the peaks at 617 cm^{-1} is due to longitudinal absorption (A_u) and at 572 and 490 cm^{-1} are due to transverse absorption (E_u) of Fe-O vibrational mode of hematite.

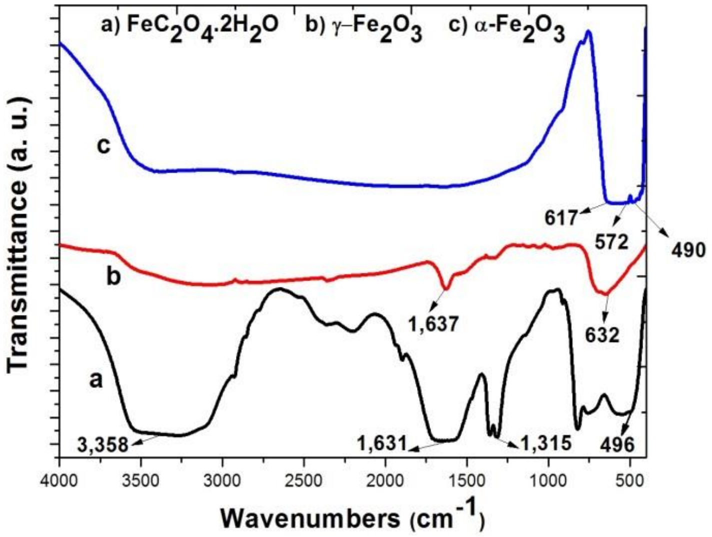

Figure 3.4 FTIR spectra of a) $FeC_2O_4.2H_2O$ nanorod, b) γ-Fe_2O_3 nanorod and c) α-Fe_2O_3 nanorod.

3.3.4. N_2 Adsorption-Desorption Isotherm

The surface area and porosity nature of the prepared nanorods was carried out by N_2 adsorption-desorption isotherm technique. The adsorption-desorption isotherm and pore size distribution are shown in figure 3.5. From figure 3.5a it is observed that, the BET and Langmuir surface areas of the prepared ferrous oxalate were found to be 27.550 and 24.945 m^2/g. From figure 3.5b, the BET and Langmuir surface areas of γ-Fe_2O_3 were found to be 129.74 and 107.35 m^2/g. Similarly, from figure 3.5c, the BET and Langmuir surface areas of α-Fe_2O_3 were found to be 22.785 and 20.575 m^2/g. From the above discussion it is observed that, the surface area of γ-Fe_2O_3 is highest among the prepared nanorods.

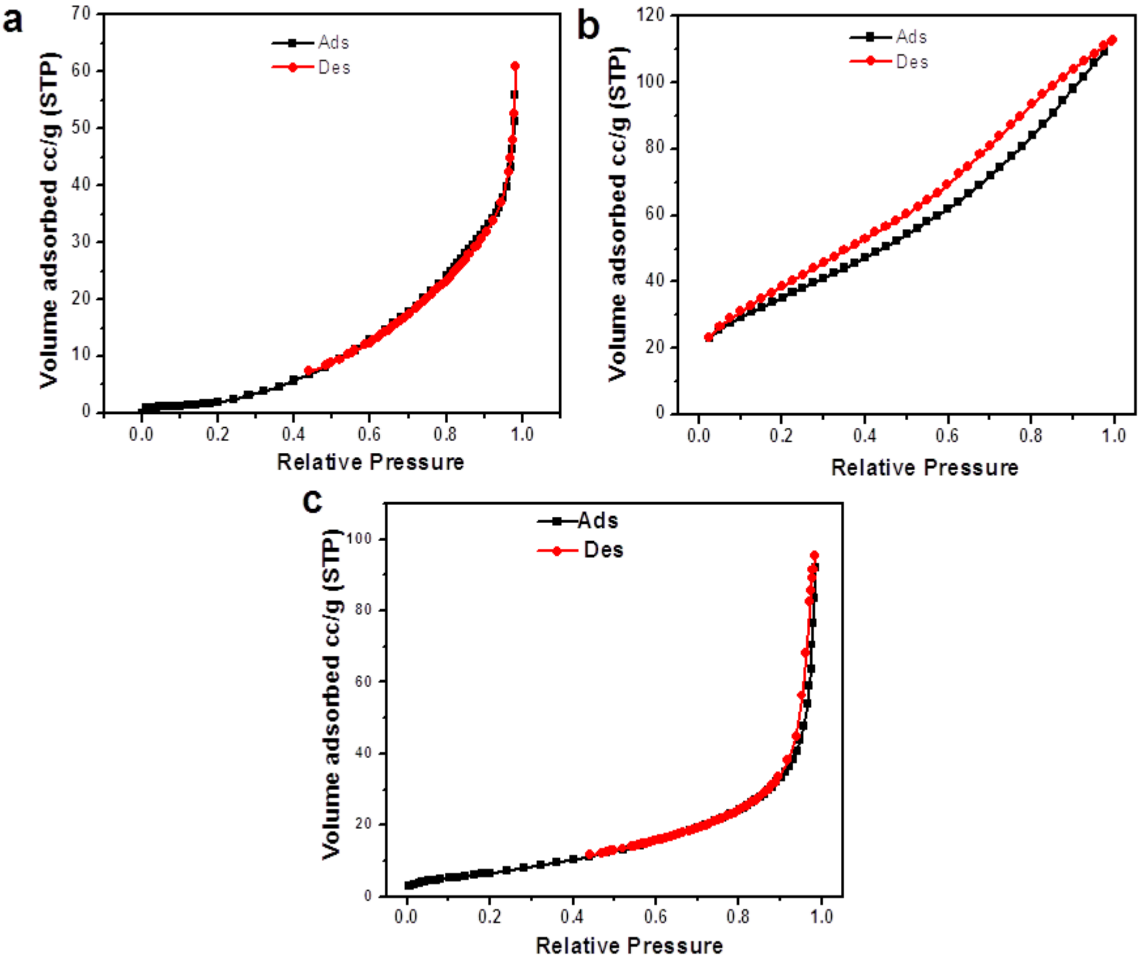

Figure 3.5 BET isotherm and BJH isotherm (inset) of (a) Ferrous Oxalate, (b) γ-Fe_2O_3, and (c) α-Fe_2O_3 nanorods.

3.3.5. Adsorption study of CR dye by different iron oxides

The different iron oxide nanorods such as: γ-Fe_2O_3, α-Fe_2O_3 and $FeC_2O_4.2H_2O$ prepared by modified wet chemical method were used as adsorbents for removal of CR dye from aqueous solution. Adsorption studies were carried out by batch experiments using 50 ml of cleaned and dry glass bottle. Figure 3.6 shows the UV−Vis spectra of Congo red solutions of concentration 100 mg L^{-1} before and after adsorption in the colloidal suspension of 0.05 g of different adsorbents, such as: $FeC_2O_4.2H_2O$ nanorod, γ-Fe_2O_3 nanorod and α-Fe_2O_3 nanorod with reaction time 30 mins. At a γ-Fe_2O_3 dosage of 0.05 g L^{-1}, the colloidal suspension is able to adsorb almost 100 % of Congo red (figure 3.6), and the photograph of before and after adsorption also confirm the removal of the Congo red at this dosage of γ-Fe_2O_3 (figure 3.6, inset).

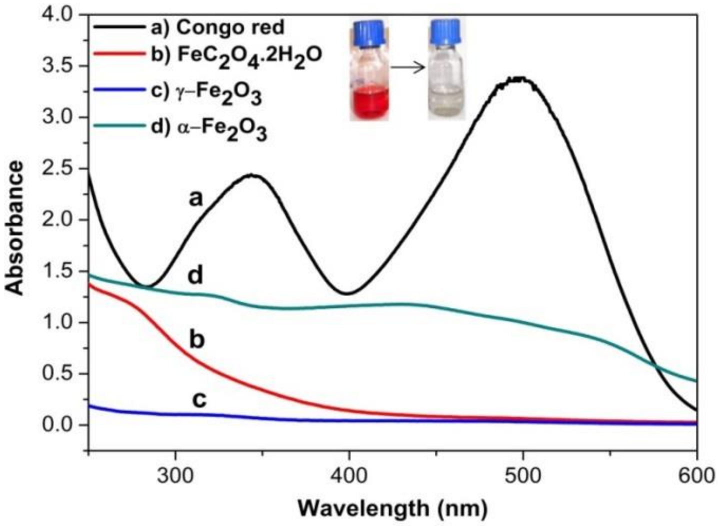

Figure 3.6 UV-Vis absorption spectra of a) initial Congo red with an initial concentration of 100 mg L^{-1} and solutions (20 ml) after treated with 0.05 g of b) $FeC_2O_4.2H_2O$, c) γ-Fe_2O_3 and d) α-Fe_2O_3 for 30 min.

3.3.5.1. Effect of adsorbent dose

Adsorbent dosage is one of the most important parameter that has been considered to determine the optimum condition for the performance of adsorption. Essentially, insufficient dosage or overdosing would result in the poor performance in adsorption. Therefore, it is significant to determine the optimum dosage in order to minimize the dosing cost and sludge formation and also to obtain the optimum performance in treatment. The effect of adsorbent doses on the removal of CR using $FeC_2O_4.2H_2O$, α-Fe_2O_3 and γ-Fe_2O_3 nanorods was performed by mixing the nanorod samples of different weight to 20 ml of 100 mg/L CR, maintaining pH=7.6 (pH at normal condition) for 30 min contact time. The weight of the adsorbents was varied in the range 0.01-0.1 g. Figure 3.7a shows the UV−vis absorption spectra of CR solutions after being treated with different dosages of the prepared nanorod adsorbents using an initial dye concentration of 100 mg L^{-1}. It is observed there is a continuous removal of CR with increase in adsorbent dose up to 0.05 g. This may be due to an increase in number of active sites of the adsorbent material with increasing amount of the adsorbent. Further increase in the amount of the adsorbent does not bring any considerable change in the adsorption i.e. approximately straight line is obtained. Therefore 0.05 g was chosen as the optimum amount for all studies of the adsorbents. The highest percentage of removal obtained for γ-Fe_2O_3 nanorod among the three adsorbents.

3.3.5.2.Effect of contact time.

Time of contact of adsorbent and adsorbate plays an important role for adsorptive removal of organic dye from aqueous solution. It is helpful in understanding the amount of dye adsorbed at various time intervals by a fixed amount of the adsorbent. Figure 3.7b shows the adsorptive removal of Congo red with time variation by using $FeC_2O_4.2H_2O$, α-Fe_2O_3 and γ-Fe_2O_3 nanorod adsorbents. In this section 0.05 g of each adsorbents were added into 20 ml of 100mg/L of CR solution maintaining pH=7.6, with varying time from 0 min to 60 min. From the figure, it is found that there is a consistent increase in percentage of removal up to 30 min and the adsorption equilibrium is attained after 30 min of contact time. This is due to the rate of adsorption decreased and a saturation stage was attained due to the accumulation of the adsorption sites by the dye ions. The highest removal of CR is found to be 97.97 % for $FeC_2O_4.2H_2O$, 99.24 % for γ-Fe_2O_3 and 84.62 % for α-Fe_2O_3 for 30 min contact time. Agitation time of 30 min was selected for further works.

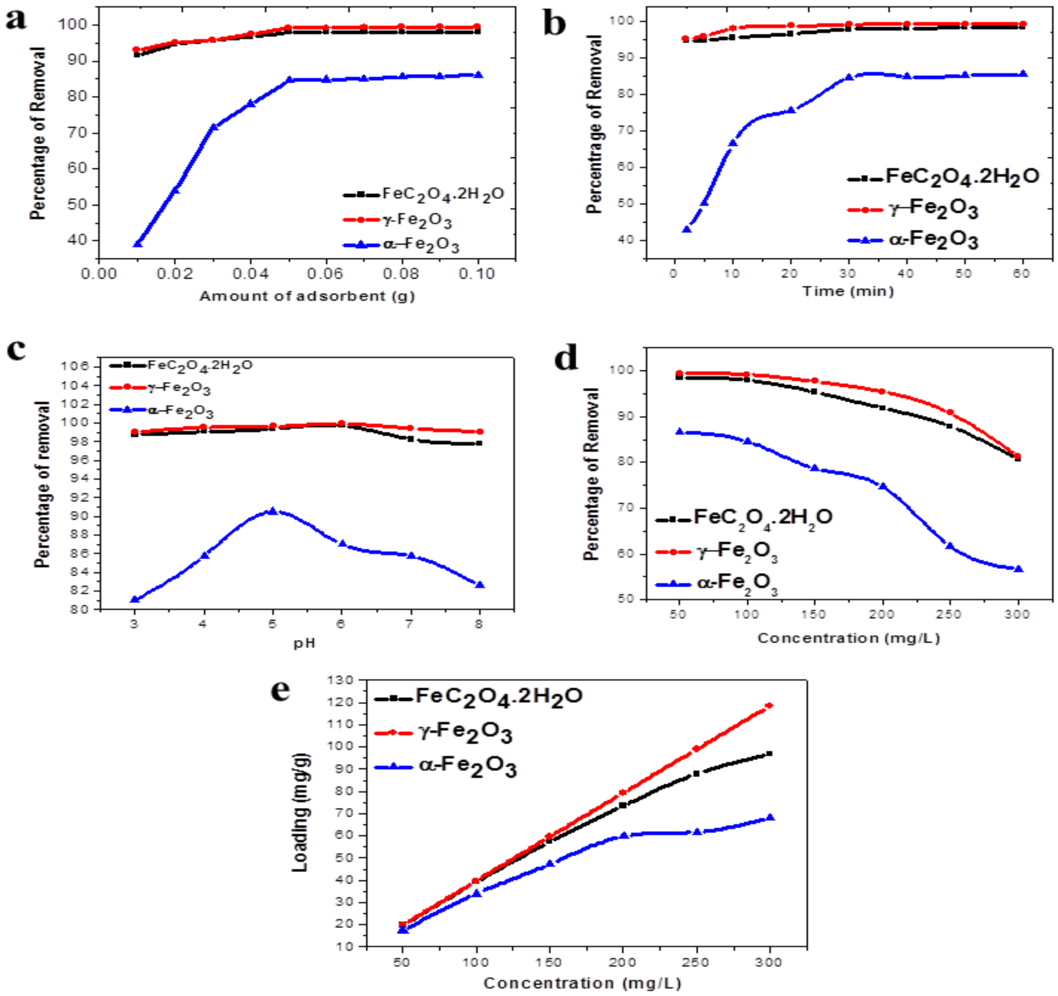

Figure 3.7 Effect of a) amount of adsorbent (dose), b) time, c) pH and d) Concentration on removal of Congo red by: ■) $FeC_2O_4.2H_2O$, ●) γ-Fe_2O_3 and ▲) α-Fe_2O_3 nanorods and e) Effect of initial dye concentration on adsorption capacity for the removal of Congo red.

3.3.5.3. Effect of pH of CR solution

Solution pH affects both aqueous chemistry and surface binding sites of the adsorbents. To investigate the effect of pH on the adsorption of CR dye the pH range 3–8 was chosen. The pH of the test solutions was adjusted by using HCl and NaOH solutions. 0.05 g of each adsorbents used in 20 ml of 100 mg/L CR solution of each pH value with 30 min agitation time. From figure 3.7c it is found that, for $FeC_2O_4.2H_2O$ and γ-Fe_2O_3, there is no significant change in the percentage adsorption by increasing pH from 3-6 and reached maximum at pH = 6 and then slightly decreased at higher pH in case of $FeC_2O_4.2H_2O$. For α-Fe_2O_3, the maximum percentage of removal occurs at pH = 5 and then decreases. This is due to for higher pH solution; the high negatively charged adsorbent surface sites did not favour the adsorption of deprotonated CR due to electrostatic repulsion (Afkhami and Moosavi, 2010).

3.3.5.4. Effect of initial dye concentration on adsorption

The initial concentration provides important information that overcomes the mass transfer resistance of all molecules between the aqueous and solid phases (Ghaedi et al., 2011). The adsorption is greatly influenced by the concentration of the solution, as the adsorptive reactions are directly proportional to the concentration of the solute (Mittal et al., 2009). It this section, 0.05 g of each adsorbent used each 20 ml of CR solution (natural pH) with concentration ranging from 50 mg/L to 300 mg/L and the agitation time was kept 30 min. It is found that with the increase in initial dye concentration, percentage adsorption decreases (figure 3.7d) while the equilibrium adsorption capacity of the adsorbent for CR increases with increasing initial dye concentration i.e. the more concentrated the dye solution, the higher the adsorption capacity (figure 3.7e). This is probably due to a high driving force for mass transfer in high dye concentration.

3.3.6. Adsorption Isotherm

To determine equilibrium relationship of amount adsorbed by a unit weight of adsorbent (q_e) with the concentration of adsorbent remaining in the medium at equilibrium (C_e), studies of various adsorption isotherm models is required, which can optimise the design of a sorption system. There is various type of adsorption models developed such as: Freundlich, Langmuir, Tempkin, D–R isothermal models, etc (Mittal et al., 2009). The most common models such as Freundlich and Langmuir equations are used to investigation of this study. The initial dye concentrations were varied from 50 to 300 mg/L using 0.05 g of each adsorbent in 20 ml of CR solution (natural pH) with agitation time 30 min.

Langmuir isotherm

The Langmuir isotherm model assumes monolayer coverage of adsorbate on a homogeneous adsorbent surface. This model does not consider surface heterogeneity of the sorbent. It assumes adsorption will take place only at specific site on the adsorbent (Chatterjee et al., 2009; Bayazit and Inci, 2013). The Langmuir equation is given as:

$$\frac{q_e a_L}{K_L} = \frac{K_L C_e}{(1+K_L C_e)} \qquad \textbf{(3.3)}$$

The linear form of the Langmuir isotherm is:

$$\frac{C_e}{q_e} = \frac{1}{K_L q_{max}} + C_e/q_{max} \qquad \textbf{(3.4)}$$

where a_L (Lmg^{-1}) and K_L (Lg^{-1}) are the Langmuir constants, q_{max}($=K_L/a_L$) is the maximum adsorption capacity corresponding to complete monolayer coverage (mg g^{-1}), which depends upon the number of adsorption sites (Rahimi et al. 2011). The values of q_{max} and K_L are calculated from the slopes and intercepts of the straight lines of plot of C_e/q_e versus C_e.

Freundlich isotherm

The Freundlich isotherm model is an empirical equation that describes the surface heterogeneity of the sorbent. It considers multilayer adsorption with a heterogeneous energetic distribution of active sites, accompanied by interactions between adsorbed molecules (Namasivayam and Kavitha, 2002). The Freundlich isotherm equation is given as (Inci et al., 2011):

$$q_e = K_F C_e^{1/n} \qquad \textbf{(3.5)}$$

The linear form of the Freundlich isotherm is:

$$\ln q_e = lnK_F + {}^{1}/_{n}\, lnC_e \qquad \textbf{(3.6)}$$

where C_e is the equilibrium concentration (mg L^{-1}), q_e is the amount adsorbed at equilibrium (mg g^{-1}) and K_F and n are Freundlich constants, related to the extent of the adsorption and the degree of nonlinearity between solution concentration and adsorption, respectively. K_F and (1/n) can be determined from the linear plot of ln q_e versus ln Ce.

The essential characteristics of Langmuir isotherm can be expressed by a dimensionless constant called equilibrium parameter (R_L) that is defined by the following equation (Chatterjee et al., 2009; Afkhami et al., 2010; Kumar et al., 2012):

$$R_L = \frac{1}{1+a_L C_0} \qquad \textbf{(3.7)}$$

where a_L and C_0 are the parameters as defined previously. The value of R_L calculated from the above expression. The nature of the adsorption process to be either unfavourable ($R_L > 1$), linear ($R_L = 1$), favourable ($0 < R_L < 1$) or irreversible ($R_L = 0$) (Lian et al., 2009). Here R_L values obtained are listed in table 3.2. The linear Langmuir and Freundlich plots for the adsorption of CR onto the three nanorod adsorbents are obtained by plotting C_e/q_e vs. C_e and ln q_e vs. ln C_e, respectively (given in figure 3.8). The isotherm constants and correlation coefficients were calculated and listed in table 3.2. By comparing the correlation coefficients r_L^2, it can be deduced that the experimental equilibrium adsorption data are well described by both the Langmuir and Freundlich models, but the Langmuir model is more suitable. The maximum adsorption capacity of 103.09 mg g^{-1}, 232.56 mg g^{-1} and 78.13 mg g^{-1} was found for $FeC_2O_4.2H_2O$, γ-Fe_2O_3, and α-Fe_2O_3, respectively. For Freundlich isotherm model, the n value between 1 and 10 indicates beneficial adsorption (Chen and Zhao, 2009).

Table 3.2 Adsorption isotherm constants for adsorption of Congo red.

	Adsorbent	**a_L (L mg^{-1})**	**K_L (Lg^{-1})**	**q_{max} (mg g^{-1})**	**r_L^2**	**R_L**
Langmuir	$FeC_2O_4.2H_2O$	0.0022	0.224	103.09	0.996	0.82
	γ-Fe_2O_3	0.0012	0.267	232.56	0.998	0.89
	α-Fe_2O_3	0.00064	0.048	78.13	0.995	0.999
	Adsorbent	**K_F**		**1/n**		**r_F^2**
Freundlich	$FeC_2O_4.2H_2O$	26.5		0.3493		0.957
	γ-Fe_2O_3	46.42		0.7434		0.993
	α-Fe_2O_3	8.99		0.442		0.914

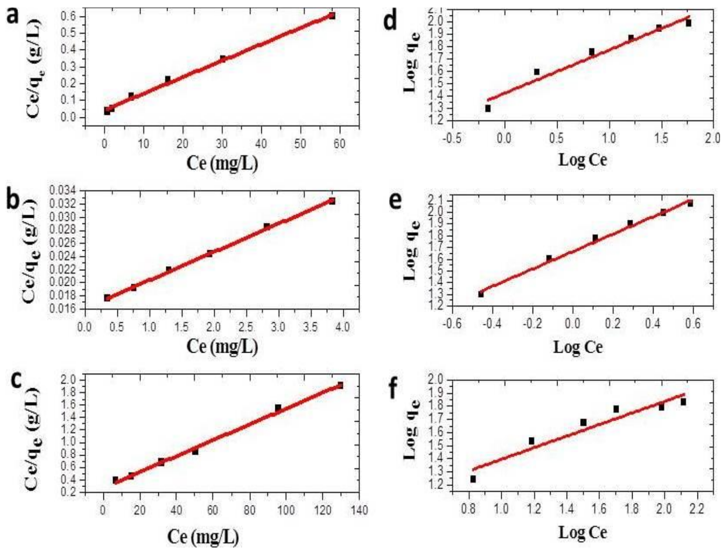

Figure 3.8 Linearization of Langmuir plots of a) $FeC_2O_4.2H_2O$, b) γ-Fe_2O_3 and c) α-Fe_2O_3 and Freundlich plots of d) $FeC_2O_4.2H_2O$, e) γ-Fe_2O_3 and f) α-Fe_2O_3 for the adsorption of Congo red.

Comparing the q_{max} values of the different adsorbents, it is observed that, γ-Fe_2O_3 nanorod have higher adsorption capacity than $FeC_2O_4.2H_2O$ and α-Fe_2O_3 nanorods.

3.3.7. Adsorption Kinetics

In order to investigate the adsorption processes of CR on the adsorbents, pseudo-second order kinetic model is used. The pseudo-second-order model is represented as (Rajesh et al., 2011):

$$\frac{t}{q} = \frac{1}{k_2 q_e^2} + \frac{t}{q_e} \qquad (3.8)$$

And the initial adsorption rate, h (mg/g min^{-1}), as t → 0 can be defined as:

$$h = k_2 q_e^2 \qquad (3.9)$$

The initial adsorption rate (h), the equilibrium adsorption capacity (q_e), and the second-order constants k_2 (g/mg min) can be determined experimentally from the slope and intercept of plot of t/q versus t. The best-fit values of h, q_e and k_2 along with correlation coefficients of the pseudo-second-order model for the three adsorbents are shown in table 3.3 and the pseudo-second-order plots of $FeC_2O_4.2H_2O$, γ-Fe_2O_3 and α-Fe_2O_3 are given in figure 3.9. The values of predicted equilibrium adsorption capacities (q_e) showed good agreement with the experimental equilibrium uptake values. Similarly, correlation coefficients are always greater than 0.99, which also explains the good fit of the model.

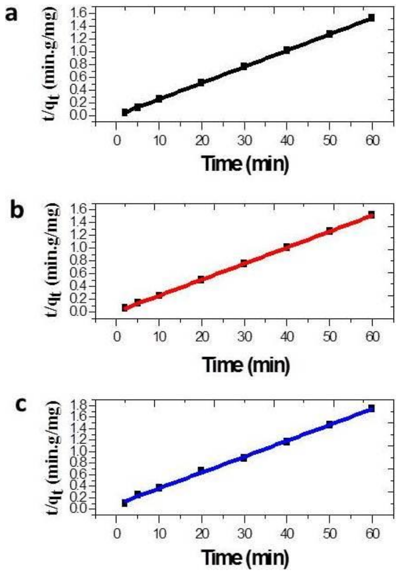

Figure 3.9 Pseudo- second-order kinetic plots of a) $FeC_2O_4.2H_2O$, b) γ-Fe_2O_3 and c) α-Fe_2O_3.

Table 3.3 Second-order kinetic parameters for the removal of Congo red.

Adsorbents	**K_2 (g mg^{-1} min^{-1})**	**q_e (mg/g)**	**q_e (mg/g) (Experimental)**	**r^2**
$FeC_2O_4.2H_2O$	0.0999	39.53	39.19	1
γ-Fe_2O_3	0.0933	40	39.7	1
α-Fe_2O_3	0.00891	36.23	34.23	0.9986

The maximum adsorption capacity (q_{max}) for the adsorption of CR on γ-Fe_2O_3 nanorod as compared to other adsorbents is listed in table 3.4.

Table 3.4 Comparison of Congo red adsorption capacities of various adsorbents.

Types of Adsorbent	**q_{max} (mg/g)**	**Surface area (m^2/g)**	**Reference**
Chitosan/montmorillonite nanocomposite	54.52	22.3	(Wang and Wang, 2007)
Montmorillonite	12.70	61.4	(Wang and Wang, 2007)
Commercial activated carbons	300	492	(Purkait et al., 2007)
Hollow α-Fe_2O_3 Nanostructures	152.42	160	(Wei et al., 2013)
Magnetic core–MnO_2 shell nanoparticles	794	42	(Zhai et al., 2009)
$Co_{0.3}Ni_{0.7}Fe_2O_4$ nanoparticles	65.29	131	(Chen et al., 2014)
γ-Fe_2O_3 nanoparticles	208.33	81.61	(Afkhami and Moosavi , 2010)
Chitosan Bead	162.32	-------	(Chatterjee et al., 2009)
γ-Fe_2O_3 nanorod	232.56	129.7	Present work
$FeC_2O_4.2H_2O$ nanorod	103.09	27.55	Present work
α-Fe_2O_3 nanorod	78.13	22.78	Present work

Table 3.4 represents a comparision on the adsorption capacities of different adsorbents reported in literature and our prepared $FeC_2O_4.2H_2O$, γ-Fe_2O_3 and α-Fe_2O_3 nanomaterials along with their BET surface area values. It is observed that, although the commercial activated carbon possesses considerably higher surface area than the prepared γ-Fe_2O_3 nanorod, but their maximum sorption capacities is not proportionately higher as compard to γ-Fe_2O_3 nanorod used in this work. Again, the prepared $FeC_2O_4.2H_2O$ and α-Fe_2O_3 nanorods possess similar surface area to other adsorbents in the table, but their maximum sorption capacities of are considerable higher than others. The above discussion indicates that the number of adsorption sites per unit surface is heigher for iron oxide based materials compared to oter materials studied. Hence, the prepared γ-Fe_2O_3 nanorod can be used as an alternative efficient adsorbent than activated carbon for adsorption of Congo red from aqueous solution. This materials can also be used as efficient adsorbent for removal other organic pollutants from waste water.

3.4. Conclusions

In this present study, we have synthesized ferrous oxalate nanorods by a modified precipitation by using ferrous sulphate and oxalic acid as starting material and CTAB as surfactant. Then the obtained nanoparticles are calcined at higher temperature to form γ-Fe_2O_3 and α-Fe_2O_3 nanorods. SEM images indicate the formation of rod shaped nanoparticles with diameter around 100-200 nm and length up to micrometres. The formation of the phase, crystallite sites, lattice parameters, lattice strains and crystal structure are determined by XRD study. It is found that the crystallite sizes are 22.6 nm, 29.4 nm and 39.1 nm, for $FeC_2O_4.2H_2O$, γ-Fe_2O_3 and α-Fe_2O_3 nanorods, respectively. Then the three prepared 1-dimensional nanomaterials such as: ferrous oxalate ($FeC_2O_4.2H_2O$), maghemite (γ-Fe_2O_3) and hematite (α-Fe_2O_3) nanorods were used as adsorbent for removal of carcinogenic organic dye such as: Congo red from aqueous solution. From the adsorption study it is found that the maximum adsorption capacities of the adsorbents are 103.09 mg g^{-1}, 232.56 mg g^{-1} and 78.13 mg g^{-1} for $FeC_2O_4.2H_2O$, γ-Fe_2O_3 and α-Fe_2O_3 nanorods respectively. This result indicates that among the three prepared 1-dimensional nanomaterials, γ-Fe_2O_3 nanorods are the most effective adsorbent for the adsorption of Congo red from aqueous solution. This result might be due to surface charge density and high surface area to volume ratio of γ-Fe_2O_3 nanorods.

PART B: Fe_2O_3-SnO_2 COMPOSITE NANORODS

3.5. Introduction

In the previous section of this chapter, adsorptive removal of Congo red dye from aqueous media has been presented using $FeC_2O_4.2H_2O$, γ-Fe_2O_3 and α-Fe_2O_3 nanorods. We have used the oxalate precipitation method for synthesis of the $FeC_2O_4.2H_2O$, γ-Fe_2O_3 and α-Fe_2O_3 rod shaped nanomaterials. In the present section, in order to improve the sorption performance of iron oxides, we have synthesized iron-tin mixed oxide (Fe_2O_3-SnO_2) composite nanomaterials using the same precipitation method followed by calcination as described in the previous part (part A).

One dimensional (1D) nanomaterial, including nanotubes, nanowires, nanofibers and nanorods possess superior properties like small dimension structure, high aspect ratio and unique device function compared to their bulk and microscale counterparts. Due to these properties, one dimensional (1D) nanomaterials are applied in the fields of electronics, photonics, chemical sensors, field emission devices, solar cells, lithium ion battery, hydrogen storages, adsorption, energy harvesting, nanoelectronics, optoelectronics, nanobiotechnology, nanofluidics and drug deliveries (Tekina and Saygi, 2013; Li et al., 2011; Fang et al., 2010; Dang et al., 2013). Inorganic semiconductor metal oxides (Fe_2O_3, ZnO, SnO_2, TiO_2, MnO_2, CuO etc.) are the most common minerals on the Earth and their 1D nanostructure are very important for their special shapes, compositions, and chemical and physical properties associated with the 1D structural confinement (Zhai et al., 2009; Anandan et al., 2010; Zhou et al., 2010). Nowadays, researchers are much more interested in field of mixed metal oxide nanocomposite/heteronanostructures. The nanocomposites/heteronanostructures, consist of chemically distinct components, are generating novel properties arise from the strong interface interactions at the nanometer scale. The said novel properties are nonexistent in the individual component materials (Mahapatra et al., 2013; Niu et al., 2010).

Water pollution is a major global problem worldwide that leads to large alterations in the hydrological cycle and causes deaths and diseases (Xiong et al., 2013). Wastewater generated from many industries such as textile, rubber, paper, leather, plastics, cosmetic, printing, etc. contains several kinds of synthetic dyestuffs, that exhibit high color and high chemical and/or biochemical oxygen demands (COD and/or BOD) (Dawood and Sen, 2012). Decomposition of dyes gives hazardous products, that are toxic and causes severe health problem to living beings. Thus the removal of dye effluents from aqueous media is highly essential for environmental remediation (Irama et al., 2010). There are several methods for removal of organic dyes from aqueous solution including chemical coagulation, oxidation, ion exchange, precipitation, phytoextraction, filtration, reverse osmosis, carbon adsorption, photo-degradation etc. (Setti et al., 2015). Amongst all the practiced methods, adsorption is considered to be a promising method for efficient removal of the dyes with it's relative operational simplicity and high efficiency (Saikia et al., 2013). Currently, nanoparticles such as nano-carbon materials and nanosized metal oxides are mostly used for adsorption applications; because they are found be powerful adsorbent materials due their large specific surface area and small internal diffusion resistance (Zhang et al., 2013).

In the present investigation, we have synthesized α-Fe_2O_3 and Fe_2O_3-SnO_2 composite nanorods by a simple wet chemical method and studied the structural and magnetic properties. Then, the prepared metal oxide composite nanorods were used as adsorbents for the removal of Congo red (CR) dye molecules from aqueous solutions. The adsorption experiments such as the effects of adsorbent dose and composition, contact time, pH, and initial concentration variation were explored in batch experiments. The adsorption isotherm and kinetic studies were also carried out to elucidate the maximum adsorption capacity and nature of the adsorption. A comparative study for maximum removal capacity using different adsorbents was also reported here.

3.6. Materials and methods

3.6.1. Materials

Ferrous sulphate heptahydrate ($FeSO_4.7H_2O$), oxalic acid dihydrate ($H_2C_2O_4.2H_2O$), cetyltrimethyl ammonium bromide (CTAB), ethanol and Congo red were procured from Merck India. Tin sulphate ($SnSO_4$) was obtained from Sigma-Aldrich. All the chemicals were used as received without any further purification.

3.6.2. Synthesis of Fe_2O_3-SnO_2 composite nanorods

Hematite (α-Fe_2O_3) and Fe_2O_3-SnO_2 composite nanorods were synthesized by wet chemical method using $FeSO_4.7H_2O$ and $SnSO_4$ as salt precursors, CTAB as structure directing agent and ethanol and double distilled water as solvent. In a typical preparation procedure, stoichiometric amount of $FeSO_4.7H_2O$ and $SnSO_4$ were dissolved in distilled water with vigorous stirring to form solution-I and required amount of oxalic acid and CTAB were dissolved in ethanol with vigorous stirring to form solution-II. Then, solution-I was added to solution-II drop wise with continuous stirring to form a yellow precipitate. The yellow precipitate changes to whitish yellow with increasing percentage of $SnSO_4$. After addition, the stirring was continued for another 5 hours. Then the precipitate obtained was centrifuged, washed thoroughly by ethanol and double distilled water and dried at 80 °C for 2 hours to form ferrous oxalate-tin oxalate nanorod. The obtained composite nanorods were calcined at 500 °C with heating rate 10 °C/min for 2 hours to form Fe_2O_3-SnO_2 composite nanorods. In order to maintain identical processing condition for comparision of adsorption properties, we have synthesized the iron oxide using the same condition applied for the composite metal oxide synthesis. Under the adopted condition, we found α-phase to be stabilizing; hence we have used α-phase for comparision.

3.6.3. Characterization techniques

The surface morphology of the prepared nanorods was characterized by a JEOL JSM-5300 scanning electron microscope (SEM) operated at an acceleration voltage of 15 and 20.0 kV. The size of the particle and selected area electron diffraction (SAED) pattern of the α-Fe_2O_3 and Fe_2O_3–SnO_2 (Fe: Sn = 6: 4) composite nanorods were observed using a high resolution transmission electron microscope (JEM-2100 HRTEM, Make-JEOL, Japan) with an acceleration voltage of 200KV. The crystalline phases were identified by means of X-ray diffraction (XRD) by a PANalytical X-ray diffractometer with Cu Kα radiation (λ) 1.54156 °A at a scan rate of 2 °/min. FTIR spectra were recorded using a Perkin-Elmer FTIR (Spectrum RX-I) spectrophotometer. Raman spectra were collected using a RAMNOR HG-2S spectrometer in a backscattering configuration, employing the 514.5 NM line of air laser as the excitation source. Specific surface area and pore size distribution (PSD) of the samples were determined from nitrogen adsorption/desorption isotherms obtained at the temperature of liquid nitrogen in an automated physisorption instrument (Autosorb-iQ, Quantachrome Instruments). Prior to the analysis, the samples were outgassed under vacuum at 150 °C for 1.5 h. Specific surface areas were calculated according to the Brunauer-Emmett-Teller (BET) method and the pore size distributions were obtained according to the Barret-Joyner-Hallenda (BJH) method from the adsorption data. The magnetic properties of the prepared α-Fe_2O_3 and Fe_2O_3–SnO_2(Fe :Sn = 8:2) nanorods were obtained on a Lakeshore 7410 series vibrating sample magnetometer (VSM) at a temperature 300 K and a magnetic field of 1.5 T.

3.6.4. Adsorption Experiment

A stock solution of CR (1 g L^{-1}) was prepared in double distilled water and desired concentrations of the dye were obtained by diluting the same with double distilled water. The calibration curve of CR was prepared by measuring the absorbance of different concentrations of CR dye at λ_{max} = 498 nm using UV–Vis spectrophotometer. The adsorption study was carried out by taking 50 mg each adsorbent into 20 ml of Congo red solution (100 mg/L) under stirring condition. In a batch adsorption process, adsorption experiments were conducted to observe the effects of various parameters such as: adsorbent composition, dose, time, pH, and initial concentration of Congo red. To evaluate the sorption capacity, the initial concentrations of Congo red solutions were varied in the range of 100−500 mg/L, and the dosage of adsorbents was kept 50 mg for each adsorbent into 20 ml of Congo red solution under constant stirring for 30 min. After adsorption, the solution was filtered and analyzed by UV–Visible spectrophotometer to know the absorbance. All the adsorption experiments were carried out three times in replicates and the mean data obtained were taken in results and discussion section.

3.7. Results and discussion

3.7.1. Characterization of Fe_2O_3-SnO_2 composite nanorods

Figure 3.10a shows the SEM image of pure α-Fe_2O_3. It suggests that the obtained nanostructure exhibits rod shaped morphology with diameter around 100-200 nm and the length up to micrometers. Figures 3.10b-f represent the SEM images of Fe_2O_3-SnO_2 composites prepared by varying mole % of iron and tin salt precursors. From the images it is found that, with decreasing mole percentage of $FeSO_4.7H_2O$ and increasing mole percentage of $SnSO_4$ the diameter of nanorods increases. Figure 3.10b represents the SEM image of Fe_2O_3–SnO_2 (Fe: Sn = 9: 1). From this image, the formation of smooth rod shaped morphology composite material is observed with a diameter slightly greater than pure α-Fe_2O_3. Following the similar trend, it is found that the rod diameter gradually increases and reaches the highest value i.e. around 500-600 nm for Fe_2O_3–SnO_2 (Fe: Sn = 5: 5). However, it is observed that the rod shaped morphology of the composite is gradually destroyed with increasing percentage of SnO_2. The energy-dispersive spectroscopy (EDS) spectrums are shown in figure 3.10g and (h) for α-Fe_2O_3 and Fe_2O_3–SnO_2 (Fe: Sn = 5: 5), respectively. Figure 3.10g spectrum demonstrates that the sample contains O, and Fe elements. Similarly from figure 3.10h, it is found that the spectrum contains O, Fe and Sn elements.

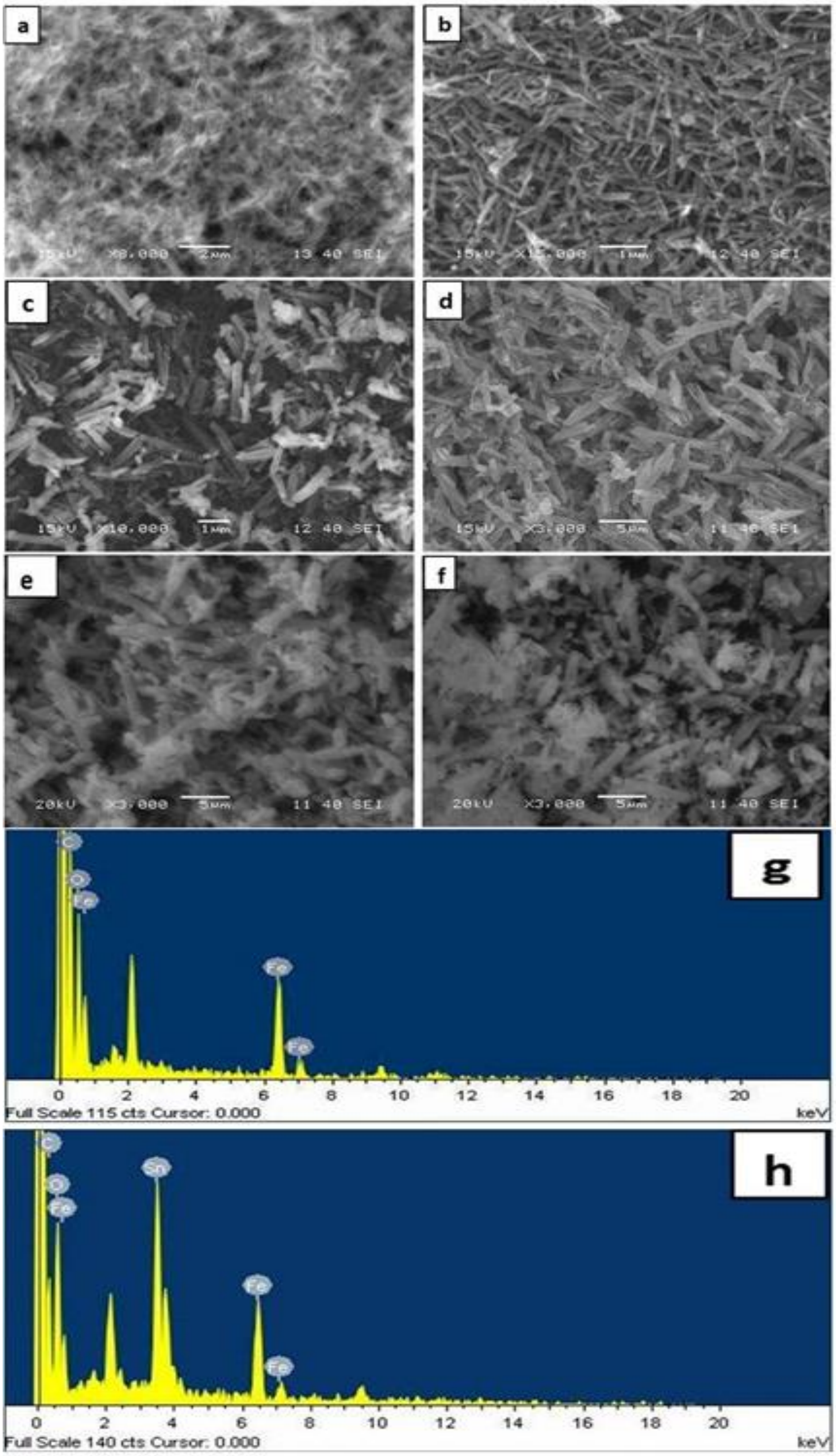

Figure 3.10 Scanning Electron micrographs of (a) α-Fe_2O_3, (b) Fe_2O_3–SnO_2 (Fe: Sn = 9: 1), (c) Fe_2O_3–SnO_2 (Fe: Sn = 8: 2), (d) Fe_2O_3–SnO_2 (Fe: Sn = 7: 3), (e) Fe_2O_3–SnO_2 (Fe: Sn = 6: 4), and (f) Fe_2O_3–SnO_2 (Fe: Sn = 5: 5), and EDAXs of (g) α-Fe_2O_3, and (h) Fe_2O_3–SnO_2 (Fe : Sn = 5: 5).

The transmission electron micrographs of α-Fe_2O_3 and Fe_2O_3–SnO_2 (Fe: Sn = 6: 4) materials are shown in figure 3.11. A typical TEM image of a single α-Fe_2O_3 nanorod is given in figure 3.11a, which indicates the diameter of the rod is around 100 nm. From figure 3.11b-c, it is observed that the morphology of Fe_2O_3–SnO_2 (Fe: Sn = 6: 4) composite is not completely rod shaped, that means with increasing percentage of SnO_2 the percentage of rod shaped morphology destroyed. The result is in agreement with SEM micrographs. The crystalline structure of Fe_2O_3–SnO_2 (Fe: Sn = 6: 4) 1D nanorod was further analyzed by SAED pattern. The SAED pattern of the nanorod (figure 3.11d) shows bright diffraction sports, due to high crystalline nature of the sample.

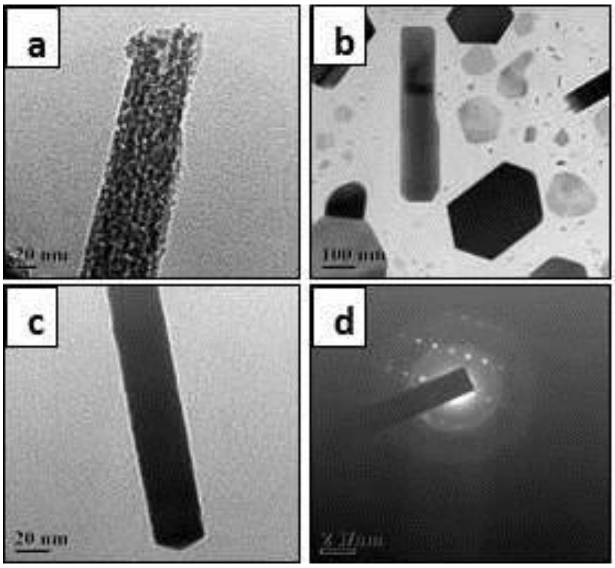

Figure 3.11 Transmission electron microscopy images of (a) α-Fe_2O_3, (b and c) Fe_2O_3–SnO_2 (Fe: Sn = 6: 4) and (d) Electron diffraction pattern of Fe_2O_3–SnO_2 (Fe: Sn = 6: 4) nanorod.

Figure 3.12 shows the XRD patterns of pure α-Fe_2O_3 and Fe_2O_3-SnO_2 composite nanorods. The pure α-Fe_2O_3 shows sharp and intense diffraction peaks at 2θ values of 24.2°, 33.2°, 35.7°, 40.9°, 49.5°, 54.1°, 57.7°, 61.5°, and 64° corresponding to the presence of highly crystalline rhombohedral phase according to JCPDS file 79-0007. The Fe_2O_3-SnO_2 composites are prepared by addition of different mole % of $SnSO_4$ with $FeSO_4.7H_2O$ salt precursor. It is observed that the presence of both magnetic γ-Fe_2O_3 and α-Fe_2O_3 phases along with SnO_2 in the Fe_2O_3-SnO_2 composites, calcined at 500 °C temperature. With increasing percentages of $SnSO_4$, the formation of γ-Fe_2O_3 phase is observed along with α-Fe_2O_3 phase. However, the maximum intensity peak (2θ=33.2°) corresponds to α-Fe_2O_3 phase gradually decreases and completely disappeared after addition of 30 % $SnSO_4$. The XRD patterns of the composite nanorods contain characteristic peaks of cubic γ-Fe_2O_3 and tetragonal SnO_2 according to JCPDS No: 39-1346 and 77-0451, respectively. Generally, it is known that at calcination temperature 500 °C the γ-Fe_2O_3 phase is unstable: as it changes to stable α-Fe_2O_3 phase. But in our study, it is observed that after calcined at 500 °C temperature, the Fe_2O_3-SnO_2 composites retain their γ-Fe_2O_3 phase. During the transition of γ-Fe_2O_3 to α-Fe_2O_3, the thermal stability of the γ-Fe_2O_3 phase in the pure iron oxide is different from that in the γ-Fe_2O_3–SnO_2 composite. In pure iron oxide, the γ-$Fe_2O_3 \rightarrow \alpha$-$Fe_2O_3$ transition occurs in the temperature higher than 300^{0}C but in the prepared Fe_2O_3–SnO_2 nanocomposite system, the γ-Fe_2O_3 stabilized after heating at 500 °C for 2 hours. The existence of the γ-Fe_2O_3 crystal phase in the presence of SnO_2 at higher temperature can be caused by diffusion hindrances to the motion of atoms during structure transformation and an increased concentration of cationic vacancies, which stabilize the spinel structure of γ-Fe_2O_3. Maghemite (γ-Fe_2O_3) is a metastable form, and the presence of SnO_2 in the nanocomposite electively stabilizes this form since the activation energy is substantially increased (Lal et al., 2003: Ivanovskaya et al., 2008).

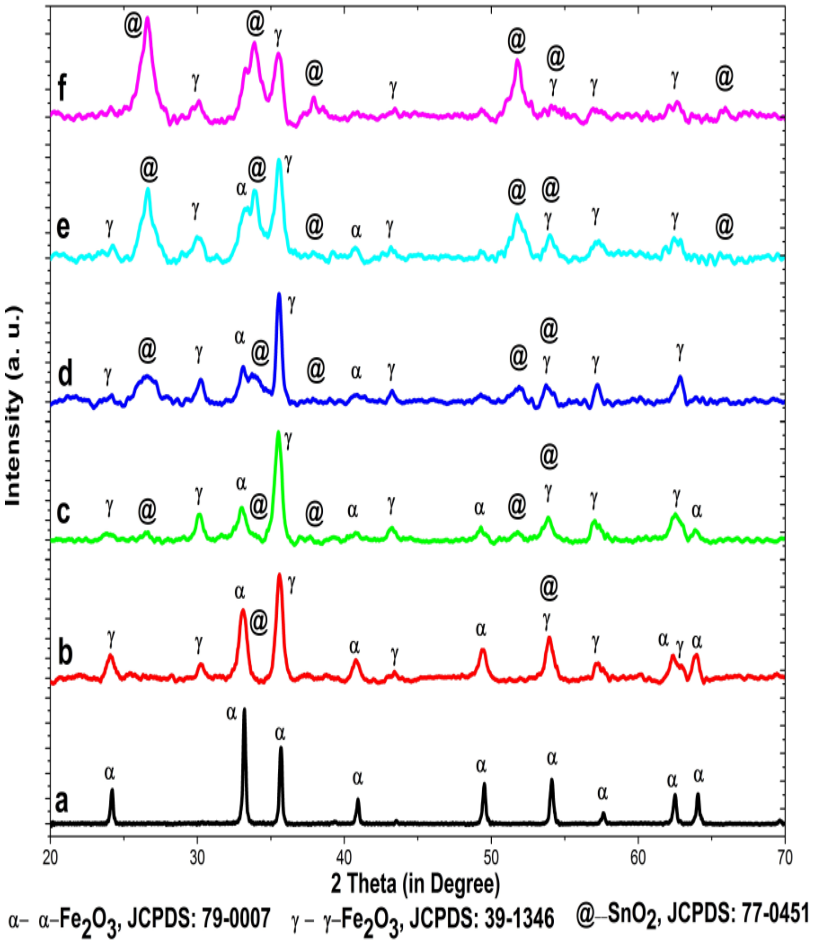

Figure 3.12 X-ray diffraction patterns of (a) pure α-Fe_2O_3, (b) Fe_2O_3–SnO_2 (Fe: Sn = 9: 1), (c) Fe_2O_3–SnO_2 (Fe: Sn = 8: 2), (d) Fe_2O_3–SnO_2 (Fe: Sn = 7: 3), (e) Fe_2O_3–SnO_2 (Fe: Sn = 6: 4), and (f) Fe_2O_3–SnO_2 (Fe: Sn = 5: 5).

Figure 3.13 shows the FTIR spectra of calcined α-Fe_2O_3 nanorod and Fe_2O_3-SnO_2 composite nanorods. In figure 3.13a pattern, the peak at 644 cm^{-1} is due to longitudinal absorption (Au) and peaks at 572 and 490 cm^{-1} are due to transverse absorption (Eu) of Fe-O vibrational mode of α-Fe_2O_3 (Ramesh et al., 2010). Figures 3.13b-f show the FTIR spectra of Fe_2O_3-SnO_2 composite nanorods. The above mentioned peaks of pure α-Fe_2O_3 are not observed in the FTIR spectra of Fe_2O_3-SnO_2 composite. In composite nanorods, the peak at 632 cm^{-1} is due to Fe-O, which is the characteristic peak of γ-Fe_2O_3 (maghemite). Again, peaks at 470 and 558 cm^{-1} are due to O-Sn-O and Sn-O stretching vibration of SnO_2, respectively (Zhang et al., 2011). Furthermore, the presence of a small peak in every pattern is observed in between 3000 to 4000 cm^{-1}. It is due to O-H mode; which indicates the presence of water of crystallization in the materials.

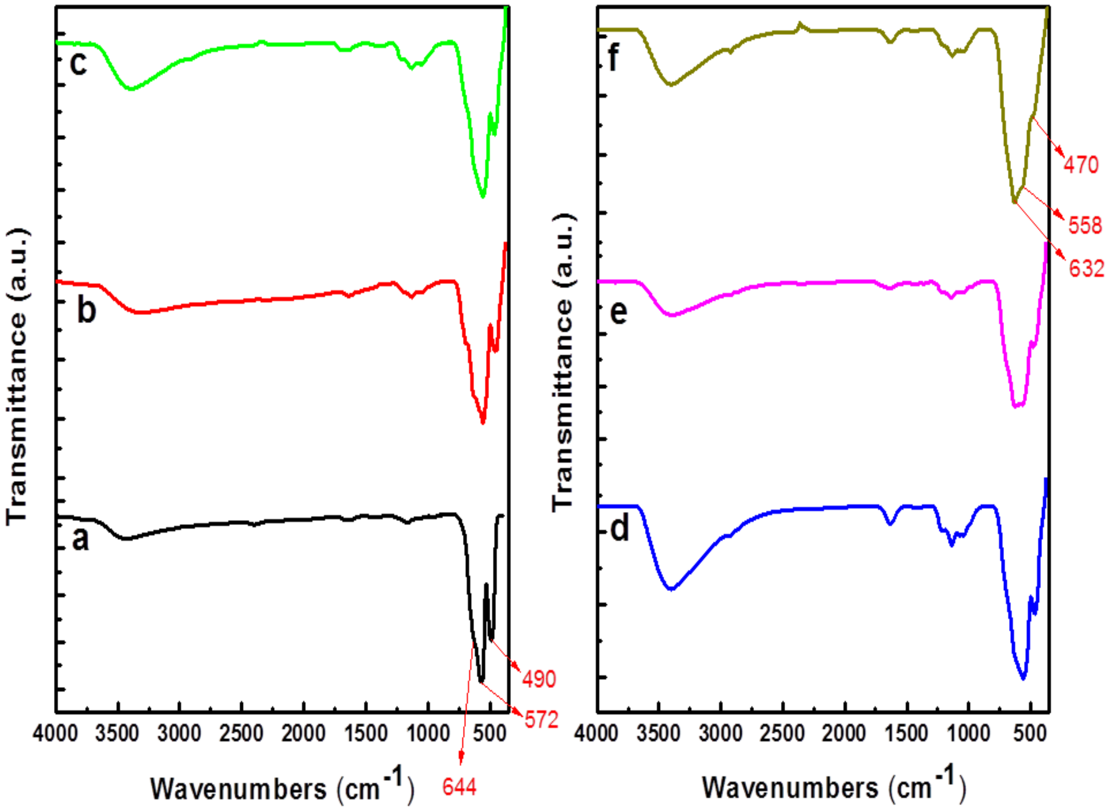

Figure 3.13 Fourier transform infrared spectra of (a) α-Fe_2O_3, (b) Fe_2O_3–SnO_2 (Fe: Sn = 9: 1), (c) Fe_2O_3–SnO_2 (Fe: Sn = 8: 2), (d) Fe_2O_3–SnO_2 (Fe: Sn = 7: 3), (e) Fe_2O_3–SnO_2 (Fe: Sn = 6: 4), and (f) Fe_2O_3–SnO_2 (Fe: Sn = 5: 5) nanorods.

Raman Spectra of the calcined α-Fe_2O_3 nanorod and Fe_2O_3-SnO_2 composite nanorods are shown in figure 3.14. The spectrum of α-Fe_2O_3 (figure 3.14a) contains peaks at 216, 276, 388, 502 and 587 cm^{-1}. The peaks at 216 and 502 cm^{-1} are assigned to A_{1g} modes and the remaining three peaks at 276, 388 and 587 cm^{-1} are assigned to E_g modes of α-Fe_2O_3. In figures 3.14b-f, the presence of peaks around at 344, 515 and 720 cm^{-1} are due to T_{2g}, E_g and A_{1g} modes of γ-Fe_2O_3, respectively (Jubb and Allen, 2010; Tamm et al., 2012). Moreover, with increasing percentage of SnO_2 in the composite nanostructures the formation of γ-Fe_2O_3 are observed and the peak intensity of α-Fe_2O_3 is gradually decreased and completely disappeared after 30 % addition of $SnSO_4$; this may be due to SnO_2, which acts as a gamma stabilizer. Again, the composites contain peaks at around 479 and 635 cm^{-1}. The peak at 479 cm^{-1} can be assigned to E_g mode of SnO_2, which is related to the vibration of oxygen in the oxygen planes and peak at 635 cm^{-1} can be assigned to A_{1g} vibrational mode of SnO_2 (Shi et al., 2010).

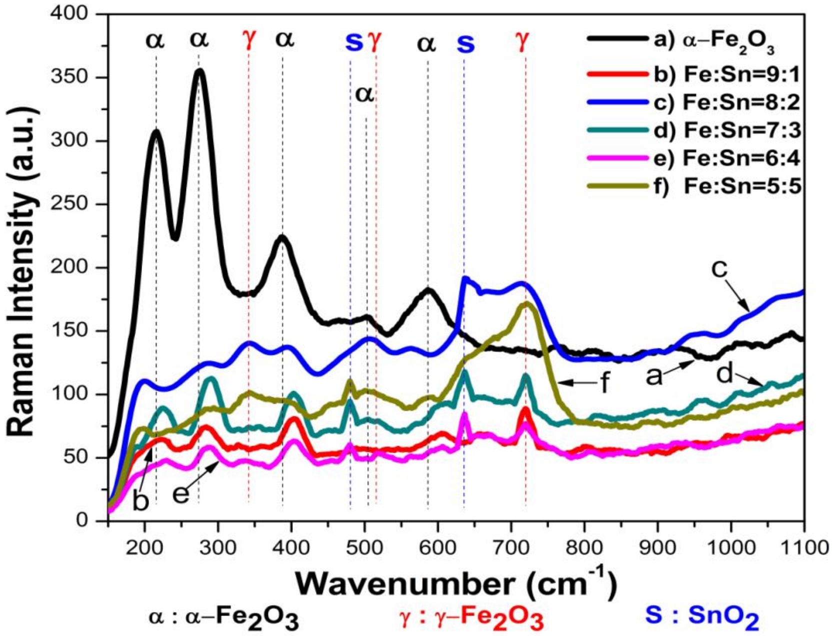

Figure 3.14 Room temperature Raman spectra of (a) α-Fe_2O_3, (b) Fe_2O_3–SnO_2 (Fe: Sn = 9: 1), (c) Fe_2O_3–SnO_2 (Fe: Sn = 8: 2), (d) Fe_2O_3–SnO_2 (Fe: Sn = 7: 3), (e) Fe_2O_3–SnO_2 (Fe: Sn = 6: 4), and (f) Fe_2O_3–SnO_2 (Fe: Sn = 5: 5).

The Brunauer–Emmett–Teller (BET) surface areas were obtained from nitrogen adsorption and desorption isotherms. The nitrogen adsorption and desorption isotherms are shown in figure 3.15. The BET surface area of pure α-Fe_2O_3 nanorod was found to be very low i.e. 22.785 m^2/g. But in case of composites the surface area increases. The surface area values are 70.676, 101.13, 66.866, 59.797, and 46.027 m^2/g, for Fe_2O_3–SnO_2 (Fe: Sn = 9: 1), Fe_2O_3–SnO_2 (Fe: Sn = 8: 2), Fe_2O_3–SnO_2 (Fe: Sn = 7: 3), Fe_2O_3–SnO_2 (Fe: Sn = 6: 4) and Fe_2O_3–SnO_2 (Fe: Sn = 5: 5), respectively. This indicates with increasing percentages of SnO_2 in the composites the surface area increases up to 20 % of SnO_2 addition and then gradually decreases. The enhanced surface area of the composite than that of pure α-Fe_2O_3 may be due to the presence of γ-Fe_2O_3 phase in the composite.

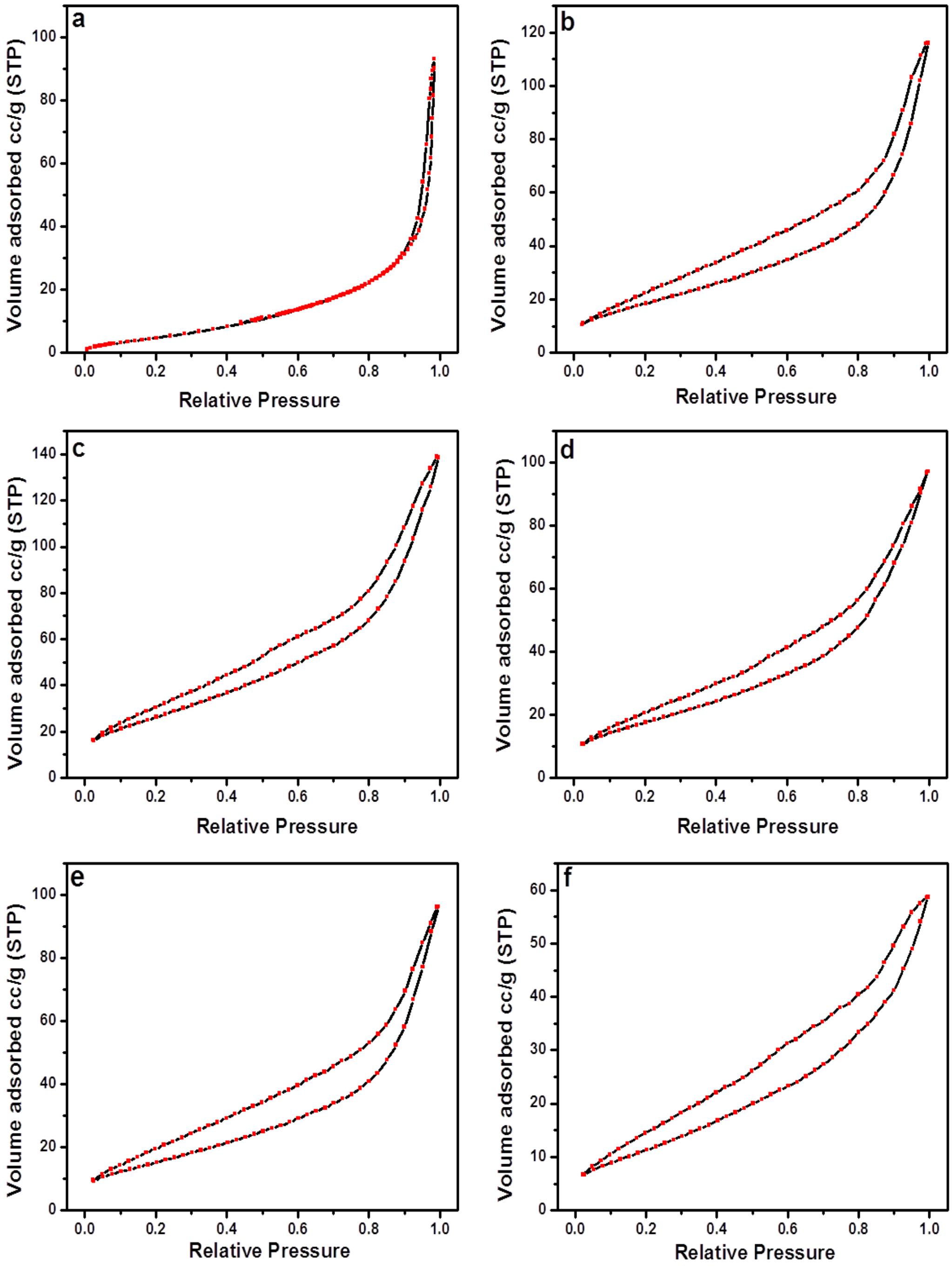

Figure 3.15 N_2 adsorption-desorption isotherm of (a) α-Fe_2O_3, (b) Fe_2O_3–SnO_2 (Fe: Sn = 9: 1), (c) Fe_2O_3–SnO_2 (Fe: Sn = 8: 2), (d) Fe_2O_3–SnO_2 (Fe: Sn = 7: 3), (e) Fe_2O_3–SnO_2 (Fe: Sn = 6: 4), and (f) Fe_2O_3–SnO_2 (Fe: Sn = 5: 5).

We have investigated the evolution of magnetic hysteresis loop of α-Fe_2O_3 nanorod and Fe_2O_3–SnO_2 (Fe: Sn = 8: 2) composite nanorod through VSM at room temperature (shown in figure 3.16). The unsaturated magnetic hysteresis loop is observed for α-Fe_2O_3 nanorod at an applied field of 1.5 T, which indicates a weak ferromagnetic behavior (Yogi and Varshney, 2013). This is due to the incompletion of magnetic domain orientation, which may require sufficient high magnetic field for saturation. Whereas for Fe_2O_3–SnO_2 (Fe: Sn = 8: 2) composite nanorod, a perfect saturated hysteresis loop obtained (with saturation magnetization Ms = 25.23 emu/g) at the same magnetic field. The presence of SnO_2 nano domains may promote the complete orientation of magnetic of magnetic domain of stable γ-Fe_2O_3 in the latter case. The interesting result in the composite is of nearly zero remnant magnetization at zero fields. But the saturation magnetization is sufficiently high, which suggests the transition of weak ferromagnetic behavior of α-Fe_2O_3 to the superparamagnetic behavior of Fe_2O_3–SnO_2 (Fe: Sn = 8: 2) composite nanorod (Wu et al., 2009; Dai et al., 2012).

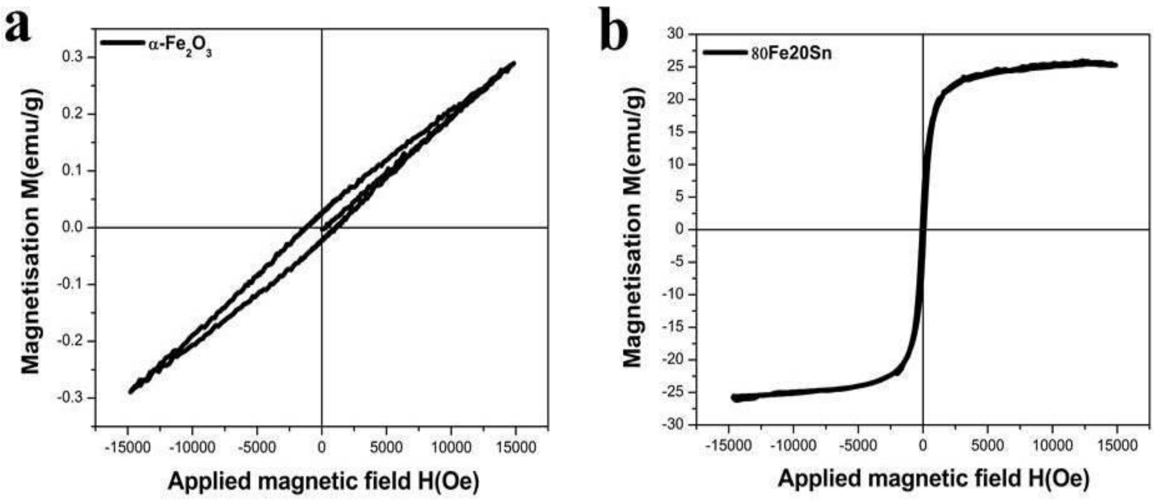

Figure 3.16 Magnetization curves of (a) α-Fe_2O_3 and (b) Fe_2O_3–SnO_2 (Fe: Sn = 8: 2) composite nanorod before and after magnetic separation by an external magnetic field at 300 K temperature.

3.7.2. Adsorption studies for Congo red dye removal

The prepared Fe_2O_3-SnO_2 mixed oxide composite nanorods have been used as adsorbents for removal of Congo red dye from aqueous system. Batch adsorption experiments were carried out by varying adsorbent dose, pH, contact time, initial concentratuion using 20 ml of Congo red dye (100 mg/L) solution in a 50 ml cleaned and capped glass bottle.

After adsorption, the amount of adsorbed q_e is calculated by equation (Klett et al., 2014):

$$q_e = \frac{c_0 - c_e}{w} V \qquad (3.10)$$

where q_e is the amount of adsorption at equilibrium in mg g^{-1}, C_0 & C_e are the initial and equilibrium concentration of the dye in mg L^{-1}, V is the volume of the dye solution taken in litre and w is the weight of the nanorod (adsorbent) in grams.

3.7.2.1. Effect of adsorbent dose and composition

Adsorbent dosage is one of the most important parameters that have been considered to determine the optimum condition for the performance of adsorption. As insufficient dosage or overdosing would result in poorer performance in adsorption. Therefore, it is significant to determine the optimum dosage in order to minimize the cost and sludge formation and also to obtain the optimum condition for performance. Similarly, by varying different adsorbent compositions, the best adsorbent can be determined. The effect of adsorbent doses and composition of adsorbent on the removal of CR using α-Fe_2O_3 and Fe_2O_3-SnO_2 composite nanorods was studied at pH=7.6 (pH at normal condition) for 20 ml of 100 mg/L CR solution and 30 min contact time. The result obtained is represented in figure 3.17. From figure 3.17a it is observed that, the percentage removal of CR dye increases with increasing percentage of SnO_2 from 0 to 20 % in the Fe_2O_3-SnO_2 composites. It is due to the existence of γ-Fe_2O_3 instead of α-Fe_2O_3 in the presence of SnO_2. The enhanced performance could be mainly attributed to the large surface area of the nanoparticles, as well as the electrostatic attraction between the γ-Fe_2O_3 surfaces and CR. On further increase in amount of SnO_2 (Fe: Sn=8: 2 to Fe: Sn= 5: 5), it is found that the percentage of removal of CR decreases. This may be due to decrease in amount of γ-Fe_2O_3 in the composite from Fe_2O_3–SnO_2 (Fe: Sn = 8: 2) to Fe_2O_3–SnO_2 (Fe: Sn = 5: 5). So, Fe_2O_3–SnO_2 (Fe: Sn = 8: 2) is regarded as the best adsorbent for removal of CR among the series of composite nanorods prepared and hence it has been selected as the adsorbent for further study. It is also observed there is a continuous increase in percentage of removal of CR with increase in adsorbent dose up to 0.05 g of Fe_2O_3–SnO_2 (Fe: Sn = 8: 2). This may be due to an increase in number of active sites of the adsorbent material with increasing amount of the adsorbent. A further increase in the amount of the adsorbent does not bring any considerable change in the adsorption i.e. approximately straight line or adsorption saturation was observed thus 0.05 g was chosen as the optimum amount for all studies of the adsorption.

3.7.2.2. Effect of contact time

The time of contact of adsorbate and adsorbent plays a significant role for the removal of pollutant species from aqueous solution during batch experimental studies. It is helpful in understanding the amount of dye adsorbed at various time intervals by a fixed amount of the adsorbent. In this section 0.05 g of Fe_2O_3–SnO_2 (Fe: Sn = 8: 2) adsorbent was used in 20 ml 100 mg/L of CR solution maintaining pH=7.6 (normal pH), with varying time from 0 min to 60 min. From figure 3.17b, it is found that there is a consistent increase in percentage of removal up to 30 min and the adsorption equilibrium is attained after 30 min of contact time. At the initial stage of adsorption, CR removal can be rapid due to surface adsorption (external surface adsorption) upto 30 min. In the later stage, rate of adsorption is slower because sorption occurred via transportation of surface-adsorbed dye to the internal adsorption sites of the adsorbent (internal surface adsorption) (Hou et al., 2012). As a result the rate of adsorption decreased and a saturation stage was attained due to the accumulation of the adsorption sites by the dye ions. It is found that, 99.9 % percentage of CR is removed within 30 min of contact time. So, agitation time of 30 min was selected for further studies.

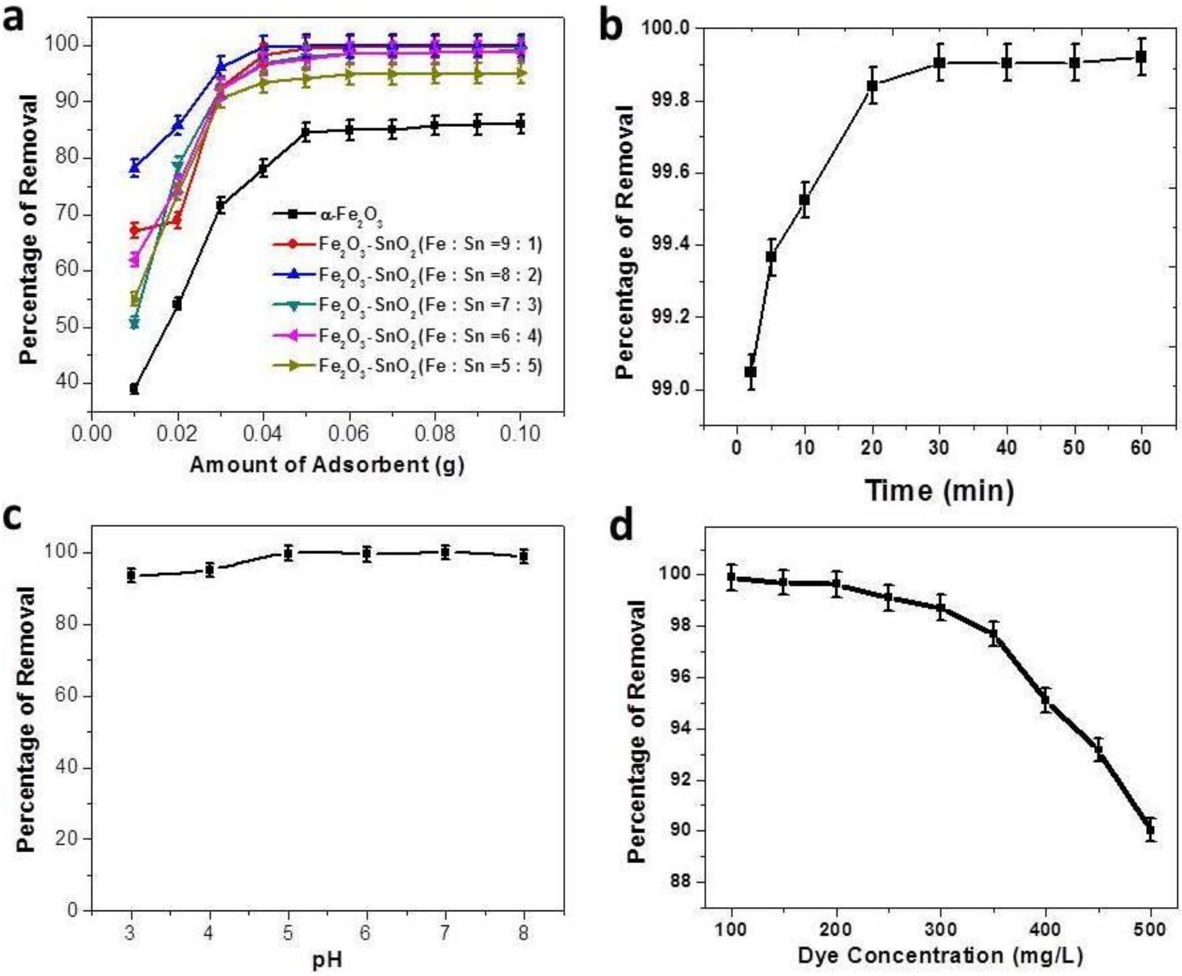

Figure 3.17 Effect of (a) amount of adsorbents and compositions of composite, (b) time for Fe_2O_3–SnO_2 (Fe: Sn = 8: 2), (c) pH for Fe_2O_3–SnO_2 (Fe: Sn = 8: 2), and (d) concentration for Fe_2O_3–SnO_2 (Fe: Sn = 8: 2), on removal of Congo red (CR) dye.

Adsorption Kinetics

In order to investigate the adsorption processes of CR on the adsorbents, the applicability of the pseudo-first-order and pseudo-second-order model was tested and the best fit model was selected according to the linear regression correlation coefficient, R^2 value. The pseudo-second-order model is represented as (Bayazit et al., 2010):

$$\frac{t}{q} = \frac{1}{k_2 q_e^2} + \frac{t}{q_e} \qquad (3.11)$$

And the initial adsorption rate, h (mg/g min^{-1}), as t → 0 can be defined as:

$$h = k_2 q_e^2 \qquad (3.12)$$

The initial adsorption rate (h), the equilibrium adsorption capacity (q_e), and the second-order constants k_2 (g/mg min) can be determined experimentally from the slope and intercept of plot of t/q versus t. The values of R^2, q_e and k_2 of the pseudo-second-order model for the adsorbent are 1, 40 mg/g and 0.89 g mg^{-1} min^{-1} respectively and the pseudo-second-order plot is given in figure 3.18. The calculated value of q_e is in good agreement with the experimental values (i.e. 39.96 mg/g). Similarly, correlation coefficients are always greater than 0.99, which also explains the good fit of the model.

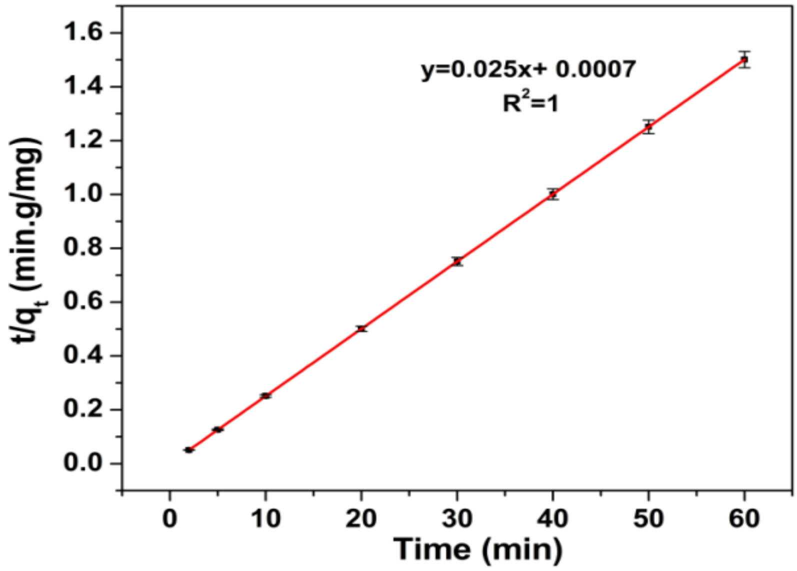

Figure 3.18 Pseudo-second-order kinetic plots for adsorption of Congo red dye by Fe_2O_3–SnO_2 (Fe: Sn = 8: 2) composite nanorod.

3.7.2.3. Effect of pH on adsorption

Original pH of Congo red solution (100 mg/L) is about 7.6. It was seen that the dye solution changes its color from red to dark blue when pH was adjusted in highly acidic range and becomes dark blue in highly basic range i.e., pH 9 and above. Therefore, the removal of CR from aqueous solution by Fe_2O_3–SnO_2 (Fe: Sn = 8: 2) nanocomposite adsorbent was studied by varying the pH of the solution over the range of 3-8. The pH of the solution was adjusted by using 0.01 mol/L HCl or NaOH solutions. The results obtained are shown in the figure 3.17c. For 100 mg/L dye concentration, it is observed that the percentage of removal increases from pH 3 to pH 5 and then the percentage of removal remain almost the same up to pH 8. These results can be explained as follows. In acidic pH range (i.e. pH 3-5), both the adsorbent surface and dye molecules are protonated and electrostatic attraction does not exist. Hence, the percentage of adsorption is comparatively less at lowers pH values. As the pH of the system increases, the number of positively charged site decreases and the surface of the adsorbent get hydroxylated. Congo red dye molecules contain amine group ($-NH_2$) groups. So that the adsorption may be occur due to strong hydrogen bonds ($O\cdots H{-}N$ and $O{-}H\cdots N$) between $-NH_2$ functional groups of adsorbate and surface hydroxyl (-OH) groups on the nanoadsorbent surface (Wu et al., 2013).

According to Wei et al., Congo red is adsorbed onto the surface of metal oxides by co-ordination effect between the metal ions (i.e. Fe^{3+} and Sn^{4+}) and amine ($-NH_2$) groups of the Congo Red molecules (Wei et al., 2013).

Hence, the mechanism of adsorption of Congo red on the surface of the composite nanoadsorbent mainly attributed to two reasons: a) hydrogen bonds between surface hydroxyl (-OH) groups of adsorbent and amine ($-NH_2$) groups of Congo red, and b) the surface co-ordination effects between metal ions of adsorbent and amine groups of Congo red dye molecules.

3.7.2.4. Effect of initial dye concentration on adsorption

In this section, 0.05 g of Fe_2O_3–SnO_2 (Fe: Sn = 8: 2) nanocomposite was used in each 20 ml of CR solution with concentration ranging from 100 mg/L to 500 mg/L and the agitation time was kept 30 min. The percentage removal of Congo red with change in concentration of the solution is shown in figure 3.17d. It is found that with the increase in initial dye concentration, the percentage removal decreases while the equilibrium adsorption capacity of the adsorbent increases. This is probably due to a high driving force for mass transfer in high dye concentration.

Adsorption Isotherm

To describe the adsorption behavior of Congo red by Fe_2O_3–SnO_2 (Fe: Sn = 8: 2) nanocomposite adsorbent, we have studied adsorption isotherms. The most common models such as Freundlich and Langmuir equations are used for investigation of this study.

Langmuir isotherm

The Langmuir isotherm model assumes monolayer coverage of adsorbate on a homogeneous adsorbent surface. This model does not consider surface heterogeneity of the sorbent. It assumes adsorption will take place only at specific site on the adsorbent (Bayazit, 2014).

The linear form of the Langmuir isotherm is:

$$\frac{C_e}{q_e} = \frac{1}{K_L q_{max}} + C_e/q_{max} \qquad (3.13)$$

where K_L is the Langmuir constant related to the energy of adsorption, q_{max} is the maximum adsorption capacity corresponding to complete monolayer coverage (mg g^{-1}), which depends upon the number of adsorption sites. The values of q_{max} and K_L are calculated from the slopes and intercepts of the straight lines of plot of C_e/q_e versus C_e (figure 3.19a).

Freundlich isotherm

The Freundlich isotherm model describes the surface heterogeneity of the sorbent and considers multilayer adsorption with a heterogeneous energetic distribution of active sites, accompanied by interactions between adsorbed molecules (Yu et al., 2013).

The linear form of the Freundlich isotherm is:

$$\ln q_e = lnK_F + {}^{1}/_{n}\, lnC_e \qquad (3.14)$$

where C_e is the equilibrium concentration (mg L^{-1}), q_e is the amount adsorbed at equilibrium (mg g^{-1}) and K_F and n are Freundlich constants, related to the extent of the adsorption and the degree of nonlinearity between solution concentration and adsorption, respectively. K_F and (1/n) can be determined from the linear plot of ln q_e versus ln C_e (figure 3.19b).

The values of q_{max}, K_L, K_F, 1/n and the correlation coefficients for Langmuir (r_L^2) and for Freundlich (r_F^2) are given in table 3.5. It can be seen that the Langmuir model yields a much better fit than the Freundlich model. According to Langmuir model the maximum adsorption capacity (q_{max}) maximum adsorption capacity is found to be 181.82 mg/g.

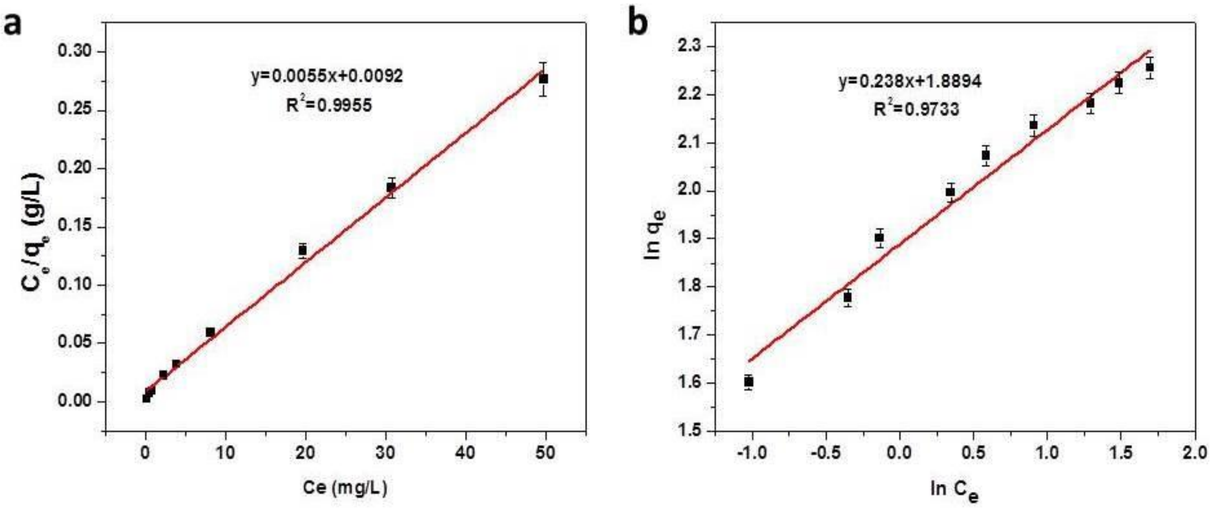

Figure 3.19 Linearization of a) Langmuir plots and b) Freundlich plots for the adsorption of Congo red dye by Fe_2O_3–SnO_2 (Fe: Sn = 8: 2) composite nanorod.

Table 3.5 Adsorption isotherm constants for adsorption of Congo red by Fe_2O_3–SnO_2 (Fe: Sn = 8: 2).

Langmuir	**K_L (Lg^{-1})**	**q_{max} (mg g^{-1})**	**r_L^2**
	0.598	181.82	0.9955
Freundlich	**K_F**	**1/n**	**r_F^2**
	77.52	0.238	0.9733

Table 3.6 Comparison of Congo red adsorption capacities of various adsorbents.

Types of Adsorbent	**q_{max} (mg g^{-1})**	**Reference**
Chitosan/montmorillonite nanocomposite	54.52	(Wang and Wang, 2007)
Montmorillonite	12.70	(Wang and Wang, 2007)
Metal hydroxides sludge	40	(Attallah et al., 2013)
Hierarchical $Ni(OH)_2$ nanosheets	82.9	(Cheng et al., 2011)
Hierarchical NiO nanosheets	151.7	(Cheng et al., 2011)
Reagent NiO nanoparticles	39.7	(Cheng et al., 2011)
Ball-milled sugarcane bagasse	38.2	(Zhang et al., 2011)
Magnetite nanoparticles	172.4	(Giri et al., 2011)
Fe_2O_3–SnO_2 (Fe: Sn = 8: 2) composite nanorod	182	Present Work

The maximum adsorption capacity (q_{max}) for the adsorption of CR on Fe_2O_3–SnO_2 (Fe: Sn = 8: 2) composite nanorod compared to other adsorbents is listed in table 3.6. It is observed that the prepared Fe_2O_3–SnO_2 (Fe: Sn = 8: 2) composite nanorod is an efficient adsorbent for adsorption of Congo red from aqueous solution.

3.7.2.5. Desorption and reusability study

Desorption of dyes from adsorbent and re-generation of the adsorbent is an important issue in view of re-usability of the adsorbent. With rising prices of raw materials and wastewater treatment processes, the attractiveness of product recovery processes has increased significantly. The main objective of the regeneration process is to restore the adsorption capacity of exhausted adsorbent and to recover valuable components present in the adsorbed phase. Desorption study was performed by mixing 0.05 g CR loaded Fe_2O_3–SnO_2 (Fe: Sn = 8: 2) nanocomposite with 20 ml of 0.01 mol L^{-1}NaOH solution and desorption was carried out for 2 hours. Then the concentration of eluted CR was measured to calculate the amount of CR desorbed. For regeneration studies, successive adsorption–desorption processes were carried out for four consecutive cycles which is shown in figure 3.20. The figure shows that about 99 and 91 % CR effectively removed on the first cycle and the second cycle, respectively. After that, the removal capacity of the adsorbent decreases as the number of cycles increases. Although there is a gradual decrease in removal capacity with increasing cycle numbers, it is observed the dye adsorption capacity still remained more than 80 % at the end of the fourth cycle.

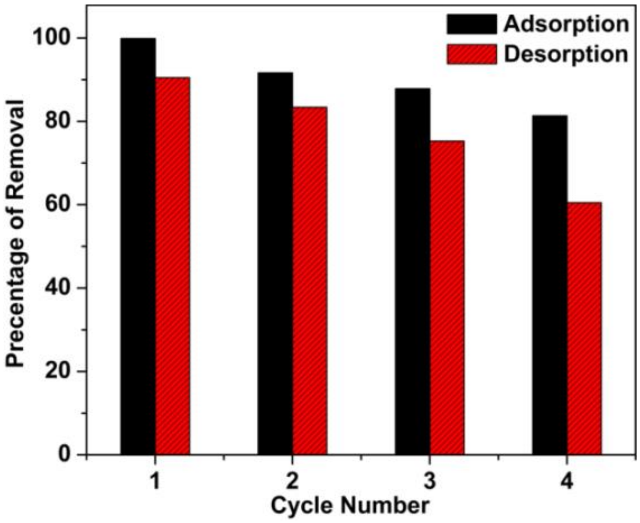

Figure 3.20 Reusability of Fe_2O_3–SnO_2 (Fe: Sn = 8: 2) nanocomposite adsorbent for adsorption/desorption of Congo red during four cycles.

The FTIR spectra and FE-SEM of Fe_2O_3–SnO_2 (Fe: Sn = 8: 2) nanocomposite after different adsorption cycles were carried out and shown in figure 3.21 and figure 3.22 respectively. From the figure 3.21 it is observed that along with the peaks of composite (previously discussed), some additional peaks are present. Peaks at 3429 cm^{-1} and 1612 cm^{-1} can be attributed to the N–H & C=C stretching vibration of the functional groups present in CR dye. New peaks around 1370 and 1180 cm^{-1} are due to the framework vibration of benzene rings of CR dye. Another peak is observed at 1038 cm^{-1}, which is due to the S=O stretching vibration of CR dye.

Figure 3.22 shows the FE-SEM images of CR adsorbed Fe_2O_3–SnO_2 (Fe: Sn = 8: 2) nanocomposite after different adsorption cycles. From the figure it is observed that, the rod shaped morphology of the composite nanorod retained up to three consecutive cycles. Thus, the Fe_2O_3–SnO_2 (Fe: Sn = 8: 2) nanocomposite can be effectively reused for CR adsorption from waste water. It is also observed from the SEM images that agglomeration of rod shaped composite nanomaterials takesplace with successive adsorption cycles. Due to the agreegated form, the surface exposure of nanorods towards dye molecules decreases and this is the primary cause of decrease in sorption capacity.

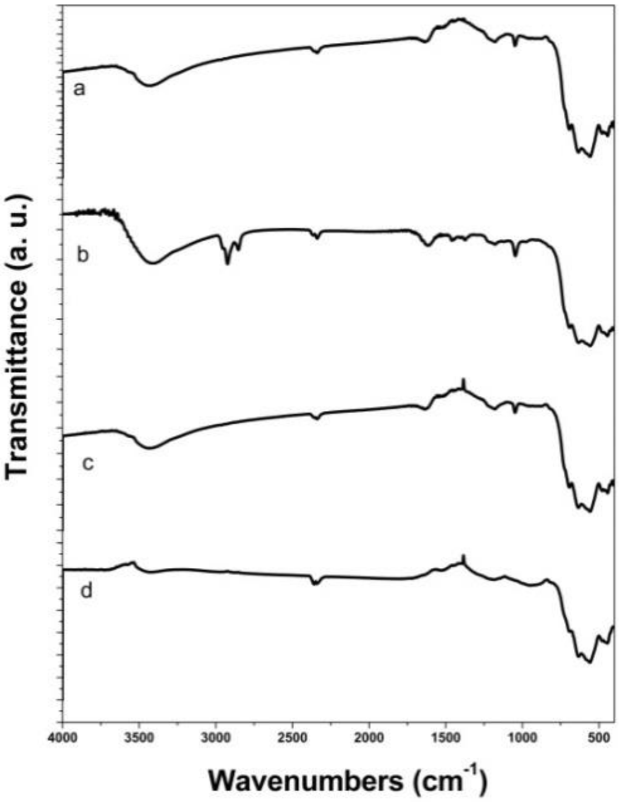

Figure 3.21 FTIR spectra of CR adsorbed Fe_2O_3–SnO_2 (Fe : Sn = 8 : 2) after (a) 1st, (b) 2nd, (c) 3rd and (d) 4th adsorption cycle.

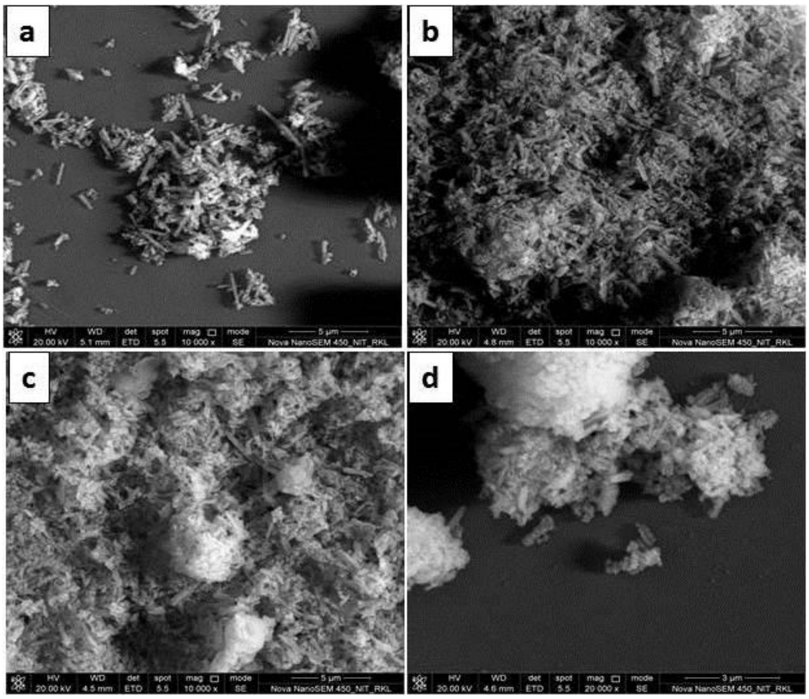

Figure 3.22 FESEM images of CR adsorbed Fe_2O_3–SnO_2 (Fe: Sn = 8: 2) after (a) 1st, (b) 2nd, (c) 3rd and (d) 4th adsorption cycle.

3.8. Conclusions

We have synthesized Fe_2O_3-SnO_2 composite nanorods by a wet chemical route using CTAB as structure directing agent. SEM and TEM results represent the formation of uniform nanorods with typical diameter 100-200 nm. It was also observed that, the shape and uniformity of the composite nanorods changes with increasing percentage of SnO_2. The XRD studies confirmed the formation of Fe_2O_3-SnO_2 mixed oxide nanocomposites. However, upon addition of Sn^{+4} ions to Fe_2O_3 matrix the formation of γ-Fe_2O_3 phase was observed at 500 °C calcination temperature. With an increase in concentration of Sn^{+4}, the peaks corresponds to γ-Fe_2O_3 phase became prominent and peak intensity of α-Fe_2O_3 gradually reduced. This observation indicates that metastable γ-Fe_2O_3 phase was selectively stabilized in case of composite oxides. The formation of mixed oxide composite was further confirmed by Raman studies. The obtained Fe_2O_3-SnO_2 composite nanorods were used as adsorbent for removal of Congo red dye from aqueous solution. All the composites show better adsorption than that the α-Fe_2O_3 nanorod and Fe_2O_3–SnO_2 (Fe: Sn = 8: 2) composite nanorod was found to be most promising adsorbent among the series for decontamination of CR dye within a short contact time of 30 min.

CHAPTER-4

IRON OXIDE IMPREGNATED MESOPOROUS MCM-41: SYNTHESIS, CHARACTERIZATION AND ADSORPTION STUDIES

4.1. Introduction

Mesoporous materials such as MCM-41, MCM-48, and SBAs have been the subject of intensive research in the field of adsorption and heterogeneous catalysis because of their high surface area, high pore volume, favorable and controllable pore uniformity, high hydrophobicity and relatively high thermal stability (Huang et al., 2013; Pouretedal and Ahmad, 2012; Jyothi et al., 2012). MCM-41 (Mobil composite material number 41, first discovered in 1992) consists of hexagonal array of uniformly sized one-dimensional pore geometry with a pore diameter of 2 to 10 nm (Ng et al., 2013). Hence, ordered mesoporous MCM-41 has been used for adsorption of various contaminants from water because of its excellent removal capacity. The modification of MCM-41 for the adsorption is very helpful in the improvement of the adsorption capacity and selectivity because of specific interactions between adsorbents and adsorbates (Santos et al., 2013). Specially, incorporation of heteroatoms such as Fe, Al, Cr and so on into the primarily inert frameworks make the structure more potential for the application in the field of catalysis and adsorption (Li et al., 2013; Parida and Dash, 2010). Due to the occurrence of high surface area of about 1000 m^2/g, porosity and amorphous structure, there is a possibility of incorporation of transition metal ion inside the mesoporous framework by substitution of Si atoms in regular tetrahedral positions (Rath and Parida, 2011; Elias et al., 2011; Rana and Viswanathan, 1998).

Among the heteroatoms, iron atom incorporated into the silica framework generates the strong acid sites. As a result of which Fe-containing mesoporous silicates have shown better performance towards catalytic activity and adsorption. Very recently, several attempts have been made for extensive study of iron-containing mesoporous materials MCM-41(Fe^{3+}) due to its considerable interest for various applications, especially for catalytic and adsorption properties (Li et al., 2012). Lan et al. (2013) have used iron-loaded MCM-41 (Fe/MCM-41), which was synthesized by a hydrothermal method, as an effective catalyst for the ozonation of p-chlorobenzoic acid. Wang et al. (2002) have reported the epoxidation of styrene with hydrogen peroxide by hydrothermally prepared Fe–MCM-41 catalyst. Bengoa and co-workers (2010) have synthesized sylilated Fe/MCM-41 for catalyst in Fischer–Tropsch reaction. Chen et al. (2011) have used magnetic nanosorbent Fe^{3+}–magMCM-41 for removal of chromium (VI) oxyanions from distilled, tap, mountain stream and river waters. Wantala et al. (2010) have synthesized Fe-MCM-41 by hydrothermal method for the removal of arsenate from aqueous solution. Similarly, other research groups have used Fe-MCM-41 as catalyst for the oxidative desulfurization dibenzothiophene (Li et al., 2012), synthesis of multi-wall carbon nanotubes by the pyrolysis of ethanol (Zhao et al., 2010), synthesis of diphenylmethane (Preethia et al., 2011), acetylation of 1, 2-dimethoxybenzene (Bachari et al., 2012), phenol hydroxylation (Choi et al., 2006), wet oxidation of phenol (Khieu et al., 2009), and phenol hydroxylation and for Friedel–Crafts alkylation (Jiang et al., 2012). Generally, MCM-41 and Fe-MCM-41 were prepared by hydrothermal method. However, a wet chemical method is the easiest method to prepare MCM-41 and metal doped MCM-41 with high yield and purity. In the previous chapter, we have synthesized iron oxide nanorods and iron oxide-tin oxide composite nanorods by a chemical precipitation method. The prepared nanomaterials were found to be efficient adsorbents for removal of an anionic dye (Congo red) from aqueous media. This chapter describes the synthesis of iron oxide impregnated mesoporous MCM-41, which can afford enough surface area along with nanosized iron oxide particles dispersed inside the porous matrix for further enhancement of sorption activities. Generally, the surface of MCM-41 is negatively charged in aqueous medium because its surface acquires a negatively charged SiO-state when in contact with water by the dissociation of silanol groups, and hence it can be used as an adsorbent to remove cataionic dye from wastewater (Zhang et al., 2014; Jambhrunkar et al., 2014). Therefore, we have used a cationic dye (Methylene blue) for adsorption purpose in this work.

In the present work, we have prepared MCM-41 and Fe-MCM-41 (iron oxide dispersed MCM-41) using a wet chemical technique. Then, the prepared materials were employed for adsorptive removal of methylene blue (MB) dye from aqueous media and a comparative study was carried out by evaluating equilibrium isotherms and kinetic data for selection of the more effective adsorbent among them.

4.2. Materials and Methods

4.2.1. Chemicals Used

Tetraethyl orthosilicate (TEOS), Cetyltrimethylammonium bromide (CTAB), Ammonium hydroxide (NH_4OH), and ferrous sulphate ($FeSO_4.7H_2O$) from Merck India pvt. Ltd. and

Ethanol from Merck Germany pvt. Ltd. All the reagents used in the synthesis and catalytic study were of analytical grade and used as received without further purification.

4.2.2. Synthesis of MCM-41

2.4 g of CTAB was dissolved in 120 mL double distilled water. Then 8 mL of NH_4OH and 10 mL of TEOS was added slowly with continuous stirring and then the stirring was continued for 12 h. Then the solid product was filtered, washed repeatedly with water and ethanol, and calcined at 823 K for 5 h.

4.2.3. Synthesis of Iron oxide dispersed MCM-41 (Fe-MCM-41)

0.05 g of $FeSO_4.H_2O$ was dissolved in 10 mL of double distilled water and 0.5 g of MCM-41 was taken in 10 mL of ethanol. The two solutions of $FeSO_4.7H_2O$ and MCM-41 was mixed and stirred for 3 h to form Fe^{2+} dispersed MCM-41. Then the obtained Fe^{2+} dispersed MCM-41 was filtered, washed with ethanol, dried at room temperature and calcined at 823K for 4 h to form Iron oxide dispersed MCM-41. A schematic illustration of the preparation process of MCM-41 and Fe-MCM-41 is shown in figure 4.1.

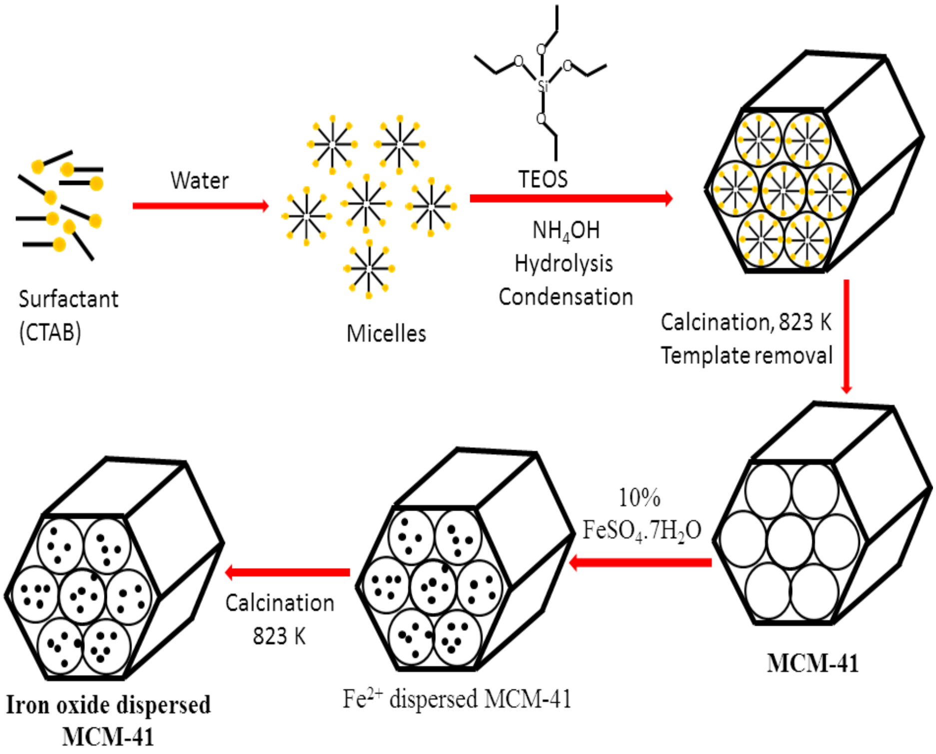

Figure 4.1 Schematic illustration of the preparation process of MCM-41 and Fe-MCM-41.

4.2.4. Characterization techniques

Small and wide X-ray diffraction (XRD) measurements of the mesoporous materials were carried out using Cu Kα radiation on a Rigaku Ultima-IV X-ray diffractometer. X-ray photoelectron spectroscopy (XPS) was determined using a VG Scientific ESCA LAB Mk-II spectrometer with Al Kα radiation (1486.6 eV) at a takeoff angle at 45°. The surface morphology of the prepared materials was characterized by a Nova Nano SEM 450 field emission scanning electron microscopy (FE-SEM) operated at an acceleration voltage of 15 and 20.0 kV. FTIR spectra were recorded using Perkin-Elmer FTIR (Spectrum RX-I) spectrophotometer. Specific surface area and pore size distribution (PSD) of the samples were determined from nitrogen adsorption/desorption isotherms obtained at the temperature of liquid nitrogen in an automated physisorption instrument (Autosorb-iQ, Quantachrome Instruments). Prior to the analysis, the samples were outgassed under vacuum at 150 ^{o}C for 1.5 h. Specific surface areas were calculated according to the Brunauer-Emmett-Teller (BET) method, and the pore size distributions were obtained according to the Barret-Joyner-Hallenda (BJH) method from the adsorption data.

4.2.5. Adsorption experiment

For the removal of MB dye from water, the adsorption experiments were carried out using the prepared MCM-41 and Fe-MCM-41 adsorbents at room temperature. A stock solution of MB (1 g L^{-1}) was prepared and desired concentrations (ranging from 50 to 500 mg L^{-1}) of the dye were obtained by diluting the same with double distilled water. The calibration curve of MB was prepared by measuring the absorbance of different concentrations of the samples at λ_{max} = 664 nm using UV–vis spectrophotometer. The amount of adsorption q_e is calculated by equation (Durán-Jiménez et al., 2014):

$$q_e = \frac{C_0 - C_e}{w} V \qquad (4.1)$$

where q_e is the amount of adsorption at equilibrium in mg g^{-1}, C_0 & C_e are the initial and equilibrium concentration of the dye in mg L^{-1}, V is the volume of the dye solution taken in litre and w is the weight of the nanorod (adsorbent) in gram. All the adsorption experiments were carried out three times in replicates and the mean data obtained were taken in results and discussion section.

4.3. Results and Discussion

4.3.1. Characterization of MCM-41 and Fe-MCM-41 nanomaterials

Figure 4.2 shows the SAXS patterns of MCM-41 and Fe-MCM-41 nanomaterials. The patterns consist of one pronounced peak each at 2θ value 2.68° and 2.42° for MCM-41 and Fe-MCM-41, respectively and these peaks are indexed to (100) reflection plane. Again, two low incensed peaks each at 2θ= 4.29° and 4.7° due to the reflection from (110) and (200) planes, respectively for MCM-41 and at 2θ= 4.23° and 4.65° due to the reflection from (110) and (200) planes, respectively for Fe-MCM-41 were observed. This indicates the formation of a well-ordered mesoporous material and these peaks are generally indexed according to the hexagonal regularity of MCM-41 (Jiang et al., 2012). These results are in good agreement with previous observations reported by Li et al. (2012) and Lan et al. (2013) However it is observed that, with the incorporation of iron atoms into the framework of MCM-41, the intensity of the peaks of Fe-MCM-41 sample decreased with a peak broadening of characteristics peak (100) (Yu et al., 2014). It indicates the possibility of formation of iron oxide cluster inside the channel as a result of calcinations at high temperature.

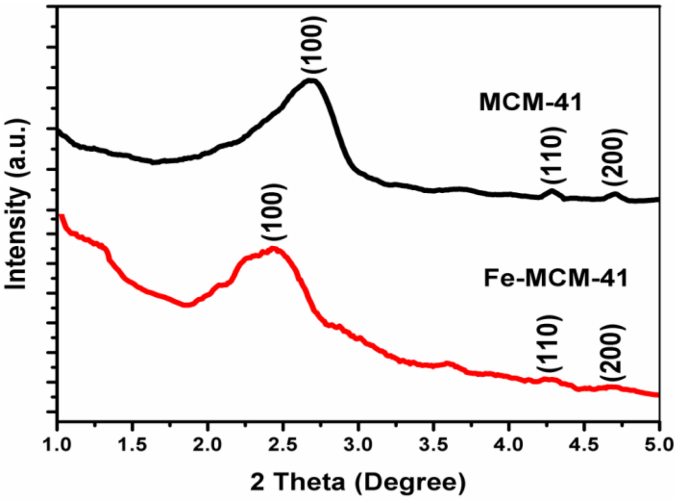

Figure 4.2 SAXS patterns of MCM-41 and Fe-MCM-41.

Wide angle XRD patterns for the calcined MCM-41 and Fe-MCM-41 are shown in figure 4.3. No characteristic peaks of iron oxide and other Fe species were observed for Fe-MCM-41, which suggested that iron oxide species might be present as finely dispersed nano dimensional particles (at least in one dimension) below the detection limits of x-ray and/or as amorphous particles in the framework of MCM-41.

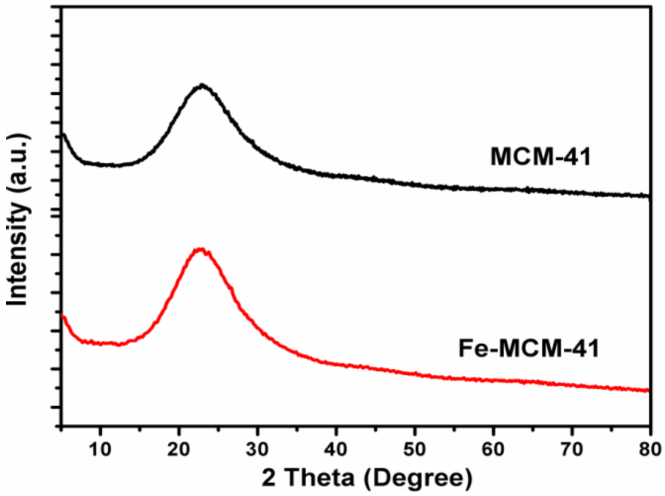

Figure 4.3 Wide angle XRD patterns of MCM-41 and Fe-MCM-41.

In order to understand the nature of the interaction between Fe ions and MCM-41 mesoporous materials, the Fe-MCM-41 sample was characterized by the XPS technique, and the results are shown in Figure 4.4. A very complex line-shape Fe 2p spectrum (figure 4.4a) is observed due to satellite structure and multiplate effects. The Fe 2p spectrum can be fitted with ten synthetic peaks. The peaks correspond to 707.5, 710.3 and 712.8 eV are associate with Fe^0, Fe^{2+} $2p_{3/2}$ and Fe^{3+} $2p_{3/2}$ spin states, respectively. Again, presence of peaks at 723.85 and 726.28 eV is due to Fe^{2+} $2p_{1/2}$ and Fe^{3+} $2p_{1/2}$ spin states, respectively. From the result it is observed that the iron oxide nanoparticles are a mixture of FeO and Fe_2O_3. Other smaller peaks are due to satellite peaks of both Fe^{2+} and Fe^{3+} ions. The BE values of Fe peaks are shown in table 4.1. A shifting of BE values around 0.5-1 eV is observed compared with literature (Davoisne et al., 2008; Carrillo et al., 2013); due to the presence of small amounts iron ions inside the MCM-41 frame work, where they have the possibility to form Fe-O-Si bonds. The Si 2p spectrum of the Fe-MCM-41 is shown in figure 4.4b. This spectrum with BE=107.6 eV, is the characteristic spectrum for the silicates. From figure 4.4c, it is observed that the spectrum can be fitted with two peaks. The peak at 285.7 is due to C 1s spin state and peak at 288.7 due to a very low concentration of carbon. The value of BE indicates that the origin of this carbon is the environmental contamination of the sample surface (Stefanis et al., 2007). The spectrum of O 1s (figure 4.4d) is composed of a single peak at 536.8 eV.

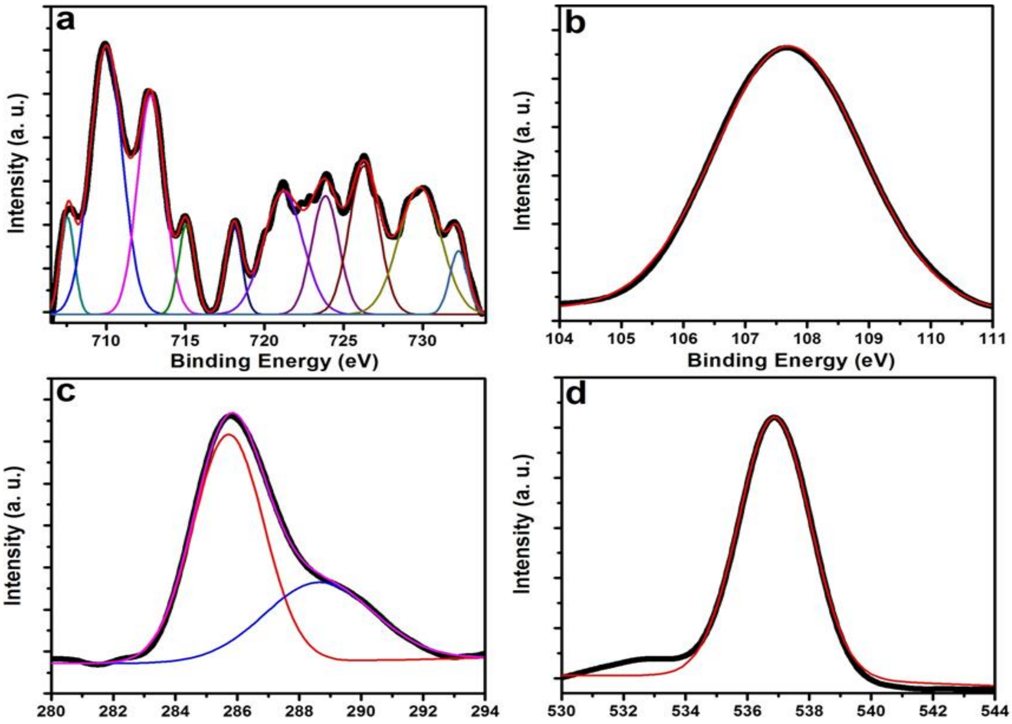

Figure 4.4 X-ray photoelectron spectra of (a) Fe 2p, (b) Si 2p, (c) C 1s, and (d) O 1s of Fe-MCM-41.

Table 4.1 Binding energies of the peaks determined for Fe spectrum of Fe-MCM-41.

Fe^0	**Fe^{2+} 2p$_{3/2}$**	**Fe^{3+} 2p$_{3/2}$**	**Fe^{2+}2p$_{1/2}$**	**Fe^{3+} 2p$_{1/2}$**	**Fe^{2+} sat. 2p$_{3/2}$**	**Fe^{3+}sat. 2p$_{3/2}$**	**Fe^{2+}sat. 2p$_{1/2}$**	**Fe^{3+} sat. 2p$_{1/2}$**
707.5	710.3	712.8	723.8	726.3	715.1 & 718.1	721.2	729.8	732.3

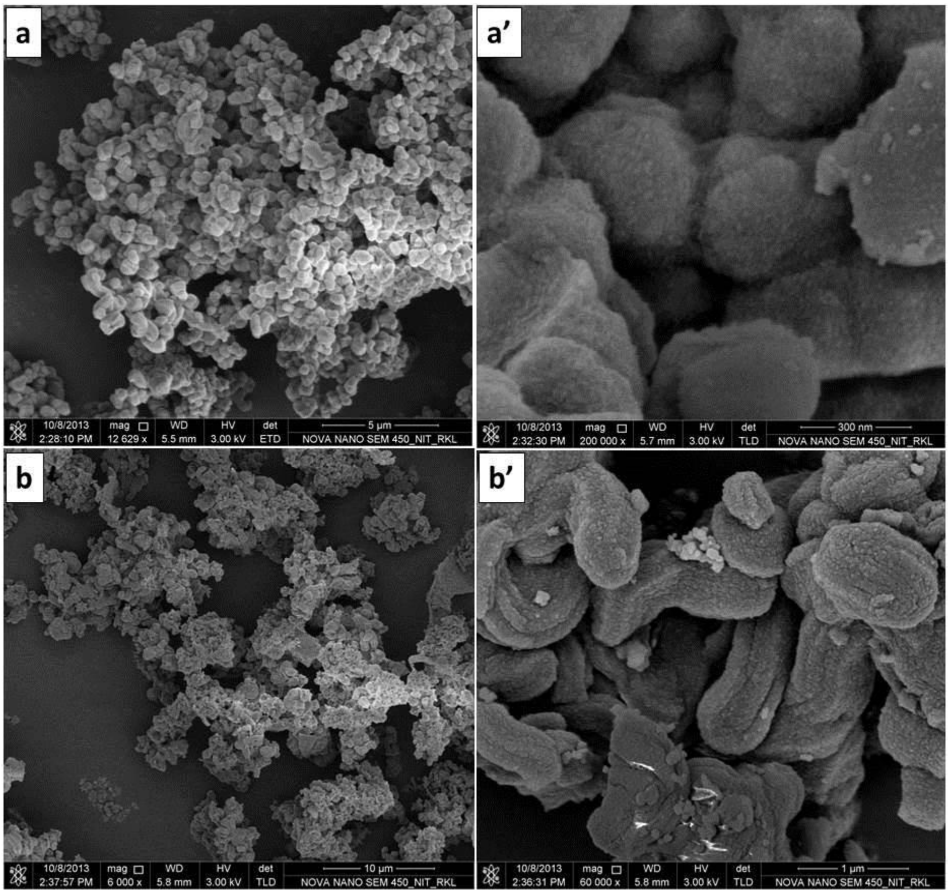

Figure 4.5 Low and high magnification FESEM images of (a, a') MCM-41 and (b, b') Fe-MCM-41.

The microstructure and morphology of the prepared mesoporous MCM-41 and Fe-MCM-41 nanomaterials were characterized by FESEM and HRTEM and are given in figure 4.5 and figure 4.6, respectively. Spherical particles havimg diameter in the range of 200-400 nm and mesoporous structure are observed in the low and high magnification FESEM images of MCM-41 (figure 4.5a, a'). In case of Fe-MCM-41, when iron atom is incorporated into the framework of MCM-4, the spherical structure distorted to elongated elliptical particles having particle diameter in the range of 400 nm and length in the range of 1 µm (as shown in figure 4.5b, b'). There is a significant difference in the particle size, observed due to incorporation of iron atom to MCM-41 framework. Figure 4.6a, b displayed the low and high magnification HRTEM images of the mesoporous Fe-MCM-41. The images suggested that the prepared materials are mesoporous with less ordered in hexagonal arrays. Less ordered mesoporous silicate frame work is observed due to incorporation of iron oxide nanoparticles inside the framework of MCM-41. The HRTEM result is in good agreement with the XRD result. The energy-dispersive spectroscopy (EDS) of Fe-MCM-41 is given in figure 4.6c. The presence of both Si and Fe atom is observed from the EDS spectrum.

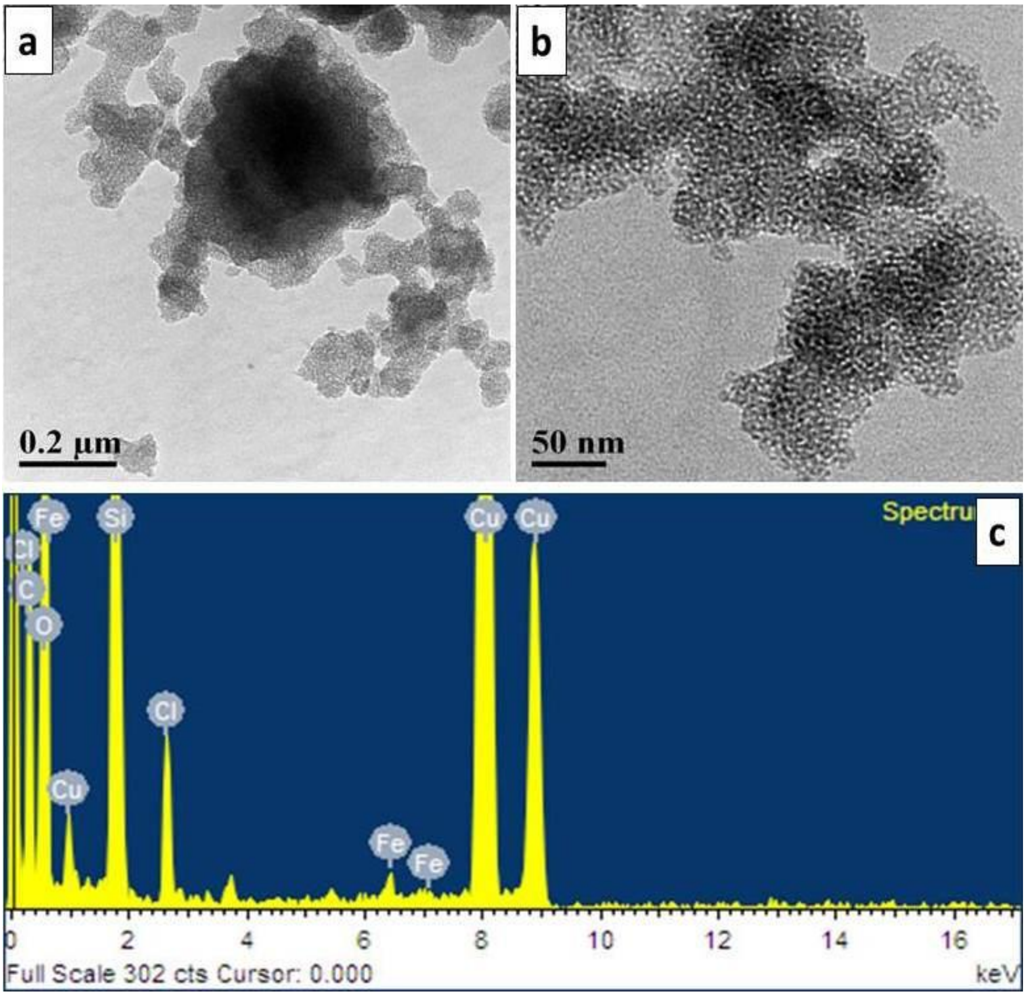

Figure 4.6 (a) Low and (b) high magnification HRTEM images of Fe-MCM-41 and (e) EDS spectrum of Fe-MCM-41

FTIR spectra of MCM-41 and Fe-MCM-41 are shown in figure 4.7. In the spectra of MCM-41, the absorption peak at 3,200-3,650 cm^{-1} is due to hydroxyl group (OH), indicating the presence of water crystallization in the sample. The peak obtained at 1630-1650 cm^{-1} is the characteristics of SiO_2. The two bands observed at 1050 and 1250 cm^{-1} belonged to internal and external asymmetric Si-O-Si stretching frequencies. The peaks at 955-965 and 795-810 cm^{-1} are due to Si-O stretching and symmetric Si-O stretching mode, respectively (Li et al., 2011; Kaya et al., 2010). It is observed that with the addition of Fe content, there is a slight red shift for the peaks around 750 to 1250 cm^{-1} corresponding to the stretching vibration of the tetrahedral TO_4 units (T = Si or Fe); these shifts indicated that the heteroatoms were incorporated into the frame-work of MCM-41 and M–O–Si bonds were formed. This is because the atomic weight of iron is larger than that of Si and the bond length of Fe-O were greater than that of Si-O, which led to a decrease in the vibration frequencies (Li et al., 2012).

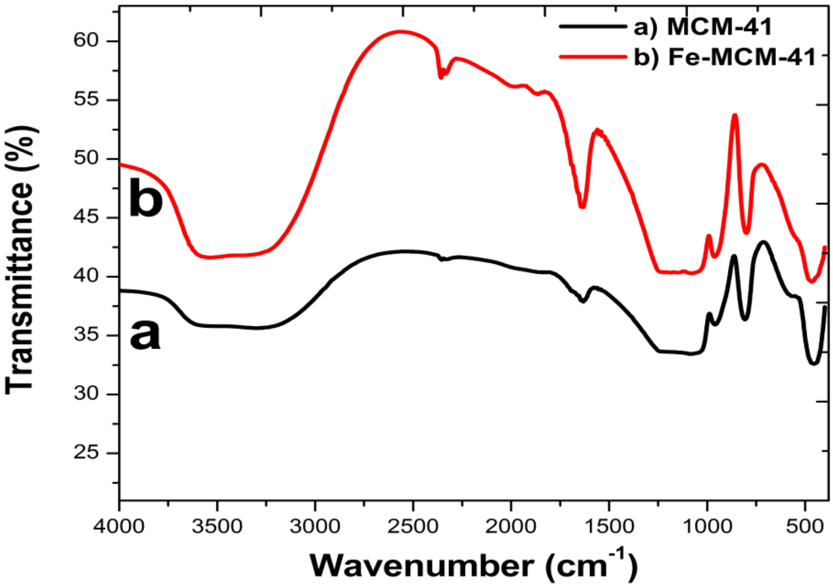

Figure 4.7 FTIR spectra of a) MCM-41, and b) Fe-MCM-41.

The surface area characterization of the prepared MCM-41 and Fe-MCM-41 was carried out by measuring their nitrogen adsorption/desorption isotherms. The N_2 adsorption–desorption isotherms and pore size distributions of both MCM-41 and Fe/MCM-41 are shown in Figure 4.8a and 4.8b, respectively. The samples exhibit pronounced steep condensation step for relative pressures 0.2 to 0.4 arising from condensation of nitrogen inside the primary mesopores which is a characteristic of typical type IV adsorption/desorption isotherm (Gaydhankar et al., 2006). The textural properties such as: inter-planar spacing ‘d’**,** unit cell parameters ‘a’, BET surface area, BJH pore diameters, total pore volume and wall thickness are given in table 4.2. The surface area of MCM-41 and Fe-MCM-41 were found to be 1266.3 and 880.4 m^2/g, respectively. From the results it is observed that incorporation of iron on MCM-41 decreased surface area and pore diameter and increased the pore wall thickness and pore volume. Increasing of the pore wall thickness and pore volume may be attributed to the increasing micelles size due to the presence of the charged ions of iron salt. Whereas, decreasing of surface with incorporation of Fe atom in the MCM-41 can be explained in terms of pore blocking of MCM-41 matrix due to the presence of Fe_2O_3 nanoparticles and their aggregates. This was likely to enhance adsorption and catalytic activity by facilitating the substrate transport and access to the confined mesopores (Huang et al., 2012). From the figure it is also found that both MCM-41 and Fe-MCM-41 exhibit narrow pore size distributions.

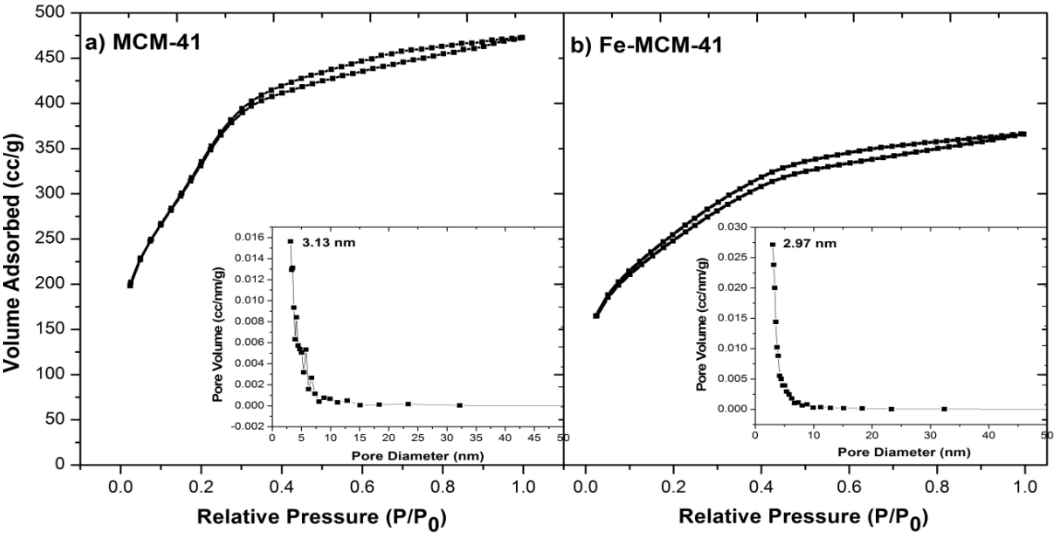

Figure 4.8 Nitrogen adsorption/desorption isotherms of (a) MCM-41 and (b) Fe-MCM-41 and the relevant pore size distribution curves (inset).

Table 4.2 Textural properties of prepared MCM-41 and Fe-MCM-41 materials

Sample	**d_{100} (nm)**	**[b]Unit cell a_0 (nm)**	**[c]Wall thickness (nm)**	**Surface area (m^2/g)**	**Pore size (nm)**	**Pore volume (cc/g)**
MCM-41	3.27	3.77	0.64	1266.3	3.13	0.149
Fe-MCM-41	3.71	4.28	1.31	880.4	2.97	0.167

[a]Pore-size distribution and pore volume were determined from N_2 adsorption isotherms at 77 K
[b]$a_0 = 2 \times d_{100}/3^{1/2}$
[c]The wall thickness was calculated as: a_0- pore size.

4.3.2. Adsorptive removal of methylene blue from aqueous media

4.3.2.1. Effect of pH on removal of MB

pH is an important parameter for adsorption as it affects both the chemistry of the dye and the adsorbent materials and also plays an important role in the whole adsorption process and for determination of maximum absorption capacity (Mahapatra et al. 2013). Figure 4.9a shows the influence of the initial solution pH from 2 to 12 on the adsorption of MB onto MCM-41 and Fe-MCM-41. The pH of the test solutions was adjusted by using HCl and NaOH solutions. 0.05 g of each adsorbent was used in 20 ml of 100 mg/L MB solution at different pH value with 30 min agitation time. The adsorptive removal percentage of MB onto MCM-41 and Fe-MCM-41was observed to be increased with increase in pH 2-9. From pH 9-12, there was no significant change in percentage of adsorption was observed. The results may be attributed to the following reasons. At lower pH, for cationic dye (MB) the lower adsorption values is probable due the presence of excess H^+ ions competating with the cationic group on the dye for adsorption site. The increased adsorption at higher pH is mainly due to enhanced association of the cationic dye with surface hydroxyl groups of MCM-41. It is related to the electrostatic force of attraction of the dye with the deprotonated hydroxyl group of adsorbents. Increase in the pH of the solution increases the electrostatic attraction between the positively charges dye and the surface of the adsorbent, which results increase in adsorption of MB dye. At high pH, OH^{-} on the surface of the adsorbent favors the adsorption of cationic dye molecules (Chen et al., 2010). Lee et al. (2007) and Monash and Pugazhenthi (2010) have also reported a similar type of observation for the influence of pH on adsorption of methylene green and methylene blue (cationic dyes), respectively onto MCM-41. Therefore, further studies were carried out with pH 9 of dye solution. Application of higher pH in the wasrewaret treatment is also an advantage because the following reason. Practically in wastewater treatment, high pH's also promote the precipitation of the toxic metal ions (if present in the waste water) as hydroxides. The metal hydroxide precipitates out from the solution and will not interfere with the competating ions of dye molecules. Therefore the dye molecules can be adsorbed more easily on the adsorbrnt surface.

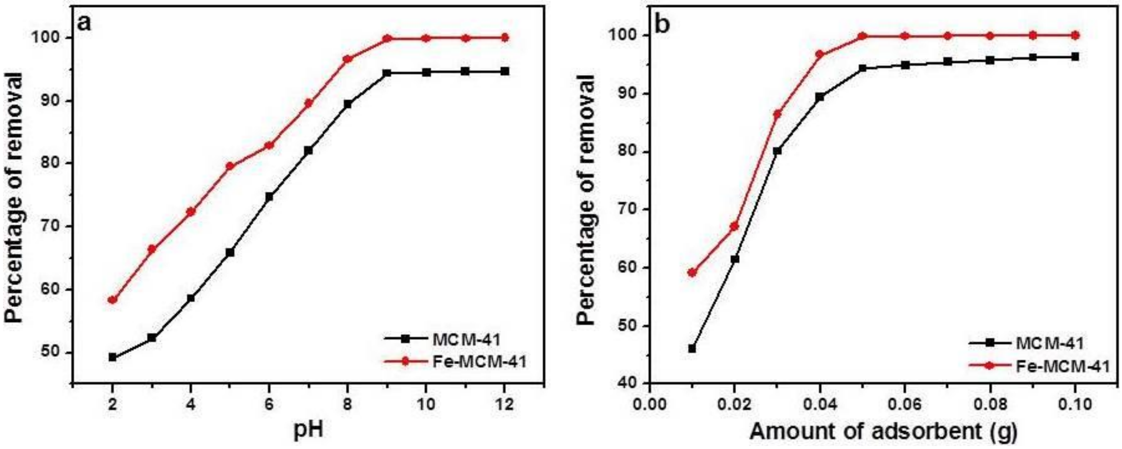

Figure 4.9 Effect of a) pH and b) amount of adsorbent (dose) on the removal of MB by MCM-41 and Fe-MCM-41.

4.3.2.2. Effect of adsorbent dose on removal of MB

The study of adsorbent dosage provides knowledge of the effectiveness of the adsorbent and also shows the ability of dye to be adsorbed. The effect of adsorbent doses on the adsorption of MB onto MCM-41 and Fe-MCM-41 surface was studied at pH=9 using 20 ml of 100 mg/L MB solution for 30 min contact time. The result obtained is represented in figure 4.9b. From the figure it is observed that, with an increase in adsorption dose from 0.01 to 0.05 g, the percentage of removal of MB increased up to a maximum value of 99.9 % for Fe-MCM-41 and 94.5 % for MCM-41, respectively. This may be due to an increase in number of active sites of the adsorbent material with increasing amount of the adsorbent. After that further increase in the amount of the adsorbent, no considerable change in the adsorption was observed. Hence, 0.05 g of each adsorbent was chosen as the optimum amount in future studies.

4.3.2.3. *Kinetic Studies*

The effect of contact time on the adsorption of MB by MCM-41 and Fe-MCM-41 was studied for initial concentration of 100 mg/L of 20 ml Methylene blue solution by using 0.05 g adsorbent at pH 9. The contact time was varied from 10 to 60 minutes and the result obtained is shown in figure 4.10. From the figure 4.10a, it is observed that maximum adsorption occurred within 30 min of contact time; thereafter the rate of removal became rather slow i.e. the adsorption reaches steady state after 30 min for both the cases. We have studied the kinetics of adsorption of MB by MCM-41 and Fe-MCM-41 adsorbents and the experimental data obtained are applied to pseudo-first-order and pseudo-second-order kinetic model. The pseudo-first-order model is based on the hypothesis that the rate of change of solute uptake with time is directly proportional to difference in saturation concentration and the amount of solid uptake with time, while the pseudo-second-order model assumes that the adsorption rate is controlled by chemical adsorption through sharing or exchange of electrons between the adsorbent and adsorbate. The differential form of pseudo-first-order kinetic model is expressed as (Wang et al., 2014):

$$\boldsymbol{ln(q_e - q_t) = lnq_e - k_1 . t} \qquad \textbf{(4.2)}$$

here, k_1 is the rate constant of pseudo-first-order adsorption (min^{-1}), q_e is the equilibrium adsorption capacity (mg/g), and q_t is the amount of dye adsorbed at time t (mg/g). The values of the pseudo-first-order rate constant k_1 and q_e can be obtained from the slope and intercept of the straight line of the plot ln (q_e–q_t) versus t.

The differential form of pseudo-second-order kinetic model is expressed as (Kumar and Rajesh, 2013):

$$\boldsymbol{\frac{t}{q_t} = \frac{1}{k_2 q_e^2} + \frac{t}{q_e}} \qquad \textbf{(4.3)}$$

here, k_2 [g/(mg min)] is the rate constant of the pseudo-second-order equation and q_e and q_t are the amounts of solute adsorbed on the adsorbent at equilibrium and at time t, respectively. The values of q_e and k_2 can be determined by the slope and intercept of the straight line of the plot t/q_t versus t, respectively. The parameters of the two kinetic models are given in table 4.3. From table, it is observed that the values of the correlation coefficients (r^2) for the pseudo-first-order model are very low, and the calculated q_e values ($q_{e,cal}$) are quite different from the experimental values ($q_{e,exp}$), indicating that the adsorption of MB onto both the MCM-41 and Fe-MCM-41 adsorbents cannot be applied to a pseudo-firstorder model. The correlation coefficients for the linear plots of pseudo-second-order model are higher ($r^2 > 0.99$), and the theoretical calculated q_e values ($q_{e,cal}$) are in good agreement with experimental q_e ($q_{e,exp}$) values for both the MCM-41 and Fe-MCM-41 adsorbents. Therefore, the adsorption process of methylene blue on both the MCM-41 and Fe-MCM-41 is in good agreement to the pseudo-second order kinetic model. The pseudo-second-order plots for the adsorption of MB by MCM-41 and Fe-MCM-41 are shown in figure 4.10b and 4.10c, respectively.

Table 4.3 Pseudo-first-order and Pseudo-second-order kinetic parameters for the removal of MB by MCM-41 and Fe-MCM-41

Adsorbent	**$q_{e,exp}$ (mg/g)**	**Pseudo-first-order model**			**Pseudo-second-order model**		
		k_1 (min^{-1})	**$q_{e,cal}$ (mg/g)**	**r^2**	**k_2 (g mg^{-1} min^{-1})**	**$q_{e,cal}$ (mg/g)**	**r^2**
MCM-41	38.15	0.0139	10.25	0.7183	0.0075	40.32	0.997
Fe-MCM-41	39.97	0.0653	16.27	0.7419	0.0086	42.19	0.998

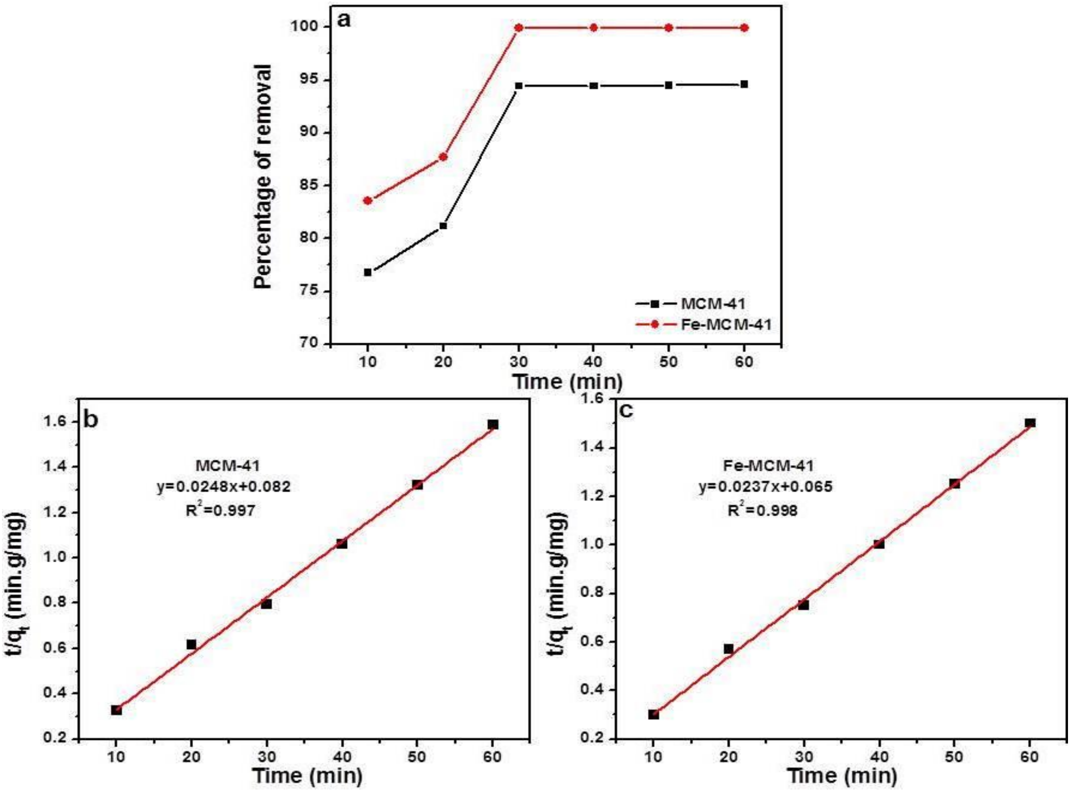

Figure 4.10 (a) Percentage removal of MB by MCM-41 and Fe-MCM-41 as a function of time (min), and Pseudo-second-order plot for removal of MB by (b) MCM-41 and (c) Fe-MCM-41.

4.3.2.4. Adsorption isotherm

We have studied the adsorption isotherms to describe the interaction of molecules of adsorbate (dye) with adsorbent surface. The isotherm provides a relationship between the concentration of dye in solution and the amount of dye adsorbed on the adsorbent when both phases are in equilibrium. The analysis of the isotherm data is of great importance by fitting them to different isotherm models to optimize the adsorption system. Several adsorption isotherms models are available, but in the present study, we have followed the most widely used Langmuir and Freundlich isotherm models.

The Langmuir isotherm model assumes monolayer coverage of adsorbate on a homogeneous adsorbent surface. This model does not consider surface heterogeneity of the sorbent. It assumes that adsorption will take place only at specific site on the adsorbent. The Langmuir equation is given as (Nassar et al., 2011):

$$\boldsymbol{q_e = \frac{K_L q_{max} C_e}{1 + C_e K_L}} \qquad \textbf{(4.4)}$$

where K_L is the Langmuir constant related to the energy of adsorption, q_{max} is the maximum adsorption capacity corresponding to complete monolayer coverage (mg g^{-1}), which depends upon the number of adsorption sites.

The Freundlich isotherm model describes the surface heterogeneity of the sorbent and considers multilayer adsorption with a heterogeneous energetic distribution of active sites, accompanied by interactions between adsorbed molecules. The Freundlich equation is given by (Nassar, 2010):

$$\boldsymbol{q_e = K_F C_e^{1/n}} \qquad \textbf{(4.5)}$$

where C_e is the equilibrium concentration (mg L^{-1}), q_e is the amount adsorbed at equilibrium (mg g^{-1}) and K_F and n are Freundlich constants, related to the extent of the adsorption and the degree of nonlinearity between solution concentration and adsorption, respectively.

The adsorption equilibrium data obtained from adsorption of MB by both MCM-41 and Fe-MCM-41 were non-linearly fitted to the Langmuir and Freundlich isotherms. The parameters and correlation coefficients calculated from the models are listed in table 4.4. It can be seen that the least-squares correlation coefficient (R^2) value of the Langmuir model is significantly higher than that of the Freundlich model for both the cases of adsorbents, indicating that the Langmuir model should better describe the methylene blue adsorption on MCM-41 and Fe-MCM-41. The Langmuir and Freundlich adsorption isotherm plots for removal of MB by

MCM-41 and Fe-MCM-41 are given in figure 4.11a and 4.11b, respectively. This result indicates that the adsorption capacities of MCM-41 and Fe-MCM-41 for adsorption of MB are 149.5 and 194 mg g^{-1}, respectively.

Table 4.4 Langmuir and Freundlich Constants for the adsorption of MB.

Adsorbent	**Langmuir isotherm model**			**Freundlich isotherm model**		
	q_{max} (mg g^{-1})	**K_L (Lg^{-1})**	**r_L^2**	**K_F**	**n**	**r_F^2**
MCM-41	149.5	0.056	0.988	27.57	2.96	0.95
Fe-MCM-41	194	0.387	0.957	73.65	3.66	0.915

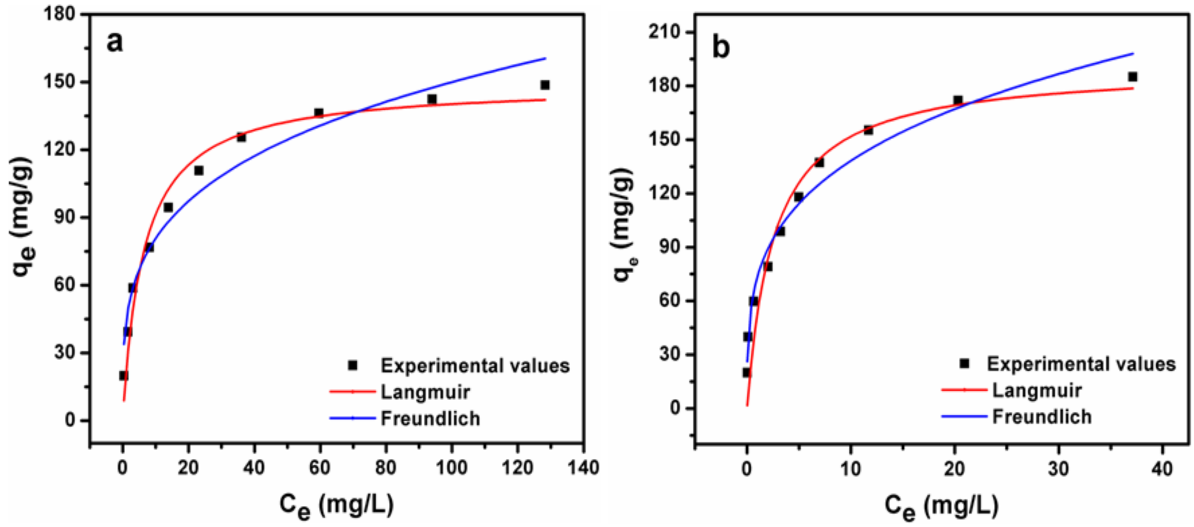

Figure 4.11 Non-linear fits of Langmuir and Freundlich isotherm models for removal of MB by (a) MCM-41 and (b) Fe-MCM-41.

4.3.2.5. Adsorption mechanism

In MCM-41 the Si atoms carry -OH groups. Adsorption process is mainly dependent upon the affinity of the adsorbates towards H^+ and OH^- ions of the adsorbents. Adsorbents surfaces possess different charges in solution with different pH values, causing electrostatic attraction or repulsion to the adsorbates. For cationic dyes, the adsorption of an adsorbent towards them increases with increasing pH, because of the electrostatic attraction. Here, at pH 9 or above the MCM-41 walls get negatively charged, which favored the adsorption of cationic MB dye. The adsorption capacity of Fe-MCM-41 towards the adsorption of methylene blue is higher than MCM-41. This may be due to presence of more negative sites (i.e. both O^- and Fe^-) on the wall of Fe-MCM-41, which causes more adsorption of methylene dye molecules (figure 4.12).

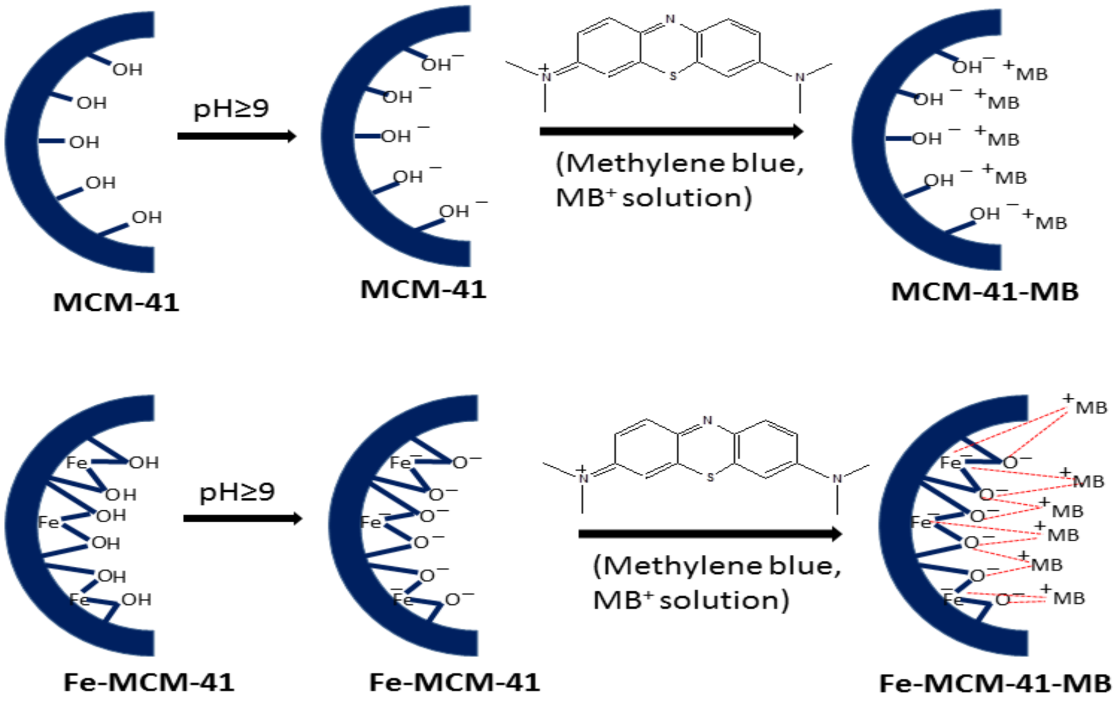

Figure 4.12 Proposed mechanism for MB adsorption on MCM-41 and Fe-MCM-41.

4.4. Conclusions

We have reported the synthesis of high surface area mesoporous MCM-41 and iron oxide impregnated MCM-41 nanomaterials by a facile wet chemical method. XRD and XPS studies suggested the presence of mixture of FeO and Fe_2O_3 inside porous matrix of MCM-41 for Fe-MCM-41. HRTEM studies revealed the formation of mesoporous structure with less ordered in hexagonal arrays of Fe-MCM-41. Again, N_2 adsorption/desorption isotherm study confirm the formation of mesoposous materials with surface areas of 1266 and 880 m^2/g for MCM-41 and Fe-MCM-41, respectively. The surface morphology of Fe-MCM-41 materials was found to elipitical in shape having diameter in therange of 300-400 nm and length up to 1 micron. The prepared mesoporous nanomaterials were used as adsorbents for adsorptive removal of Methylene blue from aqueous media. It is observed that the adsorption isotherm data fit well with Langmuir model indicating that adsorption occured by monolayer coverage. The kinetic study showed that the adsorption followed the pseudo-second-order kinetics model. It is also observed that the sorption performance of MCM 41 towards removal of methylene blue has been enhanced further by incorporation of iron oxide into mesoporous matrix. The maxium sorption capacity of prepared Fe-MCM-41 materials is found to be 194 mg g^{-1} which is comparable to the recently reported adsorbents (polyaniline nanotubes base/silica composite, 10.31 mg g^{-1} (Ayad et al., 2012), Ni-MCM-41, 157.48 mg g^{-1} (shu at al., 2015), nanoporous SBA-3, 285.7 mg g^{-1} (Anbia and Hariri, 2010)).

CHAPTER-5

IRON BASED MAGNESIUM OXIDE NANOMATERIALS FOR ADSORPTIVE REMOVAL AND PHOTOCATALYTIC DEGRADATION OF TOXIC DYES

PART A: MgO NANOSTRUCTURES: SYNTHESIS AND ADSORPTION STUDIES

5.1. Introduction

Magnesium oxide (MgO) is a typical wide band gap (7.2 eV) semiconductor, which represents an important class of functional metal oxides with a broad range of properties. It has attracted considerable attention for its novel properties and large variety of applications in the field of catalyst, catalyst supports, refractory materials, paints, toxic waste remediation, optoelectronics, microelectronics, additive in heavy fuel oil, paint, gas separation, bactericides, insulator in industrial cables, crucibles and superconductors (Liu et al., 2014; Balamurugan et al., 2014; Sutradhar et al., 2011).

Nanostructured materials have high surface areas and a large fraction of atoms available for various applications. Nanostructured alkaline earth metal oxides, in particular MgO, are very favorable candidate materials for applications as adsorbents due to their specific affinity and high surface capacity. MgO nanomaterials have been explored as a nontoxic and environmentally friendly adsorbent to remove organic pollutants and toxic metal ions from water (Wang et al., 2014). Among the various techniques for removal of organic pollutants from waste-water, adsorption process has been proven as an effective removal method, due to its efficiency, simplicity, and applicability (Mittal et al., 2010). Hence, synthesis of MgO with high surface area is of great interest for adsorption applications (Hu et al. 2010; Nga et al. 2013).

Recently, enormous efforts have been made to synthesize MgO with enhanced surface area in varying morphologies such as rods, wires, belts, tubes, and so forth. Among various synthesis methods, chemical methods are the promising approaches due to their simplicity, cost-effective, high yield of final product and low reaction temperature (Sutradhar et al., 2011). Many researchers have adopted MgO and $Mg(OH)_2$ as an absorbent to remove toxic ions and organic pollutants from water. Gao et al. (2008) have synthesized MgO with various morphologies such as nanoflakes, mesoporous microspheres composed of nanoflakes by adjusting the composition and phase structure of magnesium carbonate hydrate. They have applied the prepared MgO nanomaterials for adsorption of Cd(II), Pb(II), Cr(VI) ions and Orange G dye from waste water and found that the mesoporous MgO exhibited excellent absorption performance for both low and high valence heavy metal ions and organic pollutants in water. Venkatesha et al. (2012) have synthesized MgO nanoparticles by precipitation method and have studied their adsorption behavioue towards removal of Levafix fast red CA (LFR) and Indanthren blue BC (IB) from aqueous media. They have observed that the synthesized MgO nanoparticles regarded as an efficient adsorbent with maximum adsorption capacities of 92.16 mg/g and 86.50 mg/g for LFR and IB respectively. Tian et al. (2013) have synthesized porous hierarchical MgO by a facile and scaled-up method and reported that the MgO sample exhibited excellent adsorption properties with maximum adsorption capacity of 2409 mg g^{-1} for removal of Congo red from aqueous solution. Yu et al. (2011) have synthesized flower-like and nest-like micro-/nanostructured MgO by a simple precipitation method and have studied their adsorption behavior for removal of As(III) and As(V) ions from water. The have reported that maximum uptake capacities of flower-like and nest-like MgO for As(III) are higher than 252.34 and 643.84 mg/g, while for As(V) it could reach 343.64 and 378.79 mg/g, respectively. Hu et al. (2010) have prepared MgO nanoplates by hydrothermal method and reported that the MgO nanoplates was acted as efficient adsorbents for removal of Congo red and reactive brilliant red X3B dyes from water with maximum adsorption capacities of 303 and 278 mg g^{-1}, respectively. Similarly, Cao et al. (2012) have synthesized flowerlike MgO nanomaterials with high surface area by a facile microwave-assisted solvothermal process and applied the nanomaterials for adsorption of Pb(II) and Cd(II) ions from aqueous solution. They have reported that the flowerlike MgO nanostructures showed superb adsorption properties for Pb(II) and Cd(II), with maximum uptake capacities of 1980 mg/g and 1500 mg/g, respectively.

In the current chapter, we have selected iron oxide based alkaline earth metal oxides nanomaterials, in particular nanosized magnesium oxide (MgO), because they are very promising materials for applications as adsorbent due to high surface reactivity and adsorption capacity compared to their commercial analogs and the simplicity of its production from abundant natural minerals (Mahmoud et al., 2013). The first part of this chapter describes the synthesis of Magnesium oxide nanomaterials with different morphologies. To study the adsorption capacity of MgO nanomaterials and their applications towards adsorptive removal of range of organic dyes, we have selected both anionic Congo red (CR) and cationic Malachite green (MG) dyes in this work.

Herein, we have synthesized large scale MgO nanorods, hierarchical nanostructures and nanoflakes by chemical synthesis routs such as precipitation, reflux and hydrothermal methods, respectively. The synthesized MgO nanomaterials were used as adsorbents to remove both cationic Malachite green (MG) and anionic Congo red (CR) dyes from aqueous media. The adsorption experiments such as effects of materials type, adsorbent dose and initial concentration variation were explored in batch experiments.

5.2. Materials and methods

5.2.1. Materials used

The following chemicals were used for the synthesis of magnesium oxide nanostructures and dye adsorption experiments. Magnesium chloride ($MgCl_2.6H_2O$), ammonium carbonate $(NH_4)_2.6H_2O$) and Malachite Green (oxalate) were purchased from Merck India pvt. Ltd. Congo red was purchased from Merck Germany pvt. Ltd. All the reagents used in the synthesis were of analytical grade and used as received without further purification.

5.2.2. Synthesis of MgO nanomaterials

Stoichiometric amounts of $MgCl_2.6H_2O$ and $(NH_4)_2CO_3$ were dissolved separately in 100 ml each of double distilled water to form solution-A and B, respectively. Solution-B was added instantly to solution-A with vigorous stirring. The stirring was continued for 20 mins to obtain white colored homogeneous solution. Then we have followed three different routes to obtain MgO nanomaterials with different morphologies. The detailed synthesis procedure of MgO nanomaterials are schematically presented figure 5.1.

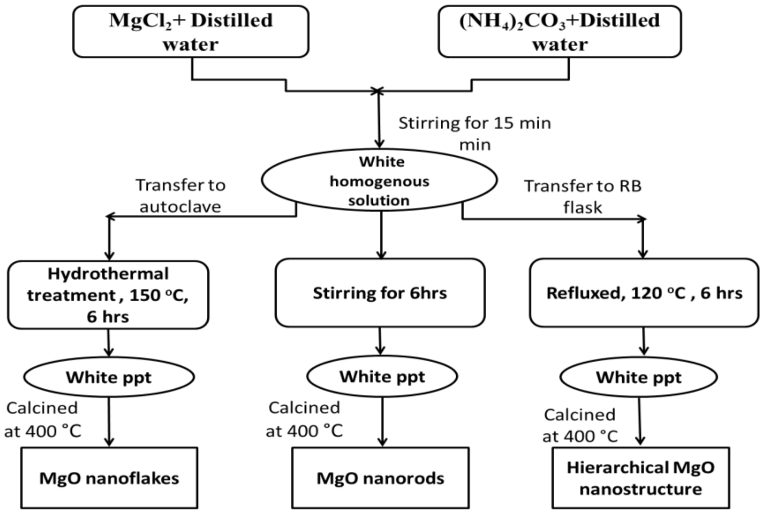

Figure 5.1 Schematic representation of the synthesis of different MgO nanomaterials.

Scheme 1: The stirring was continued for 6 hrs and the white precipitate was filtered, washed with distilled water followed by ethanol and dried at 80 °C to form artinite. Then, the product was calcined at 400 °C for 3 hrs to form MgO nanorods (named as MgO-P).

Scheme 2: The solution was transferred into a round bottomed flask and refluxed for 6 hrs at 120 °C to form hydromagnesite precursor. The obtained precursor was filtered, washed and dried at 80 °C and finally calcined at 400 °C for 3 hrs to form hierarchical MgO nanostructures (named as MgO-R).

Scheme 3: The solution was transferred into a Teflon-lined autoclave followed by hydrothermal treatment for 6 hrs at 150 °C to form hydromagnesite precursor. Then the precursor was centrifuged, washed with distilled water and then by ethanol followed by drying at 80 °C and finally calcined at 400 °C for 3 hrs to form MgO nanoflakes (named as MgO-H).

5.2.3. Characterizations

The crystalline phases of the prepared nanomaterials were investigated by X-ray powder diffraction (XRD, Rigaku Ultima-IV) using Cu Kα radiation. The field emission scanning electron microscopy (Nova Nano SEM/FEI, 20 kV) was performed to observe the shapes and morphologies. Fourier transforms infrared (FTIR) spectra were measured on Perkin-Elmer FTIR (Spectrum RX-I) spectrometric analyzer. N_2 adsorption−desorption isotherm was determined on a Quantachrome (Autosorb-iQ) physicsorption apparatus.

5.2.4. Adsorption studies of Malachite green (MG) and Congo red (CR) dyes

The different MgO nanomaterials prepared were used as adsorbents and their adsorption effeciencies were investigated by using Malachite green (MG) and Congo red (CR) dyes from aqueous media. Initially a stock solution of 1 g of Malachite green and Congo red was dissolved in 1000 ml of double distilled water. Batch adsorption experiments were conducted in order to investigate the effects of materials type (MgO-P, MgO-R and MgO-H), solution pH (3-8), adsorbent dose (0.003-0.01 g), initial dye concentration (100-500 mg/l) and contact time (15-90 min) for adsorption of MG and CR dyes. The pH of the dye solutions was adjusted using 0.1M HCl and 0.1M NH_4OH solution. After the batch adsorption experiment, the residual concentrations of the dye solutions was measured by using Shimadzu UV-2450 spectrometer at λ_{max}=615 for MG and λ_{max}=498 for CR. All the batch adsorption experiments were carried out at room temperature. All the adsorption experiments were carried out three times in replicates and the mean data obtained were taken in results and discussion section.

5.3. Results and Discussion

5.3.1. Surface Morphology and microstructure: Figure 5.2(a, a') represents the SEM and FESEM images of MgO nanomaterials synthesized by precipitation method. The images suggest the formation of smooth and randomly arranged rod shaped nanomaterials with average diameters around 400-500 nm. The SEM images of MgO nanomaterials synthesized by reflux method are shown in figure 5.2(b, b'). The low-magnification SEM image (figure 5.2(b)) demonstrates the formation of uniform flower-like hierarchical nanostructures. The high-magnification FESEM image (figure 5.2(b')) visualizes that the hierarchical nanostructures contains plates with thickness around 100-200 nm. Figure 5.2(c, c') represents the SEM images of MgO nanomaterials synthesized by hydrothermal method. The images indicate the formation of flakes like nanomaterials with diameter around 300-500 nm. The energy-dispersive spectroscopy (EDS) spectrum of hierarchical MgO nanostructures (figure 5.2(d)) demonstrates the presence of O and Mg elements without any impurities.

5.3.2. XRD analysis: Figure 5.3a shows the XRD patterns of as-synthesized and calcined nanorods obtained by precipitation method. The as-synthesized sample contains characteristics peaks of artinite (Magnesium carbonate hydroxide hydrate, $Mg_2CO_3(OH)_2(H_2O)_3$) with monoclinic crystal structure according to JCPDS file number 70-0591. After calcination at 400 °C for 4 hrs the artinite nanorods were converted to MgO nanorods. The patterns can be indexed to cubic crystalline structure according to JCPDS file number 78-0430. Figure 5.3b shows the XRD patterns of as-synthesized and calcined hierarchical nanostructures obtained by reflux method. The as-synthesized samples contain mixture of monoclinic and orthorhombic hydromagnesite crystal structures according to JCPDS file number 25-0513 and 70-1177, respectively. After calcination at 400 °C for 4 hrs, the hydromagnesite was converted to MgO and can be indexed to cubic crystalline structure according to JCPDS file number 78-0430. Again, the XRD patterns of as-synthesized and calcined nanoflakes prepared by hydrothermal method are shown in figure 5.3c. The as-synthesized nanoflakes contain mixture of monoclinic and orthorhombic hydromagnesite crystal structures according to JCPDS file number 25-0513 and 70-1177, respectively and the calcined nanoflakes contain characteristics peaks of cubic crystalline MgO according to JCPDS file number 78-0430. The XRD patterns reveal the well crystalline nature of the samples without presence of any impurities.

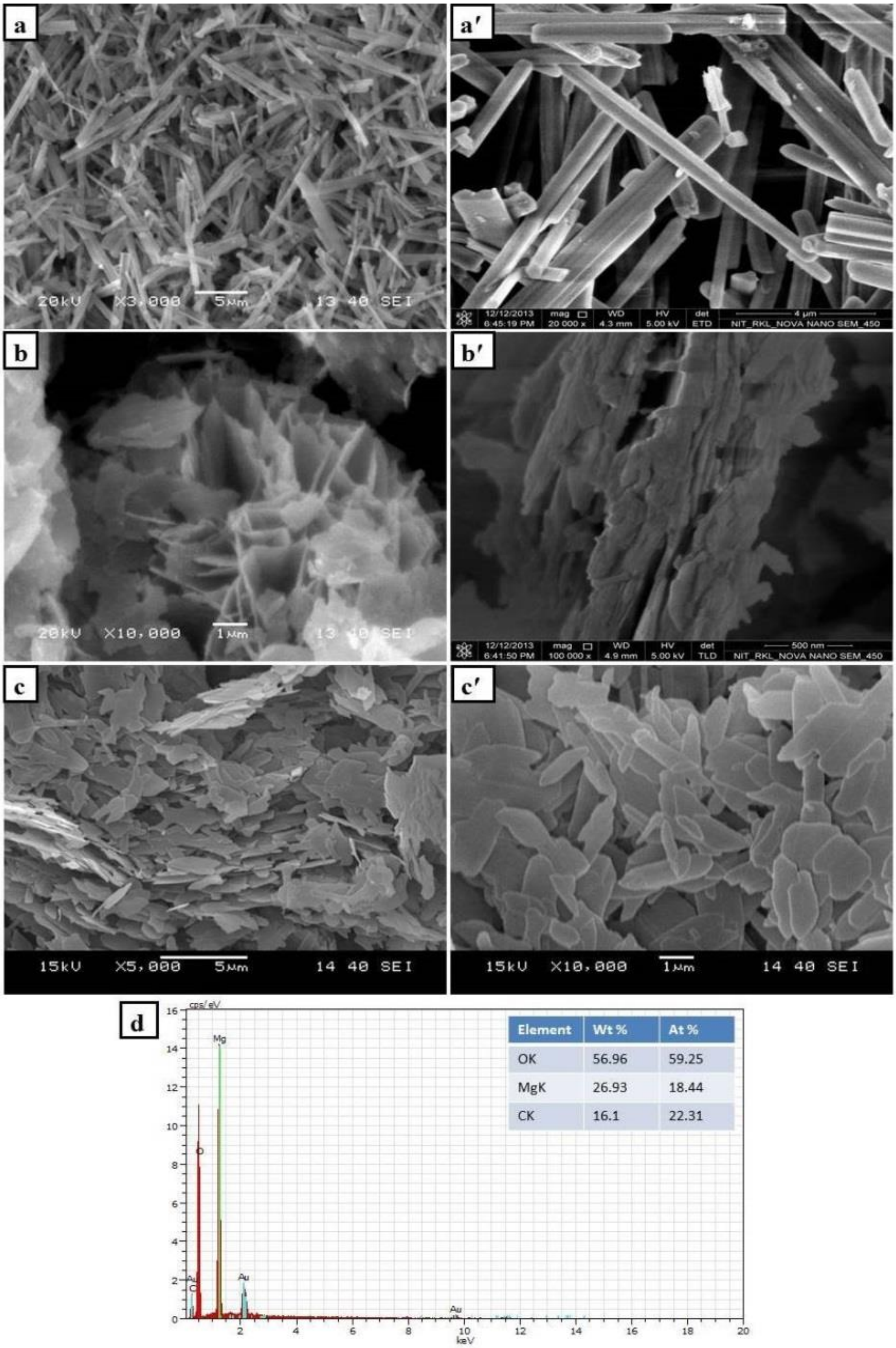

Element	Wt %	At %
OK	56.96	59.25
MgK	26.93	18.44
CK	16.1	22.31

Figure 5.2 Low and high magnification SEM and FESEM images of (a, a') MgO nanorods, (b, b') hierarchical MgO nanostructures, (c, c') MgO nanoflakes and (d) EDS of hierarchical MgO nanostructures.

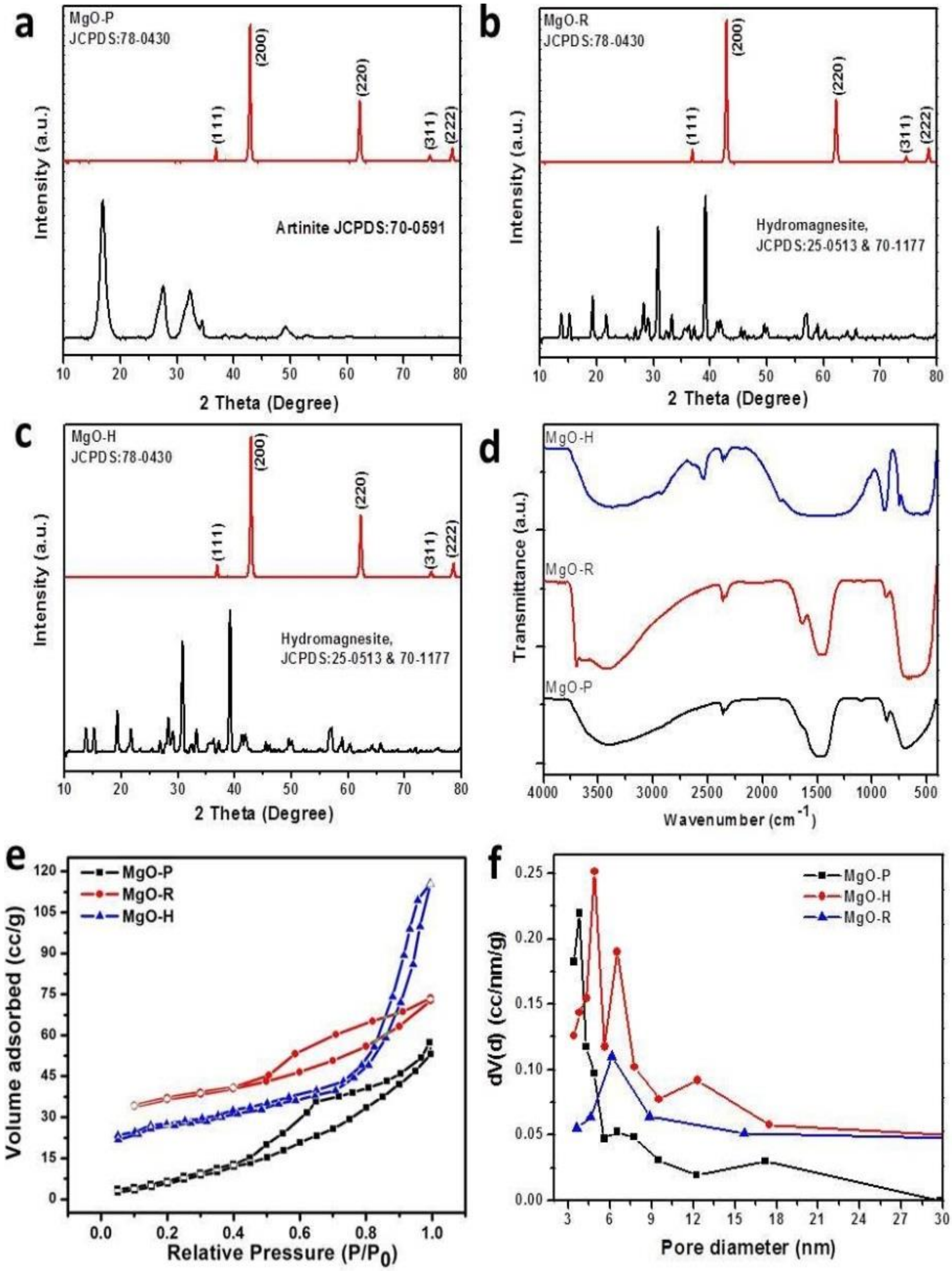

Figure 5.3 XRD patterns of (a) Artinite and MgO nanorods prepared by precipitation method, (b) hierarchical Hydromagnesite and MgO nanostructures prepared by reflux method, (c) Hydromagnesite and MgO nanoflakes prepared by hydrothermal method, (d) FTIR patterns, (e) N_2 adsorption/desorption isotherms and (f) pore-size distribution of MgO nanorods, hierarchical nanostructure and nanoflakes.

5.3.3. FTIR analysis: The FTIR patterns of prepared MgO nanomaterials are presented in figure 5.3d. Peaks at 3700-3300 cm^{-1} are corresponding to the O–H stretching mode of hydroxyl groups present on the surface due to moisture. A broad band at 1460–1400 cm^{-1} in each pattern corresponds to Mg-O stretching vibrations. Peaks at 850–900 cm^{-1} corresponds to v1 and v2 stretching vibrations of metal oxygen bond. The major peaks in the range of 440-690 cm^{-1} are due to Mg-O stretching vibrations.

5.3.4. Surface area and porosity analysis: The N_2 adsorption-desorption isotherm and pore size distribution are shown in figure 5.3e, f. From figure 5.3e, it is observed that the BET surface area of MgO nanorods, hierarchical nanostructures and nanoflakes are 48.45, 147.5 and 110.9 m^2/g, respectively. From BJH pore size distribution curve (figure 5.3f), the pore diameters of MgO nanorods, hierarchical nanostructures and nanoflakes are found to be 3.8, 4.9 and 6.15 nm.

5.3.5 Removal of Malachite green and Congo red from aqueous media

Effect of materials types on adsorption: The MgO nanorods, hierarchical nanostructures and nanoflakes were applied as adsorbents to remove Malachite green (MG) and Congo red (CR) from aqueous solutions. 0.01 g of each adsorbent was added to 20 ml of 100 mgL^{-1} solution of MG and CR separately and adsorption was carried out for 60 min. From figure 5.4a, it is observed that the percentage of removal of MG by MgO nanorods, hierarchical nanostructures and nanoflakes are 95.1, 99.98 and 97.42 %, respectively and percentage of removal of CR by MgO nanorods, hierarchical nanostructures and nanoflakes are 86.28, 99.94 and 92.68 %, respectively. The hierarchical MgO nanostructure shows better removal capacity for both the dyes than other two adsorbents. It may be due to its high surface area and hierarchical structure, which can provide more available active adsorption sites and efficient transport pathways. Hence, we have chosen hierarchical MgO nanostructure for further adsorption study by varying the pH, amount of dose, contact time and dye concentration.

Effect of pH on Adsorption: The effect of pH is an important controlling parameter on the dye adsorption capacity, which affects both aqueous chemistry and surface binding sites of the adsorbents. Figure 5.4b shows the percentage adsorption of 20 mL of 100 mg L^{-1} MG and CR dye solutions with pH =3-8. The natural pH of 100 mg L^{-1} Malachite green is 5.6-6. Below pH 3 (acidic range) the dye becomes colourless and above pH 8 the dye also becomes purely colourless, so this experiment was done in pH range of 3-8. At pH 3 the percentage removal of MG was more than 95 % and it increased with the increase in the pH upto 6 after that the adsorption percentage was remains constant. The result can be explained by the fact that at low pH, the concentration of H^+ ion is high causing a competition for the adsorption sites of the MgO surface between the H^+ ions and cationic malachite green dye molecules. When the pH increase the formation of electric double layer changes its polarity and consequently the dye uptake increases (Mittal, 2006; Gupta et al., 2004). After the pH value 6, the uptake of MG dye was slightly increased and remained virtually unchanged. This result could be attributed due to the fact that, with increase in pH from 6 to 8, the concentration of competitive H^+ ions in the solution decreases, hence the adsorption of positively charged MG dye onto MgO surface surface increases. The natural pH of 100 mg L^{-1} Congo red dye is pH of 7.6. It was found that the dye solution becomes dark blue when the pH was lowered to 3 and deep red when the pH was above 10-12. Therefore, in this study, the pH of the solution was maintained in between 3-8. It is observed from the figure 5.4b, that the adsorption increased with increasing pH from 3 to 7 and after that decreased. The removal of CR increased in pH range 3-7 due to the electrostatic attraction between the anionic dye molecules (negatively charged) and MgO surface (positively charged; pHzpc 12.4). However, the reduction of CR removal percent at higher pH might be explained by the formation of OH^- and subsequent competition with the CR molecules for adsorption site (Moussavi and Mahmoudi, 2009). Hence for all the future study we have chosen the natural pH of both the dye solutions.

Effect of adsorbent dose: Figure 5.4c shows the variation of amount of adsorbent dosage with percentage removal of MG and CR for 20 mL each of 100 mgL^{-1} dyes with 60 mins contact time. It is observed that, with increase in amount adsorbent dose from 0.003 g to 0.01 g, the percentage of adsorption increases: which may be due to increase in the active sites of the adsorbent. Further increase in the amount of the adsorbent does not bring any considerable change in the adsorption. The percentages removal of MG and CR are found to more than 99 % each for 0.01 g of adsorbent, hence we have chosen 0.01 g as the optimum amount for further study.

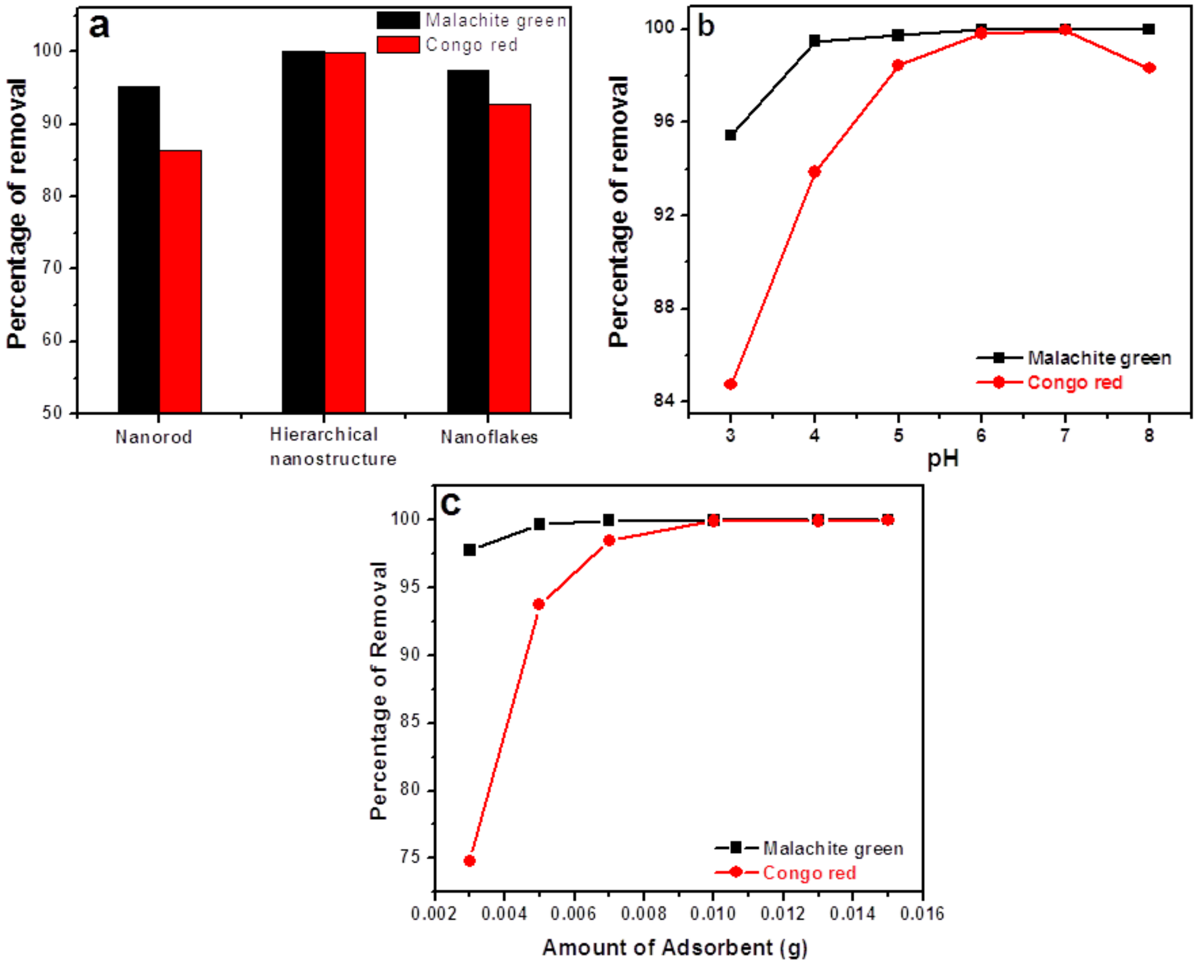

Figure 5.4 Effect of (a) material types, (b) pH and (c) amount of dose on the adsorption of MG and CR.

Adsorption Kinetics: In order to understand the dynamics of adsorption process in terms of the order of reaction and rate constant, the kinetics study for the adsorption of MG and CR dye on hierarchical MgO nanostructure has been carried out. The kinetics of adsorptiobn of Malachite green and Congo red dye on the MgO hierarchical nanostructure of is well described by using the pseudo-second-order kinetics model.

The pseudo second order model is represented by the following equation (Chen et al., 2015):

$$\frac{t}{q} = \frac{1}{k_2 q_e^2} + \frac{t}{q_e} \qquad \textbf{(5.1)}$$

The equilibrium adsorption capacity (q_e) and the second-order rate constants k_2 (g^{-1} mg min) can be determined experimentally from the slope and intercept of plot of t/q versus t. The best-fit values of h, q_e and k_2 along with correlation coefficients of the pseudo-second-order model for the three adsorbents are shown in table 5.1, and the pseudo-second-order plots of adsorption of Malachite green and Congo red are given in figure 5.5.

Table 5.1 Pseudo-second-order kinetic parameters for the removal of MG and CR

Adsobate	**K_2 (g mg^{-1} min^{-1})**	**q_e (mg/g) (Calculated)**	**q_e (mg/g) (Experimental)**	**r^2**
Malachite green	0.0277	200	199.97	0.999
Congo red	0.0053	204.08	199.98	0.999

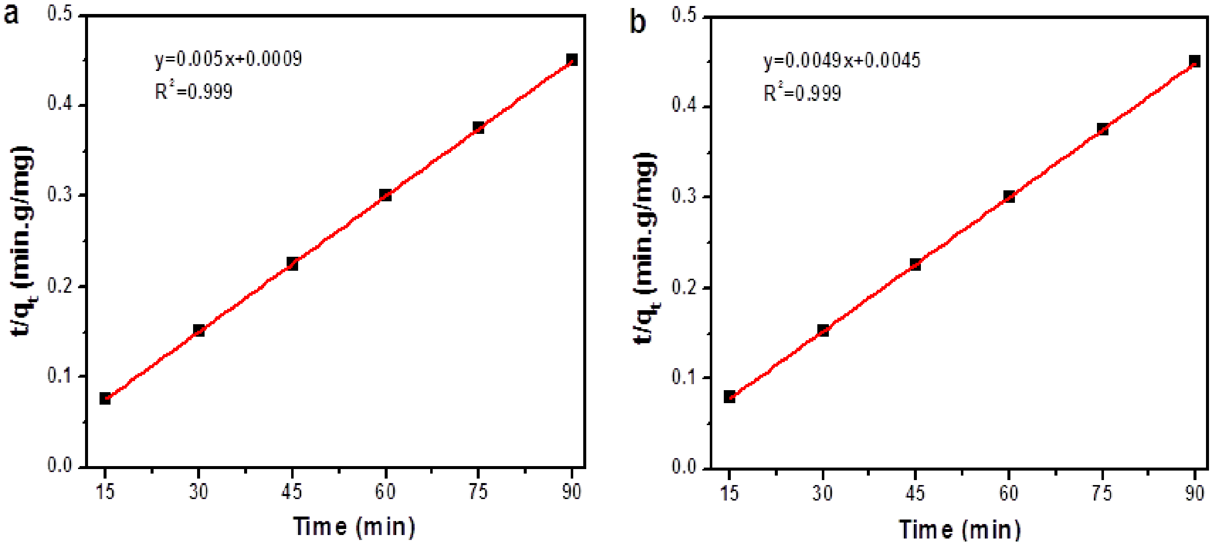

Figure 5.5 Pseudo-second-order plot for removal of (a) Malachite green and (b) Congo red

The values of predicted equilibrium adsorption capacities (q_e) showed good agreement with the experimental equilibrium uptake values. Similarly, correlation coefficients are always greater than 0.99, which also explains the good fit of the model.

Adsorption isotherm: The equilibrium adsorption isotherm is essential in describing the interaction between adsorbate and adsorbent, and to evaluate the efficacy of the prepared adsorbent for the design of an appropriate adsorption system. Several adsorption isotherms models are available. In the present study; we have followed the most widely used Langmuir and Freundlich isotherm models. Effect of initial dye concentration was studied with varying concentration ranging from 100 to 500 mg L^{-1}. Then, Langmuir and Freundlich isotherm model were used to determine the adsorption capacities of hierarchical MgO nanostructure towards removal of MG and CR.

The Langmuir equation is given as (Zhu et al., 2012):

$$q_e = \frac{K_L q_{max} C_e}{1 + C_e K_L} \qquad \textbf{(5.2)}$$

where K_L is the Langmuir constant related to the energy of adsorption, q_{max} is the maximum adsorption capacity corresponding to complete monolayer coverage (mg g^{-1}), which depends upon the number of adsorption sites.

The Freundlich equation is given by:

$$q_e = K_F C_e^{1/n} \qquad (5.3)$$

where C_e is the equilibrium concentration (mg L^{-1}), q_e is the amount adsorbed at equilibrium (mg g^{-1}) and K_F and n are Freundlich constants, related to the extent of the adsorption and the degree of nonlinearity between solution concentration and adsorption, respectively. The isotherm constants and correlation coefficients were calculated and listed in table 5.2. It is observed that the adsorptions of both MG and CR are better fitted to the Langmuir model with maximum adsorption capacities of 1205.23 and 1050.81 mg/g, respectively.

Table 5.2 Adsorption isotherm constants for Malachite green and Congo red

Adsorbate	Langmuir			Freundlich		
	q_{max} (mg g^{-1})	K_L	R^2	K_F	n	R^2
Malachite green	1205.23	12.69	0.999	1506.61	2.52	0.932
Congo red	1050.81	1.21	0.973	536.02	3.29	0.934

5.4. Conclusions

MgO nanomaterials were successfully synthesized by three different wet chemical methods such as: precipitation, reflux and hydrothermal methods. SEM and FESEM images suggested the formation of nanomaterials with three different morphologies i.e. nanorods, hierarchical nanostructures and nanoflakes by precipitation, reflux and hydrothermal methods, respectively. XRD results revealed the crystalline nature of the prepared MgO nanomaterials. FTIR result also indicates the formation of Mg-O bands. The three different MgO nanomaterials prepared were used as adsorbents towards the removal of Malachite green and Congo red from aqueous solution. The hierarchical MgO nanostructures showed excellent dye adsorption performance with maximum adsorption capacities of 1205 and 1051 mg/g for Malachite green and Congo red, respectively.

PART B: $MgFe_2O_4$-Fe_2O_3 HETEROSTRUCTURED NANOMATERIALS FOR PHOTOCATALYTIC DEGRADATION OF METHYLENE BLUE DYE

5.5. Introduction

In the first part of this chapter, we have described the synthesis of MgO nanomaterials with different morphologies by precipitation, reflux and hydrothermal methods, respectively. The MgO nanomaterials have been used as adsorbents for removal of Congo red and Malachite green dye from aqueous media. In this part, we have presented on the synthesis of Iron based magnesium oxide composites nanomaterials following the same synthetic methods. After studying the adsorption properties of iron oxide based composite materials, we intend to study complete decomposition of organic pollutants. Since adsorption process transfer on pollutant from one medium to another, hence photocatalytic process has been chosen for complete degradation of organic pollutants.

Among spinel ferrites, ecofriendly magnesium ferrite ($MgFe_2O_4$) nanostructures have shown the attention of researchers in different fields such as magnetic and catalytic materials, gas sensors and photocatalytic applications (Shen et al., 2013; Mathew et al., 2007). The perovskite or spinel related oxide photocatalysts exhibit enhanced efficiency due to the available extra catalytic sites by virtue of their crystal lattices (Dom et al., 2011). $MgFe_2O_4$ can absorb visible light due to its small bandgap (2 eV) and is not sensitive to photoanodic corrosion and hence, this material is considered a potential solar energy material for photoelectric conversion (Zhang et al., 2011). Instead of using a single metal oxide, coupling with other metal oxide forming a heterostructure has been found to suppress the recombination of electron-hole pairs, and thus leading to remarkably enhanced photocatalytic property (Barakat et a., 2013).

It is known that both $MgFe_2O_4$ and α-Fe_2O_3 are n-type semiconductors with small bandgap (2-2.2 eV). When $MgFe_2O_4$ and α-Fe_2O_3 form heterojunction, the photogenerated electrons and holes are separated efficiently, leading to enhancement in photocatalytic activity. Recently, our group has synthesized large scale MgO nanomaterials with different morphologies with excellent adsorption property by facile chemical synthesis routes (described in chapter-5, Part-A). In this present work, we have synthesized iron based magnesium oxides, $MgFe_2O_4$ and $MgFe_2O_4$-Fe_2O_3 composite nanostructures. The synthesized nanomaterials have been used for photocatalytic degradation of methylene blue under solar light irradiation. Methylene blue dye is one of the hazardous organic dyes which exist in wastewater and causes serious environmental problem. The photocatalytic degradation of MB dye by Fe_2O_3 and $MgFe_2O_4$ nanomaterials has been reported recently (Zhang et al., 2012; Liu at al., 2011; Kang et al., 2011; Shahid et al., 2013; Shakir et al., 2016). Therefore, in order to study the improve photocatalytic performance of the prepared mixed $MgFe_2O_4$-Fe_2O_3 composite nanostructures; we have selected MB as the challenging dye.

5.6. Materials and Methods

5.6.1. Materials used

The following chemicals were used for the synthesis of magnesium oxide nanostructures and dye adsorption study. Magnesium chloride ($MgCl_2.6H_2O$) from Merck India private limited, Ammonium carbonate ($(NH_4)_2.CO_3$) from Merck India private limited, Ferrous chloride ($FeCl_2.4H_2O$) from Merck Germany pvt. Ltd. and Methylene blue from Merck India pvt. ltd. All the reagents used in the synthesis were of analytical grade and used as received without further purification.

5.6.2. Synthesis procedure

2.03 g of $MgCl_2.6H_2O$ and 1.99 g of $FeCl_2.4H_2O$ was dissolved in 100 mL of distilled water to form solution-A. 6.24 g of $(NH_4)_2CO_3$ were dissolved in 100 mL of distilled water to form solution- B. Solution-B was added instantly to solution-A with vigorous stirring. The stirring was continued for 20 min to obtained homogeneous solution. Then we have followed three different synthetic routes. The detailed synthesis procedure is schematically presented in figure 5.6.

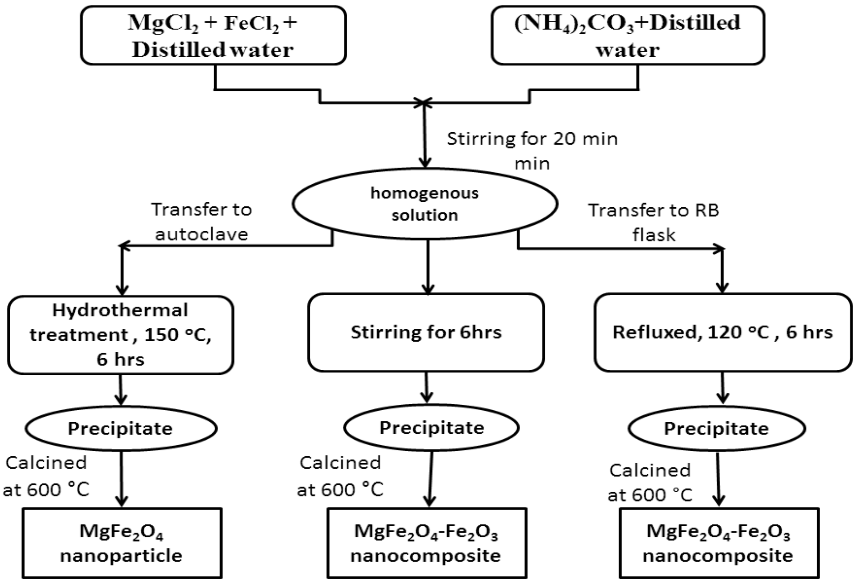

Figure 5.6 Schematic representation of the synthesis of different $MgFe_2O_4$ nanomaterials

Scheme 1: The stirring was continued for 6 h and the precipitate was filtered, washed, dried and calcined at 600° C for 3h to form $MgFe_2O_4$-Fe_2O_3 nanocomposite (named as $MgFe_2O_4$-Fe_2O_3-P). **Scheme 2:** The solution was refluxed for 6h at 120° C and then the precipitate was filtered, washed, dried and calcined at 600° C for 3h to form to form $MgFe_2O_4$-Fe_2O_3 nanocomposite (named as $MgFe_2O_4$-Fe_2O_3-R).

Scheme 3: The solution was transferred into a Teflon-lined autoclave followed by hydrothermal treatment for 6h at 150° C and then the precipitate was washed, dried and calcined at 600° C for 3h to form $MgFe_2O_4$ nanoparticles (named as $MgFe_2O_4$-H).

5.6.3. Characterization techniques: The crystalline phases of the synthesized nanomaterials were investigated by X-ray powder diffraction (XRD, Rigaku Ultima-IV). The field emission scanning electron microscopy (Nova Nano SEM/FEI, 20 kV) was performed to observe the shapes and morphologies. Fourier transforms infrared (FTIR) spectra were measured on Perkin-Elmer FTIR (Spectrum RX-I) spectrometer. N_2 adsorption-desorption isotherm was done on a Quantachrome (Autosorb-iQ) apparatus. Methylene blue (MB) photodegradation experiments were carried out under solar light irradiation. All the experiments were performed at the location of 22°15'N 84°54'E during the months of May and June (sunny days), from 09.00 AM tom 11:00 A. M., when the average solar intensity was found to be 1.0 kW m^{-2} with minimum fluctuation. Prior to photoreaction the aqueous mixture was stirred in dark for 1h to reach adsorption-desorption equilibrium. During photoreaction 3 mL of aliquot was drawn at regular time interval and centrifuged for (MB, λ_{max}=664 nm) absorbance analysis by UV-Vis spectrometer. The photocatalytic efficiency was calculated according to the following equation (Tao et al., 2013):

$$\textbf{Efficiency (\%)} = \mathbf{100} \times \left(\frac{C_0 - C_t}{C_0}\right)\% \qquad \textbf{(5.4)}$$

where C_0 and C_t were the concentrations of MB at reaction time 0 and t, respectively.

5.7. Results and discussion

5.7.1 XRD analysis: Figure 5.7a shows the XRD pattern of $MgFe_2O_4$-Fe_2O_3 nanomaterials obtained by precipitation method. The pattern contains two sets of diffraction peaks, which are ascribed to cubic $MgFe_2O_4$ according to JCPDF No: 73-1720 and rhombohedral α-Fe_2O_3 according to JCPDF No: 72-0469 to form $MgFe_2O_4$-Fe_2O_3 composite structures. Figure 5.7b shows the XRD pattern of nanoparticles obtained by reflux method. The pattern also contains diffraction peaks of cubic $MgFe_2O_4$ according to JCPDF No: 73-1720 and rhombohedral α-

Fe_2O_3 according to JCPDF No: 72-0469 to form $MgFe_2O_4$-Fe_2O_3 composite structures. But in case of nanoparticles obtained by hydrothermal method, the XRD pattern (figure 5.7c) contains only the diffraction peaks of cubic $MgFe_2O_4$ according to JCPDF No: 73-1720.

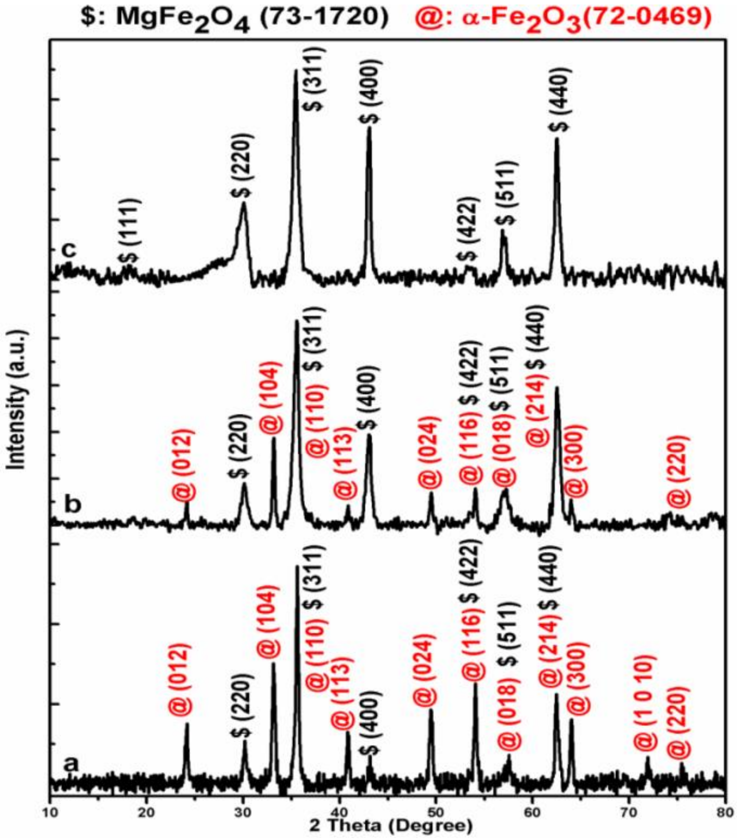

Figure 5.7 XRD patterns of (a) $MgFe_2O_4$-Fe_2O_3-P, (b) $MgFe_2O_4$-Fe_2O_3-R and (c) $MgFe_2O_4$-H.

5.7.2. FTIR analysis: Figure 5.8 shows the FTIR spectra of $MgFe_2O_4$-Fe_2O_3-P, $MgFe_2O_4$-Fe_2O_3-R and $MgFe_2O_4$-H nanomaterials. The spectrum of $MgFe_2O_4$-Fe_2O_3-P shows two persistent absorption bands of metal-oxygen bond corresponding to the vibration of tetrahedral and octahedral complexes at ν_1=573 cm^{-1} and ν_2=481 cm^{-1}, respectively. Similarly, $MgFe_2O_4$-Fe_2O_3-R shows two absorption bands of metal-oxygen bond corresponding to vibration of tetrahedral and octahedral complexes at ν_1=578 cm^{-1} and ν_2=479 cm^{-1}, respectively. Again, the FTIR spectra of $MgFe_2O_4$-H ($MgFe_2O_4$ phase) shows adsorption bands of metal-oxygen bond corresponding to vibration of tetrahedral and octahedral complexes at ν_1=567 cm^{-1} and ν_2=436 cm^{-1}, respectively. These are the evidence of formation of spinel ferrite structure. It is observed that the values of ν1 and ν2 of $MgFe_2O_4$-Fe_2O_3 composites are increased compared with single $MgFe_2O_4$. This is due to the redistribution or inversion of cations among A- and B-site of $MgFe_2O_4$ after the incorporation of α-Fe_2O_3 (Shen et al., 2012).

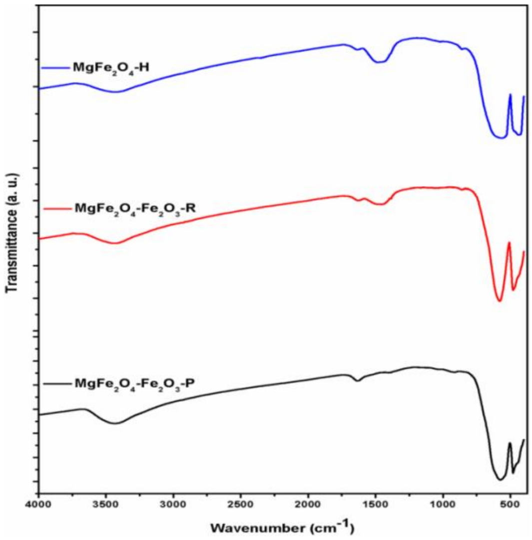

Figure 5.8 FTIR patterns of MgFe$_2$O$_4$-Fe$_2$O$_3$-P, MgFe$_2$O$_4$-Fe$_2$O$_3$-R and MgFe$_2$O$_4$-H.

5.7.3. Surface area and porosity analysis: The N$_2$ adsorption-desorption isotherm and pore size distribution are shown in Figure 5.9. From figure 5.9a, it is observed that the BET surface area of MgFe$_2$O$_4$-Fe$_2$O$_3$-P, MgFe$_2$O$_4$-Fe$_2$O$_3$-R and MgFe$_2$O$_4$-H are 67, 36 and 50 m^2/g, respectively. From BJH curve (figure 5.9b), the corresponding pore diameters are found to be 6.5, 5.6 and 4.8 nm.

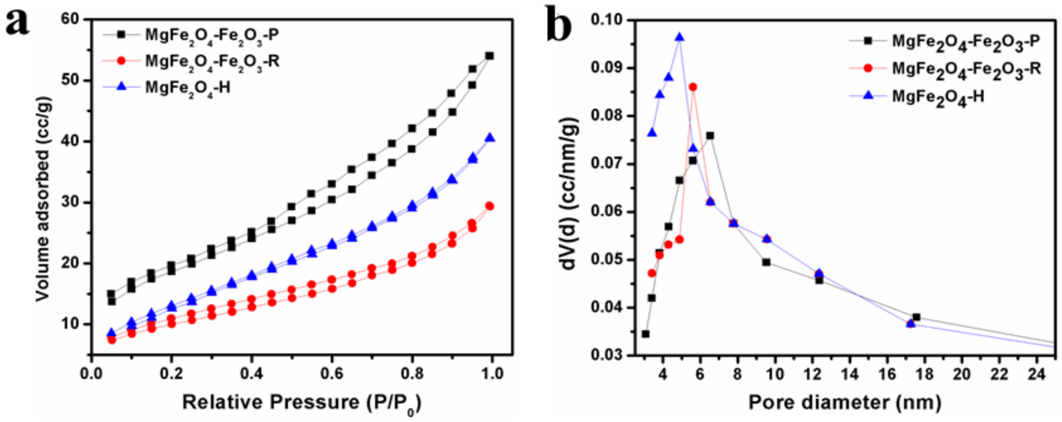

Figure 5.9 (a) N$_2$ adsorption/desorption isotherms and (b) pore-size distribution of MgFe$_2$O$_4$-Fe$_2$O$_3$-P, MgFe$_2$O$_4$-Fe$_2$O$_3$-R and MgFe$_2$O$_4$-H.

5.7.4. Surface Morphology and microstructure: Figure 5.10a, a' represents the FESEM images of MgFe$_2$O$_4$-Fe$_2$O$_3$ nanocomposites synthesized by precipitation method. The images suggest the formation of very smooth and fine spherical nanoparticles with average diameters around 20-40 nm. The FESEM images of MgFe$_2$O$_4$-Fe$_2$O$_3$ nanocomposites synthesized by reflux method are shown in figure 5.10b, b'. The low-magnified FESEM image (figure 5.10b) demonstrates the formation of both uniform microspheres and flower-like hierarchical nanostructures. The high-magnified FESEM image (figure 5.10b') represents that the hierarchical nanostructures contains plate like morphology with thickness around 100-200 nm. Figure 5.10c, c' represents the FESEM images of $MgFe_2O_4$ nanomaterials synthesized by hydrothermal method. The images indicate the formation of irregular shaped nanoparticles with diameter around 60-100 nm. The energy-dispersive x-ray spectroscopy (EDS) spectrum of $MgFe_2O_4$-Fe_2O_3 nanocomposites synthesized by precipitation method (Figure 5.10d) demonstrates the presence of O, Fe and Mg elements without any impurities.

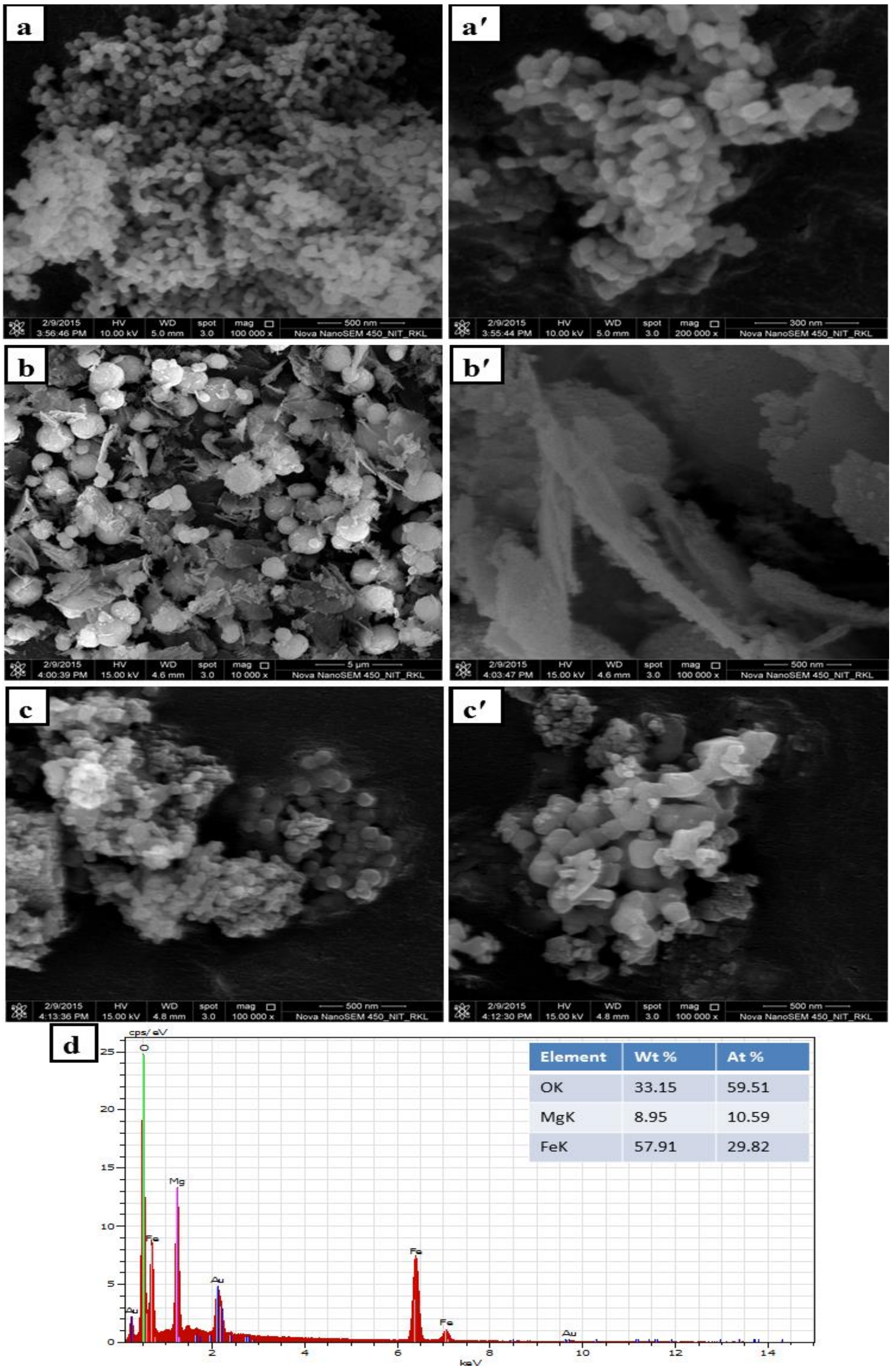

Element	Wt %	At %
OK	33.15	59.51
MgK	8.95	10.59
FeK	57.91	29.82

Figure 5.10 Low and high magnification FESEM images of (a, a') $MgFe_2O_4$-Fe_2O_3-P, (b, b') $MgFe_2O_4$-Fe_2O_3-R, (c, c') $MgFe_2O_4$-H and (d) EDS of $MgFe_2O_4$-Fe_2O_3-P.

5.7.5. Effect of types of photocatalysts: The effect of photocatalyst types on degradation of MB was evaluated by adding 0.1 g each photocatalyst powder into 100 mL of 10 mg/L MB solution. From figure 5.11, it is observed that 99.9% dye degradation occurred within 120 min of reaction time using $MgFe_2O_4$-Fe_2O_3-P photocatalyst. For $MgFe_2O_4$-Fe_2O_3-R, around 89.1 and 93.8% dye degradation occurred within 120 and 150 min of reaction time, respectively. Similarly, for $MgFe_2O_4$-H, around 93.2 and 96.7% dye degradation occurred within 120 and 150 min of reaction time, respectively. The $MgFe_2O_4$-Fe_2O_3-P photocatalyst shows better degradation capacity than other two photocatalysts. It may be due to the combined effects of high surface area (very smooth and smallest nanoparticles) and heterojunction nanostructure. In case of $MgFe_2O_4$-Fe_2O_3-R, although it possess heterojunction nanostructure but due to less surface area and higher particle size than $MgFe_2O_4$-H, its photocatalytic activity is comparatively lesser than $MgFe_2O_4$-H. We have chosen $MgFe_2O_4$-Fe_2O_3-P composite nanostructure for further photocatalytic study by varying initial dye concentration.

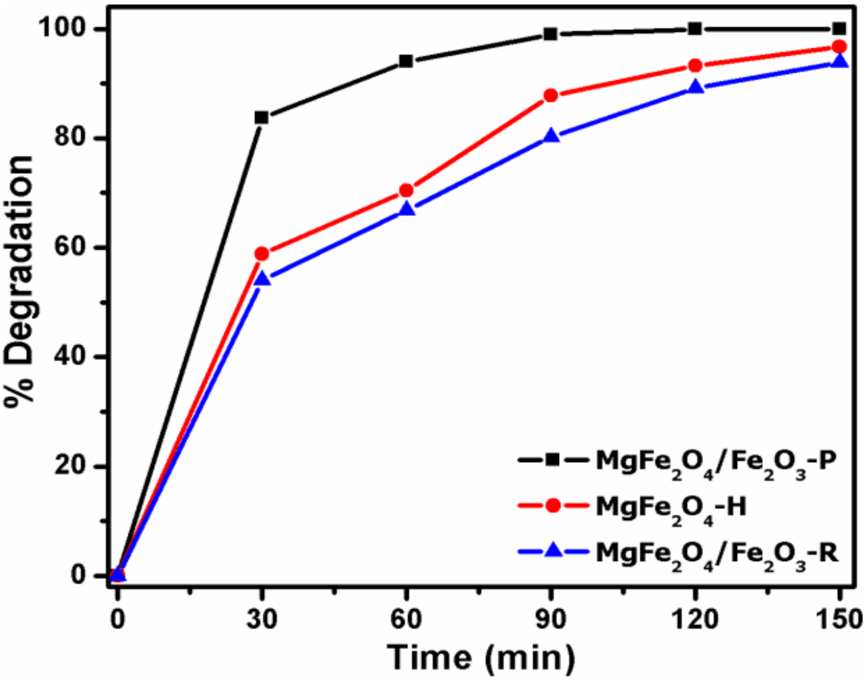

Figure 5.11 Percentage of degradation of 10 mg/L MB using the three catalysts.

5.7.6. Effect of initial concentration of MB: The effect of initial concentration of MB dye on degradation was examined using 100 mL of 5-25 mg/L of MB using 0.1 g of $MgFe_2O_4$-Fe_2O_3-P photocatalyst for 120 min irradiation time. It is observed from figure 5.12 that the degradation efficiency was gradually decreased with increase in dye concentration and around 97% degradation was occurred within 120 min for 25 mg/L MB. The primary factor controlling the degradation of MB is the formation of hydroxyl radicals on catalyst surface and interaction of such radicals with dye species. With increasing initial concentration, much more dye molecules are adsorbed on catalyst surface, and hence the generation of hydroxyl radicals would be reduced. As a result, the photodegradation efficiency decreased. Again, due to a high concentration of dye a shielding effect for light passing into solution is attained, which reduced the absorption of photons by catalyst, and thus the hydroxyl radicals formed on catalyst surface would decrease (Harraza et al., 2014).

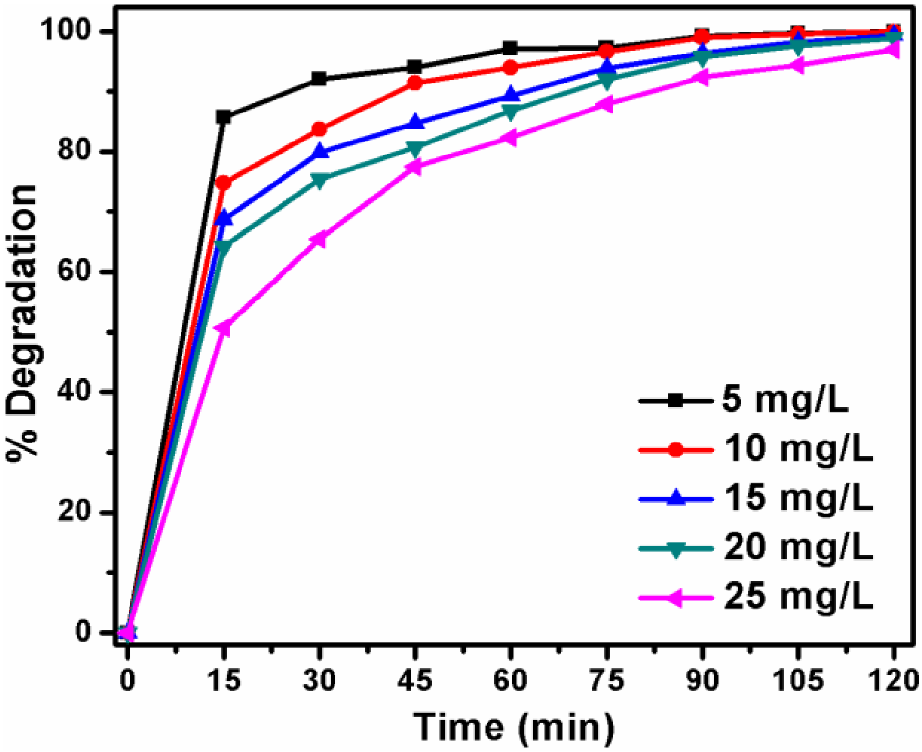

Figure 5.12 Percentage of degradation of 5-25 mg/L MB using $MgFe_2O_4$-Fe_2O_3-P.

5.7.7. Kinetics study: The apparent rate constant (k_{app}) has been chosen as the basic kinetics parameter for all the photocatalytic reaction. The k_{app} arises from the Langmuir–Hinshelwood first-order kinetics equation as (Muthirulan et al., 2013):

$$\ln\left(\frac{C_0}{C_t}\right) = kKt = k_{app}t \tag{5.5}$$

where k is the reaction rate constant (min^{-1}), K is the adsorption coefficient of dye on a catalyst particle ($L\ mol^{-1}$) and K_{app} is the apparent rate constant. Figure 5.13a, b shows the graph of $\ln(C_0/C_t)$ vs t for various photocatalysts and various concentrations. The apparent rate constants, % degradation and correlation coefficients for all photoreactions are given in table 5.3. The plots show a linear relationship with good correlation coefficient ($R^2>0.947$), indicating that the MB degradation is best fit to the above kinetic model.

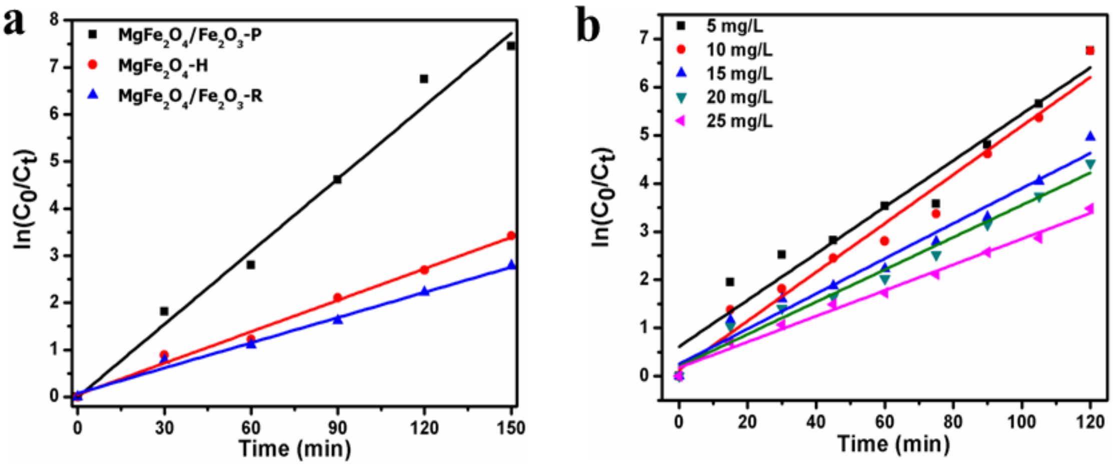

Figure 5.13 Pseudo-first-order kinetics of (a) the three catalysts for 10 mg/L MB, (b) $MgFe_2O_4$-Fe_2O_3-P for 5-25 mg/L MB.

Table 5.3 Percentage of degradation and pseudo-first-order kinetic parameters of MB dye

Photocatalysts/MB concentration (mg/L)	**Degradation (%)**	**K_{app} (min^{-1})**	**R^2**
$MgFe_2O_4$-Fe_2O_3-P/10	99.88	0.052	0.967
$MgFe_2O_4$-Fe_2O_3-R/10	89.15	0.018	0.989
$MgFe_2O_4$-H/10	93.23	0.022	0.991
$MgFe_2O_4$-Fe_2O_3-P/5	99.89	0.048	0.947
$MgFe_2O_4$-Fe_2O_3-P/15	99.30	0.036	0.968
$MgFe_2O_4$-Fe_2O_3-P/20	98.80	0.034	0.977
$MgFe_2O_4$-Fe_2O_3-P/25	96.92	0.027	0.986

5.7.8. Reusability study: The reusability and stability of photocatalysts is an important issue for practical applications. We have repeated the degradation of 10 mg/L MB solution four times using $MgFe_2O_4$-Fe_2O_3-P and the result is shown in figure 5.14. As can be seen, the repeatability of the entire process and the final result of degradation of MB are very good, which further demonstrate the excellent efficiency of the photocatalyst.

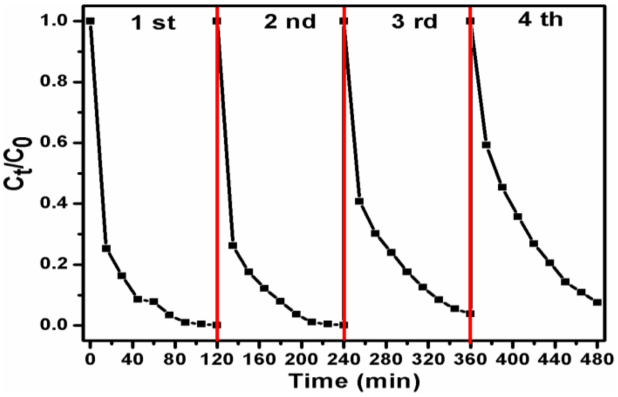

Figure 5.14 Four recycling runs of $MgFe_2O_4$-Fe_2O_3-P for MB degradations.

Photocatalytic mechanism: Heterojunction is the main reason of enhanced photocatalytic activity of $MgFe_2O_4$-Fe_2O_3-P nanocomposite. The photocatalytic processes are based on electron hole pairs generated from band gap excitation. The photoinduced electron-hole pairs migrate on the surface of the photocatalyst to react with the adsorbed reactants in the desired process, or undergo an undesired recombination. Therefore, the generation and separation of the electron-hole pairs are the key factors to influence a photocatalytic reaction. In order to explain the possible transfer mechanism of photogenerated charge carriers in $MgFe_2O_4$-Fe_2O_3-P, an energy band diagram of $MgFe_2O_4$-Fe_2O_3 has been proposed in figure 5.15. When the $MgFe_2O_4$ is excited by solar light with photon energy higher than its band gap, the electrons in the valence band (VB) move to the conduction band (CB) generating equal amounts of holes in VB. The photogenerated electrons are migrated from CB of $MgFe_2O_4$ to CB of α-Fe_2O_3 forming different valence bond edges. Which inhibits electron-hole recombination: as a result the electron-hole pairs react with the adsorbed dye molecules.

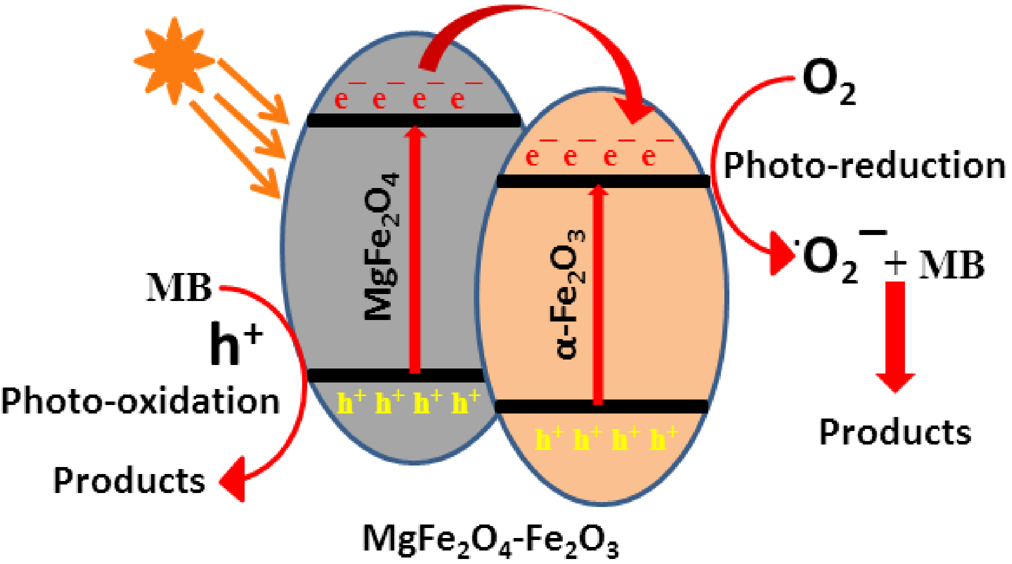

Figure 5.15 Proposed mechanism of photo-reaction.

5.8. Conclusions

We have synthesized $MgFe_2O_4$-Fe_2O_3 composite nanostructures by precipitation and reflux methods and $MgFe_2O_4$ nanostructure by hydrothermal method. XRD suggests the well crystalline nature of the nanomaterials with appropriate phase. FESEM images suggest that the $MgFe_2O_4$-Fe_2O_3 nanocomposites prepared by precipitation method contains very smooth nanoparticles with average diameters around 20-40 nm. However, the $MgFe_2O_4$-Fe_2O_3 nanocomposite prepared by reflux method contains both uniform microspheres and flower-like hierarchical nanostructures. The $MgFe_2O_4$ nanomaterials synthesized by hydrothermal method contains irregular shaped nanoparticles with diameter around 60-100 nm. These prepared nanomaterials were used as photocatalysts for degradation of Methylene blue under solar light irradation. It was observed that the $MgFe_2O_4$-Fe_2O_3 nanocomposites prepared by precipitation method shows enhanced photocatalytic activity compared to the other prepared photocatalysts.

CHAPTER-6

ONE-DIMENSIONAL Fe_2O_3-CuO NANOCOMPOSITES: SYNTHESIS, CHARACTERIZATION AND PHOTOCATALYTIC DEGRADATION OF METHYL ORANGE

6.1. Introduction

Metal oxide based semiconductor photocatalysis is considered as one of the most promising green technologies for environmental remediation due to its potential utilization of solar energy for purification of water and air (Xie et al., 2014; Yuan et al., 2014; Zhao et al., 2015; Lv et al., 2014; Wang et al., 2015). It is the facile, cheap and non-toxic natural light-induced catalytic method for decontamination of inorganic and organic pollutants from waste water. The process involves the complete mineralization of the contaminant molecules into carbon dioxide, water and mineral acids. The contaminant molecules reduced through redox reactions and include generation of electron-hole pairs on the surface of a metal oxide photocatalyst by the absorption of photons from a light source and its subsequent loss to an adsorbed molecule. Unlike other methods, this technique does not result the formation of secondary contaminants (Yan et al., 2013; Danwittayakul et al., 2013; Bhattacharjee et al., 2014).

Utilization of renewable solar energy and development of efficient visible light-driven photocatalyst has become one of the most significant topics of research recently. A large number of reports are there on the photocatalytic degradation of organic contaminants/dyes under solar light irradiation by using various metal oxide photocatalysts such as: Fe_2O_3 (Mahadik et al., 2013; Zhang et al., 2013; Bharadwaj et al., 2012), $BiFeO_3$ (Soltani et al., 2013), Cu_2O (Ma et al., 2010), TiO_2 (Kang et al., 2013; Chowdhury et al., 2012), ZnO (Sobana and Entezari, 2013), CuO (Mukherjee et al., 2011) and so on. However, the photocatalytic efficiency is suppressed by the rapid recombination rate and long migration distance of the photo-generated charge carriers. Therefore, designing and exploring photocatalysts with higher efficiency has attracted recent research efforts in the field of photo-catalysis (Hana et al., 2014). Use of heterogeneous/composite semiconductors can reduce the recombination rate of photo-generated electrons and holes and can be widely employed for improved photocatalytic efficiency. The formation of p-n heterojunctions in heteronanostructures can separate the photogenerated electron–hole pairs. This is mainly because of the inherent establishment of the internal electric field directed from the n-type to p-type semiconductor (Han et al., 2013; Liu et al., 2015; Kumar et al., 2014).

We emphasize on the development of novel low cost solar light sensitive photocatalyst with excellent photo-degradation ability and universality for decomposing various organic pollutants. Among all other metal oxides, iron oxides are considered technologically important catalytic materials, sorbents, pigments, flocculants, coatings, gas sensors and ion exchangers. Iron oxide-based catalysts have been found to be good candidates as cheap and efficient catalysts, especially in environmental catalysis (Cao et al., 2008). Similarly, copper oxide (CuO) is a low cost, low toxicity and highly available metal oxide with band gap energy near visible light (Batista et al., 2010).

A valuable approach to further engineer Fe_2O_3 properties consists in its surface modification or hybrid metal oxide composite formation by coupling with other metal oxide. Among the various possible options, an attractive choice is CuO, a biocompatible and inexpensive semiconductor oxide capable with a advantageous photocatalytic reactivity. The present work is an attempt to prepare rod shaped Fe_2O_3-CuO nanocomposite by thermal decomposition of oxalate precursor; which is an economical and facile solution state route. The prepared nanocomposites were used as novel photocatalyst under solar light that can decompose methyl orange, a carcinogenic dye, from aqueous solution. Methyl orange (an anionic azo dye) is one of the most important synthetic dye that has been widely used in textiles, foodstuffs, paper, and leather industries. The release of MO and its products in the environment cause harmful effects on human beings: it may cause eye or skin irritation, or inhalation may cause gastrointestinal irritation with nausea, vomiting, and diarrhea (Parida et al., 2008). From various recently letratures, we have found that Fe_2O_3 and CuO nanomaterials are used as effective photocatalysts for degradation of methyl orange from aqueous system (Li et al., 2012; Sathyamoorthy and Mageshwari, 2013; Cao and Zhu, 2008; Zhou et al., 2009; Xie at al., 2009; Sharma et al., 2014). Hence, for further evaluation of the photocatalytic activity of prepared Fe_2O_3-CuO nanocomposite under solar light irradiation we have choosen methyl orange as the model organic dye in this work.

6.2. Materials and methods

6.2.1. Materials

Ferrous sulphate heptahydrate ($FeSO_4.7H_2O$), copper chloride dihydrate ($CuCl_2.2H_2O$), oxalic acid dihydrate ($H_2C_2O_4.2H_2O$), cetyltrimethyl ammonium bromide (CTAB), ethanol, and Methyl orange were procured from Merck India. All the chemicals were used as received without any further purification.

6.2.2. Synthesis of α-Fe_2O_3-CuO nanocomposite

α-Fe_2O_3-CuO nanocomposite were synthesized by a simple co-precipitation method using $FeSO_4.7H_2O$ and $CuCl_2.2H_2O$ as salt precursor, CTAB as structure directing agent and ethanol and double distilled water as solvent. For the preparation of α-Fe_2O_3-CuO nanocomposite, 0.7 g (2.5 mmol) of $FeSO_4.7H_2O$ and 0.43 g (2.5 mmol) of $CuCl_2.2H_2O$ were dissolved in distilled water with vigorous stirring to form solution-I and 0.63 g of oxalic acid and 0.5 g of CTAB were dissolved in ethanol with vigorous stirring to form solution-II. Then, solution-I was added drop wise to solution-II with continuous stirring to form yellowish green precipitate. After addition the stirring was continued for another 5 hours. Then, the precipitate obtained was centrifuged, washed thoroughly by ethanol and double distilled water and dried at 80 ^oC for 2 hours to form ferrous oxalate-copper oxalate nanorods. The obtained composite nanorod was calcined at 500 ^oC with heating rate 10 ^oC/min for 2 hours to form α-Fe_2O_3-CuO composite nanorods. For comparison, α-Fe_2O_3 and CuO samples were also prepared using the same method by using $FeSO_4.7H_2O$ and $CuCl_2.2H_2O$ as salt precursors and keeping reaction the other conditions same as that of α-Fe_2O_3-CuO nanocomposite synthesis.

6.2.3. Characterization techniques

The surface morphology of the prepared composite materials was characterized by a Nova Nano SEM 450 Field Emission *s*canning electron microscopy (FE-SEM) operated at an acceleration voltage of 15 and 20 kV. The size of the particle and selected area electron diffraction (SAED) pattern of the α-Fe_2O_3-CuO nanocomposite was observed using a high resolution transmission electron microscope (JEM-2100 HRTEM, Make-JEOL, Japan) with an acceleration voltage of 200 kV. The phases were identified by means of X-ray diffraction (XRD) by a Rigaku Ultima-IV X-ray diffractometer using Cu Kα radiation ($\lambda = 1.54156\ ^oA$) at a scan rate of 5^o/min. FTIR spectra were recorded using Perkin-Elmer FTIR (Spectrum RX-I) spectrophotometer. X-ray photoelectron spectroscopy (XPS) was determined using a VG Scientific ESCA LAB Mk-II Spectrometer with Al Kα radiation (1486.6 eV) at a takeoff angle at 45°. The UV-Visible absorbance spectra of the sample were recorded using Shimadzu spectrometer (model 2450) with $BaSO_4$ coated integration sphere in the range of 200-800 nm.

6.2.4. Photocatalytic degradation study

The photodegradation efficiency of all synthesized catalysts was tested towards degradation of Methyl orange (MO) under natural solar light radiation. Initially a stock solution of 1 g/L was prepared by dissolving 1 g of MO in 1000 ml of double distilled water. In a typical experiment, 0.1 gm of catalyst was added to 100 ml of 20 mg/L MO solution in a 250 ml of beaker. Before irradiation, the suspension was magnetically stirred in dark for 2 hour to ensure the establishment of the adsorption/desorption equilibrium of the dye onto the surface of photocatalysts. Afterwards the solution was exposed to natural sunlight with continuous stirring. All the experiments were performed at the location of 22°15'N 84°54'E during the months of December and January (sunny days), from 11:00 AM to12:30 PM, when the average solar intensity was 0.25 kW m^{-2} with minimum fluctuation. During photoreaction 3 ml of the suspension was collected at 15 min time interval and centrifuged to remove the particles. After that, the MO concentration of the solution was analyzed by UV–VIS spectrometer (Shimadzu spectrometer, model-2450) at its maximum adsorption wavelength (λ_{max}) of 463 nm. This process was repeated till the complete degradation of dye from the aqueous solution. The percentage of degradation of MO was calculated by the following equation (Dong et al., 2014):

$$\textbf{Percentage of degradation} = \mathbf{100} \times \left(\frac{C_0 - C_t}{C_0}\right)\% \qquad \textbf{(6.1)}$$

where C_0 and C_t were the concentration of MO when reaction time was 0 and t and A_0 and A_t were the absorbance of MO when reaction time was 0 and t, respectively.

6.3. Results and discussion

6.3.1. Characterization of photocatalysts

The surface morphology and size of the nanocomposite photocatalysts were analyzed by FESEM and TEM. Figure 6.1 shows the SEM and high magnification FESEM (inset) images of α-Fe_2O_3, CuO, and α-Fe_2O_3-CuO nanocomposite and TEM and SAED patterns of α-Fe_2O_3-CuO nanocomposite. Figure 6.1a represents the SEM and FESEM images of the as-synthesized α-Fe_2O_3 nanorods. The nanorods have smooth surfaces with the diameter in the range of 100-200 nm and the length up to micrometers. The SEM and FESEM images of CuO nanoparticles are shown in figure 6.1b; which indicate very fine spherical shaped particles with particle diameter in the range of 30-40 nm. Figures 6.1c, d represent SEM, FESEM and TEM images of α-Fe_2O_3-CuO nanocomposites. From the figures it is observed that, there are numerous spherical CuO nanoparticles decorated on the surface of the α-Fe_2O_3

nanorods. These nanoparticles are uniformly distributed. The spherical nanoparticles of CuO are attached to the α-Fe_2O_3 nanorods and oriented along one-dimensional direction to form α-Fe_2O_3-CuO composite nanorods. The SAED pattern taken from (given in figure 6.11d) shows bright diffraction sports, due to high crystalline nature of the nanocomposite.

Figure 6.2 shows the SEM-EDS spectra of the prepared photocatalysts. The spectrum of α-Fe_2O_3 indicates the presence of Fe and O elements, spectrum of CuO indicates the presence of Cu and O elements, while the spectrum of composite α-Fe_2O_3-CuO indicates the presence of Fe, Cu and O elements. No other elements present in the spectrum besides Pt (which is used for coating). This indicates the prepared nanomaterials are highly pure.

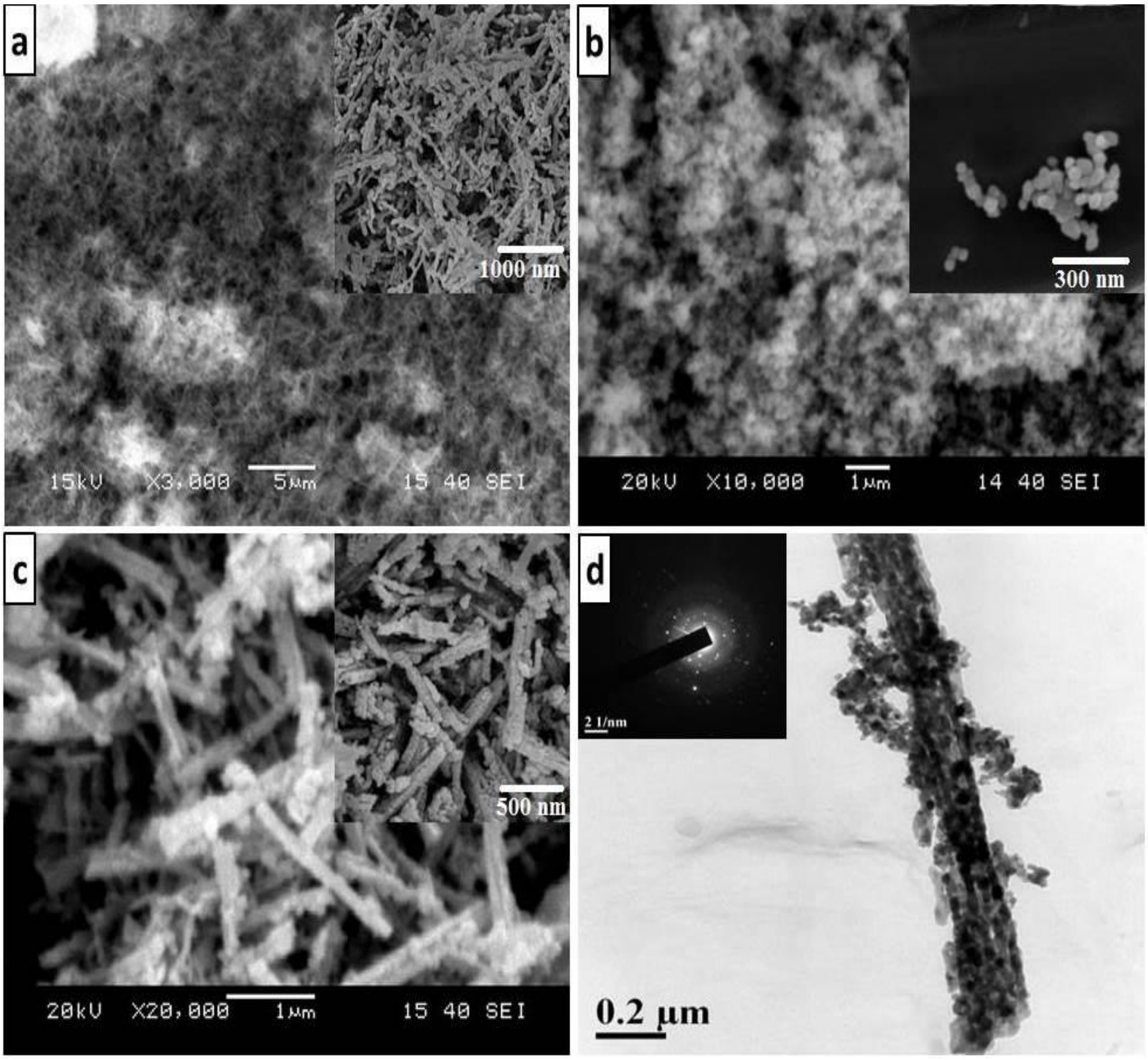

Figure 6.1 SEM and FESEM images of a) α-Fe_2O_3 nanorod, b) CuO nanoparticles and c) α-Fe_2O_3-CuO nanocomposite, d) TEM image and SAED patterns of α-Fe_2O_3-CuO nanocomposite.

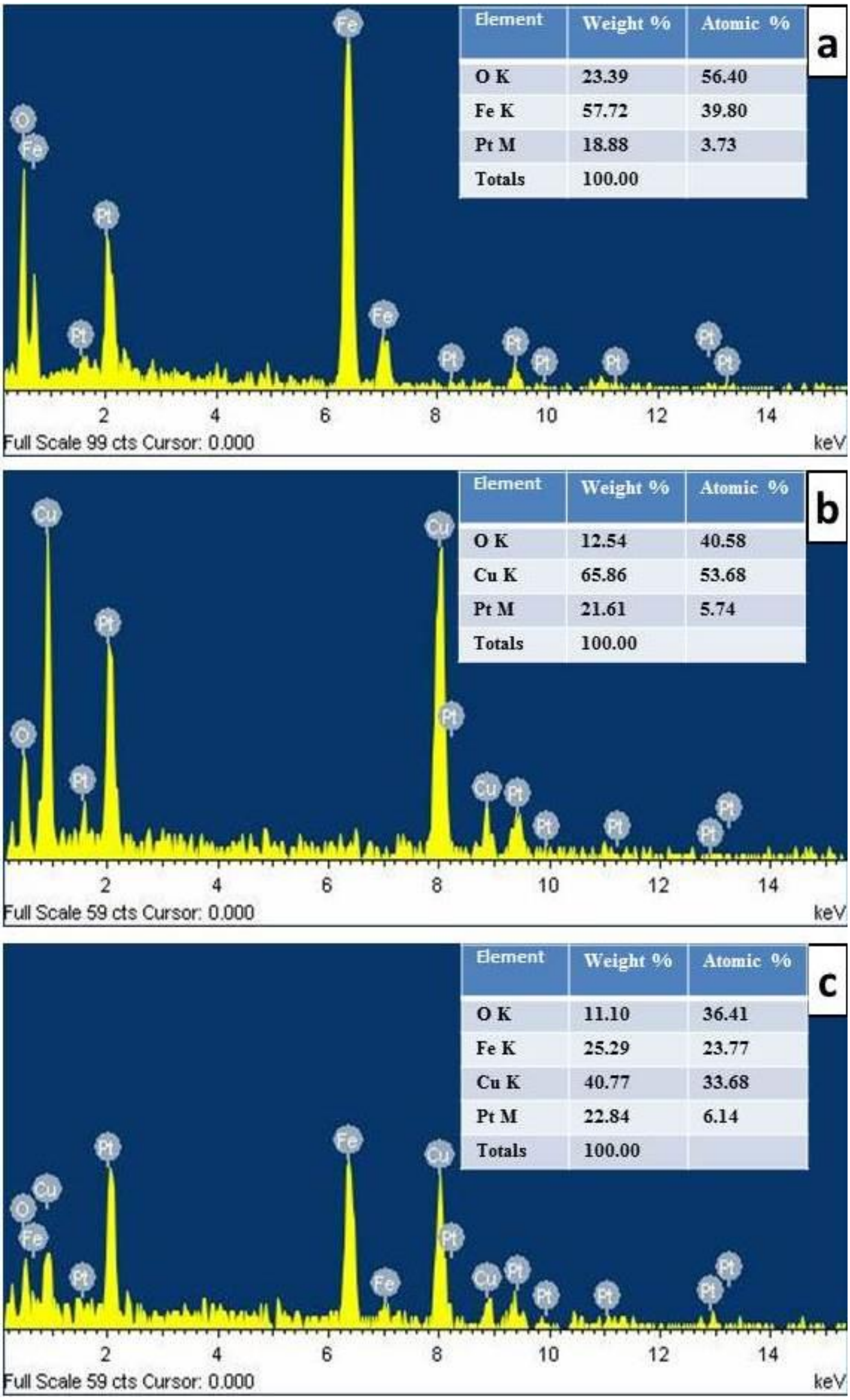

Element	Weight %	Atomic %
O K	23.39	56.40
Fe K	57.72	39.80
Pt M	18.88	3.73
Totals	100.00	

Element	Weight %	Atomic %
O K	12.54	40.58
Cu K	65.86	53.68
Pt M	21.61	5.74
Totals	100.00	

Element	Weight %	Atomic %
O K	11.10	36.41
Fe K	25.29	23.77
Cu K	40.77	33.68
Pt M	22.84	6.14
Totals	100.00	

Figure 6.2 EDAXs of (a) α-Fe_2O_3 nanorods, (b) CuO nanoparticles and (c) α-Fe_2O_3-CuO nanocomposite.

Figure 6.3 represents the XRD patterns of as prepared $FeC_2O_4.2H_2O$, $CuC_2O_4.xH_2O$, and $FeC_2O_4.2H_2O$-$CuC_2O_4.xH_2O$ along with calcined α-Fe_2O_3, CuO, and α-Fe_2O_3-CuO nanocomposite. The XRD pattern in figure 6.3a contains the characteristics peaks of ferrous oxalate dihydrate ($FeC_2O_4.2H_2O$) and can be index to orthorhombic crystal structure according to JCPDS No: 22-0635. Figure 6.3b contains the characteristics peaks of copper oxalate hydrate ($CuC_2O_4.xH_2O$) and can be index to orthorhombic crystal structure according to JCPDS No: 21-0297. Similarly, the composite sample (figure 6.3c) contains characteristics peaks of both $FeC_2O_4.2H_2O$ and $CuC_2O_4.xH_2O$. The XRD patterns of 500 °C calcined samples are shown in figure 6.3d-f. All diffraction peaks in figure 6.3d, and 6.3e are in good agreement with those of the standard patterns of rhombohedral α-Fe_2O_3 (JCPDS No: 79-0007) and monoclinic CuO (JCPDS Card No. 05-0661), respectively. Figure 6.3f represents two sets of diffraction peaks for the α-Fe_2O_3-CuO sample, which are correspondingly ascribed to rhombohedral α-Fe_2O_3 and monoclinic CuO. All the X-ray diffractograms well defined, revealing the well-crystalline character of the samples. The broadening of the peaks also indicates the decrease in the diameter and an increase in the surface area to volume ratio of the compounds.

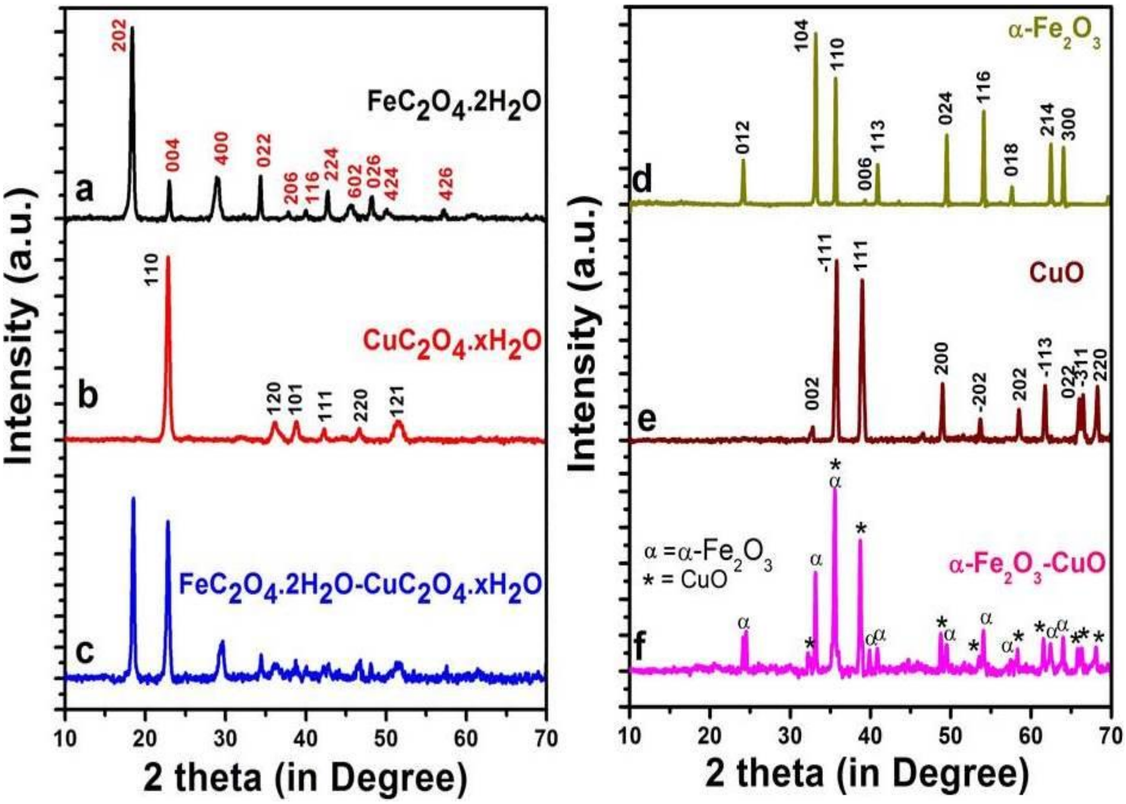

Figure 6.3 X-ray diffraction patterns of (a) $FeC_2O_4.2H_2O$, (b) $CuC_2O_4.xH_2O$, (c) $FeC_2O_4.2H_2O$-$CuC_2O_4.xH_2O$, (d) α-Fe_2O_3 nanorods, (e) CuO nanoparticles and (f) α-Fe_2O_3-CuO nanocomposite.

To investigate the chemical binding states of the α-Fe_2O_3-CuO nanocomposite, the XPS analysis was performed. Figure 6.4a shows the general survey spectrum of the nanocomposite, which reveals that the surface of the sample contains Fe, Cu, O and C elements. The chemical states of Fe and Cu were determined from Fe2p and Cu2p peaks, respectively. The high-resolution XPS spectra (figure 6.4b–d) of the mixed metal oxide show the presence of Cu 2p, Fe 2p and O 1s peaks. In figure 6.4b the peaks at about 956.05 and 934.27 eV are attributed to Cu $2p_{1/2}$ and $Cu2p_{3/2}$, respectively. Along with the two peaks of, the existence of strong shake-up features for Cu (2p) are the major XPS characteristics of CuO. Figure 6.4c displays the electron binding energies of 714.9 and 728.1 eV, which are due to the presence of Fe $2p_{3/2}$ and $Fe2p_{1/2}$, respectively and a satellite at 720.6 eV. These parameters correspond to the Fe^{3+} surface species in α-Fe_2O_3 (Cao et al., 2008; Liu et al., 2009). The O 1s region (Figure 6.4d) can be deconvoluted into two peaks at about 533.6 and 535.5 eV, which indicates the existence of two different oxygen species. The XPS studies confirmed the existence of independent species of Fe_2O_3 and CuO in the composite.

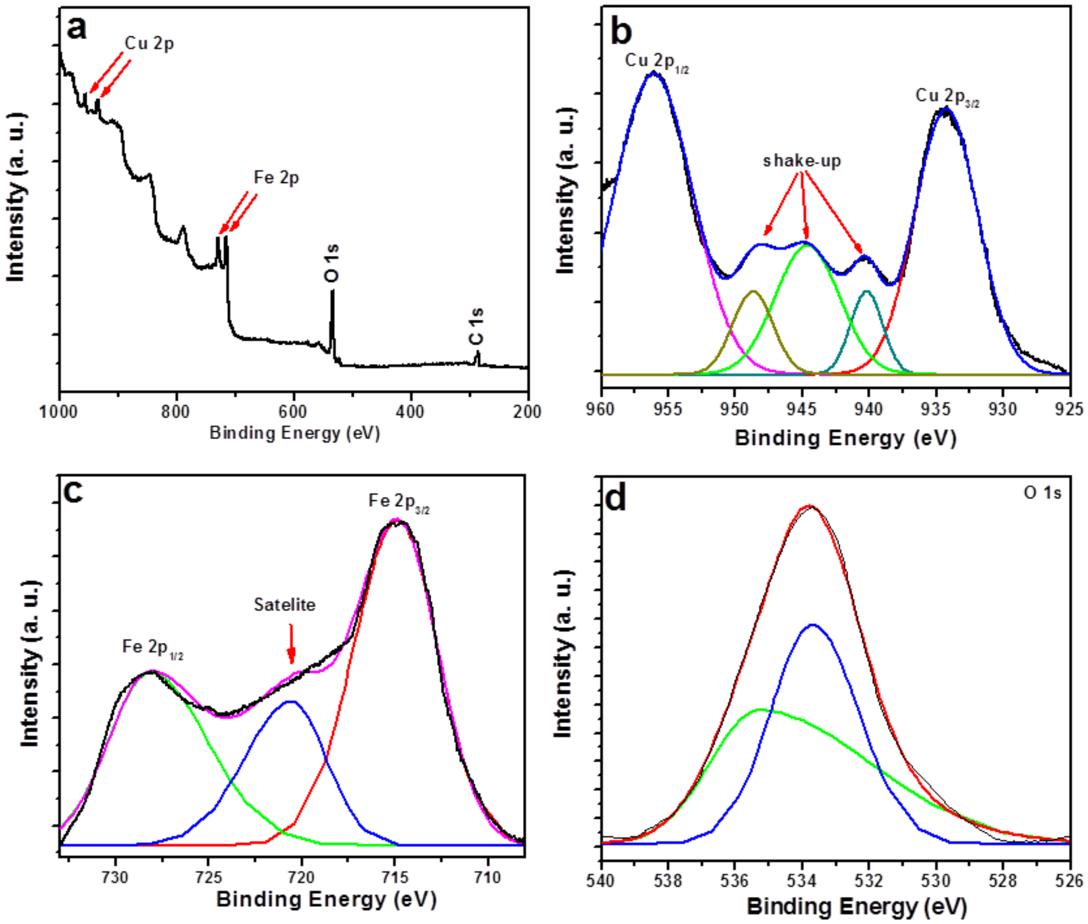

Figure 6.4 (a) XPS pattern of α-Fe_2O_3-CuO nanocomposites and high resolution XPS of (b) Cu2p, (c) Fe2p and O 1s core levels of α-Fe_2O_3-CuO nanocomposite.

The UV-vis absorption behavior of the prepared nanomaterials was analyzed due to their potential application in photo-irradiation. The optical absorption property and migration of the light-induced electrons and holes of a semiconductor are the key factors in determining its photo-catalytic activity (Hou et al., 2012). Figure 6.5a shows the UV-visible absorption spectra for α-Fe$_2$O$_3$, CuO and α-Fe$_2$O$_3$-CuO nanocomposites. For α-Fe$_2$O$_3$, absorption bands at 548 and 377 nm corresponding to the ligand-free ($^6A_1 \rightarrow {}^4E_g$) and a ligand-to-metal charge transfer ($6t_{1u} \rightarrow 2t_{2g}$) transitions, respectively (Sivula et al., 2010). The steep shape of the absorption between 750 and 950 nm in case of CuO indicates that the light absorption is due to the intrinsic band-gap transition (Mageshwari et al., 2012). At lower wavelength, adsorption peaks are distinguished between 250 nm to 300 nm due to O^{2-} to Cu^{2+} charge-transfer transitions (Prasetyanto et al., 2007). In case of α-Fe$_2$O$_3$-CuO nanocomposites, in addition to the peaks of α-Fe$_2$O$_3$, steep shape of the absorption between 850 and 950 nm is observed. Figures 6.5b-d show the plot of the hν vs $(F(R)h\nu)^2$ for different composite oxides. The direct band gap energy (Eg) is calculated from the abscise interception. The band gap values of α-Fe$_2$O$_3$, CuO and α-Fe$_2$O$_3$-CuO are 2.12, 1.47 and 1.85 eV respectively.

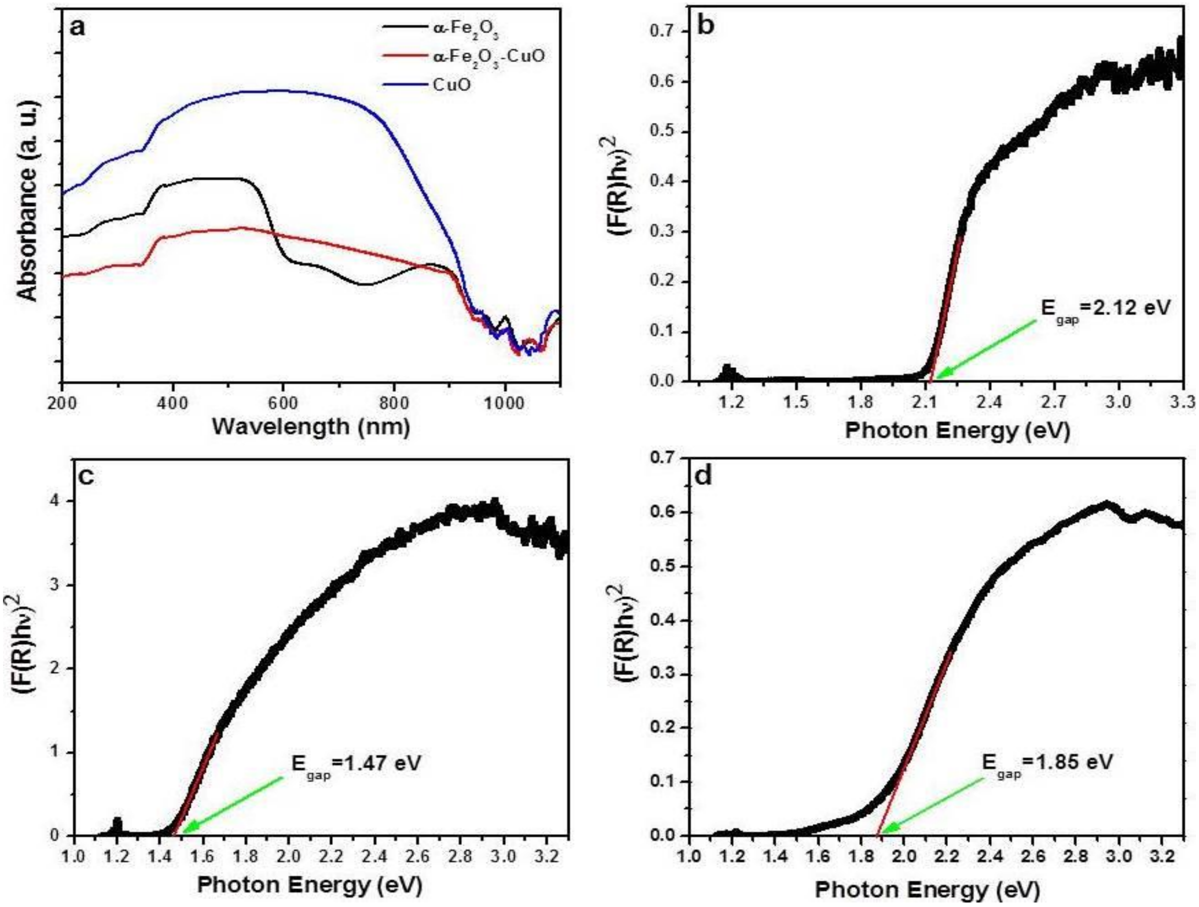

Figure 6.5 (a) Optical absorbance spectra and calculated band-gap energy of (a) α-Fe$_2$O$_3$ nanorods, (b) CuO nanoparticles and (c) α-Fe$_2$O$_3$-CuO nanocomposite.

6.4. Photocatalytic degradation of MO in natural sunlight

The catalytic activity of the prepared photocatalysts was evaluated by heterogeneous degradation of methyl orange (MO) wastewater under natural solar light irradiation. All the experiments were conducted under following conditions: MO concentration 20 mg/L and catalyst concentration 1 g/L. The UV-Vis spectra of MO aqueous solution in the process of photodegradation are displayed figure 6.6a-c. From the figure it is observed that, the absorbance at 463 nm of MO diminishes gradually with time elapsed: which indicates the reduction of MO from orange to colorless. The absorption peak completely disappeared in 90 min in the presence of α-Fe_2O_3-CuO nanocomposite as photocatalyst. The photograph of MO solution before and after solar light irradiation is given in figure 6.6d, which also confirms the complete degradation of the MO in 90 min.

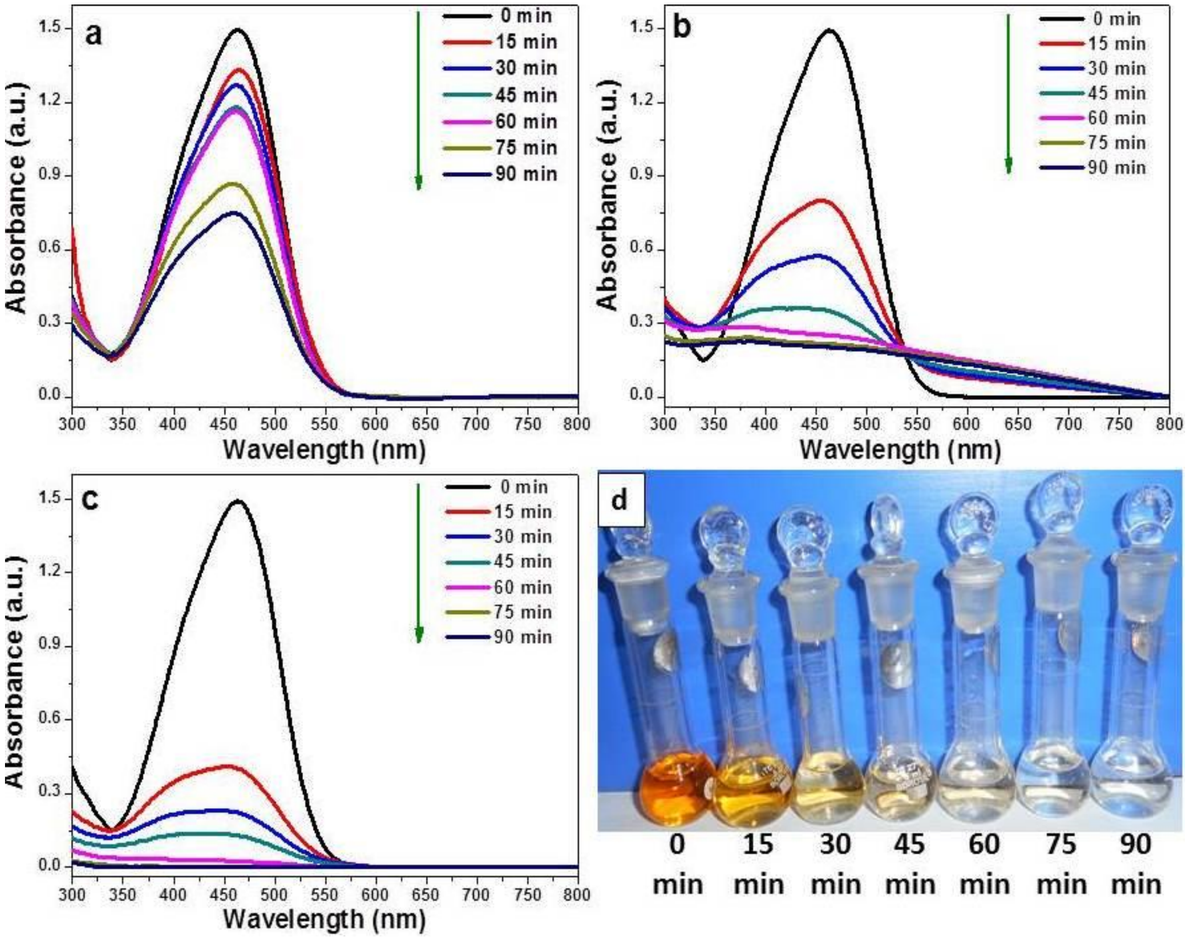

Figure 6.6 UV–visible absorption spectra showing the temporal evolution of the degradation of MO upon sun-light irradiation using (a) α-Fe_2O_3 nanorods, (b) CuO nanoparticles and (c) α-Fe_2O_3-CuO nanocomposite and (d) Optical image of the degradation of MO with the increase of time using α-Fe_2O_3-CuO nanocomposite photocatalyst.

Figure 6.7 shows the percentage of degradation of MO with time. For the photocatalytic experiments, prior to solar light irradiation, the adsorption properties of the phtocatalysts were initially studied. Prior to solar light irradiation, the reaction mixture was magnetically stirred for 120 min in dark in order to obtain a homogeneous suspension having adsorption–desorption equilibrium and the adsorption amount of all these photocatalysts for the MO was found to be negligible. After 90 min of solar light irradiation the degradation percentage of MO in the absence photocatalyst is only 3 % whereas it is observed to be 50.2, 86.5 and 99.9 % using α-Fe_2O_3, CuO and α-Fe_2O_3-CuO photocatalysts, respectively. From this result it is confirmed that the degradation of MO takes place due to the presence of these photocatalysts under solar light irradiation and the photocatalytic activity is found to follow a sequence: α-Fe_2O_3 < CuO < α-Fe_2O_3-CuO. It is observed that α-Fe_2O_3-CuO nanocomposite demonstrated the highest photocatalytic activity, and the MO can be completely degraded under solar light irradiation within 90 min reaction.

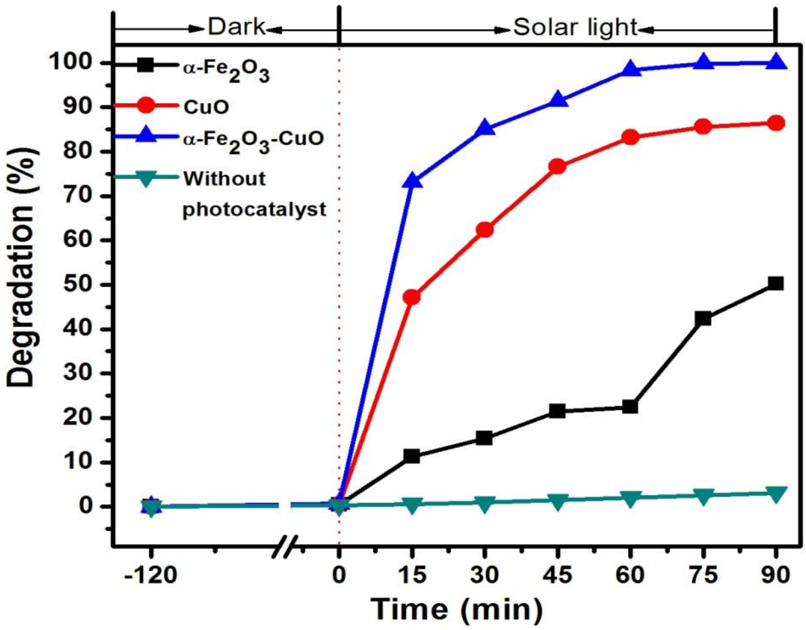

Figure 6.7 Percentage of degradation of MO as a function of reaction time by using α-Fe_2O_3 nanorods, CuO nanoparticles and α-Fe_2O_3-CuO nanocomposite.

The kinetics of degradation can be mainly studied by pseudo-first-order equation. According to Langmuir–Hinshelwood model, when the initial concentration C_0 is very small the following pseudo-first-order rate equation is used (Tanveer et al., 2014):

$$\ln(C_0/C_t) = K_1 t \qquad \textbf{(6.2)}$$

where K_1 is pseudo first order rate constant (min^{-1}) and C_t is the concentration at time t. A plot of $\ln(C_0/C_t)$ vs t gives the value of K_1. The reaction rate constants (K_1) for all the three photocatalysts were determined from the slope of the fitted curves (figure 6.8) by means of linear regression and the values are given in table 6.1. A good linear relationship between $\ln(C_0/C_t)$ and the irradiation time is observed for all the photocatalyst and the rate constant for α-Fe_2O_3-CuO photocatalyst is highest i.e. 0.0827 min^{-1} with good regression constant value (R^2=0.9534), showing α-Fe_2O_3-CuO nanocomposite is the best among them.

Table 6.1 Percentage of degradation and pseudo-first-order kinetic parameters of MO.

Photocatalyst	**Degradation (%)**	**K_1 (min^{-1})**	**R^2**
α-Fe_2O_3	50.2	0.0072	0.9015
CuO	86.5	0.0224	0.9373
α-Fe_2O_3-CuO	99.9	0.0827	0.9534

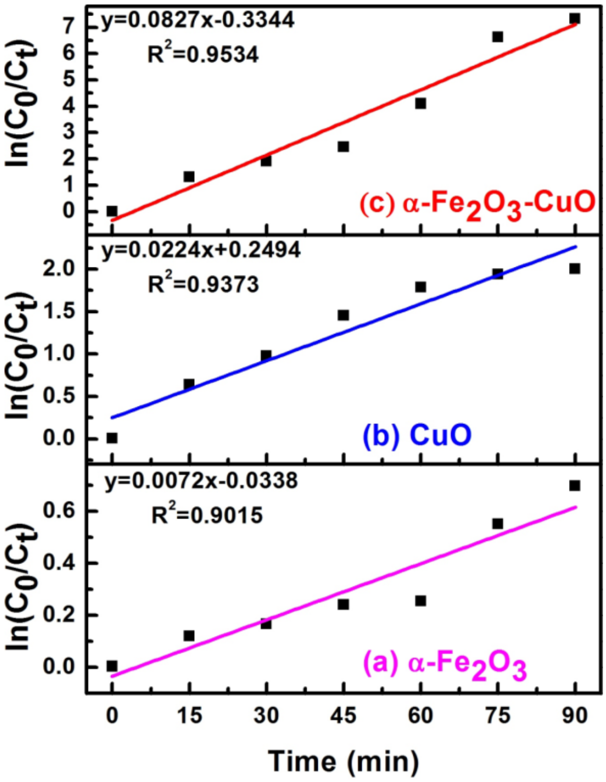

Figure 6.8 Pseudo-first-order reaction kinetic linear relationship curves for degradation of MO by (a) α-Fe_2O_3 nanorods, (b) CuO nanoparticles and (c) α-Fe_2O_3-CuO nanocomposite.

The stability of catalysts is an important issue for their practical applications. To prove the stability and the reusability of α-Fe_2O_3-CuO nanocomposite photocatalyst, we have repeated the experiemnts consugaive four cycles for degradation of the MO and the result is shown in figure 6.9. It is observed that, the repeatability of the entire process and the final results of degradation of MO are very good, which further demonstrate the excellent efficiency of the photocatalyst.

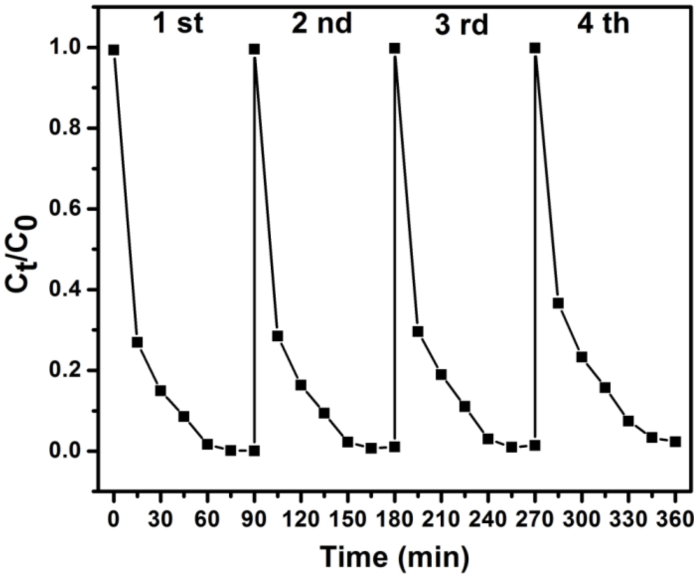

Figure 6.9 Repeating experiments for the photocatalytic degradation of MO using α-Fe2O3-CuO nanocomposite under solar light irradiation.

Photocatalytic Mechanism: The photocatalytic processes are based on electron hole pairs generated from band gap excitation. The photoinduced electron-hole pairs migrate to the surface of the materials and react with the adsorbed reactants in the due process, or undergo an undesired recombination. Therefore, the generation and separation of the photoinduced electron-hole pairs are the key factors that influence a photocatalytic reaction. From the experimental result, it is observed that CuO deposition have improved the photocatalytic activity of the α-Fe_2O_3 nanorod. Although α-Fe_2O_3 has a narrow bandgap and good absorption in the visible region, the still narrower bandgap of CuO modified the α-Fe_2O_3 nanorods such that they were activated by solar light absorption. The α-Fe_2O_3 nanorod is an n-type semiconductor with bandgap 2.12 eV and CuO is a p-type semiconductor with bandgap 1.47 eV. The α-Fe_2O_3-CuO nanocomposite system formed a stable p–n junction that efficiently separated electron–hole pairs that were photogenerated within each semiconductor material. Efficient charge separation contributed to the enhanced photocatalytic activity of the α-Fe_2O_3-CuO heteronanostructures (Ren et al., 2013; Jung et al., 2011; Chen et al., 2012). In CuO there is a chance of recombination of photo-formed electrons and holes due to small band gap. But in α-Fe_2O_3-CuO nanocomposite, when the CuO is excited by solar light with photon energy higher than band gaps of CuO, the electrons in the valence band (VB) move to the conduction band (CB) generating equal amounts of holes in VB. The photogenerated electrons are migrated from the CB of CuO to the CB of α-Fe_2O_3 forming different valence bond edges. Which inhibits electron-hole recombination: as a result the electron-hole pairs react with the adsorbed molecules (dye molecules). The proposed mechanism of photocatalytic decomposition of MO can be described as follow (Shi et al., 2014):

$\mathbf{CuO + Solar\ light\ (h\nu) \rightarrow CuO(e^-) + CuO(h^+)}$

$\mathbf{CuO(e^-) + \alpha\text{-}Fe_2O_3 \rightarrow \alpha\text{-}Fe_2O_3(e^-) + CuO}$

$\mathbf{\alpha\text{-}Fe_2O_3(e^-) + O_2 \rightarrow {}^{\bullet}O_2^- + \alpha\text{-}Fe_2O_3}$

$\mathbf{CuO(h^+) + H_2O \rightarrow {}^{\bullet}OH + H^+}$

$\mathbf{{}^{\bullet}O_2^- + H_2O \rightarrow HO_2^{\bullet} + {}^-OH}$

$\mathbf{HO_2^{\bullet} + H_2O \rightarrow H_2O_2 + {}^{\bullet}OH}$

$\mathbf{H_2O_2 \rightarrow {}^{\bullet}OH + {}^{\bullet}OH}$

$\mathbf{{}^{\bullet}OH + Methyl\ orange \rightarrow Degradation\ products}$

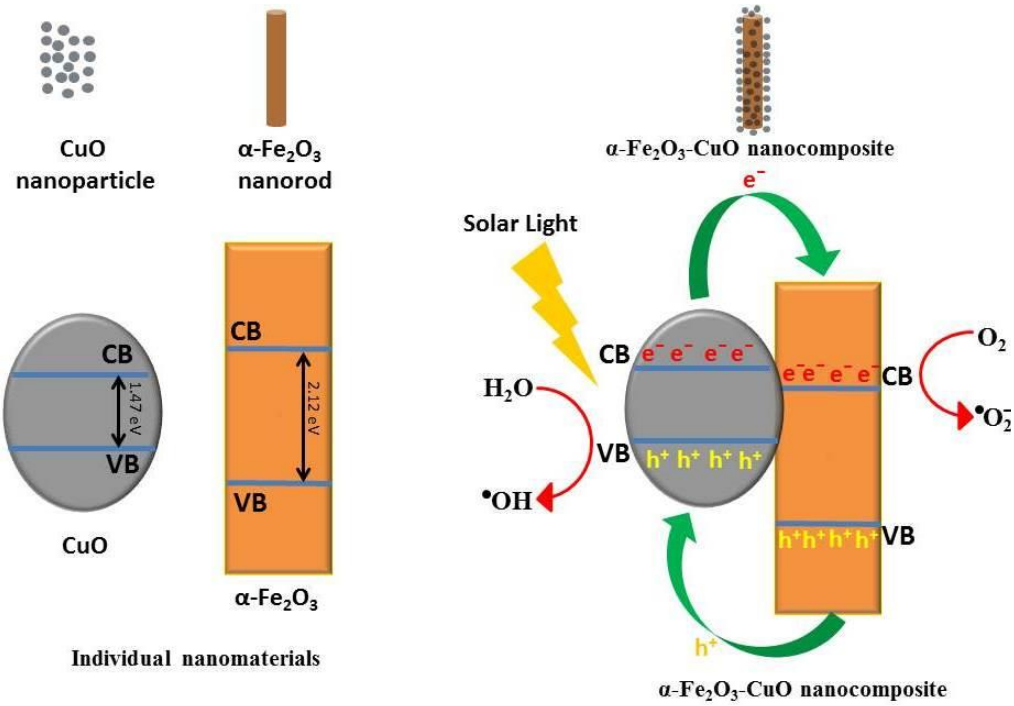

Figure 6.10 Proposed mechanism of photocatalytic degradation of MO using α-Fe_2O_3-CuO nanocomposite.

Here, the generated conduction band electrons (e^-) react with dissolved oxygen molecules to yield superoxide radical anions (${}^{\bullet}O_2^-$). The superoxide radical ion reacts with water to form hydrogen peroxide which on further decomposition produces hydroxyl radical (${}^{\bullet}$OH). Again, the generated valence band holes (h^+) reacts with water to generate hydroxyl radical (${}^{\bullet}$OH). The hydroxyl radical (${}^{\bullet}$OH) is a strong oxidizing agent causes the degradation of dye molecules. Schematic of photocatalytic mechanism in aqueous solution for the degradation of methyl orange by α-Fe_2O_3-CuO nanocomposite is illustrated in figure 6.10.

6.5. Conclusion

In summary, we have synthesized solar light sensitive photocatalysts of α-Fe_2O_3 nanorods, CuO nanoparticles and α-Fe_2O_3-CuO nanocomposites with various morphologies by a facile low cost wet chemical method. XRD result gives the well crystalline nature of the prepared samples with appropriate phase without the presence of any impurity. FE-SEM images indicate formation of rod shaped α-Fe_2O_3 nanomaterials with diameter 100-200 nm and spherical shaped CuO nanoparticles with particle diameter 30-40 nm. But in case of α-Fe_2O_3-CuO nanocomposite, the very fine spherical CuO particles are attached to the α-Fe_2O_3 nanorod and oriented in one-dimensional manner. XPS studies also confirmed the formation of Fe_2O_3-CuO composite nanomaterials.The narrow band gap semiconducting nature of the samples was analyzed by UV-Vis-DRS technique. The band-gap E_g of values of α-Fe_2O_3, CuO and α-Fe_2O_3-CuO, calculated by the Kubelka–Munk function, are found to be 2.12, 1.47 and 1.85 eV, respectively. This prepared nanomaterial catalysts were used for photocatalytic degradation of Methyl orange under natural solar light. It was observed that the α-Fe_2O_3-CuO nanocomposites show enhanced photocatalytic activity compared to both individual α-Fe_2O_3 and CuO nanoparticles. The enhanced photocatalytic activity is due to the efficient separation of photogenerated electron–hole pairs in the α-Fe_2O_3-CuO heteronanostructures.

CHAPTER-7

HYDROTHERMAL SYNTHESIS AND ENHANCED PHOTOCATALYTIC ACTIVITY OF TERNARY $Fe_2O_3/ZnFe_2O_4/ZnO$ NANOCOMPOSITE THROUGH CASCADE ELECTRON TRANSFER

7.1. Introduction

Semiconducting metal oxide nanoparticles have received remarkable attention because of their potential application for the removal of organic pollutants from aqueous media through photocatalytic degradation (Khakpash et al., 2012; Qurashi et al., 2010; Zhang et al., 2015; Xing et al., 2015). The semiconductor photocatalysis process utilizes energy from solar light especially visible light or UV light to clean water, air and Surfaces. The basic decomposition process can be described as (Asiltürk et al., 2009; Alshammari et al., 2015; Vignesh et al., 2015):

$$\boldsymbol{Organic\ Pollutant + O_2 \xrightarrow[Semiconductor]{h\upsilon \geq E_g} CO_2 + H_2O + Minerals} \qquad \textbf{(7.1)}$$

Here minerals are generated from hetero atoms such as S, N and Cl, containing organic pollutants and E_g is the band gap of the semiconductor. During the photocatalytic process, electron–hole pairs are generated in valence and conduction bands of a semiconductor due to presence of free radical, attack the molecules of pollutants (Gómez-Solís et al., 2012).

Generally, semiconducting metal oxide such as: TiO_2, WO_3, MnO_2, CeO_2 and ZnO, are used in photocatalytic degradation process (Liu et al., 2011; Kole et al., 2013). All these metal oxides are wide band semiconductors; hence these materials can only be used be excited for photocatalysis under UV light irradiation. It is known that more than 90% solar light reaches earth surface is in the range of visible light (mostly 400–600 nm) since most UV is filtered by ozone layer. Thus, it is a challenging area of research to develop novel photocatalysts with high efficiency of utilization of solar irradiation, high energy transfer efficiency, nontoxicity and low cost. Photocatalysis with artificial light sources need high electrical power which is costly and hazardous, but solar energy is an abundant natural source of energy, which will meet the requirements of future environmental and energy technologies (Wu and Chen, 2004; Li and Wang, 2010; Kim et al., 2005; Muruganandham and Swaminathan, 2004). Among the candidate materials, different forms of iron oxides, because of their small band gaps are considered to very suitable materials for solar light driven photocatalytic reaction. The band gap of α-Fe_2O_3 is around 2.2 eV, which can be activated with visible light region and collects up 40 % of the solar spectrum energy (Jang et al., 2009; Karunakaran and Senthilvelan, 2006). The drawbacks of α-Fe_2O_3 materials are high electron-hole recombination rates, small optical absorption coefficient in the visible region, and short hole diffusion lengths. To overcome these disadvantages, one of the important factors is using nanostructuring techniques i.e. using α-Fe_2O_3 nanomaterial to increase performance of α-Fe_2O_3 for photoresponse. Because nanomaterials exhibit large surface area compared to bulk counterpart, without an increase of the geometric area, reduced the scattering of free electrons, and enhanced the electrons mobility (Zhang et al., 2010). Similarly, another promising approach to overcome this disadvantage is making composite with α-Fe_2O_3 by coupling with other wide band gap semiconductors such as: ZnO, TiO_2, SnO_2, etc. As a result the performance the composite increases by mutual transfer of charge carriers i.e. electron excited under visible light may transfer from the conduction band of narrow band gap semiconductor to that of wide band gap semiconductor inside the composite. Thus positive charged electron centers could be formed with compatible chemical and electrical properties, which may lead to great improvement of photocatalytic efficiency of the composite (Zhang et al., 2007). Recently, a number of research groups studied the photocatalytic activity of nanocomposite such as: Fe_2O_3-ZnO (Liu et al., 20007), Fe_2O_3-SnO_2 (Xia et al., 2008), ZnO-CuO (Li and Wang, 2010), TiO_2-Fe_2O_3 (Zhou et al., 2008), CeO_2-SiO_2 (Mohamed and Aazam, 2012), Fe_2O_3-TiO_2 (Peng et al., 2010), SnO_2-Fe_2O_3 (Kang et al., 2011), and so on. They found that these composite semiconductor photocatalysts show enhanced photocatalytic efficiency and also exhibit fine optical properties compared to the corresponding parent component. Many binary metal oxide nanocomposites have been studied for this purpose, and the overall activity can be even more enhanced if a ternary hybrid system is employed (Kim et al., 2011). Hence, very recent research focused on designing multiple heterojunction structures with improved photogenerated electron−hole separation by engineering the energy band (Sun et al., 2014). Researchers are preparing ternary metal oxide nanocomposites by multi-step synthesis; which is difficult for large scale production due to high cost, long time taken and complex process (Kim et al., 2011; Sun et al., 2014).

In the present work, we have selected Zn salt with iron salt precursor to form mixed oxide Fe_2O_3-ZnO composite nanomaterials by maintaining indentical reaction conditions using hydrothermal method. Intrestingly we have observed the formation of Fe_2O_3/$ZnFe_2O_4$/ZnO ternary nanocomposite in single step by changing molar ratios of Fe and Zn. The synthesized novel $Fe_2O_3/ZnFe_2O_4/ZnO$ nanocomposite oxides were used as photocatalysts towards catalytic degradation of organic contaminants/dye (Malachite green) from aqueous media. The hydrothermal method was choosen as the preferred method for the synthesis of ternary composite in order to acieve high surface area and morphology control which are essential parameters which affects the photocatalytic performance. For photocatalytic degradation purpose we use cationic dye like Malachite green. Malachite green (MG), a triarylmethane dye, has been extensively used in the textile industry for dyeing wool and silk, and also has a widespread use in the paper, leather, and pharmaceutical industries. It is also used illegally for various purposes including in aquaculture as a fungicide on larvae and juvenile fish, as a parasiticide, and in the food, textile and other industries. Hence, relatively high levels of MG are always present in industrial wastewaters, and are harmful to human and others due to its genotoxic and carcinogenic properties, including its effects on the immune system and reproductive system and cause carcinogenesis, mutagenesis, teratogenicity, genotoxicity and respiratory toxicity. Thus, it is of particular significance to efficiently remove MG from wastewaters (Chen et al., 2007; Ju et al., 2008).

7.2. Materials and Methods

7.2.1. Materials used

Ferric nitrate ($Fe(NO_3)_3.9H_2O$) from s d Fine-Chem limited, Zinc sulphate ($ZnSO_4.7H_2O$) from Universal laboratory, Ethylenediamine from Merck India, Oxalic acid dehydrate from Merck India, Malachite green (MG) from Merck India, and Ethanol from Merck Germany. All the reagents used in the synthesis and catalytic study were of analytical grade and used as received without further purification.

7.2.2. Synthesis of α-Fe_2O_3 nanoparticles

Iron oxide (α-Fe_2O_3**)** was synthesized by hydrothermal method keeping the starting material ferric nitrate ($Fe(NO)_3.9H_2O$). 1.212 gm of ferric nitrate was dissolved in 150 ml of water under vigorous stirring. Under this condition 10 g of ethylenediamine was added drop wise for maintain the pH 11. After the addition of ethylenediamine, a brown precipitate was formed and the stirring was continued for half an hour to form a homogeneous solution. Then the solution was kept into a Teflon-linked sealed autoclave followed by hydrothermal treatment at 150 °C for 12 hr. Then the sample was washed and centrifuged for several times with ethanol and distilled water and then dried at 60 °C for 2 hours. Then the dried sample was calcined at 500 °C for 2 hours with heating rate 10 °C/min to form α-Fe_2O_3 nanoparticles.

7.2.3. Synthesis of α-Fe_2O_3/ $ZnFe_2O_4$/ZnO nanocomposites

For the synthesis of α-Fe_2O_3/$ZnFe_2O_4$ mixed nanocomposite, we followed the same above hydrothermal procedure, taking the starting materials ferric nitrate and zinc sulphate ($ZnSO_4.7H_2O$) by varying the molar ratio ferric nitrate: Zinc sulphate = 90:10, 80:20, 70:30, 60:40 and 50:50 followed by calcination at 500 °C to form Fe_2O_3/$ZnFe_2O_4$, Fe_2O_3/$ZnFe_2O_4$/ZnO and $ZnFe_2O_4$/ZnO nanocomposites. The details of the synthesis of Fe_2O_3/$ZnFe_2O_4$/ZnO nanocomposites are schematically presented in Scheme 7.1.

Scheme 1 Schematic representation of the synthesis of Fe_2O_3/ $ZnFe_2O_4$/ZnO nanocomposite.

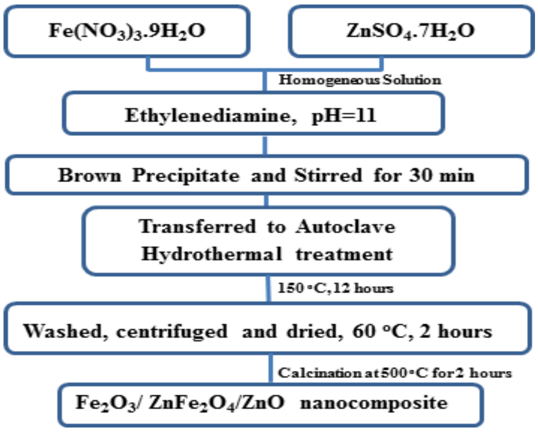

7.2.4. Characterization techniques

The surface morphology of the prepared composite materials was characterized by a Nova Nano SEM 450 Field Emission scanning electron microscopy (FE-SEM) operated at an acceleration voltage of 15 and 20 kV. The size of the particle and selected area electron diffraction (SAED) pattern of the nanocomposite was observed using a high resolution transmission electron microscope (JEM-2100 HRTEM, Make-JEOL, Japan) with an acceleration voltage of 200 kV. The phases were identified by means of X-ray diffraction (XRD) by a PANalytical X-ray diffractometer with Cu Kα radiation (λ) 1.54156 ^{o}A at a scan rate of 2^{o}/min. X-ray photoelectron spectroscopy (XPS) was determined using a VG Scientific ESCA LAB Mk-II Spectrometer with Al Kα radiation (1486.6 eV) at a takeoff angle at 45°. The UV-Visible absorbance spectra of the sample were recorded using Shimadzu spectrometer (model 2450) with $BaSO_4$ coated integration sphere in the range of 200-800 nm. Specific surface area and pore size distribution (PSD) of the samples were determined from nitrogen adsorption/desorption isotherms obtained at the temperature of liquid nitrogen in an automated physisorption instrument (Autosorb-iQ, Quantachrome Instruments). Steady-state fluorescence emission spectra were recorded using Jobin-Yvon Spectrofluorimeter (Fluoromax-4P) at an excitation wavelength of 420 nm with 5/5 slit.

7.2.5. Photocatalytic activity study

The photodegradation efficiency of all synthesized catalysts was tested towards degradation of Malachite green (MG) under natural solar light radiation. All the experiments were performed at the location of 22°15'N 84°54'E during the months of May and June (sunny days), from 09.00 AM tom 11:00 A. M., when the average solar intensity was 1.0 kW m^{-2} with minimum fluctuation. Initially a stock solution of 1 g/L was prepared by dissolving 1 g of Malachite green (oxalate) in 1000 ml of double distilled water. In a typical experiment, 0.1 gm of catalyst was added to 100 ml of 20 mg/L MG solution in a 250 ml of beaker. Before irradiation, the suspension was magnetically stirred in dark for 2 hour to ensure the establishment of the adsorption/desorption equilibrium of the dye onto the surface of photocatalysts. Afterwards the solution was exposed to natural sunlight with continuous stirring. At given time interval (every 15 min) the solution (3 ml) sampled and filtered. Then the solution was put into a quartz cell, and adsorption spectrum was measured using Shimadzu UV-2450 spectrometer. This process was repeated until complete degradation of dye from the aqueous solution. TOC before and after 90 min of photodegradation studies was measured using a TOC analyzer (SHIMADZU TOC-L).

7.3. Results and Discussion

7.3.1. Detailed characterizations and properties of the prepared nanocomposites

Morphology and compositional analysis: FE-SEM images and EDAX pattern of the synthesized α-Fe_2O_3 nanoparticles and the nanocomposites with different molar proportion of Fe and Zn are shown in figure 7.1. Figure 7.1a shows the FESEM image of α-Fe_2O_3 nanoparticles. The image suggests the formation of very fine particles with irregular shape and morphology. The sizes of the particles are in the range of 80-100 nm. Figures 7.1b-f represents the FESEM images of α-Fe_2O_3/$ZnFe_2O_4$/ZnO nanocomposites prepared by varying mole % of iron and zinc. From the images it is observed that, with increasing percentage of Zn in the nanocomposite the morphology of the nanocomposites gradually changes from irregular (for α-Fe_2O_3) to cubical and when Zn percentage reaches 50 % the shape of the nanocomposite becomes cubical with uniform size. The sizes of all the nanocomposites are in the range of 100-200 nm. The EDAX patterns of $ZnFe_2O_4$/ZnO (Fe: Zn=50:50) is shown in figure 7.1g. The patterns demonstrate that the nanocomposite contains O, Fe and Zn elements. The transmission electron micrographs and SAED pattern of $ZnFe_2O_4/ZnO$ (Fe:Zn=50:50) nanocomposite are shown in figure 7.2. From figure 7.2a-c, it is observed that, apart from some irregular particles the major morphological feature is regular cubic shape with mean edge length in the range 100-200 nm. Figure 7.2d shows the corresponding SAED pattern of the nanocomposite, which demonstrates the crystalline nature.

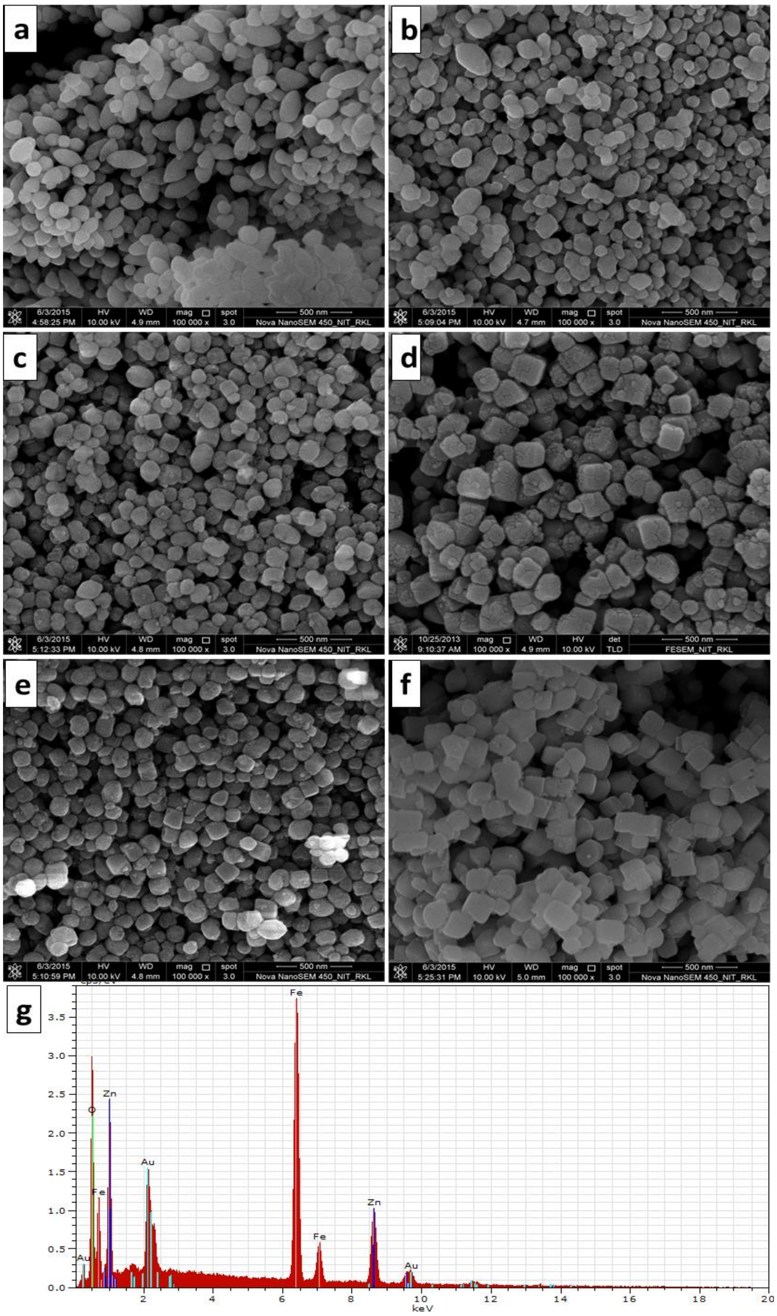

Figure 7.1 FE-SEM images of of a) α-Fe_2O_3, b) $Fe_2O_3/ZnFe_2O_4$ (Fe:Zn=90:10), c) $Fe_2O_3/ZnFe_2O_4$ (Fe:Zn=80:20), d) $Fe_2O_3/ZnFe_2O_4/ZnO$ (Fe:Zn=70:30), e)$Fe_2O_3/ZnFe_2O_4/ZnO$ (Fe:Zn=60:40), f) $ZnFe_2O_4/ZnO$ (Fe:Zn=50:50) and EDAX pattern of $ZnFe_2O_4/ZnO$ (Fe:Zn=50:50).

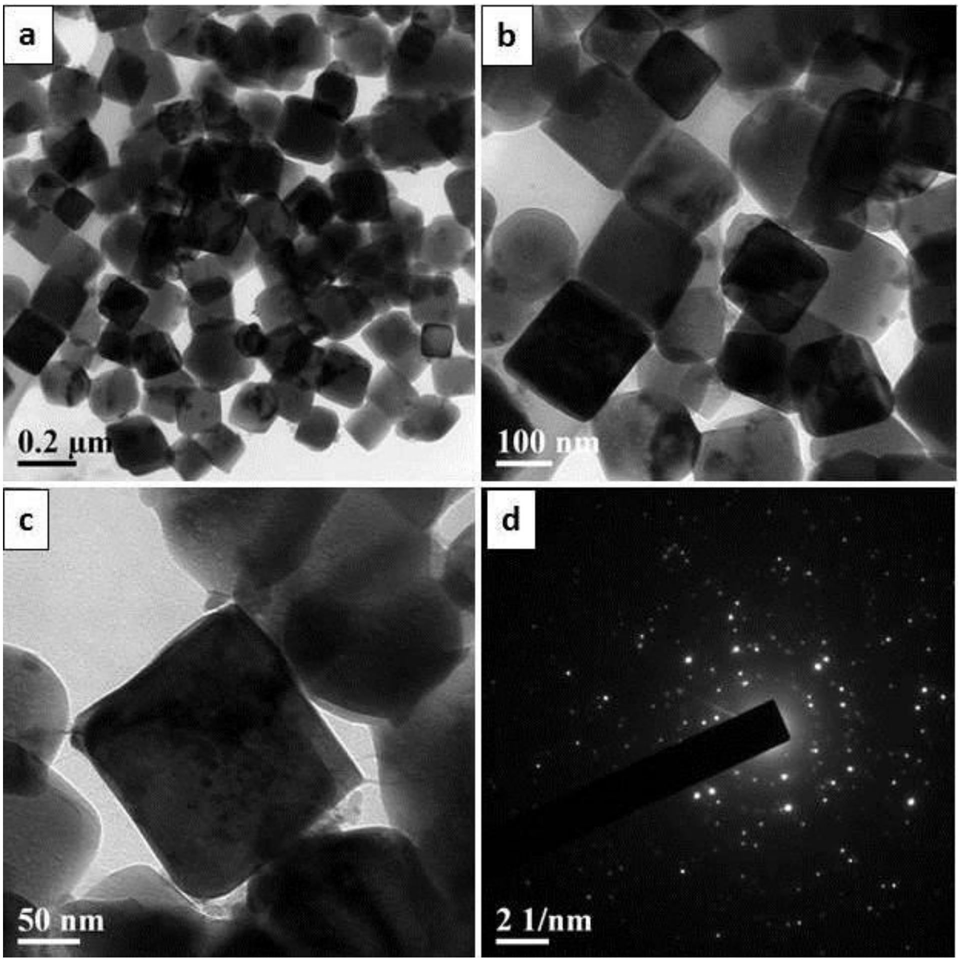

Figure 7.2 (a-c) TEM images and (d) SAED pattern of $ZnFe_2O_4$/ZnO (Fe:Zn=50:50).

XRD analysis: Figure 7.3 shows the XRD patterns of the α-Fe_2O_3 and Fe_2O_3/$ZnFe_2O_4$ and Fe_2O_3/$ZnFe_2O_4$/ZnO nanocomposites (with different molar ratios). The pattern of α-Fe_2O_3 (figure 7.3a) contains characteristics peaks at 2θ= 24.12°, 33.15°, 35.62°, 39.21°, 40.85°, 49.47°, 54.08°, 57.62° and 62.44° (marked as: α) and can be indexed as (012), (104), (110), (112), (024), (116), (018), (214) and (300) reflections, respectively of the rhombohederal crystal structure of α-Fe_2O_3 according to JCPDS No: 79-0007. Figure 7.3b-f show the XRD patterns of nanocomposite system prepared by taking (100-x) mole % $Fe(NO_3)_3.9H_2O$ and x mole % $ZnSO_4.7H_2O$ as the initial precursors (where x=10, 20, 30, 40 and 50). For x = 10 (figure 7.3b), the presence of $ZnFe_2O_4$ with cubic crystal structure peaks are detected according to JCPDS card no. 22–1012; which confirms its formation along with α-Fe_2O_3. The prominence of peaks (figure 7.3c) corresponding to $ZnFe_2O_4$ for x = 20 in expense of parent phase indicates the evolution of a well composite system of α-Fe_2O_3 and $ZnFe_2O_4$. When x varied to 30, the appearance of some new peaks is observed which are detected to be of ZnO compound with hexagonal wurtzite crystal structure according to JCPDS no: 01–1136, but simultaneously parent phase also found to be weakened. The presence of ZnO phase gradually increases with $ZnFe_2O_4$ as their corresponding peaks become more prominent for next higher percentage of x = 40, shown in figure 7.3d, along with minute presence of α-Fe_2O_3 phase. This confirms a well formulated composite system with the presence of three compounds. For x = 50, the peaks corresponding to α-Fe_2O_3 is completely absence in the XRD pattern (figure 7.3e). But the corresponding peaks of other two compounds still appear which indicates the formation of a composite system of $ZnFe_2O_4$ and ZnO.

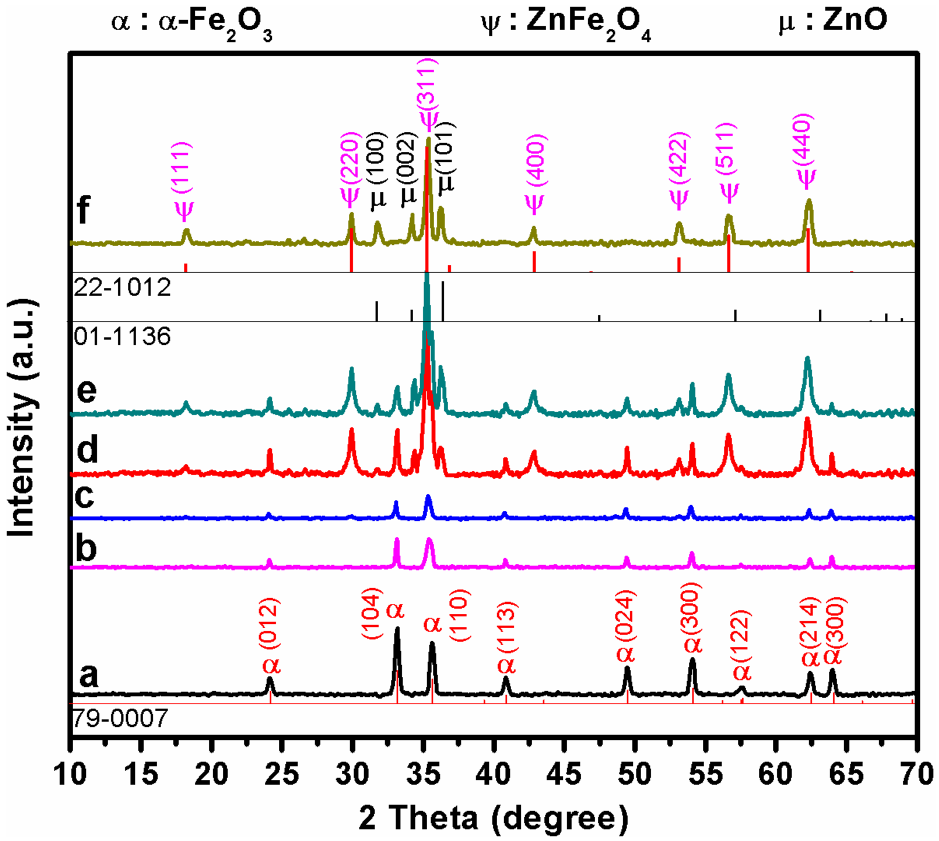

Figure 7.3 XRD patterns of a) α-Fe_2O_3 nanoparticle, b) $Fe_2O_3/ZnFe_2O_4$ (Fe:Zn=90:10), c) $Fe_2O_3/ZnFe_2O_4$ (Fe:Zn=80:20), d) $Fe_2O_3/ZnFe_2O_4/ZnO$ (Fe:Zn=70:30), e) $Fe_2O_3/ZnFe_2O_4/ZnO$ (Fe:Zn=60:40), f) $ZnFe_2O_4/ZnO$ (Fe:Zn=50:50) nanocomposites.

XPS analysis: Figure 7.4a gives the full XPS survey spectrum for the $Fe_2O_3/ZnFe_2O_4/ZnO$ (Fe:Zn=70:30) nanocomposite. The presence Fe, Zn, O and C elements are observed from the spectra. Carbon is due to the adventitious hydrocarbon from the XPS instrument itself. Figure 7.4b displays the high resolution XPS spectra of Fe 2p, in which two peaks at 712.7 and 726.8 eV correspond to Fe 2p1/2 and Fe 2p3/2, respectively. In addition, the presence of satellite peak at 718.3 suggests that only Fe^{3+} exists in the nanocomposite. The high resolution spectrum of Zn 2p is displayed in figure 7.4c. The peaks at binding energy of 1043.5 and 1022.1 eV can be attributed to Zn 2p1/2 and Zn 2p3/2, respectively. It suggests that the oxidation state of Zn is 2+ in the present nanocomposites. The spectrum of O 1s is shown in figure 7.4d. The broad asymmetric curve can be de-convoluted into three peaks with binding energies at 532.8, 531.6 and 530.2 eV, respectively. The peak at 530.2 eV is due to surface lattice oxygen (O^{2-}) in metal oxide framework and the other peaks at around 531.6 and 532.8 eV are ascribed to surface adsorbed oxygen species such as O^- and O_2^- (Lv et al., 2010; Wang et al., 2015).

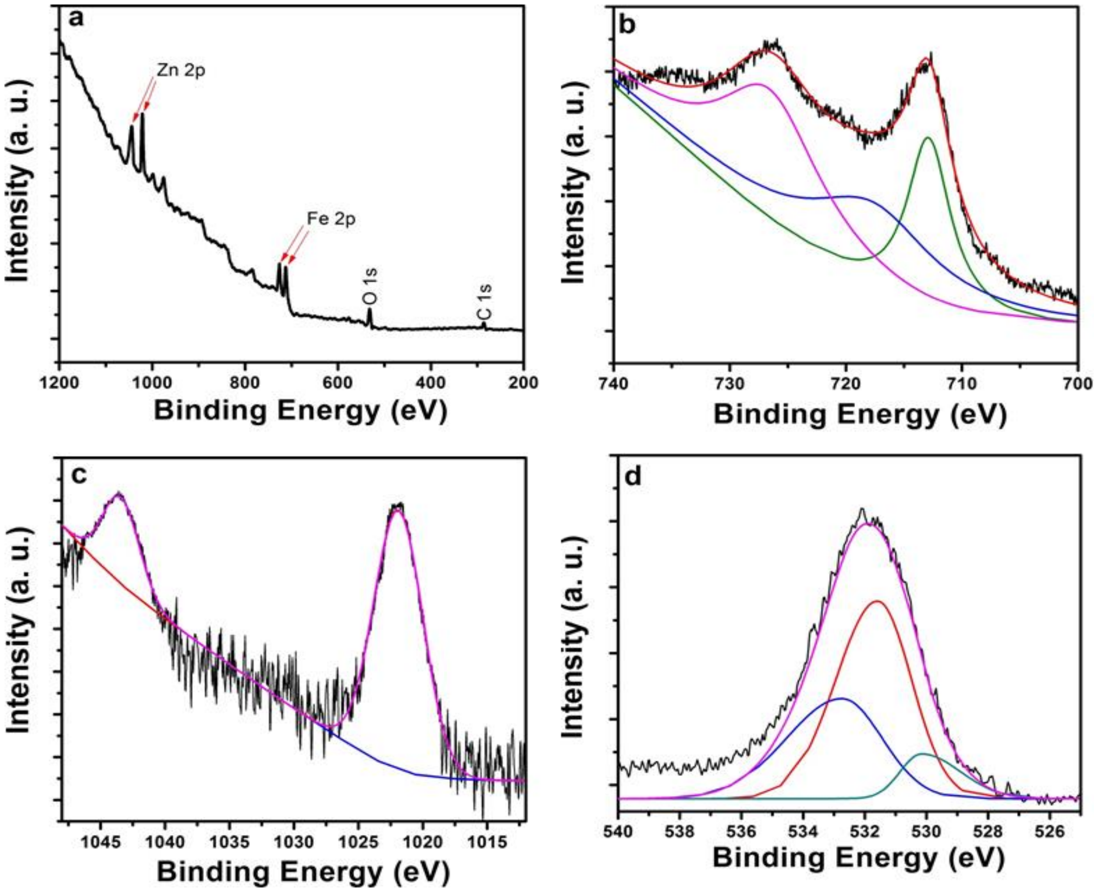

Figure 7.4 XPS patterns of (a) survey, (b) Fe 2p, (c) Zn 2p, (d) O 1s of the $Fe_2O_3/ZnFe_2O_4/ZnO$ (Fe:Zn=70:30) nanocomposite.

UV-Vis-DRS study and calculation of band gap: Because of the importance of the optical absorption properties and the electronic nature of band gap of the prepared nanocompoaites for solar energy photocatalytic reaction, we have studied changes in the optical properties of pure α-Fe_2O_3 nanoparticle with addition of Zn to form α-$Fe_2O_3/ZnFe_2O_4/ZnO$ nanocomposite, by UV-vis spectroscopy. The band-gap E_g can be calculated by the Kubelka-Munk function (Mariappan et al., 2015):

$$\mathbf{(\alpha h\nu)^2 = B\ (h\nu\text{-}E_g)^n} \qquad \mathbf{(7.2)}$$

where hν is the photon energy, α is the absorption coefficient, B is a constant. The band-gap can be derived from the plot of the Kubelka–Munk function versus the absorption energy. The value of n is determined from the nature of optical transition. n=2 or 3 for indirect allowed and indirect forbidden transition, respectively and n=1/2 or 3/2 for direct allowed and direct forbidden transition, respectively. The band-gap of all the synthesized photocatalysts is shown in figure 7.5b-g. It is estimated from the plot of $(\alpha h\nu)^n$ versus hν by extrapolating the straight line to the X axis intercept. From the graph it is observed that there is a sharp increase of the absorptivity between wavelength range 550 and 600 nm. Figure 7.5a shows the absorption coefficient, α, as a function of wavelength for pure α-Fe_2O_3 and Fe_2O_3/$ZnFe_2O_4$/ZnO nanocomposites. For α-Fe_2O_3, absorption bands at 593 and 366 nm corresponding to the ligand-free ($^6A_1 \rightarrow {}^4E$) and a ligand-to-metal charge transfer ($6t_{1u} \rightarrow 2t_{2g}$) transitions, respectively (Sivula et al., 2010). Upon increasing percentage of Zn in the composite from 0 % to 20 %, the adsorption edges show a red shift and also increases in intensity of the absorption spectra in the visible light region compared to α-Fe_2O_3. The red shift indicated that the band gap of the composite decreases and the size quantization effect exists (Frost et al., 2006). The band-gap energy of α-Fe_2O_3 is 2.42. When percentage of Zn in the composite increases to 20 %, the band-gap adsorption edge shifted to 631 nm, indicating that the Eg is 2.08 eV. However, further increasing the Zn amount to 30 % in the composite brings a slightly blue shift of the maximum adsorption peak and band-gap adsorption edge. The band gap of Fe_2O_3/$ZnFe_2O_4$/ZnO (Fe:Zn=70:30) is 2.01. The slightly blue shift and increase in band gap of the composite is due to formation of a small amount of ZnO in the nanocomposite. When the percentage of Zn again increases to 40 and 50 %, the band gap of the composites increases to 2.03 and 2.55 for Fe_2O_3/$ZnFe_2O_4$/ZnO (Fe:Zn=60:40) and $ZnFe_2O_4$/ZnO (Fe:Zn=50:50) nanocomposites respectively. The increase in band gap for the nanocomposite is due to formation of extra ZnO phase in the nanocomposites.

Surface area and porosity measurement: Based on N_2 adsorption-desorption measurements, the isotherms and corresponding pore size distribution curves for prepared α-Fe_2O_3 and Fe_2O_3/$ZnFe_2O_4$/ZnO nanoparticles are shown in figure 7.6. The BET surface area of pure α-Fe_2O_3 nanoparticle was found to be very low i.e. 18.555 m^2/g. But in case of composites the surface areas were found to be 21.2, 26.076, 32.775, 38.494 and 49.464 m^2/g for Fe_2O_3/$ZnFe_2O_4$ (Fe:Zn=90:10), Fe_2O_3/$ZnFe_2O_4$ (Fe:Zn=80:10), Fe_2O_3/$ZnFe_2O_4$/ZnO (Fe:Zn=70:30), Fe_2O_3/$ZnFe_2O_4$/ZnO (Fe:Zn=60:40) and $ZnFe_2O_4$/ZnO (Fe:Zn=50:50), respectively. It is observed that with increasing percentages of Zn in the nanocomposites the surface area increases slowly. From the BJH pore size distribution curve sharp peaks were observed at 2.5, 3.4, 3.4, 3.8, 3.3 and 3.5 nm for α-Fe_2O_3, Fe_2O_3/$ZnFe_2O_4$ (Fe:Zn=90:10), Fe_2O_3/$ZnFe_2O_4$ (Fe:Zn=80:10), Fe_2O_3/$ZnFe_2O_4$/ZnO (Fe:Zn=70:30), Fe_2O_3/$ZnFe_2O_4$/ZnO

(Fe:Zn=60:40) and $ZnFe_2O_4$/ZnO (Fe:Zn=50:50), respectively; which demonstrates the existence of inter-particle voids with pore-size distribution in the nanostructures.

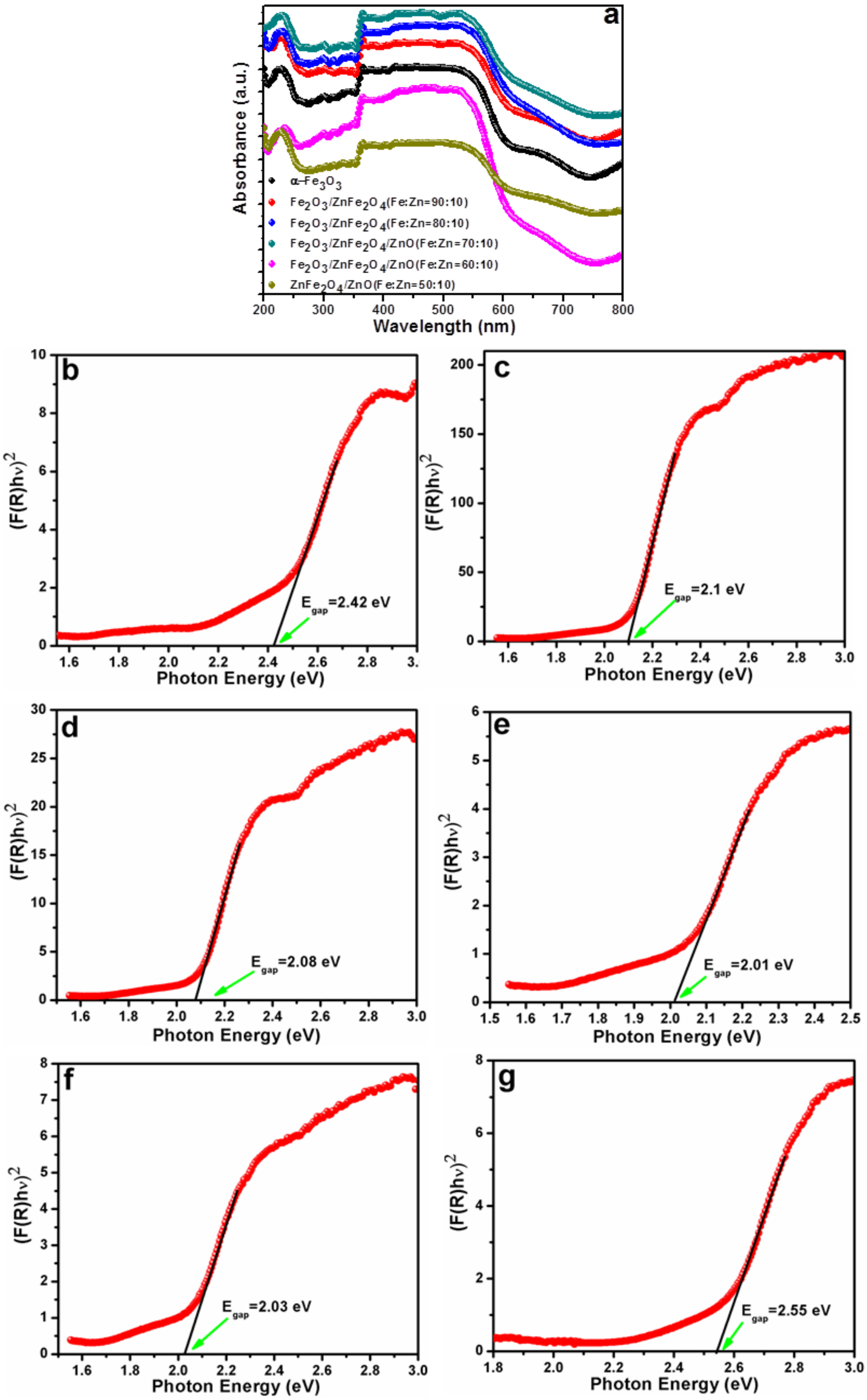

Figure 7.5 a) Optical absorbance spectra and b) calculated band-gap energy of b) α-Fe_2O_3 nanoparticle, c) Fe_2O_3/$ZnFe_2O_4$ (Fe:Zn=90:10), d) Fe_2O_3/$ZnFe_2O_4$ (Fe:Zn=80:20), e) Fe_2O_3/$ZnFe_2O_4$/ZnO (Fe:Zn=70:30), f)Fe_2O_3/$ZnFe_2O_4$/ZnO (Fe:Zn=60:40), g) $ZnFe_2O_4$/ZnO (Fe:Zn=50:50) nanocomposites.

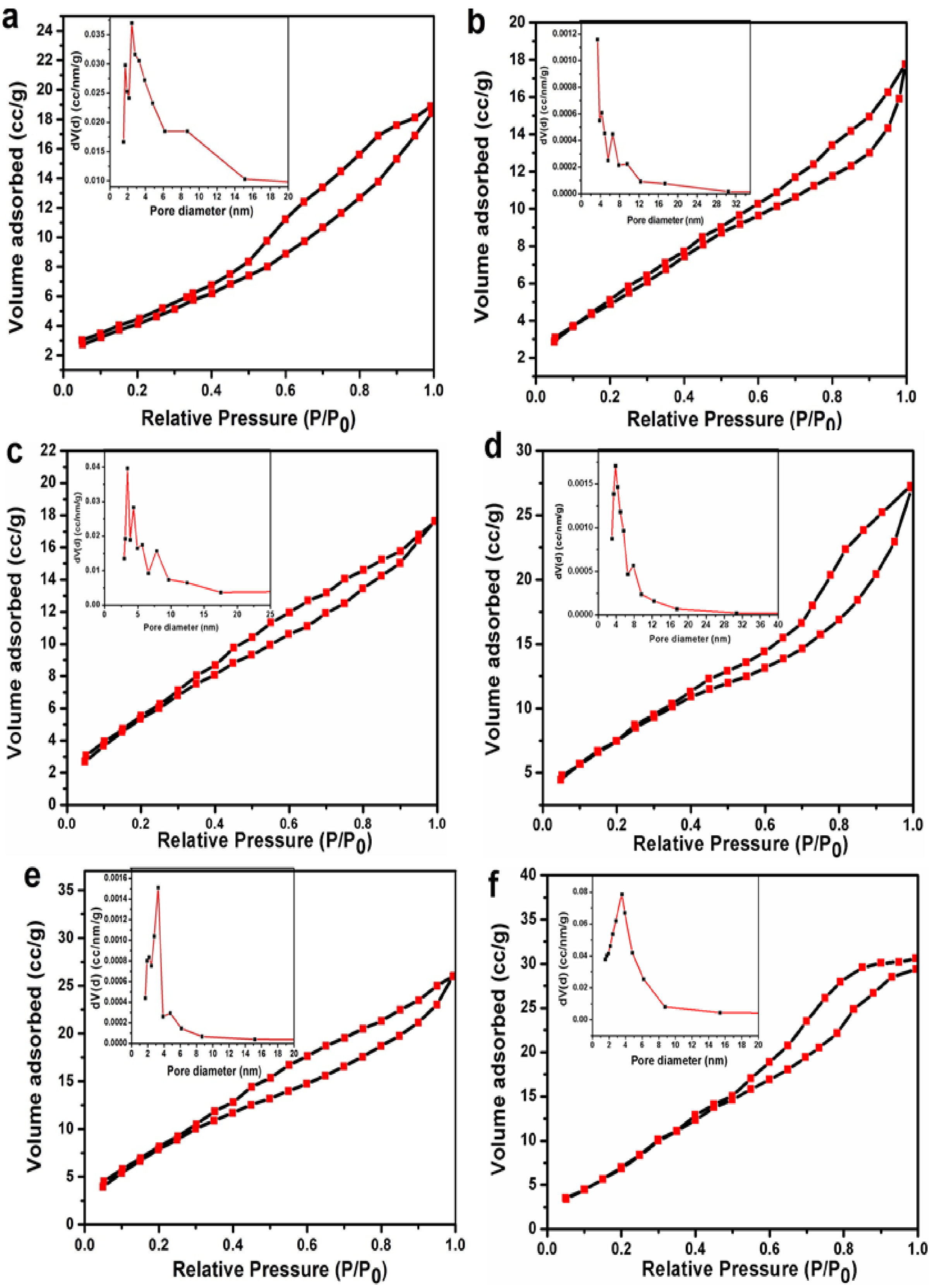

Figure 7.6 BET isotherm of and Pore size distribution curves (incet) based on the BJH method for a) α-Fe_2O_3 nanoparticle, b) $Fe_2O_3/ZnFe_2O_4$ (Fe:Zn=90:10), c) $Fe_2O_3/ZnFe_2O_4$ (Fe:Zn=80:20), d) $Fe_2O_3/ZnFe_2O_4/ZnO$ (Fe:Zn=70:30), e) $Fe_2O_3/ZnFe_2O_4/ZnO$ (Fe:Zn=60:40), f) $ZnFe_2O_4/ZnO$ (Fe:Zn=50:50) nanocomposites.

7.3.2. Photocatalytic degradation of MG under solar light irradiation

The photocatalytic activities of the prepared α-Fe_2O_3 nanoparticle, $Fe_2O_3/ZnFe_2O_4$, $Fe_2O_3/ZnFe_2O_4/ZnO$ and $ZnFe_2O_4/ZnO$ nanocompoaites with variable Fe:Zn ratios are evaluated by photocatalytic degradation of MG from aqueous solution under natural sunlight irradiation by monitoring the intensity of the characteristic absorption peak at 618 nm of malachite green. The degradation percentage of MG was calculated by the following equation:

$$\textbf{Degradation percentage} = \mathbf{100} \times \left(\frac{C_0 - C_t}{C_0}\right)\% = \mathbf{100} \times \left(\frac{A_0 - A_t}{A_t}\right)\% \qquad \textbf{(7.3)}$$

where C_0 and C_t were the concentration of MG when the reaction time was 0 and t and A_0 and A_t were the absorbance of MG when the reaction time was 0 and t, respectively. The UV-vis spectral changes of MG aqueous solution in the process of photodegradation for $Fe_2O_3/ZnFe_2O_4/ZnO$ (Fe:Zn=70:30) nanocomposites is displayed figure 7.7. From the figure it is observed that, the absorbance at 618 nm of MG diminishes gradually with time elapsed: which indicates the reduction of MG from blue to colorless. The absorption peak completely disappeared in 90 min. The photograph of MG solution before and after solar light irradiation with different time is given in figure 7.7 (inset), which also confirms the complete degradation of the MG in 90 min.

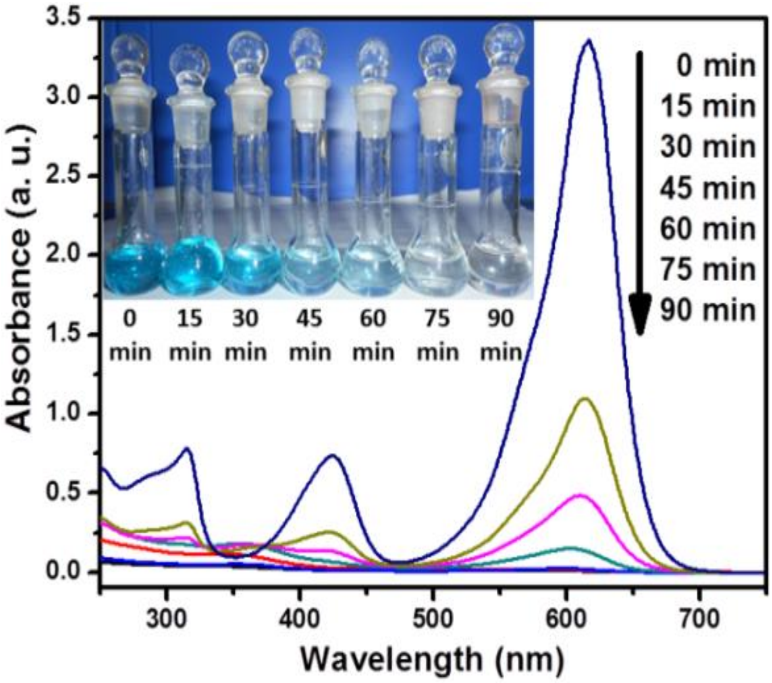

Figure 7.7 UV-vis spectral changes and optical images (inset) of Malachite green during degradation process as a function of reaction time using $Fe_2O_3/ZnFe_2O_4/ZnO$ (Fe:Zn=70:30) nanocomposite Photocatalyst (100 ml of 20 mg L^{-1} MG solution, 0.1 g catalyst and natural solution pH).

Effect of pH of the solution: The solution pH is a significant parameter in photocatalytic degradation process. The influence of different pH (4-8) value on the degradation efficiency of MG was investigated using 0.1 g of $Fe_2O_3/ZnFe_2O_4/ZnO$ (Fe:Zn=70:30) photocatalyst in 100 ml of 20 mg/L MG solution and the result is shown in figure 7.8. The natural pH value of 20 mg/L MG solution was found to be 5.7. The pH value was adjusted using dilute HCl or dilute NaOH solution for the experiment. Before the irradiation to sunlight, the MG solutions with the photocatalyst was kept in dark condition with constant stirring for 2 h, but the reduction in concentration was found to be around 2 %; this might be due to adsorption rather than photodecomposition. However with the exposure of sunlight, the performances of the photoreaction were extremely improved. The experimental results reveal that the percentage of degradation increases with pH. The increase in rate of photocatalytic degradation might be due to the more availability of OH^- ions in alkaline medium which will generate more $^\bullet OH$ radicals by combining with holes which are formed due to the electronic excitation in catalyst (Pare et al., 2011). For more alkaline solution pH (pH ≥ 10), it was observed a total decolorization of malachite green within a few seconds. This is because, malachite green dye changes to a colorless leuco compound at highly alikaline medium (Charanpahari et al., 2015). Hence, all further experiments were done at the natural pH of the dye solution.

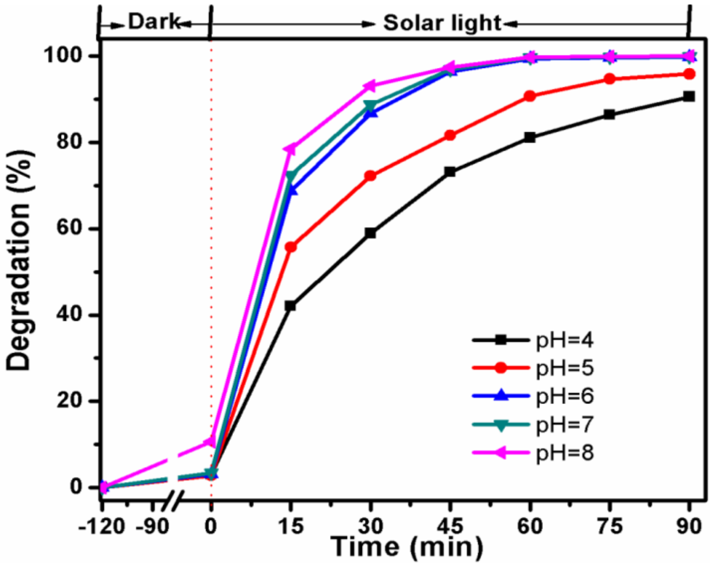

Figure 7.8 Variation of percentage degradation of 100 ml of 20 mg L^{-1} MG with different pH using 0.1 g of $Fe_2O_3/ZnFe_2O_4/ZnO$ (Fe:Zn=70:30) nanocomposite under solar light irradiation.

Effect of dye solution concentration: The effect of initial dye concentration of MG was investigated using 0.1 g of $Fe_2O_3/ZnFe_2O_4/ZnO$ (Fe:Zn=70:30) photocatalyst in 100 ml of dye solutions of different concentrations ranging from 10 to 40 mg L^{-1}. From figure 7.9, it is observed that the percentage of degradation was found to be almost same for 10 and 20 mg L^{-1} concentrations of dye. Before the irradiation to sunlight, the adsorption of MG solutions with the photocatalyst was studied in dark condition with constant stirring for 2 h, but the sorption percentage was found to be 0.5–2%. The percentage of degradation under solar light irradiation was found to decrease with increase in dye concentration. The reason for this decrease is attributed to the shielding effect of dye at high concentration that hinders the penetration of solar light to the dye molecules deposited over the catalyst surface (Tarigh et al., 2015). Hence, further experiments were carried out with 20 mg L^{-1} concentration of dye.

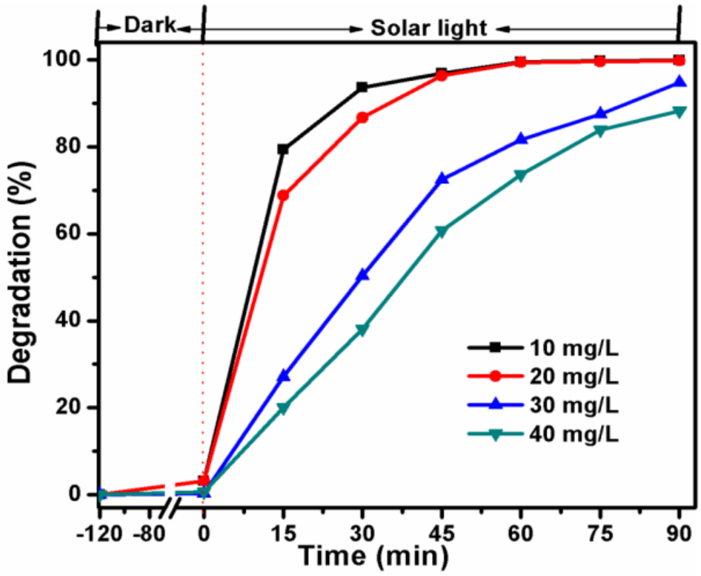

Figure 7.9 Variation of percentage degradation of 100 ml of MG with different concentration using 0.1 g of $Fe_2O_3/ZnFe_2O_4/ZnO$ (Fe:Zn=70:30) nanocomposite under solar light irradiation.

Effect of catalyst compositions and kinetics study: Figure 7.10a shows the percentage of photodegradation and figure 7.10b shows the decrease in concentration of malachite green with respect to time using 0.1 g of α-Fe_2O_3 nanoparticle and $Fe_2O_3/ZnFe_2O_4$ (Fe:Zn=90:10), $Fe_2O_3/ZnFe_2O_4$ (Fe:Zn=80:10), $Fe_2O_3/ZnFe_2O_4/ZnO$ (Fe:Zn=70:30), $Fe_2O_3/ZnFe_2O_4/ZnO$ (Fe:Zn=60:40) and $ZnFe_2O_4/ZnO$ (Fe:Zn=50:50) nanocomposites catalysts each in 100 ml of 20 mg L^{-1}. In the absence of catalyst, no degradation of MG dye was observed (not shown in graph) which indicated that photolysis did not occur under solar light. We have repeated the sorption experiment in dark, prior to photocatalysis studies in all the experiments as described previously. The decrease in dye concentration due to adsorption is found to be around 2% in all cases. It is observed that the proportion degradation of MG increases with increase in solar light exposure time and almost all the MG molecules were decomposed within 90 min with

$Fe_2O_3/ZnFe_2O_4/ZnO$ (Fe:Zn=70:30) nanocomposite photocatalyst. When α-Fe_2O_3 nanoparticle was used as photocatalyst the percentage of degradation was 81.86 % after 90 min of irradiation. The degradation percentages are more in case of nanocomposites i.e. 88.37, 94.37 and 99.77 % after 90 min irradiation time using $Fe_2O_3/ZnFe_2O_4$ (Fe:Zn=90:10), $Fe_2O_3/ZnFe_2O_4$/ (Fe:Zn=80:20) and $Fe_2O_3/ZnFe_2O_4/ZnO$ (Fe:Zn=70:30) nanocomposites, respectively. The percentage of degradation again decreased when percentage of Zn in the nanocomposites increased i.e. 98.29 and 96.92 % for $Fe_2O_3/ZnFe_2O_4/ZnO$ (Fe:Zn=60:40) and $ZnFe_2O_4/ZnO$ (Fe:Zn=50:50) nanocomposites, respectively. Hence, it may be inferred that addition of Zn effectively enhances the photocatalytic activity of α-Fe_2O_3 up to 30 % and upon further addition up to 40 and 50 %, the photocatalytic activity decreases (figure 7.10c).

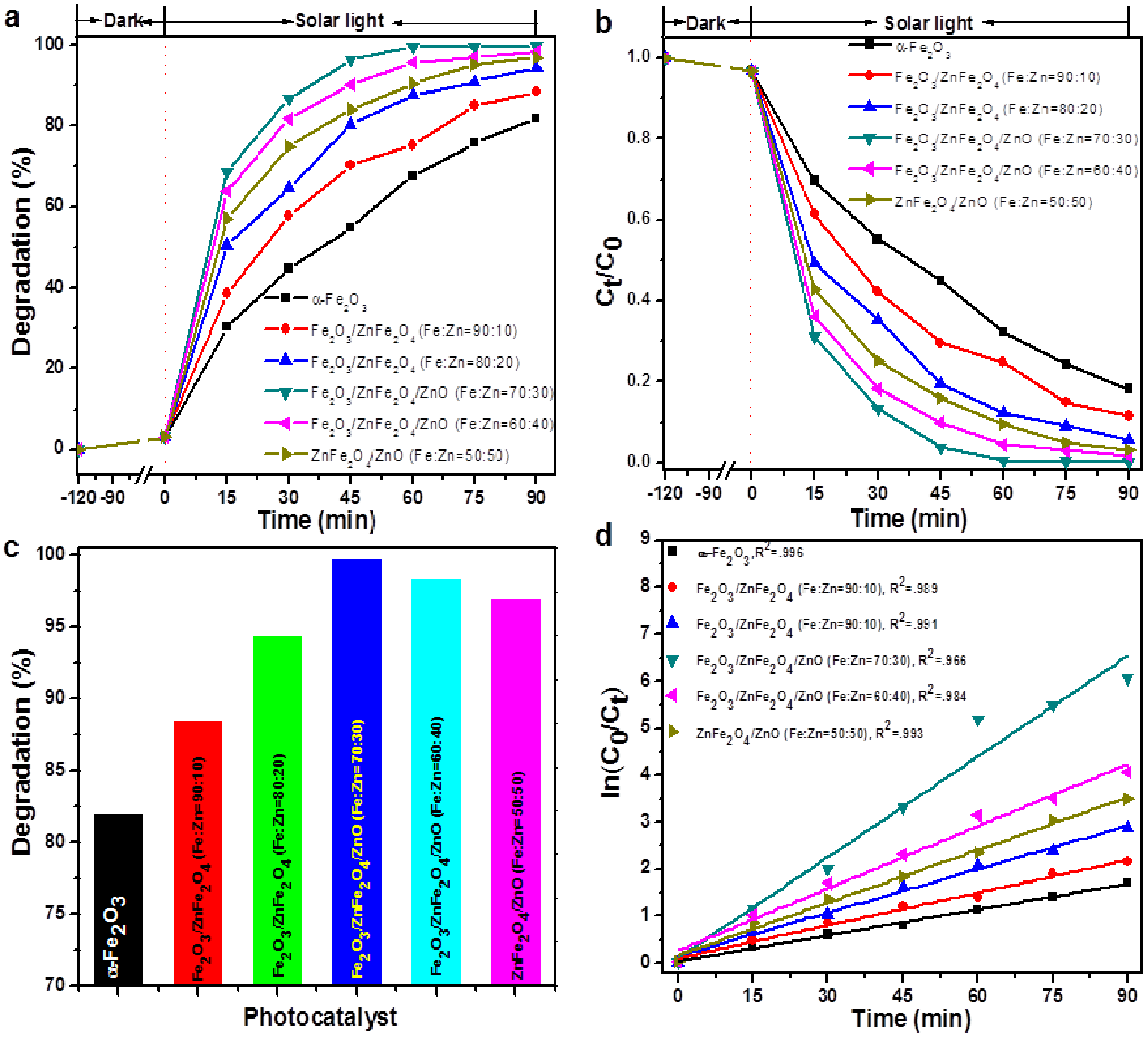

Figure 7.10 a) percentage of photocatalytic degradation, b) concentration changes of MG, c) degradation of MG over all the synthesized photocatalysts and, d) pseudo-first-order reaction kinetic linear relationship curves for different photocatalysts (100 ml of 20 mg L^{-1} MG solution, 0.1 g catalyst and natural solution pH).

The degradation patterns suggested that the degradation of MG followed a pseudo-first order kinetic model and the rate constant could be determined according to the following equation (Chandraboss et al., 2015):

$$\ln\left(\frac{C_0}{C_t}\right) = kKt = k_{app}t \qquad (7.4)$$

where r is the reaction rate (mol L^{-1} min^{-1}), C_0 is the initial concentration of MG dye (mol L^{-1}), C_t is the concentration of MG dye at time t (mol L^{-1}), t is the irradiation time (min), k is the reaction rate constant (min^{-1}), K is the adsorption coefficient of dye on a photocatalyst particle (L mol^{-1}). Figure 7.10d shows the graph of $\ln(C_0/C_t)$ versus reaction time (t). The reaction rate constants (K_1) for all the six photocatalysts were determined from the slope of the fitted curves (figure 7.10d) by means of linear regression and the values are given in table 7.1. All the plots show a linear relationship with good correlation coefficient ($R^2 > 0.966$), indicating that the MG degradation by the prepared photocatalysts under natural solar light degradation follows the pseudo-first-order kinetic model below: Here, it is observed that the highest apparent reaction rate constants k_{app}, 0.0714 min^{-1} was calculated for $Fe_2O_3/ZnFe_2O_4/ZnO$ (Fe:Zn=70:30) nanocomposite. Furthermore, the extent of mineralization is evaluated by measuring the total organic carbon (TOC). After solar light irradiation for 90 min, the percentage of mineralization was found to be 71 % by using $Fe_2O_3/ZnFe_2O_4/ZnO$ (Fe:Zn=70:30) nanocomposite photocatalyst (0.1 g) in 100 ml of 20 mg L^{-1} MG solution.

Table 7.1 Percentage of degradation and pseudo-first-order kinetic parameters of MG

Photocatalyst	Degradation (%)	K_1 (min^{-1})	R^2
α-Fe_2O_3	81.86	0.0183	0.996
$Fe_2O_3/ZnFe_2O_4$ (Fe:Zn=90:10)	88.37	0.0231	0.989
$Fe_2O_3/ZnFe_2O_4$ (Fe:Zn=80:20)	94.37	0.0309	0.991
$Fe_2O_3/ZnFe_2O_4/ZnO$ (Fe:Zn=70:30)	99.77	0.0714	0.966
$Fe_2O_3/ZnFe_2O_4/ZnO$ (Fe:Zn=60:40)	98.29	0.0441	0.984
$ZnFe_2O_4/ZnO$ (Fe:Zn=50:50)	96.92	0.0373	0.993

The stability of catalysts is an important issue for their practical applications. To prove the stability and the reusability of $Fe_2O_3/ZnFe_2O_4/ZnO$ (Fe:Zn=70:30) nanocomposite photocatalyst, we have repeated it four times for degradation of the MG and the result is shown in figure 7.11. Here, we have calculated the percentage of degradation only after dark reaction. As can be seen, the repeatability of the entire process and the final result of degradation of MG are very good, which further demonstrate the excellent efficiency of the photocatalyst.

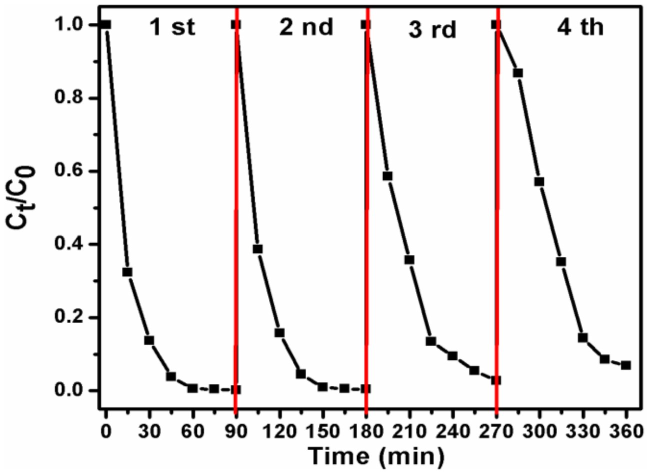

Figure 7.11 Repeating experiments for the photocatalytic degradation of MO using $Fe_2O_3/ZnFe_2O_4/ZnO$ (Fe:Zn=70:30) nanocomposite under solar light irradiation.

7.3.3. Mechanism on enhancement of photocatalytic activity

The photocatalytic activity is influenced by some crucial factors like surface area, optical absorption, phase structure and separation efficiency of photo-generated charge carriers (Aslam et al., 2015). From the experimental results, it is observed that the photocatalytic activities of $Fe_2O_3/ZnFe_2O_4$, $Fe_2O_3/ZnFe_2O_4/ZnO$ and $ZnFe_2O_4/ZnO$ nanocomposites are higher than that of pristine α-Fe_2O_3 nanoparticle. This can be attributed to the formation of the hetero-nanostructure. The evolution of phase/nanocomposites with addition of Zn salt precursor up to 30 % results with (a) increased surface area, (b) reduced band gap and (c) easily separation of generated electron-hole pair due to formation of hetero-nanostructures. But for $Fe_2O_3/ZnFe_2O_4/ZnO$ (Fe:Zn=70:30) nanocomposites, additional mechanism of cascade electron transfer is presumed due to the presence of ternary hybrid structure; which is not possible in binary hybrid/composite system. Similar type of evidences is also reported by Kim et al. (2011). The mechanism is schematically described in figure 7.12. When the $Fe_2O_3/ZnFe_2O_4/ZnO$ (Fe:Zn=70:30) ternary nanocomposite was irradiated by solar light, the energy of solar light exceeds band gap of $ZnFe_2O_4$ (1.92 eV), the VB e^- of $ZnFe_2O_4$ were excited to CB (E_{CB} = -1.54 V_{NHE}) creating h^+ in the VB. Then the photogenerated e^- of $ZnFe_2O_4$ was immediately transferred to CB of ZnO (E_{CB} = -0.31 V_{NHE}). Again the photogenerated e^- from ZnO were transferred to the CB of α-Fe_2O_3 (E_{CB} = +0.35 V_{NHE}). As a result, a high concentration of free electrons was formed in the conduction band of α-Fe_2O_3. This makes the charge separation more effective and hence the electrons and holes migrate to the surface of respective particles and participate in the redox reaction. In the reaction mechanism, the photogenerated electrons reduced the dissolved oxygen into peroxide ($^-O_2^\bullet$) or hydroxyl ($HO^\bullet$) radicals; meanwhile the photogenerated holes likely to oxidize H_2O to form $HO^\bullet$ radicals. The $HO^\bullet$ radicals form both the process can effectively oxidize MG into minerals as end products (Ahmed et al., 2015; Lin et al., 2013; Dai et al., 2014). But in case of only $ZnFe_2O_4$ or α-Fe_2O_3 single phase, the usual recombination of electron-hole pairs takes place and a few of e^- and h^+ can participate in photocatalytic process.

For addition of 40 % Zn salt precursor, the percentage of ZnO phase in the $Fe_2O_3/ZnFe_2O_4/ZnO$ (Fe:Zn=60:40) nanocomposite is increased with slightly increase in the net band gap of nanocomposite. This results in the decrease of photocatalytic activity compared to $Fe_2O_3/ZnFe_2O_4/ZnO$ (Fe:Zn=70:30) nanocomposite. Again for 50 % Zn salt precursor, the formation of binary $ZnFe_2O_4/ZnO$ (Fe:Zn=50:50) phase is observed. Therefore cascade electron transfer is not possible and electron-hole pair recombination becomes more predictable mechanism. Hence, the photocatalytic activity for degradation of MG dye was found to be highest for $Fe_2O_3/ZnFe_2O_4/ZnO$ (Fe:Zn=70:30) nanocomposites than the series of photocatalysts prepared by varying the mole % of Zn from 10-50 %.

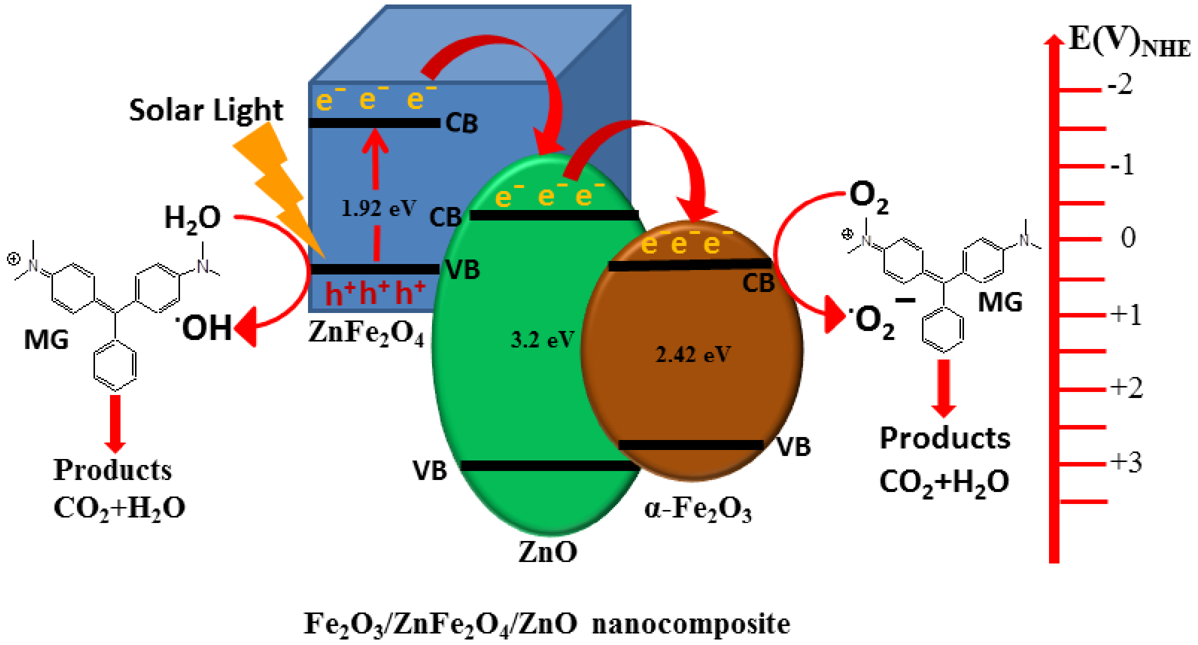

Figure 7.12 A proposed solar light photodegradation mechanism of $Fe_2O_3/ZnFe_2O_4/ZnO$ nanocomposite.

To examine photogenerated charge transfer pathways, photoluminescence (PL) emission spectra were obtained for the nanomaterials excited at wavelengths of 420 nm with 5/5 slit. The PL spectrum is related to the transfer behavior of the photoinduced electrons and holes so that it can reflect the separation and recombination of photoinduced charge carriers (Liu et al., 2007; Khan et al., 2013). Figure 7.13 shows the PL spectra of pure α-Fe_2O_3, Fe_2O_3/$ZnFe_2O_4$ (Fe:Zn=90:10), Fe_2O_3/$ZnFe_2O_4$ (Fe:Zn=80:20), Fe_2O_3/$ZnFe_2O_4$/ZnO (Fe:Zn=70:30), Fe_2O_3/$ZnFe_2O_4$/ZnO (Fe:Zn=60:40) and $ZnFe_2O_4$/ZnO (Fe:Zn=50:50) nanoparticles. It can be seen that the PL intensity decreased dramatically when the α-Fe_2O_3 was coupled with the $ZnFe_2O_4$ to form Fe_2O_3/$ZnFe_2O_4$ nanocomposites. The reason behind the decrease in intensity is formation of heterojunctions between Fe_2O_3 and $ZnFe_2O_4$. The potential difference between Fe_2O_3 and $ZnFe_2O_4$ allowed photoelectrons to easily migrate from the Fe_2O_3 surfaces to the $ZnFe_2O_4$ conduction band. This resulted in a decrease in the radiation combination of photoinduced electrons on the composite surfaces and hence weakening the PL intensity. In case of Fe_2O_3/$ZnFe_2O_4$/ZnO, the decrease in PL intensity is more significant and lowest for Fe_2O_3/$ZnFe_2O_4$/ZnO (Fe:Zn=70:30). After that in case of $ZnFe_2O_4$/ZnO (Fe:Zn=50:50) the PL intensity increases. This indicates that the ternary nanocomposites are more effective in inhibiting the charge recombination than binary nanocomposite. It is presumed that photogenerated electrons are effectively transported from $ZnFe_2O_4$ to Fe_2O_3 through ZnO. This is considerable evidence for the cascaded electron transfer.

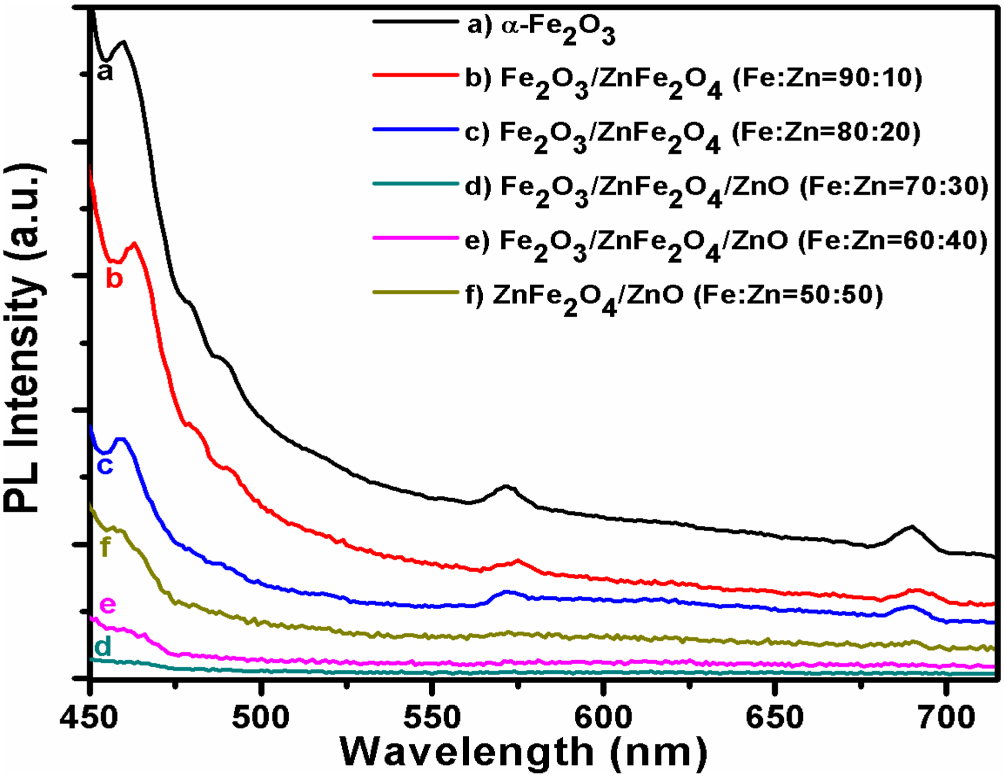

Figure 7.13 Photoluminescence emission spectra of a) α-Fe_2O_3 nanoparticle, b) Fe_2O_3/$ZnFe_2O_4$ (Fe:Zn=90:10), c) Fe_2O_3/$ZnFe_2O_4$ (Fe:Zn=80:20), d) Fe_2O_3/$ZnFe_2O_4$/ZnO (Fe:Zn=70:30), e)Fe_2O_3/$ZnFe_2O_4$/ZnO (Fe:Zn=60:40), f) $ZnFe_2O_4$/ZnO (Fe:Zn=50:50) nanocomposites an excitation wavelength of 420 nm.

7.4. Conclusions

In summary, we have synthesized natural solar light sensitive photocatalysts of α-Fe_2O_3 nanoparticles and $Fe_2O_3/ZnFe_2O_4$, $Fe_2O_3/ZnFe_2O_4/ZnO$ and $ZnFe_2O_4/ZnO$ nanocomposites with various morphologies by a facile hydrothermal method. Morphology, crystalline phase, BET surface area and optical absorption of the nanostructures are strongly influenced by the molar ratio of Fe^{3+} and Zn^{2+}. XRD result gives the well crystalline nature of the prepared samples with appropriate phase without the presence of any impurity. From FE-SEM, we have observed irregular shape α-Fe_2O_3 nanoparticles having diameter in the range of 80-100 nm, which gradually becomes cubical shape in due formation of $Fe_2O_3/ZnFe_2O_4/ZnO$ & $ZnFe_2O_4/ZnO$ mixed oxide nanocomposite with an increase in zinc content. The narrow band gap semiconducting nature of the samples was analyzed by UV-Vis-DRS technique. This prepared composite nanomaterials were used for photocatalytic degradation of Malachite green (MG) under natural solar light. It was observed that the nanocomposites show enhanced photocatalytic activity compared to pristine α-Fe_2O_3 nanoparticles. The $Fe_2O_3/ZnFe_2O_4/ZnO$ (Fe:Zn=70:30) exhibits highest photocatalytic activity than other compositions. It is due to the effective cascaded electron transfer of photogenerated electrons from $ZnFe_2O_4$ to Fe_2O_3 through ZnO.

CHAPTER-8

SUMMARY AND CONCLUSIONS

In this research work, we have successfully synthesized different metal oxide nanomaterials especially iron oxides and iron oxide based mixed oxide composites nanomaterials such as Fe_2O_3-SnO_2, Fe_2O_3-CuO, $Fe_2O_3/ZnFe_2O_4/ZnO$ and $MgFe_2O_4/Fe_2O_3$ using precipitation, hydrothermal and reflux methods. We have also prepared iron oxide impregnated mesoporous MCM-41 by wet chemical impregnated method. The formation, phase, structure, size, shape, surface morphology, surface area and sorption studies of the synthesized iron based mixed oxide composite nanomaterials have been characterized by using different characterization techniques such as: XRD, SEM, FESEM, EDAX, TEM, XPS, FTIR, UV-VIS and BET analytical techniques. The obtained composite nanomaterials were used as adsorbents and photocatalysts for adsorptive removal and photocatalytic degradation of toxic organic dyes. Both cationic and anionic dyes having different functional groups such as Congo red (CR), Methylene blue (MB), Malachite green (MG) and Methyl orange (MO) have been selected as model organic pollutants in this study. The following major conclusions have been drawn from this study.

MAJOR CONCLUSIONS

- Among the three Fe based nanorods ($FeC_2O_4.2H_2O$, γ-Fe_2O_3 and α-Fe_2O_3) synthesized by precipitation method, maghemite (γ-Fe_2O_3) nanorods are demonstrated as very good adsorbent for removal of Congo red (CR) dye with maximum sorption capacity of 232 mg/g.
- The rod shaped Fe_2O_3-SnO_2 composite nanomaterials were synthesized by same precipitation method by varying the molar ratio of Fe and Sn salt precursors. The diameter of the nanocomposite were found to be in the range of 100-200 nm
- Presence of SnO_2 in the Fe_2O_3 matrix selectibly stablizes the γ-Fe_2O_3 phase in the Fe_2O_3-SnO_2 nanocomposite. The Fe_2O_3–SnO_2 (Fe: Sn = 8: 2) composite nanorod showed highest percentage adsorption with sorption capacity of 182 mg/g, which is better than that of α-Fe_2O_3 nanomaterials.
- The iron oxide impregnated mesoporous MCM-41 (Fe-MCM-41) prepared by a facile wet chemical method and is regarded as a very efficient adsorbent for removal of Methylene blue (MB) dye. It is observed that the impregnation of iron oxides into

MCM-41 matrix improve the sorption performances. The maximum sorption capacity of Fe-MCM-41 is found to be 194 mg/g.

- MgO nanostructures with different morphologies have been prepared by using above mentioned wet chemical methods. Among the various prepared MgO nanostructures, the hierarchical MgO nanomaterials prepared by reflux method exibits excellent sorption capacities of 1205 and 1051 mg/g, for the adsorptive removal of Malachite green and Congo red dyes, respectively from aqueous syetem.
- An attempt has been made to prepare Fe_2O_3-MgO using the identical synthetic procrdure. Intrestingly, we have obtained $MgFe_2O_4$-Fe_2O_3 nanocomposites. The $MgFe_2O_4$-Fe_2O_3 nanocomposite prepared by precipitation method was found to be an efficient visible light photocatalyst for effective degradation of Methylene blue.
- We have also prepared Fe_2O_3-CuO nanocomposite by precipitation method, which exhibits enhanced photocatalytic activity than individual Fe_2O_3 and CuO nanoparticles for degradation of Methyl orange from aqueous media under solar light irradiation.
- Furthermore, the Fe_2O_3-ZnO mixed oxide nanocomposites obtained by varying different molar ratio of Fe and Zn salt contents using hydrothermal method. Depending upon the composition, Fe_2O_3-$ZnFe_2O_4$, Fe_2O_3-$ZnFe_2O_4$-ZnO and $ZnFe_2O_4$-ZnO mixed oxide nanocomposites were obtained in single step.
- Among all the nanocomposite materials, the ternary Fe_2O_3-$ZnFe_2O_4$-ZnO (Fe:Zn=70:30) nanocomposite exhibits highest photocatalytic activity for catalytic degradation of Malachite green using solar light irradiation. The mechanism of degradation follows a cascade electron transfer from $ZnFe_2O_4$ to ZnO to Fe_2O_3 in the ternary hybrid nanostructure.

REFERENCES

Afkhami, A. and Moosavi, R., “Adsorptive removal of Congo red, a carcinogenic textile dye, from aqueous solutions by maghemite nanoparticles,” J. Hazard. Mater., **174**, 398-403 (2010).

Afkhami, A., Saber-Tehran, M. and Bagheri H., “Modified maghemite nanoparticles as an efficient adsorbent for removing some cationic dyes from aqueous solution,” Desalination., **263**, 240–248 (2009).

Ahmad, R., and Kumar, R., “Conducting Polyaniline/Iron Oxide Composite: A Novel Adsorbent for the Removal of Amido Black 10B,” J. Chem. Eng. Data, **55**, 3489–3493 (2010).

Ahmad, R., Vaseem, M., Tripathy, N., and Hahn, Y., “Wide Linear-Range Detecting Nonenzymatic Glucose Biosensor Based on CuO Nanoparticles Inkjet-Printed on Electrodes,” Anal. Chem., **85**, 10448−10454 (2013).

Ahmed, M. N. Z., Chandrasekhar, K. B., Jahagirdar, A. A., Nagabhushana, H., and Nagabhushana, B. M., “Photocatalytic activity of nanocrystalline ZnO, α-Fe_2O_3 and $ZnFe_2O_4$/ZnO,” Appl. Nanosci., DOI 10.1007/s13204-014-0395-1 (2015).

Ahmed, M. N. Z., Chandrasekhar, K. B., Jahagirdar, A. A., Nagabhushana, H., and Nagabhushana, B. M., “Photocatalytic activity of nanocrystalline ZnO, α-Fe_2O_3 and $ZnFe_2O_4$/ZnO,” Appl. Nanosci., DOI: 10.1007/s13204-014-0395-1 (2015).

Akhbarizadeh, R., Shayestefar, M. R., Darezereshki, E., “Competitive removal of metals from wastewater by maghemite nanoparticles: A comparison between simulated wastewater and AMD,” Mine. Water Environ., **33**, 89–96 (2014).

Alshammari, A. S., Chi, L., Chen, X., Bagabas, A., Kramer, D., Alromaeh, A., and Jiang, Z., “Visible-light photocatalysis on C-doped ZnO derived from polymer-assisted pyrolysis,” RSC Adv., **5**, 27690–27698 (2015).

Anandan, S., Lee, G. J., Chen, P. K., Fan, C. and Wu, J. J., “Removal of Orange II Dye in Water by Visible Light Assisted Photocatalytic Ozonation Using Bi_2O_3 and Au/Bi_2O_3 Nanorods,” Ind. Eng. Chem. Res., **49**, 9729–9737 (2010).

Anbia, M., and Hariri, S. A., “Removal of methylene blue from aqueous solution using nanoporous SBA-3,” Desalination, **261**, 61–66 (2010).

Asama. N. N., Azhar S. N. and Abdulla. M. S., “Preparation and Characterization of SnO_2 Nanoparticles,” Int. J. Innov. Res. Sci. Eng. Technol., **2**, 7068-7072 (2013).

Asiltürk, M., Sayılkan F., and Arpac, E., “Effect of Fe^{3+} ion doping to TiO_2 on the photocatalytic degradation of Malachite Green dye under UV and vis-irradiation,” J. Photochem. Photobiol., A, **203**, 64–71 (2009).

Aslam, I., Cao, C., Tanveer, M., Farooq, M. H., Khan, W. S., Tahir, M., Idreesa, F., and Khalid, S., “A novel Z-scheme WO_3/$CdWO_4$ photocatalyst with enhanced visible-light photocatalytic activity for the degradation of organic pollutants,” RSC Adv., **5**, 6019–6026 (2015).

Attallah, M. F., Ahmed, I. M. and Hamed, M. M., “Treatment of industrial wastewater containing Congo Red and Naphthol Green B using low-cost adsorbent,” Environ. Sci. Pollut. Res., **20**, 1106–1116 (2013).

Ayad, M. M., El-Nasr, A. A., and Stejskal, J., “Kinetics and isotherm studies of methylene blue adsorption onto polyaniline nanotubes base/silica composite,” Journal of Industrial and Engineering Chemistry, **18**, 1964–1969 (2012).

Azami, M., Bahram, M., Nouri, S., and Naseri, A., “A central composite design for the optimization of the removal of the azo dye, methyl orange, from waste water using the Fenton reaction,” J. Serb. Chem. Soc., **77**, 235–246 (2012).

Azhari, A., Sharif, Sh. M., Golestanifard, F. and Saberi, A., “Phase evolution in Fe_2O_3/MgO nanocomposite prepared via a simple precipitation method,” Mater Chem. Phys., **124** 658–663 (2010).

Bachari, K., Chebout, R., Guerroudj, R. M., and Lamouchi, M., “Properties and reactivity of Fe-MCM-41 catalysts prepared by microwave irradiation method for acetylation of 1,2-dimethoxybenzene,” J. Porous Mater., **19**, 615–622 (2012).

Bagheri, S., Chandrappa, K. G., and Hamid, S. B. A., “Facile synthesis of nano-sized ZnO by direct precipitation method,” Der Pharma Chemica., **5**, 265-270 (2013).

Bakhtiari F. and Darezereshki, E., “One-step synthesis of tenorite (CuO) nano-particles from $Cu_4(SO_4)(OH)_6$ by direct thermal-decomposition method,” Mater. Lett., **65**, 171–174 (2011).

Balamurugan, S., Ashna, L., and Parthiban, P., “Synthesis of Nanocrystalline MgO Particles by Combustion Followed by Annealing Method Using Hexamine as a Fuel,” Journal of Nanotechnology, Article ID 841803, DOI: 10.1155/2014/841803 (2014).

Balzani, V., “Nanoscience and nanotechnology: A personal view of a chemist,” Small, **1**, 278–283 (2005).

Bandgar, A. B., Sabale, S. R., and Pawar, S. H., “Synthesis of nanocrystalline titanium dioxide using refluxed aqueous peroxy titanium complex solution,” Micro Nano Lett., **6**, 816–819 (2011).

Barakat, N. A. M., Kanjwal, M. A., Chronakis, I. S., and Kim, H. Y., “Influence of temperature on the photodegradation process using Ag-doped TiO_2 nanostructures: Negative impact with the nanofibers,” J.Mol. Catal. A Chem., **366**, 333–340 (2013).

Baruwati, B., Rana, R. K. and Manorama, S. V., “Further insights in the conductivity behavior of nanocrystalline $NiFe_2O_4$,” J. Appl. Phys. 101, 014302 (2007).

Basu, T. and Ghosh, U. C., “Nano-structured iron(III)–cerium(IV) mixed oxide: Synthesis, characterization and arsenic sorption kinetics in the presence of co-existing ions aiming to apply for high arsenic groundwater treatment,” Appl. Surf. Sci., **283**, 471– 481 (2013).

Batista, A. P. L., Carvalho, H. W. P., Luz, G. H. P., Martins, P. F. Q., Goncalves, M., and Oliveira, L. C. A., “Preparation of CuO/SiO_2 and photocatalytic activity by degradation of methylene blue,” Chem. Lett., **8**, 63–67 (2010).

Bayazit, Ş. S., “Magnetic Multi-Wall Carbon Nanotubes for Methyl Orange Removal from Aqueous Solutions: Equilibrium, Kinetic and Thermodynamic Studies,” Separ. Sci. Technol., **49**, 1389–1400 (2014).

Bayazit, S. S., and Inci, I., “Adsorption of Pb(II) ions from aqueous solutions by carbon nanotubes oxidized different methods,” J. Ind. Eng. Chem., **19**, 2064–2071, (2013).

Bayazit, S. S., Inci, I., and Uslu, H., “Adsorption of Glutaric Acid and Glyoxylic Acid onto Weakly Basic Ion-Exchange Resin: Equilibrium and Kinetics,” J. Chem. Eng. Data, **55**, 679–684 (2010).

Bengoa, J. F., Fellenz, N. A., Cagnoli, M. V., Cano, L. A., Gallegos, N. G., Alvarez, A. M., and Marchetti, S. G., “Fe/MCM-41 sylilated catalyst: structural changes determination during the Fischer–Tropsch reaction,”Hyperfine Interact., **195**, 5–13 (2010).

Bharadwaj, L., Bhardwaj, M., and Sharma, M. K., “An analysis of Fe_2O_3 assisted photocatalytic degradation of Congo red dye,” Toxicol. Environ. Health. Sci., **4**, 62-69 (2012).

Bharathi, S., Nataraj, D., Mangalaraj, D., Masuda, Y., Senthil, K., and Yong, K., “Highly mesoporous α-Fe_2O_3 nanostructures: preparation, characterization and improved photocatalytic performance towards Rhodamine B (RhB),” J. Phys. D: Appl. Phys., **43**, 015501 (2010).

Bhattacharjee, A., Ahmaruzzaman, Md., and Sinha, T., “Surfactant effects on the synthesis of durable tin-oxide nanoparticles and its exploitation as a recyclable catalyst for the elimination of toxic dye: a green and efficient approach for wastewater treatment,” RSC Adv., **4**, 51418–51429 (2014).

Bhattacharyya, K. G. and Sharma, A., “Azadirachta indica leaf powder as an effective biosorbent for dyes: a case study with aqueous Congo Red solutions,” J. Environ. Manage., **71**, 217-229 (2004).

Bhoumik, M., Maity, A., Srinivasu, V.V., and Onyango M. S., “Enhanced removal of Cr(VI) from aqueous solution using polypyrrole/Fe_3O_4 magnetic nanocomposite,” J. Hazard. Mater., **190**, 381-390 (2011).

Binupriya, A. R., Sathishkumar, M., Swaminathan, K., Ku, C. S. and Yun, S. E., “Comparative studies on removal of Congo red by native and modified mycelial pellets of Trametes versicolor in various reactor modes,” Bioresource Technology **99**, 1080-1088 (2008).

Borel, N. N. M., Foba-Tendo, J., Yufanyi, D. M., Etape, E. P., Eko, J. N. and Ngolui, L. J., "Averrhoa carambola: A Renewable Source of Oxalic Acid for the Facile and Green Synthesis of Divalent Metal (Fe, Co, Ni, Zn, and Cu) Oxalates and Oxide Nanoparticles," Journal of Applied Chemistry, Article ID **767695** (2014).

Bose, A. C., Kalpana, D., Thangadurai, P., and Ramasamy, S., "ynthesis and characterization of nanocrystalline SnO_2 and fabrication of lithium cell using nano-SnO_2," J. Power Sources, **107**, 138–141 (2002).

Byrappa, K., and Adschiri, T., "Hydrothermal technology for nanotechnology," Prog. Cryst. Growth Charact. Mater., **53**,117-166 (2007).

Callister, W. D., Jr., Calister's Material Science and Engineering.New Delhi: Wiley India (P) Ltd, (2007).

Camargo, P. H. C., Satyanarayana, K. G., and Wypych, F., "Nanocomposites: synthesis, structure, properties and new application opportunities," Mater. Res., **12**, 1-39, (2009).

Cao, C., Qu, J., Wei, F., Liu, H., and Song, W., "Superb Adsorption Capacity and Mechanism of Flowerlike Magnesium Oxide Nanostructures for Lead and Cadmium Ions," ACS Appl. Mater. Interfaces, 4, 4283−4287 (2012).

Cao, C., Xiao, L., Chen, C. and Cao, Q., "Magnetically separable Cu_2O/chitosan–Fe_3O_4 nanocomposites: Preparation, characterization and visible-light photocatalytic performance," Appl. Surf. Sci., **333**, 110–118(2015).

Cao, C., Xiao, L., Chen, C., Shi, X., Cao, Q., Gao, and L., "In situ preparation of magnetic Fe_3O_4/chitosan nanoparticles via a novel reduction–precipitation method and their application in adsorption of reactive azo dye," Powder Technol., **260**, 90–97 (2014).

Cao, G., Su, L., Zhang, X., and Li, H., "Hydrothermal synthesis and catalytic properties of a- and b-MnO_2 nanorods," Mater. Res. Bull., **45**, 425-428 (2010).

Cao, J., Wang, Y., Yu, X., Wang, S., Wu, S., and Yuan, Z., "Mesoporous CuO–Fe_2O_3 composite catalysts for low-temperature carbon monoxide oxidation," Appl. Catal. B, **79**, 26–34 (2008).

Cao, S., and Zhu, Y., "Hierarchically Nanostructured α-Fe_2O_3 Hollow Spheres: Preparation, Growth Mechanism, Photocatalytic Property, and Application in Water Treatment," J. Phys. Chem. C, **112**, 6253-6257 (2008).

Carrillo, A. I., Serrano, E., Luque, R., and García-Martínez, J., "Microwave-assisted catalysis by iron oxide nanoparticles on MCM-41: Effect of the support morphology," Appl. Catal., A, **453**, 383– 390 (2013).

Chakraborty, S., Purkait, M. K., Dasgupta, S., De, S. and Basu J. K. "Nanofiltration of textile plant effluent for color removal and reduction in COD," Sep. Purif. Technol., **31**, 141–151 (2003).

Chan, L. S., Cheung, W. H., Allen S. J, and McKay G., "Separation of acid-dyes mixture by bamboo derived active carbon," Sep. Purif. Technol., **67**, 166-172 (2009).

Chandraboss, V. L., Kamalakkannan, J., Prabha, S., and Senthilvelan, S., “An efficient removal of methyl violet from aqueous solution by an AC-Bi/ZnO nanocomposite material,” RSC Adv., **5**, 25857–25869 (2015).

Chang, T., Li, Z., Yun, G., Jia, Y., Yang, H., “Enhanced Photocatalytic Activity of ZnO/CuO Nanocomposites Synthesized by Hydrothermal Method,” Nano-Micro Lett. **5**, 163-168 (2013).

Charanpahari, A., Ghugal, S. G., Umare, S. S., and Sasikala, R., “Mineralization of malachite green dye over visible light responsive bismuth doped TiO_2–ZrO_2 ferromagnetic nanocomposites,” New J. Chem., **39**, 3629-3638 (2015).

Chatterjee, S, Lee, MW, Woo, SH “Adsorption of congo red by chitosan hydrogel beads impregnated with carbon nanotubes,” Bioresource Technology **101**, 1800-1806 (2010).

Chatterjee, S., Lee M. W. and Woo S. H., “Enhanced adsorption of Congo red from aqueous solutions by chitosan hydrogel beads impregnated with cetyl trimethyl ammonium bromide,” Bioresource Technology **100**, 2803-2809 (2009).

Chaudhari S. and Srinivasan, M., “1D hollow α-Fe_2O_3 electrospun nanofibers as high performance anode material for lithium ion batteries,” J. Mater. Chem., **22**, 23049–23056 (2012).

Chaudhary, G. R., Saharan, P., Mehta, S. K., Mor, S., and Umar, A., “Fast and efficient removal of hazardous congo red from its aqueous solution using γ-Fe_2O_3 nanoparticles,” J. Nanoeng. Nanomanuf., **3**, 142–146, (2013).

Chaudhuri, R. G., and Paria, S., “Core/shell nanoparticles: classes, properties, synthesis mechanisms, characterization, and applications,” Chem. Rev., **112**, 2373–243 (2012).

Chen, C. C., Lu, C. S., Chung, Y. C., and Jan, J. L., “UV light induced photodegradation of malachite green on TiO_2 nanoparticles,” Journal of Hazardous Materials, **141**, 520–528 (2007).

Chen, C. C., Liu, P. and Lu, C., “Synthesis and characterization of nano-sized ZnO powders by direct precipitation method,” Chem. Eng. J., **144**, 509–513 (2008).

Chen, H. and Zhao, J “Adsorption study for removal of Congo red anionic dye using organo-attapulgite,” Adsorption **15**, 381-389 (2009).

Chen, L., Wang, H., Wei, H., Guo, Z., Khan, M. A., Young D. P., and Zhu, J., “Carbon monolith with embedded mesopores and nanoparticles as a novel adsorbent for water treatment,” RSC Adv., **5**, 42540–42547 (2015).

Chen, L., Zhang, Q., Huang, R., Yin, S., Luo, S., and Au, C., “Porous peanut-like Bi_2O_3–$BiVO_4$ composites with heterojunctions: one-step synthesis and their photocatalytic properties,” Dalton Trans., **41**, 9513-9518 (2012).

Chen, M., Chen, Y., and Diao, G., “Adsorption kinetics and thermodynamics of methylene Blue onto p-tert-Butyl-calix[4,6,8]arene-bonded silica gel,” J. Chem. Eng. Data, 55, 5109–5116 (2010).

Chen, Wang, W, Zhao, X., Zhang, Y., Wu, S., and Li, F., “Rapid hydrothermal synthesis of magnetic $Co_xNi_{1-x}Fe_2O_4$ nanoparticles and their application on removal of Congo red,” Chemical Engineering Journal, **242**, 226–233 (2014).

Chen, X., Lam, K. F., and Yeung, K. L., “Selective removal of chromium from different aqueous systems using magnetic MCM-41 nanosorbents,” Chem. Eng. J., **172**, 728–734 (2011).

Chen, X., Zhang, Z., Qiu, Z., Shi, C., Li, X., “A facile biomolecule-assisted approach for fabricating α-Fe_2O_3 nanowires in solution,” Solid State Commun., **140**, 267–269 (2006).

Cheng, B., Le, Y., Cai, W. and Yu, J., “Synthesis of hierarchical $Ni(OH)_2$ and NiO nanosheets and their adsorption kinetics and isotherms to Congo red in water,” J. Hazard. Mater., **185**, 889–897 (2011).

Cheng, W., Deka, J. R., Chiang, Y., “Antoine Rogeau, and Shih-Yuan Lu, One-Step, Surfactant-Free Hydrothermal Method for Syntheses of Mesoporous TiO_2 Nanoparticle Aggregates and Their Applications in High Efficiency Dye-Sensitized Solar Cells,” Chem. Mater., **24**, 3255−3262 (2012).

Cherian, C. T., Sundaramurthy, J., Kalaivani, M., Ragupathy, P., Kumar, P. S., Thavasi, V., Reddy, M. V., Sow, C. H., Mhaisalkar, S. G., Ramakrishna S. and Chowdari, B. V. R., “Electrospun α-Fe_2O_3 nanorods as a stable, high capacity anode material for Li-ion batteries,” J. Mater. Chem., **22**, 12198–12204 (2012).

Choi, J., Yoon, S., Jang, S., and Ahn, W. S., “Phenol hydroxylation using Fe-MCM-41 catalysts,” Catal. Today, **111**, 280–287 (2006).

Chowdhury, A. K., Sarkar, A. D. and Bandyopadhyay, A., “Rice Husk Ash as a Low Cost Adsorbent for the Removal of Methylene Blue and Congo Red in Aqueous Phases,” Clean–Soil Air Water., **37**, 581-591 (2009).

Chowdhury, P., Moreira, J., Gomaa, H., and Ray, A. K., “Visible-solar-light-driven photocatalytic degradation of phenol with dye-sensitized TiO_2: Parametric and kinetic study,” Ind. Eng. Chem. Res., **51**, 4523-4532 (2012).

Chowdhury, S.R., and Yanful, E. K., “Arsenic and chromium removal by mixed magnetite-maghemite nanoparticles and the effect of phosphate on removal,” J. Environ. Manage., **92**, 2238-2247 (2010)..

Chu, D., Zeng, Y., Jiang, D., Masuda, Y., “In_2O_3–SnO_2 nano-toasts and nanorods: Precipitation preparation, formation mechanism, and gas sensitive properties,” Sensor Actuat. B, **137**, 630–636 (2009).

Ciesla, U., and Schuth, F., “Ordered mesoporous materials,” Micropor. Mesopor. Mat., **27**, 131–149 (1999).

Comini, E., Faglia, G., Ferroni, M., Ponzoni, A., Vomiero, A., and Sberveglieri, G., “Metal oxide nanowires: preparation and application in gas sensing,” J. Mol. Catal. A: Chem., **305**, 170–177 (2009).

Dai, K., Li, D., Lu, L., Liu, Q., Liang, C., Lv, J., Zhu, G., “Plasmonic $TiO_2/AgBr/Ag$ ternary composite nanosphere with heterojunction structure for advanced visible light photocatalyst,” Appl. Surf. Sci., **314**, 864-871 (2014).

Dai, P., Wang, Y., Wu, M. and Xu, Z., “Optical and magnetic properties of γ-Fe_2O_3 nanoparticles encapsulated in SBA-15 fabricated by double solvent technique,” Micro Nano Lett., **7**, 219 – 222 (2012).

Dang, T. D., Banerjee, A. N., Joo, S. W. and Min, B. K., “Effect of Potassium Ions on the Formation of Crystalline Manganese Oxide Nanorods via Acidic Reduction of Potassium Permanganate,” Ind. Eng. Chem. Res., **52**, 14154−14159 (2013).

Danwittayakul, S., Jaisai M., Koottatep, T., and Dutta, J., “Enhancement of photocatalytic degradation of methyl orange by supported zinc oxide nanorods/zinc stannate (ZnO/ZTO) on porous substrates,” Ind. Eng. Chem. Res., **52**, 13629−13636 (2013).

Daou, T. J., Pourroy, G., Be´gin-Colin, S., Grene`che, J. M., Ulhaq-Bouillet, C., Legare, P., Bernhardt, P., Leuvrey, C., and Rogez, G., “Hydrothermal synthesis of monodisperse magnetite nanoparticles,” Chem. Mater., **18**, 4399-4404 (2006).

Dara, M. A., Kim, Y. S., Kim, W. B., Sohn, J. M. and Shin, H. S., “Structural and magnetic properties of CuO nanoneedles synthesized by hydrothermal method,” Appl. Surf. Sci. **254**, 7477–7481 (2008).

Davoisne, C., Leroux, H., Frère, M., Gimblot, J., Gengembre, L., Djouadi, Z., Ferreiro, V., d’Hendecourt, L., and Jones, A., “Chemical and morphological evolution of a silicate surface under low-energy ion irradiation,” Astron. Astrophys., **482**, 541–548 (2008),

Dawood, S. and Sen, T. K., “Removal of anionic dye Congo red from aqueous solution by raw pine and acid-treated pine cone powder as adsorbent: Equilibrium, thermodynamic, kinetics, mechanism and process design,” Water Res., **46**, 1933-1946 (2012).

Deligeer, W., Gao, Y. W., and Asuha, S., “Adsorption of methyl orange on mesoporous γ-Fe_2O_3/SiO_2 nanocomposites,” Appl. Surf. Sci., **257**, 3524–3528 (2011).

Deng, J., Ma, J., Mei, L., Tang, Y., Chen, Y., Lv, T., Xu Z.and Wang, T., “Porous α-Fe_2O_3 nanosphere-based H_2S sensor with fast response, high selectivity and enhanced sensitivity,” J. Mater. Chem. A., **1**, 12400–12403 (2013).

Deng, J., Wang, L., Lou Z. and Zhang, T., “Design of CuO–TiO2 heterostructure nanofibers and their sensing performance,” J. Mater. Chem. A., **2**, 9030–9034 (2014).

Dhal, J. P., Mishra, B. G. and Hota, G., “Ferrous oxalate, maghemite and hematite nanorods as efficient adsorbents for decontamination of Congo red dye from aqueous system,” Int. J. Environ. Sci. Technol., **12**, 1845–1856 (2015).

Dhal, J. P., Mishra, B. G. and Hota, G., “Synthesis, Characterization and Photocatalytic Application of Ultra-Fine α-Fe_2O_3 Nanofiber,” Asian J. Chem., **25**, S22-S26 (2013).

Dhaouadi, H., Chaabane, H. and Touati, F., “$Mg(OH)_2$ Nanorods Synthesized by A Facile Hydrothermal Method in the Presence of CTAB,” Nano-Micro Lett., **3**, 153-159 (2011).

Dick, K. A., “A review of nanowire growth promoted by alloys and non-alloying elements with emphasis on Au-assisted III-V nanowires,” Prog. Cryst. Growth Charact. Mater., **54**, 138-173 (2008).

Dizge, N., Aydiner, C., Demirbas, E., Kobya, M. and Kara, S., “Adsorption of reactive dyes from aqueous solutions by fly ash: Kinetic and equilibrium studies,” J. Hazard. Mater., **150**, 737-746 (2008).

Djurisic, A. B., Ng, A. M. C., and Chen, X. Y., “ZnO nanostructures for optoelectronics: Material properties and device applications,” Prog. Quantum Electron., **34**, 191–259 (2010).

Dom, R., Subasri, R., Radha, K., Borse, P. H., “Synthesis of solar active nanocrystalline ferrite, MFe_2O_4 (M: Ca, Zn, Mg) photocatalyst by microwave irradiation,” Solid State Commun, **151**, 470–473 (2011).

Dong, S., Hu, L., Feng, J., Pi, Y., Li, Q., Li, Y., Liu, M., Sun, J., and Sun, J., “Ultrasonic-assisted rational design of uniform rhombus-shaped ZnMoOx on graphene for advanced sunlight-driven photocatalysts, functional supercapacitor electrodes, and antibacterial platforms,” RSC Adv., **4**, 64994–65003 (2014).

Du, N., Xu, Y., Zhang, H., Zhai, C. and Yang, D., “Selective Synthesis of Fe_2O_3 and Fe_3O_4 Nanowires Via a Single Precursor: A General Method for Metal Oxide Nanowires,” Nanoscale Res. Lett., **5**, 1295–1300 (2010).

Durán-Jiménez, G.. Hernández-Montoya, V., Montes-Morán, M. A., Bonilla-Petriciolet, A., Rangel-Vázquez, N. A., “Adsorption of dyes with different molecular properties on activated carbons prepared from lignocellulosic wastes by Taguchi method,” Micropor. Mesopor. Mat. **199**, 99–107 (2014).

Edelstein, A.S., and Cammaratra, R.C., “Nanomaterials: synthesis, properties and applications,” Second Edition, CRC Press, 01-Jan-1998, New York.

Elías, V., Vaschetto, E., Sapag, K., Olivac, M., Casuscelli, S., Eimer, G., “MCM-41-based materials for the photo-catalytic degradation of Acid Orange 7,” Catal. Today, 172, 58–65 (2011).

El-Molla, S. A., Fagal, G. A., Hassan, N. A. and Mohamed, G. M., “Effect of the method of preparation on the physicochemical and catalytic properties of nanosized Fe_2O_3/MgO,” Res. Chem. Intermed ., **41**, 679–689 (2015).

Fan, H. M., You, G. J., Li, Y., Zheng, Z., Tan, H. R., Shen, Z. X., Tang, S. H. and Feng, Y. P., “Shape-Controlled Synthesis of Single-Crystalline Fe_2O_3 Hollow Nanocrystals and Their Tunable Optical Properties,” J. Phys. Chem. C., **113**, 9928–9935 (2009).

Fang, X., Hu, L., Ye, C. and Zhang, L., “One-dimensional inorganic semiconductor nanostructures: A new carrier for nanosensors,” Pure Appl. Chem., **82**, 2185–2198 (2010).

Farre, M., Gajda-Schrantz, K., Kantiani, L., and Barcelo, D., “Ecotoxicity and analysis of nanomaterials in the aquatic environment,” Anal. Bioanal. Chem., **393**, 81–95 (2009).

Farshad Taleshi and Ali A Hosseini, Synthesis of uniform MgO/CNT nanorods by precipitation method, Journal of Nanostructure in Chemistry 2012, 3:4, DOI: 10.1186/2193-8865-3-4.

Fernandez-Garcia, M., Martinez-Arias, A., Hanson, J. C., and Rodriguez, J. A., “Nanostructured oxides in chemistry: characterization and properties,” Chem. Rev., **104**, 4063-4104 (2004).

Frost, R. L., Hong, T., Ma, H., and Yang, J., “Synthesis of MCM-41 Mesoporous Silica by Microwave Irradiation and ZnO Nanoparticles Confined in MCM-41,” Chin. J. Process Eng., **6**, 268-271 (2006).

Fu, Y. and Viraraghavan, T., “Removal of Congo Red from an aqueous solution by fungus Aspergillus niger.” Adv. Environ. Res., **7**, 239-247 (2002).

Fu, Z., Jiang, T., Liua, Z., Wang, D., Wang, L. and Xie, T., “Highly photoactive Ti-doped α-Fe_2O_3 nanorod arrays photoanode prepared by a hydrothermal method for photoelectrochemical water splitting,” Electrochim. Acta., **129**, 358–363 (2014).

Gao, C., Zhang, W., Li, H., Lang, L., and Xu, Z., “Controllable Fabrication of Mesoporous MgO with Various Morphologies and Their Absorption Performance for Toxic Pollutants in Water,” Cryst. Growth Des., **8**, 3785–3790 (2008).

Gao, P., Li, A., Sun, D. D. and Ng, W., J., “Effects of various TiO_2 nanostructures and graphene oxide on photocatalytic activity of TiO_2,” J. Hazard. Mater., **279**, 96-104 (2014)

Gao, Q., Luo, J., Wang, X., Gao C., and Ge, M., “Novel hollow α-Fe_2O_3 nanofibers via electrospinning for dye adsorption,” Nanoscale Res. Lett., 10, 176, DOI: 10.1186/s11671-015-0874-7 (2015).

Gao, R., Liang, Z., Tian, J., Zhang, Q., Wang, L. and Cao, G., “ZnO nanocrystallite aggregates synthesized through interface precipitation for dye-sensitized solar cells,” Nano Energy **2**,40-48 (2013).

Gaydhankar, T. R., Samuel, V., and Joshi, P. N., “Hydrothermal synthesis of MCM-41 using differently manufactured amorphous dioxosilicon sources,” Mater. Lett., **60**, 957–961 (2006).

Ge, F,, Ye, H,, Li, M. M. and Zhao, B. X., “Efficient removal of cationic dyes from aqueous solution by polymer-modified magnetic nanoparticles,” Chem. Eng. J., **198**, 11-17 (2012).

Genuino, H., Huang, H., Njagi, E., Stafford, L., and Suib, S. L., “A Review of Green Synthesis of Nanophase Inorganic Materials for Green Chemistry Applications,” Handbook of Green Chemistry, Volume 8: Green Nanoscience, First Edition, Wiley-VCH Verlag GmbH & Co. KGaA, (2012).

Ghaedi, M., Hassanzadeh, A., and Kokhdan, S. N., “Multiwalled Carbon Nanotubes as Adsorbents for the Kinetic and Equilibrium Study of the Removal of Alizarin Red S and Morin,” J. Chem. Eng. Data, 56, 2511–2520 (2011).

Giri, S. K., Das, N. N. and Pradhan, G. C., "Synthesis and characterization of magnetite nanoparticles using waste iron ore tailings for adsorptive removal of dyes from aqueous solution," Colloid. Surface A., **389**, 43–49 (2011).

Gómez-Solís, C., Juárez-Ramírez, I., Moctezuma, E., and Torres-Martínez, L. M., "Photodegradation of indigo carmine and methylene blue dyes in aqueous solution by SiC–TiO_2 catalysts prepared by sol–gel," J. Hazard. Mater., **217–218**, 194–199 (2012).

Goswami, A., Raul P. K., and Purkait, M. K., "Arsenic adsorption using copper (II) oxide nanoparticles," Chem. Eng. Res. Des., **90**, 1387–1396 (2012).

Gupta, K., and Ghosh, U. C., "Arsenic removal using hydrous nanostructure iron(III)–titanium(IV) binary mixed oxide from aqueous solution," Journal of Hazardous Materials, **161**, 884–892 (2009).

Gupta, V. K., Mittal, A., Krishnan, L., and Gajbe, V., "Adsorption kinetics and column operations for the removal and recovery of malachite green from wastewater using bottom ash," Separation and Purification Technology, **40**, 87–96 (2004).

Gupta, V. K., and Suhas, "Application of low-cost adsorbents for dye removal – A review," Journal of Environmental Management, **90**, 2313–2342 (2009).

Habibi, M. H. and Habibi, A. H., "Effect of the thermal treatment conditions on the formation of zinc ferrite nanocomposite, $ZnFe_2O_4$, by sol–gel method," J. Therm. Anal. Calorim., **113**, 843–847(2013).

Haider, S., Bukhari, N., Park, S. Y., Iqbal, Y. and Al-Masry W. A., "Adsorption of bromophenol blue from an aqueous solution onto thermally modified granular charcoal," Chem. Eng. Res. Des., **89**, 23-28 (2011).

Han, M., Sun, T., Tan, P. Y., Chen, X., Tan, O. K., Tse, M. S., "m-$BiVO_4$@g-Bi_2O_3 core–shell p–n heterogeneous nanostructure for enhanced visible-light photocatalytic performance," RSC Adv., **3**, 24964–24970 (2013).

Hana, C., Gea, L., Chen, C., Li, Y., Xiao, X., Zhang, Y., and Guo, L., "Novel visible light induced Co_3O_4-g-C_3N_4 heterojunction photocatalysts for efficient degradation of methyl orange," Appl. Catal., B, **147**, 546–553 (2014).

Harraza, F. A., Mohamed, R. M., Rashada, M. M., Wang, Y. C., Sigmund. W., "Magnetic nanocomposite based on titania-silica/cobalt ferrite for photocatalytic degradation of methylene blue dye," Ceram. Int., **40**, 375-384 (2014).

Hernandez-Velez, M., "Nanowires and 1D arrays fabrication: An overview," Thin Solid Films, **495**, 51-63 (2006).

Hou, H., Zhou, R., Wu, P., and Wu, L., "Removal of Congo red dye from aqueous solution with hydroxyapatite/chitosan composite," Chemical Engineering Journal, **211–212**, 336–342 (2012).

Hou, L., Yang, L., Li, J., and Tan, J. "Efficient Sunlight-Induced Methylene Blue Removal over One-Dimensional Mesoporous Monoclinic $BiVO_4$ Nanorods," J. Anal. Method Chem., Article ID 345247, doi:10.1155/2012/345247 (2012).

Hu, J., Song, Z., Chen, L., Yang, H., Li, J. and Richards R., "Adsorption Properties of MgO(111) Nanoplates for the Dye Pollutants from Wastewater," J. Chem. Eng. Data **55**, 3742-3748 (2010).

Hu, X., Liu, S., Qu, B., and You, X., "Starfish-shaped $Co_3O_4/ZnFe_2O_4$ Hollow Nanocomposite: Synthesis, Supercapacity, and Magnetic Properties," ACS Appl. Mater. Interfac., **7**, 9972−9981 (2015).

Hu, X., Yu, J. C. and Gong, J., "Fast Production of Self-Assembled Hierarchical α-Fe_2O_3 Nanoarchitectures," J. Phys. Chem. C., **111**, 11180-11185 (2007).

Hu, Z., Chen, H., Ji, F. and Yuan, S., "Removal of Congo Red from aqueous solution by cattail root," J. Hazard. Mater., **173**, 292-297 (2010).

Huang, R., Lan, B., Chen, Z., Yan, H., Zhang, Q., Bing, J., and Li, L., Catalytic ozonation of p-chlorobenzoic acid over MCM-41 and Fe loaded MCM-41," Chem. Eng. J., **180**, 19–24 (2012).

Huang, Z., Miao, H., Li, J., Wei, J., Kawi, S., and Lai, M. W., "Modifier-enhanced supercritical CO_2 extraction of organic template from aluminosilicate MCM-41 materials: Effect of matrix Al/Si ratios and different modifiers," Sep. Purif. Technol., **118**, 170–178 (2013).

Iijima, S., "Helical microtubules of graphite carbon," Nature, **354**, 56-58 (1991).

Inci, I., Bayazit, S. S., and Asci, Y. S., "Separation of Succinic Acid from Aqueous Solution by Alumina Adsorption," J. Chem. Eng. Data, 56, 4449–4453 (2011).

Iram, M., Guo, C., Guan, Y., Ishfaq, A., and Liu, H., "Adsorption and magnetic removal of neutral red dye from aqueous solution using Fe_3O_4 hollow nanospheres," J. Hazard. Mater., **181**, 1039-1050 (2010).

Irama, M, . Guo, C., Guan, Y., Ishfaq, A. and Liu, H., "Adsorption and magnetic removal of neutral red dye from aqueous solution using Fe_3O_4 hollow nanospheres," J. Hazard. Mater., **181**, 1039-1050 (2010).

Ivanovskaya, M. I., Kotikov, D. A. and Orlik, D. R., "The Influence of Structural Factors on the Gas-Sensitive Properties of Fe_2O_3–SnO_2," Russ. J. Phys. Chem. A., **82**, 127–132 (2008).

Jain, R. and Sikarwar, S., "Removal of hazardous dye congo red from waste material," J. Hazard. Mater., 152, 942-948 (2008).

Jambhrunkar, S., Qu, Z., Popat, A., Yang, J., Noonan, W., Acauan, L., Nor, Y. A., Yu, C., and Karmakar, S., "Effect of Surface Functionality of Silica Nanoparticles on Cellular Uptake and Cytotoxicity," Mol. Pharmaceutics, 11, 3642−3655 (2014).

Jang, J. S., Lee, J., Ye, H., Fan, F. F., and Bard, A. J., "Rapid screening of effective dopants for Fe_2O_3 photocatalysts with scanning electrochemical microscopy and investigation of their photoelectrochemical properties," J. Phys. Chem. C., **113**, 6719–6724 (2009).

Jehng, J. M., Tung, W. C., Huang, C. H., and Wachs, I. E., “Structural characteristics and reactivity properties of the tantalum modified mesoporous silicalite (MCM-41) catalysts,” Microporous Mesoporous Mater., **99**, 299–307 (2007).

Jiang, Q., Li, Y., Du, G., Liu, Y. and Zhao, H., “A novel structure of SnO_2 nanorod arrays synthesized via a hydrothermal method,” Mater. Lett., **105**, 95–97 (2013).

Jiang, Y., Lin, K., Zhang, Y., Liu, J., Li, G., and Sun, J., and Xu, X., “Fe-MCM-41 nanoparticles as versatile catalysts for phenol hydroxylation and for Friedel–Crafts alkylation,” Appl. Catal., A, **445– 446**, 172–179 (2012).

Johanna Lindberg b, Ioannis S. Chronakis Yu, F., Gao, L., Wang, W., Zhang, G., and Ji, J., “Bio-fuel production from the catalytic pyrolysis of soybean oil over Me-Al-MCM-41 (Me = La, Ni or Fe) mesoporous materials,” J. Anal. Appl. Pyrolysis, **104**, 325–329 (2013).

Ju, Y., Yang, S., Ding, Y., Sun, C., Zhang, A., and Wang, L., “Microwave-Assisted Rapid Photocatalytic Degradation of Malachite Green in TiO_2 Suspensions: Mechanism and Pathways,” J. Phys. Chem. A, 112, 11172–11177 (2008).

Jorge, E., Munoz, J. C., Rodrigo E., and Gerardo R., “Iron nanoparticles produced by high-energy ball milling,” J. Nanopart. Res., **9**, 945–950 (2007).

Juan Xie, Hu Wang, Ming Duan, Liehui Zhang, Synthesis and photocatalysis properties of ZnO structures with different morphologies via hydrothermal method, Applied Surface Science 257 (2011) 6358–6363.

Jubb, A. M. and Allen, H. C., “Vibrational Spectroscopic Characterization of Hematite, Maghemite, and Magnetite Thin Films Produced by Vapor Deposition,” ACS Appl. Mater. Interfaces., **2**, 2804–2812 (2010).

Jung, S., and Yong, K., “Fabrication of CuO–ZnO nanowires on a stainless steel mesh for highly efficient photocatalytic applications,” Chem. Commun., **47**, 2643–2645 (2011).

Jyothi, D., Deshpande, P. A., Venugopal, B. R., Chandrasekaran, S., and Madras, G., “Transition metal oxide loaded MCM catalysts for photocatalytic degradation of dyes,” J. Chem. Sci., **124**, 385–393 (2012).

Kaneti, Y. V., Moriceaub, J., Liu, M., Yuan, Y., Zakaria, Q., Jiang, X. and Yu, A., “Hydrothermal synthesis of ternary α-Fe_2O_3-ZnO-Au nanocomposites with high gas-sensing performance,” Sens. Actuator B., **209**, 889–897(2015).

Kang, J., Kuang, Q., Xie, Z., and Zheng, L., “Fabrication of the SnO_2/α-Fe_2O_3 Hierarchical Heterostructure and Its Enhanced Photocatalytic Property,” J. Phys. Chem. C, **115**, 7874–7879 (2011).

Kang, W., Spanjers, C. S., Rioux, R. M., and Hoefelmeyer, J. D., “Synthesis of brookite TiO_2 nanorods with isolated Co(II) surface sites and photocatalytic degradation of 5,8-dihydroxy-1,4-naphthoquinone dye,” J. Mater. Chem. A, **1**, 7717-7728 (2013).

Kanjwal, M. A., Sheikh, F. A., Barakat, N. A. M., Li, X., Kim, H. Y., and Chronakis, I. S., "Zinc oxide's hierarchical nanostructure and its photocatalytic properties," Appl. Surf. Sci., **258**, 3695–3702 (2012).

Kanjwal, M. A., Sheikh, F. A., Barakat, N. A. M., Li, X., Kim, H. Y., Chronakis, I. S., and Kim, H. Y., "Co_3O_4-ZnO hierarchical nanostructures by electrospinning and hydrothermal methods," Appl. Surf. Sci., **257**, 7975–7981 (2011).

Karunakaran, C., and Senthilvelan, S., "Fe_2O_3-photocatalysis with sunlight and UV light: oxidation of aniline," Electrochem. Commun., **8**, 95–101 (2006).

Kaya, E., Oktar, N., Karakas, G., and Murtezaoglu, K. "Synthesis and characterization of Ba/MCM-41," Turk. J. Chem., **34**, 935 – 943 (2010).

Kerkez, O., and Bayazit, S. S., Magnetite decorated multi-walled carbon nanotubes for removal of toxic dyes from aqueous solutions, J. Nanopart. Res., **16**, 2431 (2014).

Khadhraoui, M., Trabelsi, H., Ksibi, M., Bouguerra, S. and Elleuch, B., "Discoloration and detoxification of Congo red dye solution by means of ozone treatment for a possible water reuse," J. Hazard. Mater., **161**, 974-981 (2009).

Khakpash, N., Simchi, A., and Jafari, T., "Adsorption and solar light activity of transition-metal doped TiO_2 nanoparticles as semiconductor photocatalyst," J. Mater. Sci.: Mater. Electron., **23**, 659–667 (2012).

Khan, G., Choi, S. K., Kim, S., Lim, S. K., Jang, J. S., and Park, H., "Carbon nanotubes as an auxiliary catalyst in heterojunction photocatalysis for solar hydrogen," Appl. Catal., B., **142-143**, 647– 653 (2013).

Khieu, D. Q., Quang, D. T., Lam, T. D., Phu, N. H., Lee, J. H., and Kim, J. S., "Fe-MCM-41 with highly ordered mesoporous structure and high Fe content: synthesis and application in heterogeneous catalytic wet oxidation of phenol," J. Incl. Phenom. Macrocycl. Chem., **65**, 73–81 (2009).

Kim, H. G., Borse, P. H., Choi, W., and Lee, J. S., "Photocatalytic Nanodiodes for Visible-Light Photocatalysis," Angew. Chem., **117**, 4661–4665 (2005).

Kim, H., Kim, J., Kim, W., and Choi, W., "Enhanced Photocatalytic and Photoelectrochemical Activity in the Ternary Hybrid of $CdS/TiO_2/WO_3$ through the Cascadal Electron Transfer," J. Phys. Chem. C, **115**, 9797–9805 (2011).

Klett, C., Barry, A., Balti, I., Lelli, P., Schoenstein, F. and Jouini, N., "Nickel doped Zinc oxide as a potential sorbent for decolorization of specific dyes, methylorange and tartrazine by adsorption process," J. Environ. Chem. Eng., **2**, 914–926 (2014).

Kole, A. K., Tiwary, C. S., and Kumbhakar, P., Ethylenediamine assisted synthesis of wurzite zinc sulphide nanosheets and porous zinc oxide nanostructures: near white light photoluminescence emission and photocatalytic activity under visible light irradiation," Cryst. Eng. Comm., **15**, 5515–5525 (2013).

Kumar, A. S. K., and Rajesh, N., "Exploring the interesting interaction between graphene oxide, Aliquat-336 (a room temperature ionic liquid) and chromium(VI) for wastewater treatment," RSC Adv., **3**, 2697–2709 (2013).

Kumar, A. S. K., Gupta, T., Kakan, S. S., Kalidhasan, S., Manasi, Rajesh, V., and Rajesh, N., "Effective adsorption of hexavalent chromium through a three center (3c) co-operative interaction with an ionic liquid and biopolymer," J. Hazard. Mater., **239–240**, 213–224 (2012).

Kumar, A. S. K., Ramachandran, R., Kalidhasan, S., Rajesh, V., and Rajesh, N., "Potential application of dodecylamine modified sodium montmorillonite as an effective adsorbent for hexavalent chromium," Chem. Eng. J., **211–212**, 396–405 (2012).

Kumar, H., Manisha, and Sangwan, P., "Synthesis and Characterization of MnO_2 Nanoparticles using Co-precipitation Technique," International Journal of Chemistry and Chemical Engineering, **3**, 155-160 (2013).

Kumar, J. and Bansal, A., "Photodegradation of amaranth in aqueous solution catalyzed by immobilized nanoparticles of titanium dioxide," Int. J. Environ. Sci. Technol., **9**, 479-484 (2012).

Kumar, S., Kumar, B., Surendar, T., Shanker, V., "g-C_3N_4/$NaTaO_3$ organic–inorganic hybrid nanocomposite: High-performance and recyclable visible light driven photocatalyst," Mater. Res. Bull., **49**, 310–318 (2014).

Lai, J., Shafi, K. V. P. M., Loos, K., Ulman, A., Lee, Y., Vogt, T., Estournes, C., "Doping γ-Fe2O3 Nanoparticles with Mn(III) Suppresses the Transition to the α-Fe2O3 Structure," J. Am. Chem. Soc., **125**, 11470-11471 (2003).

Lan, B., Huang, R., Li, L., Yan, H., Liao, G., Wang, X., and Zhang, Q., "Catalytic ozonation of p-chlorobenzoic acid in aqueous solution using Fe-MCM-41 as catalyst," Chem. Eng. J., **219**, 346–354 (2013).

Lanje, A, S., Sharma, S. J., Ningthoujam, R. S., Ahn, J.-S., and Pode, R. B., "Low temperature dielectric studies of zinc oxide (ZnO) nanoparticles prepared by precipitation method," Adv. Powder Technol., **24**, 331–335 (2013).

Lee, C., Liu, S., Juang, L., Wang, C., Lin, K., and Lyu, M., "Application of MCM-41 for dyes removal from wastewater," J Hazard Mater, **147**, 997–1005 (2007).

Lee, S. S., Bai, H., Liu, Z. and Sun, D. D., "Novel-structured electrospun TiO_2/CuO composite nanofibers for high efficient photocatalytic cogeneration of clean water and energy from dye wastewater," Water Res., **47**, 4059-4073 (2013).

Lezanska, M., Szymanski, G. S., Pietrzyk, P., Sojka Z., and Lercher, J. A., "Characterization of Cr-MCM-41 and Al,Cr-MCM-41 Mesoporous Catalysts for Gas-Phase Oxidative Dehydrogenation of Cyclohexane," J. Phys. Chem. C., **111**, 1830-1839 (2007).

Li, B., and Wang, Y., "Facile synthesis and photocatalytic activity of ZnO-CuO nanocomposite," Superlattice Microst., **47**, 615-623 (2010).

Li, B., Wu, K., Yuan, T., Han, C., Xu, J., and Pang, X., “Synthesis, characterization and catalytic performance of high iron content mesoporous Fe-MCM-41,” Microporous Mesoporous Mater., **151**, 277–281 (2012).

Li, B., Wu, K., Yuan, T., Han, C., Xu, J., and Pang, X., “Synthesis, characterization and catalytic performance of high iron content mesoporous Fe-MCM-41,” Microporous Mesoporous Mater., **151**, 277–281 (2012).

Li, D., McCann, J. T., and Xia, Y., “Electrospinning: A simple and versatile technique for producing ceramic nanofibers and nanotubes,” J. Am. Ceram. Soc., **89**, 1861-1869 (2006).

Li, D., Min, H., Jiang, X., Ran, X., Zou, L., and Fan, J., “One-pot synthesis of Aluminum-containing ordered mesoporous silica MCM-41 using coal fly ash for phosphate adsorption,” J. Colloid Interface Sci., **404**, 42–48 (2013).

Li, F., Liu, X., Zhang, Q., Kong, T, and Jin, H., “Fabrication and photocatalytic property of CuO nanosheets via a facile solution route,” Cryst. Res. Technol., **47**, 1140–1147 (2012).

Li, Q., Wang, Y. and Zhang, C., “Chemical precipitation synthesis and magnetic properties of Hematite nanorods,” Defect Diffus Forum., **293**, 77-82 (2009).

Li, X., and Zhai, Q., “Characterization of methylated nanoscale MCM-41 material,” J. Iran. Chem. Soc., **8**, S1-S8 (2011).

Li, X., China, E., Sunb, H., Kurupc P., and Gu, Z., “Fabrication and integration of metal oxide nanowire sensors using dielectrophoretic assembly and improved post-assembly processing,” Sens. Actuator B., **148**, 404–412 (2010).

Li, X., Meng, G., Xu, Q., Kong, M., Zhu, X., Chu, Z. and Li, A. P., “Controlled Synthesis of Germanium Nanowires and Nanotubes with Variable Morphologies and Sizes,” Nano Lett.,. **11**, 1704-1709 (2011).

Li, X., Meng, G., Xu, Q., Kong, M., Zhu, X., Chu, Z., and Li, A. P., “Controlled synthesis of germanium nanowires and nanotubes with variable morphologies and sizes,” ACS Nano Lett., **11**, 1704-1709 (2011).

Li, X., Xiao, W., Hea, G., Zheng, W., Yu, N. and Tan, M., “Pore size and surface area control of MgO nanostructures using a surfactant-templated hydrothermal process: High adsorption capability to azo dyes,” Colloids Surf. A., **408**, 79–86 (2012).

Li, X., Xiao, W., Hea, G., Zheng, W., Yu, N., Tan, M., “Pore size and surface area control of MgO nanostructures using a surfactant-templated hydrothermal process: High adsorption capability to azo dyes,” Colloids and Surfaces A: Physicochem. Eng. Aspects, **408** 79–86 (2012).

Li, X., Yu, H., He, Y., and Xue, X., “Synthesis of Fe-MCM-41using iron ore tailings as the silicon and iron source,” J. Anal. Methods Chem., **2012**, doi:10.1155/2012/928720 (2012).

Li, Z., Fei, H., Tan, Y., Zhang, X., Xie, Z., and Zhang, Z., "Synthesis and characterization of self-assembled three-dimensional flower-like iron(III) oxide–indium(III) oxide binary nanocomposites," RSC Adv., **5**, 38093–38099 (2015).

Li, Z., Lai, X., Wang, H., Mao, D., Xing, C. and Wang, D., "Direct hydrothermal synthesis of single-crystalline hematite nanorods assisted by 1,2-propanediamine," Nanotechnology., **20**, DOI:10.1088/0957-4484/20/24/245603, (2009).

Lian, L., Guo, L. and Guo, C., "Adsorption of Congo red from aqueous solutions onto Ca-bentonite," J. Hazard. Mater., **161**, 126-131 (2009).

Lin, C., Song, Y., Cao, L., and Chen, S., "TiO_2 nanotubes/ZnO/CdS ternary nanocomposites: preparation, characterization and photocatalysis," J. Chin. Adv. Mater. Soc., **1**, 188–199 (2013).

Lin, D., Wu, H., Zhang, R. and Pan, W., "Enhanced Photocatalysis of Electrospun Ag-ZnO Heterostructured Nanofibers", Chem. Mater., **21**, 3479–3484 (2009).

Lin, Q., Li, Y., and Yang, M., "Tin oxide/graphene composite fabricated via a hydrothermal method for gas sensors working at room temperature," Sens. Actuators, B, **173**, 139–147 (2012).

Lin, Y., Abel, P. R., Heller, A. and Mullins, C. B., "α-Fe_2O_3 Nanorods as Anode Material for Lithium Ion Batteries," J. Phys. Chem. Lett., **2**, 2885–2891 (2011).

Liu, G., Li, J., Wang, F., Chen, Y.. "Nanoflake-modified MgO microspheres prepared by flame spraying," Mater. Lett., **115**, 226–228 (2014).

Liu, X., Yin, W., Miao, S., and Ji, B., "Fabrication of CuO/Fe_2O_3 hollow hybrid microspheres," Mater. Chem. Phys., **113**, 518–522 (2009).

Liu, Y., Yu, H., Zhan, S., Li, Y., Lv, Z., Yang, X. and Yu, Y., "Fast degradation of methylene blue with electrospun hierarchical α-Fe_2O_3 nanostructured fibers," J. Sol-Gel Sci. Technol., **58**, 716–723 (2011).

Liu, Y., Yu, L., Hu, Y., Guo, C., Zhang, F., and Lou, X. W., "A magnetically separable photocatalyst based on nest-like γ-Fe_2O_3/ZnO double-shelled hollow structures with enhanced photocatalytic activity," Nanoscale, **4**, 183–187 (2012).

Liu, Z. S., Wub, B. T., Niu, J. N., Feng, P. Z., and Zhu, Y. B., "$BiPO_4$/BiOBr p–n junction photocatalysts: One-pot synthesis and dramatic visible light photocatalytic activity," Mater. Res. Bull., **63**, 187–193 (2015).

Liu, Z., Sun, D. D., Guo, P., and Leckie, J. O., "An efficient bicomponent TiO_2/SnO_2 nanofiber photocatalyst fabricated by electrospinning with a side-by-side dual spinneret method," Nano Lett., **7**, 1081-1085 (2007).

Lorenc-Grabowska, E. and Gryglewicz, G. "Adsorption characteristics of Congo Red on coal-based mesoporous activated carbon," Dyes Pigments., **74**, 34-40 (2007).

Love, J. C., Estroff, L. A., Kriebel, J. K., Nuzzo, R. G., and Whitesides, G. M., "Self-assembled monolayers of thiolates on metals as a form of nanotechnology," Chem. Rev., **105**, 1103−1169 (2005).

Lucas, M. S. and Peres, J. A., "Decolorization of the azo dye Reactive Black 5 by Fenton and photo-Fenton oxidation," Dyes Pigments., **71**, 236-244 (2006).

Lv, H., Liu, Y., Hu, J., Li, Z., and Lu, Y., "Ionic liquid-assisted hydrothermal synthesis of Bi_2WO_6–reduced graphene oxide composites with enhanced photocatalytic activity," RSC Adv., **4**, 63238–63245 (2014).

Lv, H., Ma, L., and Zeng, P., "Synthesis of floriated ZnFe2O4with porous nanorod structures and its photocatalytic hydrogen production under visible light," J. Mater. Chem., **20**, 3665–3672 (2010).

Ma, J., Lian, J., Duan, X., Liu, X. and Zhen, W., "α-Fe_2O_3: Hydrothermal Synthesis, Magnetic and Electrochemical Properties," J. Phys. Chem. C, **114**, 10671–10676 (2010).

Ma, L., Li, J., Sun, H., Qiu, M., Wang, J., Chen, J., and Yu, Y., "Self-assembled Cu_2O flowerlike architecture: Polyol synthesis, photocatalytic activity and stability under simulated solar light," Mater. Res. Bull., **45**, 961–968 (2010).

Madrakian, T., Afkhami, A., Haryania R., and Ahmadi, M., "Synthesis of γ-Fe_2O_3/TiO_2 nanocomposite and its application in removal of dyes from water samples by adsorption and degradation processes," RSC Adv., **4**, 44841–44847 (2014).

Mageshwari, K., and Sathyamoorthy, R., "Organic free synthesis of flower-like hierarchical CuO microspheres by reflux condensation approach," Appl. Nanosci., **3**, 161–166 (2013).

Mageshwari, K., Nataraj, D., Pal, T., Sathyamoorthy, R., Park, J., "Improved photocatalytic activity of ZnO coupled CuO nanocomposites synthesized by reflux condensation method," J. Alloys Compd., **625**, 362–370 (2015).

Mageshwari, K., Sathyamoorthy, R., and Park, J., "Photocatalytic activity of hierarchical CuO microspheres synthesized by facile reflux condensation method," Powder Technol., **278**, 150-156 (2015).

Mageshwari, K., Sathyamoorthy, R., Lee, J. Y., and Park, J., "Novel $CuCr_2O_4$ embedded CuO nanocomposites for efficient photodegradation of organic dyes," App. Surf. Sci., **353**, 95-102 (2015).

Mahadik, M. A., Shinde, S. S., Rajpure, K. Y., and Bhosale, C. H., "Photocatalytic oxidation of Rhodamine B with ferric oxide thin films under solar illumination," Mater. Res. Bull., **48**, 4058–4065 (2013).

Mahapatra, A., Mishra B. G., and Hota G., "Synthesis of ultra-fine α-Al_2O_3 fibers via electrospinning method," Ceram. Int., **37**, 2329–2333 (2011).

Mahapatra, A., Mishra, B. G. and Hota, G., "Adsorptive removal of Congo red dye from wastewater by mixed iron oxide–alumina nanocomposites," Ceram. Int. **39**, 5443–5451 (2013).

Mahapatra, A., Mishra, B. G., and Hota, G., “Electrospun Fe_2O_3–Al_2O_3 nanocomposite fibers as efficient adsorbent for removal of heavy metal ions from aqueous solution, J. Hazard. Mater., **258–259**, 116–123 (2013).

Mohapatra, M., and Anand, S., “Synthesis and applications of nano-structured iron oxides/hydroxides– a review,” International Journal of Engineering, Science and Technology, **2**, 127-146 (2010).

Mahmoud, H. R., El-Molla, S., and Saif, A. M., “Improvement of physicochemical properties of Fe_2O_3/MgO nanomaterials by hydrothermal treatment for dye removal from industrial wastewater,” Powder Technology, **249**, 225–233 (2013).

Makhlup, S., Dror, R., Nitzan, Y., Abramovich, Y., Jelinek R., and Gedanken, A., “Microwave-assisted synthesis of nanocrystalline MgO and its use as Bacteriocide,” Adv. Funct. Mater. **15**, 1708-1715 (2005).

Marechal, M. L., Slokar, Y.M. and Taufer T., “Decolouration of chlorotriazine reactive azo dyes with H_2O_2/UV,” Dyes Pigments., **33**, 281-298 (1997).

Mariappan, C. R., Kumar, R., and Prakash, G. V., “Functional properties of $ZnCo_2O_4$ nano-particles obtained by thermal decomposition of a solution of binary metal nitrates,” RSC Adv., **5**, 26843–26849 (2015).

Mathew, D. S., and Juang, R., “An overview of the structure and magnetism of spinel ferrite nanoparticles and their synthesis in microemulsions,” Chem. Eng. J., **129**, 51–65 (2007).

Meng, L., Chen, W., Chen, C., Zhou, H., Peng, Q., and Li, Y., “Uniform α-Fe2O3 Nanocrystal Moniliforme-Shape Straight-Chains,” Crys. Growth Des., **10**, 479–482. (2010).

Mittal, A., “Adsorption kinetics of removal of a toxic dye, Malachite Green, from wastewater by using hen feathers,” Journal of Hazardous Materials, **B133**, 196–202 (2006).

Mittal, A., Mittal, J,, Malviya, A. and Gupta, V. K., “Adsorptive removal of hazardous anionic dye ‘‘Congo red” from wastewater using waste materials and recovery by desorption,” J. Colloid Interface Sci., **340**, 16-26 (2009).

Mohamed, R. M., and Aazam, E. S., “Synthesis and Characterization of CeO_2-SiO_2 Nanoparticles by Microwave-Assisted Irradiation Method for Photocatalytic Oxidation of Methylene Blue Dye,” Int. J. Photoenergy, DOI:10.1155/2012/928760 (2012).

Moharram, A. H., Mansour, S. A., Hussein, M. A. and Rashad, M., “Direct Precipitation and Characterization of ZnO Nanoparticles,” J. Nanomater., Article ID 716210, DOI: 10.1155/2014/716210, (2014).

Monash, P., and Pugazhenthi, G., “Investigation of equilibrium and kinetic parameters of methylene blue adsorption onto MCM-41,” Korean J. Chem. Eng., **27**, 1184-1191 (2010).

Moussavi, G., and Mahmoudi, M., “Removal of azo and anthraquinone reactive dyes from industrial wastewaters using MgO nanoparticles,” Journal of Hazardous Materials, 168, 806–812 (2009).

Mukherjee, N., Show, B., Maji, S. K., Madhu, U., Bhar, S. K., Mitra, B. C., Khan, G. G., and Mondal, A., “CuO nano-whiskers: Electrodeposition, Raman analysis, photoluminescence study and photocatalytic activity,” Mater. Lett., **65**, 3248–3250 (2011).

Muruganandham, M., and Swaminathan, M., “Solar photocatalytic degradation of a reactive azo dye in TiO_2-suspension,” Sol. Energ. Mat. Sol., C, **81**, 439–457 (2004).

Muthirulan, P., Devi, C. K. N., Sundaram, M. M., “Facile synthesis of novel hierarchical TiO_2@Poly(o-phenylenediamine) core–shell structures with enhanced photocatalytic performance under solar light,” J. Environ. Chem. Eng., **1**, 620–627 (2013).

Mutong Niu, Feng Huang, Lifeng Cui, Ping Huang, Yunlong Yu, and Yuansheng Wang, Hydrothermal Synthesis, Structural Characteristics, and Enhanced Photocatalysis of $SnO_2/\alpha\text{-}Fe_2O_3$ Semiconductor Nanoheterostructures, ACS Nano 2010, 4 (2) 681–688.

Nagata, H., Takimur, Yamasaki Y., and Nakahira, A., “Syntheses and Characterization of Bulky Mesoporous Silica MCM-41 by Hydrothermal Hot-Pressing Method,” Mater. Trans., **47**, 2103-2105 (2006).

Namasivayam, C. and Kavitha D., “Removal of Congo Red from water by adsorption onto activated carbon prepared from coir pith, an agricultural solid waste,” Dyes Pigments., **54**, 47-58 (2002).

Narkiewicz, U., Sibera, D., Kuryliszyn-Kudelska, I., Kilanski, L., Dobrowolsk, W. and Romcevi, N., “Synthesis by Wet Chemical Method and Characterization of Nanocrystalline ZnO Doped with Fe_2O_3,” Acta Phys. Pol., A **113**, 1695-1700 (2008).

Narkiewicz, U., Sibera, D., Kuryliszyn-Kudelska, I., Kilanski, L., Dobrowolski, W., and Romcevi, N., “Synthesis by Wet Chemical Method and Characterization of Nanocrystalline ZnO Doped with Fe_2O_3,” Acta Physica Polonica A, 113, 1695-1700 (2008).

Nassar, N. N., “Kinetics, Equilibrium and Thermodynamic Studies on the Adsorptive Removal of Nickel, Cadmium and Cobalt from Wastewater by Superparamagnetic Iron Oxide Nanoadsorbents,” Can. J. Chem. Eng., 90, 1231-1238 (2012)

Nassar, N. N., “Rapid removal and recovery of Pb(II) from wastewater by magnetic Nanoadsorbents,” J. Hazard. Mater., **184**, 538–546 (2010).

Nassar, N. N., Hassan, A.r and Pereira-Almao, P., “Metal Oxide Nanoparticles for Asphaltene Adsorption and Oxidation,” Energy Fuels, **25**, 1017–1023 (2011).

Nazari, M., Ghasemi, N., Maddah, H., and Motlagh, M. M., “Synthesis and characterization of maghemite nanopowders by chemical precipitation method,” J. Nanostruct. Chem., **4**, 99 (2014).

Nethaji, S., Sivasamy, A. and Mandal A. B., “Adsorption isotherms, Kinetics and mechanisms for the adsorption of cationic and anionic dyes onto carbonaceous particles prepared from Juglans regia shell biomass,” Int. J. Environ. Sci. Technol., **10**, 231-242 (2012).

Ng, E. P., Goh, J. Y., Ling, T. C., and Mukti, R. R., "Eco-friendly synthesis for MCM-41 nanoporous materials using the non-reacted reagents in mother liquor," Nanoscale Res. Lett., **8:120** (2013).

Nga, N. K., Hong, P. T. T., Lam, T. D., Huy, T. Q., "A facile synthesis of nanostructured magnesium oxide particles for enhanced adsorption performance in reactive blue 19 removal," J. Colloid Interface Sci., **398**, 210–216 (2013).

Ning Du, Yanfang Xu, Hui Zhang, Chuanxin Zhai, Deren Yang, Selective Synthesis of Fe_2O_3 and Fe_3O_4 Nanowires Via a Single Precursor: A General Method for Metal Oxide Nanowires, Nanoscale Res Lett (2010) 5:1295–1300.

Ning Xiao, Zhonghua Li, Jiawen Liu, Yuan Gao, A facile template-free method for preparing bi-phase TiO_2 nanowire arrays with high photocatalytic activity, Materials Letters 64 (2010) 1776–1778.

Niu, M., Huang, F., Cui, L., Huang, P., Yu, Y. and Wang, Y., "Hydrothermal Synthesis, Structural Characteristics, and Enhanced Photocatalysis of $SnO_2/\alpha\text{-}Fe_2O_3$ Semiconductor Nanoheterostructures," ACS Nano., **4**, 681-688 (2010).

Niu, M., Huang, F., Cui, L., Huang, P., Yu, Y., and Wang, Y., "Hydrothermal Synthesis, Structural Characteristics, and Enhanced Photocatalysis of $SnO_2/\alpha\text{-}Fe_2O_3$ Semiconductor Nanoheterostructures," ACS Nano., **4**, 681–688 (2010).

Olteanu, N. L., and Meghea, A., "Microemulsion – based silica templates for multifunctional nanomaterials," U.P.B. Sci. Bull., Series B, **75**, (2013).

Oskam, G., "Metal oxide nanoparticles: synthesis, characterization and application," J. Sol-Gel Sci. Techn., **37**, 161–164 (2006).

Panda, G. C., Das, S. K. and Guha, A. K., "Jute stick powder as a potential biomass for the removal of congo red and rhodamine B from their aqueous solution," J. Hazard. Mater., **164**, 374-379 (2009).

Panda, P. K., Jaleel, V. A., and Devi, S. U., "Hydrothermal synthesis of boehmite and a-alumina from Bayer's alumina trihydrate," J. Mater. Sci. 41, 8386–8389 (2006).

Pare, B., Sarwan, B., and Jonnalagadda, S. B., "Photocatalytic mineralization study of malachite green on the surface of Mn-doped BiOCl activated by visible light under ambient condition," Appl. Surf. Sci., **258**, 247–253 (2011).

Parida, K. M., and Dash, S. K., "Adsorption of Cu^{2+} on spherical Fe-MCM-41 and its application for oxidation of adamantine," J. Hazard. Mater., **179**, 642–649 (2010).

Parida, K. M., Sahu, N., Biswal, N. R., Naik, B., and Pradhan, A. C., "Preparation, characterization, and photocatalytic activity of sulfate-modified titania for degradation of methyl orange under visible light," Journal of Colloid and Interface Science, **318,** 231–237 (2008).

Park, J. B., Graciani, J., Evans, J., Stacchiola, D., Ma, S., Liu, P., Nambu, A., Sanzc, J. F., Hrbek, J. and Rodriguez, J. A., "High catalytic activity of $Au/CeOx/TiO_2(110)$ controlled by the nature of the mixed-metal oxide at the nanometer level," PNAS **106**, 4975– 4980 (2009) .

Park, J., Hwang, K., Lee, J., Lee, I., “Fabrication and characterization of electrospun Ag doped TiO_2 nanofibers for photocatalytic reaction,” J. Mater. Sci., **46**, 7240–7246 (2011).

Pavan, F. A., Dias, S. L. P., Lima, E. C. and Benvenutti, E. V., “Removal of Congo red from aqueous solution by anilinepropylsilica xerogel,” Dyes Pigments., **76**, 64-69 (2008) .

Peng, L., Xie, T., Lu, Y., Fan, H., and Wang, D., “Synthesis, photoelectric properties and photocatalytic activity of the Fe_2O_3/TiO_2 heterogeneous photocatalysts,” Phys. Chem. Chem. Phys., **12**, 8033–8041 (2010).

Peng, X. H., Qian, X., Mao, H., Wang, A. Y., Chen, Z., Nie, S., Shin, D. M. “Targeted magnetic iron oxide nanoparticles for tumor imaging and therapy,” Int. J. Nanomedicine, ***3***, 311–321(2008).

Pereira, C., Pereira, A. M., Fernandes, C., Rocha, M., Mendes, R., Fernandez-Garcia, M. P., Guedes, A., Tavares, P. B., Greneche, J. M., jo, J. P. A., and Freire, C., “Superparamagnetic MFe_2O_4 (M = Fe, Co, Mn) nanoparticles: tuning the particle size and magnetic properties through a novel one-step coprecipitation route,” Chem. Mater., **24**, 1496−1504 (2012).

Perreault, F., de Faria A. F., and Elimelech, M., “Environmental applications of graphene-based nanomaterials,” Chem. Soc. Rev., DOI: 10.1039/c5cs00021a (2015).

Ponnusami, V., Vikram, S., and Srivastava S. N., “Guava (Psidium guajava) leaf powder: Novel adsorbent for removal of methylene blue from aqueous solutionsGuava (Psidium guajava) leaf powder: Novel adsorbent for removal of methylene blue from aqueous solutions,” Journal of Hazardous Materials, **152**, 276–286 (2008).

Pouretedal, H.R., and Ahmadi, M., “Synthesis, characterization, and photocatalytic activity of MCM-41 and MCM-48 impregnated with CeO_2 nanoparticles,” Int. Nano Lett., **2:10** (2012).

Pradhan, G. K., and Parida, K. M., “Fabrication, Growth Mechanism, and Characterization of α-Fe_2O_3 Nanorods,” Appl. Mater. Interfaces., **3**, 317–323 (2011).

Prasetyanto, E. A., Lee, S. S., and Park, S., “Highly dispersed CuO nanoparticles on SBA-16 type mesoporous silica with Cyclam SBA-16 as a precursor,” Bull. Korean Chem. Soc., **28**, 2359-2362 (2007).

Prasetyanto, E. A., Sujandi, Lee, S., and Park, S., “Highly Dispersed CuO Nanoparticles on SBA-16 Type Mesoporous Silica with Cyclam SBA-16 as a Precursor,” Bull. Korean Chem. Soc., **28**, 2359-2362 (2007).

Preethia, M. E. L., Sivakumar, T., and Palanichami, M., “Room temperature efficacious synthesis of diphenylmethane over Fe/Al-MCM-41 catalysts,” Catal. Commun., **11** 876–879 (2010).

Purkait, M. K., Dasgupta, S. and De, S., “Removal of congo red using activated carbon and its regeneration,” J. Hazard. Mater., **145**, 287-295 (2007).

Purkait, M. K., Dasgupta, S. and De, S., “Removal of dye from wastewater using micellar-enhanced ultrafiltration and recovery of surfactant.” Sep. Purif. Technol. **37**, 81-92 (2004).

Qiu, G., Dharmarathna, S., Genuino, H., Zhang, Y., Huang, H., and Suib, S. L., “Facile Microwave-Refluxing Synthesis and Catalytic Properties of Vanadium Pentoxide Nanomaterials,” ACS Catal., **1**, 1702–1709 (2011).

Qiuping Jiang, Yuehua Li, Guofang Du, Yongjun Liu, Heyun Zhao, A novel structure of SnO_2 nanorod arrays synthesized via a hydrothermal method, Materials Letters 105 (2013) 95–97.

Qu, J., Yu, Y., Cao, C., and Son, W., “α-Fe_2O_3 Nanodisks: Layered Structure, Growth Mechanism, and Enhanced Photocatalytic Property,” Chem. Eur. J., **19**, 11172–11177 (2013).

Qu, X., Alvarez, P. J. J., and Li, Q., “Applications of nanotechnology in water and wastewater treatment,” Water Res., **47**, 3931-3946 (2013).

Qurashi, A., Zhong, Z., and Alam, M. W., “Synthesis and photocatalytic properties of α-Fe_2O_3 nanoellipsoids,” Solid State Sci., **12**, 1516-1519 (2010).

Rahimi, R,, Kerdari, H,, Rabbani, M. and Shafiee M., “Synthesis, characterization and adsorbing properties of hollow Zn-Fe_2O_4 nanospheres on removal of congo red from aqueous solution,” Desalination., **280**, 412-418 (2011).

Rahnama, A. and Gharagozlou, M., “Preparation and properties of semiconductor CuO nanoparticles via a simple precipitation method at different reaction temperatures,” Opt. Quant. Electron., **44**, 313–322 (2012).

Rajesh, N., Kumar, A. S. K., Kalidhasan, S., and Rajesh, V., “Trialkylamine Impregnated Macroporous Polymeric Sorbent for the Effective Removal of Chromium from Industrial Wastewater,” J. Chem. Eng. Data, **56**, 2295–2304 (2011).

Ramesh, R., Ashok, K., Bhalero, G. M., Ponnusamy, S. and Muthamizhchelvan, C., “Synthesis and properties of α-Fe_2O_3 nanorods,” Cryst. Res. Technol., **45**, 965–968 (2010).

Rana, R. K., and Viswanathan, B., “Mo incorporation in MCM-41 type zeolite, Catal. Lett., **52**, 25–29 (1998).

Rao, C. N. R., and Müller, A., “ The chemistry of nanomaterials, A.K. Cheetham (Eds.), Wiley-VCH, Weinheim, 3rd Reprint, 2005, Vol. 1, p. 113.

Raoufi, D., “Synthesis and microstructural properties of ZnO nanoparticles prepared by precipitation method,” Renew. Energ., **50**, 932-937 (2013).

Rath, D., and Parida, K. M., “Copper and nickel modified MCM-41 an efficient catalyst for hydrodehalogenation of chlorobenzene at room temperature,” Ind. Eng. Chem. Res., **50**, 2839–2849 (2011).

Reddy, S., Kumara Swamy, B.E., Jayadevappa, H., “CuO nanoparticle sensor for the electrochemical determination of dopamine,” Electrochim. Acta, **61**, 78–86 (2012).

Ren, P., Fan, H., and Wang, X., "Solid-state synthesis of Bi_2O_3/$BaTiO_3$ heterostructure: preparation and photocatalytic degradation of methyl orange," Appl. Phys. A, **111**, 1139–1145 (2013).

Ren, P., Fan, H., and Wang, X., "Solid-state synthesis of Bi_2O_3/$BaTiO_3$ heterostructure: preparation and photocatalytic degradation of methyl orange," Appl. Phys., A, **111**, 1139–1145 (2013).

Ren, T., He, P., Niu, W., Wu, Y., Ai, L., and Gou, X., "Synthesis of α-Fe_2O_3 nanofibers for applications in removal and recovery of Cr(VI) from wastewater," Environ. Sc.i Pollut. Res., **20**, 155–162 (2013).

Sachdeva, S., and Kumar, A., "Preparation of nonporous composite carbon membrane for separation of Rhodamine B dye," J. Membr. Sci., **329**, 2-10 (2009).

Saha, S., and Bhunia, A. K.,"Synthesis of Fe_2O_3 Nanoparticles and Study of its Structural, Optical Properties," J. Phy. Sci., **17**,191-195 (2013).

Sahay. R., Kumar, P. S., Aravindan, V., Sundaramurthy, J., Ling, W., C., Mhaisalkar, S. G., Ramakrishna, S. and Madhavi, S., "High Aspect Ratio Electrospun CuO Nanofibers as Anode Material for Lithium-Ion Batteries with Superior Cycleability," J. Phys. Chem. C., **116**, 18087−18092 (2012).

Şahin, A., "Hydrothermal Synthesis and Characterization of Transition Metal Oxides," M.Sc. Thesis, İzmir Institute of Technology İzmir, Turkey (2004).

Saha, P., Chowdhury, S., Gupta, S., and Kumar, I. "Insight into adsorption equilibrium, kinetics and thermodynamics of Malachite Green onto clayey soil of Indian origin," Chemical Engineering Journal, **165**, 874–882 (2010).

Sahoo, S. K., Agarwal, K., Singh, A .K., Polke B. G. and Raha K. C., "Characterization of γ- and α-Fe_2O_3 nano powders synthesized by emulsion precipitation-calcination route and rheological behaviour of α-Fe_2O_3," Int. J. Eng. Sci. Technol., **8**, 118-126 (2010).

Saikia, J., Sikdar, Y., Saha, B. and Das, G., "Malachite nanoparticle: A potent surface for the adsorption of xanthene dyes," J. Environ. Chem. Eng., **1**, 1166–1173 (2013).

Salleh, M. A. M., Mahmoud, D. K., Karim, W. A. W. A., and Idris, A., "Cationic and anionic dye adsorption by agricultural solid wastes: A comprehensive review," Desalination, **280**, 1–13, (2011).

Sangari, N. U. and Devi, S. C., "Synthesis and characterization of nano ZnO rods via microwave assisted chemical precipitation method," J. Solid State Chem., **197**, 483–488 (2013).

Santos, D. O., Santos, M. L. N., Costa, J. S.A., de Jesus, R. A., Navickiene, S., Sussuchi, E. M., and Mesquita, M. E., "Investigating the potential of functionalized MCM-41 on adsorption of Remazol Red dye," Environ. Sci. Pollut. Res., **20**, 5028–5035 (2013).

Sarangi, P. P., Naik, B. and Ghosh N.N., "Low temperature synthesis of single-phase α-Fe_2O_3 nano-powders by using simple but novel chemical methods," Powder Technol., **192**, 245–249 (2009).

Sathyamoorthy, R., and Mageshwari, K., “Synthesis of hierarchical CuO microspheres: Photocatalytic and antibacterial activities,” Physica E, **47**, 157–161(2013).

Sathyamoorthy, R., Mageshwari, K., Mali, S. S., Priyadharshini, S., and Patil, P. S., “Effect of organic capping agent on the photocatalytic activity of MgO nanoflakes obtained by thermal decomposition route,” Ceram. Int., **39**, 323–330 (2013).

Setti, N. D., Jouini, N. and Derriche, Z., “Sorption study of an anionic dye – benzopurpurine 4B – on calcined and uncalcined Mg–Al layered double hydroxides,” J. Phys. Chem. Solids., **71**, 556–559 (2010).

Shafiu, S., Kavas, H., and Bayka, A., “Synthesis and Characterization of Superparamagnetic Co_3O_4@ZnO Nanocomposite,” J. Supercond. Nov. Magn., **27**, 1751–1755 (2014).

Shahid, M., Jingling, L., Ali, Z., Shakir, I., Warsi, M. F., Parveen, R., Nadeem, M., “Photocatalytic degradation of methylene blue on magnetically separable MgFe2O4 under visible light irradiation,” Materials Chemistry and Physics, **139**, 566-571 (2013).

Shakir, I., Sarfraz, M., Ali, Z., Aboud, M. F. A., Agboola, P. O., “Magnetically separable and recyclable graphene-$MgFe_2O_4$ nanocomposites for enhanced photocatalytic applications,” Journal of Alloys and Compounds, **660**, 450-455 (2016).

Shankar, K. S., and Raychaudhuri, A. K., “Fabrication of nanowires of multicomponent oxides: Review of recent advances,” Mater. Sci. Eng., C, **25**, 738-751 (2005).

Sharma, P., Kumar, R., Chauhan, S., Singh, Dilbag; Chauhan, M. S., “Facile Growth and Characterization of α-Fe2O3 Nanoparticles for Photocatalytic Degradation of Methyl Orange,” Journal of Nanoscience and Nanotechnology, **14**, 6153-6157(5) (2014).

Shen, G., Chen, P. C., Ryu K., and Zhou, C., “Devices and chemical sensing applications of metal oxide nanowires,” J. Mater. Chem., **19**, 828-839 (2009).

Shen, Y., Wu, Y., Li, X., Zhao, Q., and Hou, Y., “One-pot synthesis of $MgFe_2O_4$ nanospheres by solvothermal method,” Mater. Lett., **96**, 85–88 (2013).

Shen, Y., Zhao, Q., Li, X., Houa, Y., Chen, G., “Surface photovoltage property of magnesium ferrite/hematite heterostructured hollow nanospheres prepared with one-pot strategy,” Colloids Surf, A, **403**, 35-40 (2012).

Shi, L., Xu, Y. and Li, Q., “Controlled fabrication of SnO_2 arrays of well-aligned nanotubes and nanowires,” Nanoscale., **2**, 2104–2108 (2010).

Shi, Y., Zhou, K., Wang, B., Jiang, S., Qian, X., Gui, Z., Yuen, R. K. K., and Hu, Y., “Ternary graphene–$CoFe_2O_4$/CdS nanohybrids: preparation and application as recyclable photocatalysts, J. Mater. Chem. A, **2**, 535-544 (2014).

Shi, Y., Zhou, K., Wang, B., Jiang, S., Qian, X., Gui, Z., Yuen, R. K. K., and Hu, Y., “Ternary graphene–$CoFe_2O_4$/CdS nanohybrids: preparation and application as recyclable photocatalysts,” J. Mater. Chem., A, **2**, 535-544 (2014).

Shinde, T. J., Gadkari, A. B. and Vasambekar, P. N., “DC resistivity of Ni–Zn ferrites prepared by oxalate precipitation method,” Mater. Chem. Phy. **111**, 87–91 (2008).

Shu, Y., Shao, Y., Wei, X., Sun, Q., Zhang, Q., and Li, L., "Synthesis and characterization of Ni-MCM-41 for methyl blue adsorption," Microporous and Mesoporous Materials, 214, 88-94 (2015).

Singh, D. P., and Ali, N., "Synthesis of TiO_2 and CuO nanotubes and nanowires," Sci. Adv. Mater., **2**, 295–335 (2010).

Singh, P., Mondal, K. and Sharma, A., "Reusable electrospun mesoporous ZnO nanofiber mats for photocatalytic degradation of polycyclic aromatic hydrocarbon dyes in wastewater," J. Colloid Interf. Sci., **394**, 208–215 (2013).

Sivula, K., Zboril, R., Formal, F. L., Robert, R., Weidenkaff, A., Tucek, J., Frydrych, and J., Gratzel, M., "Photoelectrochemical Water Splitting with Mesoporous Hematite Prepared by a Solution-Based Colloidal Approach," J. Am. Chem. Soc., **132**, 7436–7444 (2010).

Sobana, N., Krishnakumar, B., and Swaminathan, M., "Synergism and effect of operational parameters on solar photocatalytic degradation of an azo dye (Direct Yellow 4) using activated carbon-loaded zinc oxide," Mater. Sci. Semicond. Process., **16**, 1046-1051 (2013).

Soltani, T., and Entezari, M. H., "Sono-synthesis of bismuth ferrite nanoparticles with high photocatalytic activity in degradation of Rhodamine B under solar light irradiation," Chem. Eng. J., **223**, 145-154 (2013).

Soltani, T., and M. H., Entezari, "Solar photocatalytic degradation of RB5 by ferrite bismuth nanoparticles synthesized via ultrasound," Ultrason. Sonochem., **20**, 1245-1253 (2013).

Song, H. J., Liu, L., Jia, X. H. and Min, C., "Synthesis of multi-walled carbon nanotubes/β-FeOOH nanocomposites with high adsorption capacity," J. Nanopart. Res., **14**, 1–8 (2012).

Song, L., Zhang, S., Chen, B., Ge, J., and Jia, X., "A hydrothermal method for preparation of α-Fe_2O_3 nanotubes and their catalytic performance for thermal decomposition of ammonium perchlorate," Colloids Surf., A, **360**, 1–5 (2010).

Song, Y. L., Li, J. T. and Chen H., "Degradation of C.I. Acid red 88 aqueous solution by combination of Fenton's reagent and ultrasound irradiation," J. Chem. Technol. Biotechnol., **84**, 578-583 (2009).

Stefanis, A. D., Kaciulis, S., and Pandolfi, L., "Preparation and characterization of Fe-MCM-41 catalysts employed in the degradation of plastic materials," Microporous Mesoporous Mater., **99**, 140–148 (2007).

Suchanek, W. L., and Riman, R. E., "Hydrothermal synthesis of advanced ceramic powders," Adv. Sci. Technol., **45**, 184-193 (2006).

Sun, J., Li, X., Zhao, Q., Ke, J. and Zhang, D. "Novel V2O5/BiVO4/TiO2 Nanocomposites with High Visible-LightInduced Photocatalytic Activity for the Degradation of Toluene," J. Phys. Chem. C **118**, 10113−10121 (2014).

Sun, P., Cai, Y., Du, S., Xu, X., You, L., Ma, J., Liu, F., Liang, X., Sun, Y., and Lu, G., "Hierarchical α-Fe_2O_3/SnO_2 semiconductor composites: Hydrothermal synthesis and gas sensing properties," Sensor Actuat. B-Chem, **182**, 336–343 (2013).

Sutradhar, N., Sinhamahapatra, A., Pahari, S. K., Pal, P., Bajaj, H. C., Mukhopadhyay, I., and Panda, A. B., "Controlled synthesis of different morphologies of MgO and their use as solid base catalysts," J. Phys. Chem. C, **115**, 12308–12316 (2011).

Taleshi, F. and Hosseini, A. A., "Synthesis of uniform MgO/CNT nanorods by precipitation method," J. Nanostructure Chem., 3:4, DOI: 10.1186/2193-8865-3-4, (2012).

Tamm, A., Dimri, M. C., Kozlova, J., Aidla, A., Tatte, T., Arroval, T., Maeorg, U., Mandar, H., Stern, R. and Kukli, K., "Atomic layer deposition of ferromagnetic iron oxide films on three-dimensional substrates with tin oxide nanoparticles," J. Cryst. Growth, **343**, 21-27 (2012).

Tanveer, M., Cao, C., Aslam, I., Ali, Z., Idrees, F., Tahir, M., Khan, W. S., Butt, F. K., and Mahmood, A., "Effect of the morphology of CuS upon the photocatalytic degradation of organic dyes,"RSC Adv., **4**, 63447–63456 (2014).

Tao, S., Wang, Y., Yu, Y., An, Y., Shi, W., "Hierarchically porous tungstophosphoric acid/silica hybrid for high performance vis-light photocatalysis," J. Environ. Chem. Eng., **1**, 719–727 (2013).

Tarigh, G. D., Shemirani, F., and Mazhari, N. S., "Fabrication of a reusable magnetic multi-walled carbon nanotube–TiO2 nanocomposite by electrostatic adsorption: enhanced photodegradation of malachite green," RSC Adv., **5**, 35070–35079 (2015).

Tekina, D. and Saygi, B., "Photoelectrocatalytic decomposition of Acid Black 1 dye using TiO_2 nanotubes," J. Environ. Chem. Eng., **1**, 1057–1061 (2013).

Tina B., Ghosh, U. C., "Nano-structured iron(III)–cerium(IV) mixed oxide: Synthesis, characterization and arsenic sorption kinetics in the presence of co-existing ions aiming to apply for high arsenic groundwater treatment," Appl. Surf. Sci., **283**, 471– 481 (2013).

Toor, M. and Jin, B., "Adsorption characteristics, isotherm, kinetics, and diffusion of modified natural bentonite for removing diazo dye," Chem. Eng. J., **187**, 79-88 (2012).

Udom, I., Ram, M. K., Stefanakos, E. K., Hepp, A. F., and Goswami, D. Y., "One dimensional-ZnO nanostructures: synthesis, properties and environmental applications," Mater. Sci. Semicond. Process., **16**, 2070–2083 (2013).

Umare, S. S., Shambharkar, B. H., "Synthesis, Characterization, and Corrosion Inhibition Study of Polyaniline-α-Fe_2O_3 Nanocomposite," J. Appl. Polym. Sci., **127**, 3349-3355 (2013).

Valiev, R., "Nanomaterial advantage," Nature, **419**, 887-888 (2002).

Vayssieres, L., "On the design of advanced metal oxide nanomaterials," Int. J. of Nanotechnology, **1**, 1-40 (2004).

Veldurthi, S., Shin, C., Joo, O., and Jung, K., “Synthesis of mesoporous MgO single crystals without templates,” Micropor. Mesopor. Mat., **52**, 31–36 (2012).

Venkatesha, T. G., Viswanatha, R., Nayaka, Y. A., Chethana, B. K., “Kinetics and thermodynamics of reactive and vat dyes adsorption on MgO nanoparticles,” Chem. Eng. J., **198–199**, 1–10 (2012).

Vignesh, K., Kang, S., Kwak, B. S., and Kang, M., “Facile synthesis of meso-porous ZnO nano-triangular prisms with enhanced photocatalytic activity,” RSC Adv., **5**, 30120–30124 (2015).

Vijayakumar, G., Dharmendirakumar, M., Renganathan, S., Sivanesan, S., Baskar, G. and Elango, K. P., “Removal of Congo Red fromAqueous Solutions by Perlite,” Clean-Soil Air Water., **37**, 355-364 (2009).

Vivekanandhan, S., http://shodhganga.inflibnet.ac.in/bitstream/10603/1303/8/08_chapter%202.Pdf (2010).

Vu, D., Li, X., Li, Z. and Wang, C., “Phase-Structure Effects of Electrospun TiO_2 Nanofiber Membranes on As(III) Adsorption,” J. Chem. Eng. Data., **58**, 71−77 (2013).

Wang, L., and Wang A., “Adsorption properties of Congo Red from aqueous solution onto surfactant-modified montmorillonite.” J. Hazard. Mater., **160**, 173-180 (2008).

Wang, L., and Wang, A., “Adsorption characteristics of congo red onto the chitosan/montmorillonite nanocomposite,” J. Hazard. Mater., **147**, 979-985 (2007).

Wang, L., Li, J., Wang, Y., Zhao, L. and Jiang, Q., “Adsorption capability for Congo red on nanocrystalline MFe_2O_4 (M = Mn, Fe, Co, Ni) spinel ferrites.” Chem. Eng. J., **181**, 72-79 (2012).

Wang, L., Wu, X. L., Xu, W. H., Huang, X. J., Liu, J. H. and Xu, A. W., “Stable Organic−Inorganic Hybrid of Polyaniline/α-Zirconium Phosphate for Efficient Removal of Organic Pollutants in Water Environment.” ACS Appl. Mater. Interfaces., **4**, 2686-2692 (2012).

Wang, P., Shi, P., Hong, Y., Zhou, X., and Yao, W., “Facile deposition of Ag_3PO_4 on graphene-like MoS_2 nanosheets for highly efficient photocatalysis,” Mater. Res. Bull., **62**, 24–29 (2015).

Wang, S., Zhang, J., Yang, J., Gao, X., Zhang, H., Wang, Y., and Zhu, Z., “Spinel $ZnFe_2O_4$ nanoparticles-decorated rod-like ZnO nanoheterostructures for enhanced gas sensing performances,” RSC Adv., **5**, 10048-10057 (2015).

Wang, T., Kailasam, K., Xiao, P., Chen, G., Chen, L., Wang, L., Li, J., Zhu, and J., “Adsorption removal of organic dyes on covalent triazine framework (CTF),” Micropor. Mesopor. Mat., **187**, 63–70 (2014).

Wang, T., Xu, Y., Su, Q., Yang, R., Wang, L., Liu, B., Shen, S., Jiang, G., Chen, W., Wang, S., “Hierarchical porous nanosheet-assembled MgO microrods with high adsorption capacity.” Mater. Lett., **116**, 332–336 (2014).

Wang, W., Qiao, X., Chen, J. and Li, H., “Facile synthesis of magnesium oxide nanoplates via chemical precipitation,” Mater. Lett., **61**, 3218–3220 (2007).

Wang, X., and Li, Y., “Solution-based synthetic strategies for 1-D nanostructures,” Inorg. Chem., **45**, 7522−7534 (2006).

Wang, Y., Sun, H., Ang, H. M., Tadé, M. O. and Wang, S., “Facile Synthesis of Hierarchically Structured Magnetic $MnO_2/ZnFe_2O_4$ Hybrid Materials and Their Performance in Heterogeneous Activation of Peroxymonosulfate,” ACS Appl. Mater. Interfac., **6**, 19914−19923 (2014).

Wang, Y., Xu, J., Wu, H., Xu, M., Peng, Z. and Zheng, G., “Hierarchical SnO_2–Fe_2O_3 heterostructures as lithium-ion battery anodes,” J. Mater. Chem., **22**, 21923–21927 (2012).

Wang, Y., Zhang, Q., Shishido, T., and Takehira, K., “Characterizations of iron-containing MCM-41 and its catalytic properties in epoxidation of styrene with hydrogen peroxide,” J. Catal., **209**, 186–196 (2002).

Wantala, K., Sthiannopkao, S., Srinameb, B., Grisdanurak, N., and Kim, K. W., “Synthesis and characterization of Fe-MCM-41 from rice husk silica by hydrothermal technique for arsenate adsorption,” Environ. Geochem. Health, **32**, 261–266 (2010).

Wawrzkiewicz M “Comparison of the Efficiency of Amberlite IRA 478RF for Acid, Reactive, and Direct Dyes Removal from Aqueous Media and Wastewaters.” Ind. Eng. Chem. Res. **51**, 8069-8078 (2012).

Wawrzkiewicz M, Hubicki Z “Equilibrium and kinetic studies on the sorption of acidic dye bymacro porous anion exchange.” Chem. Eng. J. **157**, 29-34 (2010).

Wei, Z., Xing, R., Zhang, X, . Liu, S., Yu, H. and Li, P., “Facile Template-Free Fabrication of Hollow Nestlike α-Fe_2O_3 Nanostructures for Water Treatment,” Appl. Mater. Interfaces., **5**, 598−604 (2013).

Wen, Z., Zhu, L., Li, L., Sun, L., Cai H. and Ye, Z., “A fluorine-mediated hydrothermal method to synthesize mesoporous rhombic ZnO nanorod arrays and their gas sensor application,” Dalton Trans., **42**, 15551–15554 (2013).

Whitesides, G. M., “Nanoscience, nanotechnology, and chemistry,” Small, **1**, 172-179 (2005).

Woo, K., Hong, J., Choi, S., Lee, H., Ahn, J., Kim, C. S. and Lee, S. W., “Easy Synthesis and Magnetic Properties of Iron Oxide Nanoparticles,” Chem. Mater., **16**, 2814-2818 (2004).

Wu, J. C. S., and Chen, C., “A visible-light response vanadium-doped titania nanocatalyst by sol–gel method,” J. Photochem. Photobiol., A, **163**, 509–515 (2004).

Wu, J., Wang, J., Li, H., Du, Y., Huang, K. and Liu, B., “Designed synthesis of hematite-based nanosorbents for dye removal,” J. Mater. Chem. A., **1**, 9837–9847 (2013**)**.

Wu, K., Liu, T., Xue, W., and Wang, X., “Arsenic(III) oxidation/adsorption behaviors on a new bimetal adsorbent of Mn-oxide-doped Al oxide,” Chemical Engineering Journal, **192**, 343–349 (2012).

Wu, W., Xiao, X., Zhang, S., Li, H., Zhou, X. and Jiang, C., “One-Pot Reaction and Subsequent Annealing to Synthesis Hollow Spherical Magnetite and Maghemite Nanocages,” Nanoscale Res. Lett. **4**, 926–931 (2009).

Wu, Z. G., and Gao, J. F., “Synthesis of γ-Fe_2O_3 nanoparticles by homogeneous co-precipitation method,” Micro Nano Lett., 7, 533 – 535 (20120.

Xia, G., Li, N., Li, D., Liu, R., Wang, C., Li, Q., Lü, X., Spendelow, J. S., Zhang J. and Wu, G., “Graphene/Fe_2O_3/SnO_2 Ternary Nanocomposites as a HighPerformance Anode for Lithium Ion Batteries,” Appl. Mater. Interfac., **5**, 8607−8614 (2013).

Xia, H., Zhuang, H., Zhang, T., and Xiao, D., “Visible-light-activated nanocomposite photocatalyst of Fe_2O_3/SnO_2” Mater. Lett., **62**, 1126–1128 (2008).

Xiao, N., Li, Z., Liu, J. and Gao, Y., “A facile template-free method for preparing bi-phase TiO_2 nanowire arrays with high photocatalytic activity,” Mater. Lett., **64**, 1776–1778 (2010).

Xiao, Z., Xia, Y., Ren, Z., Liu, Z., Xu, G., Chao, C., Li, X., Shen G. and Han, G.,“Facile synthesis of single-crystalline mesoporous α-Fe_2O_3 and Fe_3O_4nanorods as anode materials for lithium-ion batteries,” J. Mater. Chem., 2012, 22, 20566–20573.

Xie, J., Wang, H., Duan, M. and Zhang, L., “Synthesis and photocatalysis properties of ZnO structures with different morphologies via hydrothermal method,” Appl. Surf. Sci., **257**, 6358–6363 (2011).

Xie, J., Wu, Q. and Zhao, D., “Electrospinning synthesis of $ZnFe_2O_4$/Fe_3O_4/Ag nanoparticle-loaded mesoporous carbon fibers with magnetic and photocatalytic properties,” Carbon **50**, 800–807 (2012).

Xie, M., Meng, Q., Luan, P., Feng Y., and Jing, L., “Synthesis of mesoporous TiO_2-coupled Fe_2O_3 as efficient visible nano-photocatalysts for degrading colorless pollutants,” RSC Adv., **4**, 52053–5205 (2014).

Xie, X., Yang, H., Zhang, F., Li, L., Ma, J., Jiao, H., and Zhang, J., “Synthesis of hollow microspheres constructed with α-Fe_2O_3 nanorods and their photocatalytic and magnetic properties,” Journal of Alloys and Compounds, 477, 90–99 (2009).

Xing, Y., Que, W., Yin, X., Liu, X., Javed, H. M. A., Yang, Y., and Kong, L. B., “Fabrication of $Bi_2Sn_2O_7$-ZnO heterostructures with enhanced photocatalytic activity” RSC Adv., **5**, 27576–27583 (2015).

Xiong, P., Wang, L., Sun, X., Xu, B. and Wang, X .“Ternary Titania−Cobalt Ferrite−Polyaniline Nanocomposite: A Magnetically Recyclable Hybrid for Adsorption and Photodegradation of Dyes under Visible Light,” Ind. Eng. Chem. Res., **52**, 10105−10113 (2013).

Xu, J., Wang, W., Shang, M., Gao, E., Zhang, Z. and Ren, J., “Electrospun nanofibers of Bi-doped TiO_2 with high photocatalytic activity under visible light irradiation,” J. Hazard Mater., **196**, 426-430 (2011).

Xu, L., Sithambaram, S., Zhang, Y., Chen, C. H., Jin, L., Joesten, R., and Suib, S. L., “Novel urchin-like CuO synthesized by a facile reflux method with efficient olefin epoxidation catalytic performance,” Chem. Mater., **21**, 1253–1259 (2009).

Xu, P., Zeng, G. M., Huang, D. L., Feng, C. L., Hu, S., Zhao, M. H., Lai, C., Wei, Z., Huang, C., Xie, G. X., and Liu, Z. F., “Use of iron oxide nanomaterials in wastewater treatment: A review,” Sci. Total Environ., **424**, 1–10 (2012).

Xu, S., and Wang, Z. L., “One-dimensional ZnO nanostructures: solution growth and functional properties,” Nano Res., **4**, 1013–1098 (2011).

Yadav, B.C., Srivastava, R, Dwivedi, C. D. and Pramanik P., “Moisture sensor based on ZnO nanomaterial synthesized through oxalate route,” Sens. Actuators B., **131**, 216–222 (2008).

Yan, L., Cheng, Y., Yuan, S., Yan, X., Hu, X., and Oh, K., “Photocatalytic degradation kinetics of methyl orange in TiO_2–SiO_2–$NiFe_2O_4$ aqueous suspensions,” Res. Chem. Intermed., **39**, 1673–1684 (2013).

Yang, M., and He, J., “Fine tuning of the morphology of copper oxide nanostructures and their application in ambient degradation of methylene blue” J. Colloid Interf. Sci., **355**, 15-22 (2011).

Yao, X., Tang, C., Yuan G., Cui, P., Xu, X. and Liu, Z., “Porous hematite (α-Fe_2O_3) nanorods as an anode material with enhanced rate capability in lithium-ion batteries,” Electrochem. Commun., **13**, 1439–1442 (2011).

Yin, Z., Li, Y., Jiang, L., Rana, R. K., Synthesis and electrocatalytic activity of haemin-functionalised, iron(II, III) oxide nanoparticles, Analytica Chimica Acta 781, 48–53 (2013).

Yogi, A., and Varshney, D., “Magnetic and structural properties of pure and Cr-doped haematite: α-$Fe_{2-x}Cr_xO_3(0 \leq x \leq 1)$,” J. Adv. Ceram. **2**, 360–369 (2013).

Yosef, I., and Avnir, D, “Entrapment of dye molecules within submicron silver particles.” J Nanopart. Res **13**, 3929–3937 (2011).

Yoshimatsu, K., Ye, Lei., Lindberg, J., and Chronakis, I. S., “Selective molecular adsorption using Electrospun nanofiber affinity membranes,” Biosens. Bioelect., **23**, 1208–1215 (2008).

Yu, B., Xu, J., Liu, J., Yang, S., Luo, J., Zhou, Q., Wan, J., Liao, R., Wang, H., and Liu, Y., “Adsorption behavior of copper ions on graphene oxide–chitosan aerogel,” J. Environ. Chem. Eng., **1**, 1044–1050 (2013).

Yu, C., Dong, X., Guo, L., Li, J., Qin, F., Zhang, L., Shi, J., Yan, D., “Template-Free Preparation of Mesoporous Fe_2O_3 and Its Application as Absorbents.” J. Phys. Chem. C **112**, 13378-13382 (2008).

Yu, J., Shi, J. L., Wang, L. Z., Ruan, M. L., and Yan, D. S., “Preparation of high thermal stability MCM-41 in the low surfactant/silicon molar ratio synthesis system,” Mater.Lett., **48**, 112–116 (2001).

Yuan, S., Li, X., and Dai, X., “Efficient degradation of organic pollutants with a sewage sludge support and in situ doped TiO_2 under visible light irradiation conditions,” RSC Adv., **4**, 61036–61044 (2014).

Zeng, S., Tang K. and Li, T., “Controlled synthesis of α-Fe2O3 nanorods and its size-dependent optical absorption, electrochemical, and magnetic properties,” J. Colloid Interfac. Sci., **312**, 513–521 (2007).

Zeng, S., Tang, K., and Li, T., “Controlled synthesis of α-Fe_2O_3 nanorods and its size-dependent optical absorption, electrochemical, and magnetic properties,” J. Colloid Interface Sci., **312**, 513–521 (2007).

Zewen Fu, Tengfei Jiang, Zhipeng Liua, Dejun Wang, Lingling Wang, Tengfeng Xie, Highly photoactive Ti-doped α-Fe_2O_3 nanorod arrays photoanode prepared by a hydrothermal method for photoelectrochemical water splitting, Electrochimica Acta 129 (2014) 358–363.

Zhai, T., Fang, X., Liao, M., Xu, X., Zeng, H., Yoshio, B. and Golberg, D. “A Comprehensive Review of One-Dimensional Metal-Oxide Nanostructure Photodetectors,” Sensors, **9**, 6504-6529 (2009).

Zhai, Y., Zhai, J., Zhou, M., and Dong, S., “Ordered magnetic core–manganese oxide shell nanostructures and their application in water treatment,” J. Mater. Chem., **19**, 7030–7035 (2009).

Zhan, S., Gong, C., Chen, D., and Jiao, X., “Preparation of $ZnFe_2O_4$ Nanofibers by Sol-Gel Related Electrospinning Method,” J. Dispersion Sci. Technol., **27**, 931–933, (2006).

Zhang, B., Tian, Y., Zhang, J. X. and Cai, W., “Structural, optical, electrical properties and FTIR studies of fluorine doped SnO_2 films deposited by spray pyrolysis,” J. Mater. Sci., **46**, 1884–1889 (2011).

Zhang, G. Y., Feng, Y., Xu, Y. Y., Gao, D. Z., and Sun, Y. Q., “Controlled synthesis of mesoporous α-Fe_2O_3 nanorods and visible light photocatalytic property,” Mater. Res. Bull., **47**, 625–630 (2012).

Zhang, H., Liang, C., Liu, J., Tian, Z., Wang, G. and Cai, W.,“Defect-Mediated Formation of Ag Cluster-Doped TiO_2 Nanoparticles for Efficient Photodegradation of Pentachlorophenol,” Langmuir, **28**, 3938−3944 (2012).

Zhang, J. Huang, T., Liu, Z., Yu, A., Mesoporous Fe_2O_3 nanoparticles as high performance anode materials for lithium-ion batteries, Electrochem. Commun., 29, 17–20 (2013).

Zhang, J. Z., Optical Properties and Spectroscopy of Nanomaterials. World Scientific, Singapore, (2009).

Zhang, J., Huang, T., Liu, Z. and Yu, A., “Mesoporous Fe_2O_3 nanoparticles as high performance anode materials for lithium-ion batteries,” Electrochem. Commun., **29**, 17–20 (2013).

Zhang, L., Heb, Y., Wua, Y., Wu, T., “Photocatalytic degradation of RhB over $MgFe_2O_4/TiO_2$ composite materials,” Mater, Sci, Eng, B, **176**, 1497-1504 (2011).

Zhang, M., Li, L., and Zhang, X., "One-dimensional Ag_3PO_4/TiO_2 heterostructure with enhanced photocatalytic activity for the degradation of 4-nitrophenol," RSC Adv., **5**, 29693–29697 (2015).

Zhang, M., "Nonaqueous synthesis of metal oxide nanoparticles and their surface coating," Ph.D. University of New Orleans, 2008. Print.

Zhang, O., Zhang, K., Xu, D., Yang, G., Huang, H., Nie, F., Liu, C., and Yang, S., "CuO nanostructures: synthesis, characterization, growth mechanisms, fundamental properties, and applications," Prog. Mater Sci., **60**, 208–337 (2014).

Zhang, W., Meng, Z., Zhai, J., and Heng, L., "Ion current behaviors of mesoporous zeolite–polymer composite nanochannels prepared by water-assisted self-assembly," Chem. Commun., **50**, 3552-3555 (2014).

Zhang, X., Zhang, P., Wub, Z., Zhang, L., Zeng, G. and Zhou, C.,"Adsorption of methylene blue onto humic acid-coated Fe_3O_4 nanoparticles," Colloid. Surface A., **435**, 85–90 (2013).

Zhang, Y., Ma, L., Li, J., and Ying, Y., "In situ Fenton reagent generated from TiO_2/Cu_2O composite film: a new way to utilize TiO_2 under visible light irradiation," Environ. Sci. Technol., **41**, 6264-6269 (2007).

Zhang, Z., Hossain, M. F., and Takahashi, T., "Self-assembled hematite (α-Fe_2O_3) nanotube arrays for photoelectrocatalytic degradation of azo dye under simulated solar light irradiation," Appl. Catal., B, **95**, 423–429 (2010).

Zhang, Z., Moghaddam, L., O'Hara, I. M. and Doherty, W. O. S., "Congo Red adsorption by ball-milled sugarcane bagasse," Chem. Eng. J., **178**, 122–128 (2011).

Zhang, Z., Shao, C., Li, X., Zhang, L., Xue, H., Wang, C. and Liu, Y., "Electrospun Nanofibers of ZnO-SnO_2 Heterojunction with High Photocatalytic Activity," J. Phys. Chem. C., **114**, 7920–7925 (2010).

Zhanj, Y., and Zhu, J., "Synthesis and characterisation of several one dimensional materials," Micron, **33**, 523-534 (2002).

Zhao, D., Wang Y., and Zhang, Y., "High-performance Li-ion batteries and super-capacitors based on prospective 1-D nanomaterials," Nano- Micro Lett., **3**, 62-71 (2011).

Zhao, Q., Li, Y., Zhou, X., Jiang, T., Li, C., and Yin, H., "Synthesis of multi-wall carbon nanotubes by the pyrolysis of ethanol on Fe/MCM-41 mesoporous molecular sieves," Superlattices Microstruct., **47**, 432-441 (2010).

Zhao, W., Guo, Y., Wang, S., He, H., Sun, C., and Yang, S., "A novel ternary plasmonic photocatalyst: ultrathin g-C_3N_4 nanosheet hybrided by $Ag/AgVO_3$ nanoribbons with enhanced visible-light photocatalytic performance," Appl. Catal., B, **165**, 335–343 (2015).

Zhong, L., Hu, J., Liang, H., Cao, A., Song, W., and Wan, L., "Self-Assembled 3D Flowerlike Iron Oxide Nanostructures and Their Application in Water Treatment," Adv. Mater., **18**, 2426–2431 (2006).

Zhou, W., Fu, H., Pan, K., Tian, C., Qu, Y., Lu, P., and Sun, C., "Mesoporous TiO_2/α-Fe_2O_3: Bifunctional Composites for Effective Elimination of Arsenite Contamination through Simultaneous Photocatalytic Oxidation and Adsorption," J. Phys. Chem. C, **112**, 19584–19589 (2008).

Zhou, W., He, W., Ma, J., Wang, M., Zhang, X., Yan, S., Tian, X., Sun, X., and Han, X., "Biosynthesis of mesoporous organic–inorganic hybrid Fe_2O_3 with high photocatalytic activity," Materials Science and Engineering C, **29**, 1893–1896 (2009).

Zhou, W., Liu, H., Boughton, R. I., Du, G., Lin, J., Wang, J. and Liu, D., "One-dimensional single-crystalline Ti–O based nanostructures: properties, synthesis, modifications and applications," J. Mater. Chem., **20**, (2010) 5993–6008.

Zhou, X., Xiao, Y., Wang, M., Sun, P., Liu, F., Liang, X., Li, X., and Lu, G., "Highly enhanced sensing properties for ZnO nanoparticle-decorated round-edged α-Fe_2O_3 hexahedrons," ACS Appl. Mater. Interfaces, **7**, 8743−8749 (2015).

Zhu M, Wang Y, Meng D, Qin X, Diao G "Hydrothermal Synthesis of Hematite Nanoparticles and their Electrochemical Properties." J. Phys. Chem. C **116**, 16276-16285 (2012).

Zhu, J., Sadu, R., Wei, S., Chen, D. H., Haldolaarachchige, N., Luo, Z., Gomes, J. A., Young, D. P., and Guo, Z., "Magnetic Graphene Nanoplatelet Composites toward Arsenic Removal," ECS J. Solid State Sci. Technol., **1**, M1-M5 (2012).

Zhu, J., Simon Ng, K. Y., and Deng, D., "Micro single crystals of hematite with nearly 100% exposed {104} facets: preferred etching and lithium storage," Cryst. Growth Des., **14**, 2811−2817 (2014).

Zhu, J., Wei, S., Zhang, L., Mao, Y., Ryu, J., and Haldolaarachchige, N., Young, D. P., and Guo, Z., "Electrical and dielectric properties of polyaniline–Al_2O_3 nanocomposites derived from various Al_2O_3 nanostructures," J. Mater. Chem., **21**, 3952–3959 (2011).

Zhu, T., Chen, J. S. and Lou, X. W. D., "Highly Efficient Removal of Organic Dyes from Waste Water Using Hierarchical NiO Spheres with High Surface Area," J. Phys. Chem. C., **116**, 6873-6878 (2012).

LIST OF PUBLICATIONS

Journal Papers

1. J. P. Dhal, B. G. Mishra and G. Hota, Hydrothermal synthesis and enhanced photocatalytic activity of ternary $Fe_2O_3/ZnFe_2O_4/ZnO$ nanocomposite through cascade electron transfer, *RSC Advances*, **2015**, 5, 58072-58083.
2. J. P. Dhal, M. Sethi, B. G. Mishra and G. Hota, MgO nanomaterials with different morphologies and their sorption capacity for removal of toxic dyes, *Materials Letters*, 141, **2015**, 267-271.
3. J. P. Dhal, B. G. Mishra and G. Hota, Ferrous oxalate, maghemite and hematite nanorods as efficient adsorbents for decontamination of Congo red dye from aqueous system, *International Journal of Environmental Science and Technology*, 12, **2015**, 1845-1856.
4. J. P. Dhal, B. G. Mishra and G. Hota; Fe_2O_3-SnO_2 composite nanorods; facile synthesis and sorption properties, *Journal of Environmental Chemical Engineering*, 2, **2014**, 2188-2198.
5. J. P. Dhal, B. G. Mishra and G. Hota, Synthesis, characterization and photocatalytic application of ultra-fine α-Fe_2O_3 nanofiber, *Asian Journal of Chemistry*, 25, **2013**, S22-S26.
6. J. P. Dhal, B. G. Mishra and G. Hota, Iron oxide impregnated mesoporous MCM-41: synthesis, characterization and adsorption studies (Under Review).
7. J. P. Dhal, B. G. Mishra and G. Hota, Photocatalytic activity of $MgFe_2O_4$-Fe_2O_3 heterostructured nanomaterials synthesized by chemical routes (Under Review).
8. J. P. Dhal, B. G. Mishra and G. Hota, One-dimensional Fe_2O_3-CuO nanocomposites: synthesis, characterization and photocatalytic degradation of Methyl orange (Under Review).
9. J. P. Dhal, B. G. Mishra and G. Hota, Rod shaped maghemite (γ-Fe_2O_3) nanomaterials for adsorption of Chromium (VI) and Fluoride ions from aqueous media (To be communicated).

Conference Papers

1. J. P. Dhal, B. G. Mishra and G. Hota, Synthesis and characterization of novel metal oxide nanostructures for adsorption/catalytic degradation of organic pollutants from aqueous stream, Research Scholars Week, May 11-13, **2015**, NIT Rourkela.
2. J. P. Dhal, B. G. Mishra and G. Hota, Electrospun α-Fe_2O_3 nanofiber for natural solar light driven photocatalytic degradation of Methylene Blue dye, ACBIR-2014, 10-11 January **2014**, NIT Rourkela.
3. J. P. Dhal, B. G. Mishra and G. Hota: Synthesis and characterization of iron oxide nanorods for decontamination of organic dye from aqueous media, CTSST 2014, 28 February **2014**, Sambalpur University, Odisha.
4. J. P. Dhal, B. G. Mishra and G. Hota, Synthesis, characterization and photocatalytic application of α-Fe_2O_3 nanorod, ICMAT 2013, 30 June to 5 July **2013**, Suntec, Singapore.
5. J. P. Dhal, B. G. Mishra and G. Hota; Synthesis, characterization and photocatalytic application of ultra-fine α-Fe_2O_3 nanofiber, International conference of Nano Science and Nanotechnology (ICONN 2013), at SRM University, Chennai, 18-20th March, **2013**.

CURRICULUM VITAE

Name: **Jyoti Prakash Dhal**

Date of Birth: 28-06-1984

Educational Qualifications: M.Tech. (Metallurgical & Materials Engineering), National Institute of Technology, Rourkela, India (2011).

M. Sc. (Chemistry), Utkal University, Bhubaneswar, India (2006)

B. Sc. (Chemistry Honors), Utkal University, Bhubaneswar, India (2004)

Class XII, Christ College, Cuttack, CHSE-Odisha, India (2001)

Class X, Barunei High School, Jajpur, BSE-Odisha, India (1999)

Research Experience: 4 years research experience in the field of Material Science. Published 5 papers and communicated 4 papers in International journals.

Professional Experience: Three years of teaching experiences to Intermediate and U. G. students.

Awards & Achivements: Senior Research Fellow, MHRD, Govt. of India– July 2011 to till date.

Junior Research Fellow, MHRD, Govt. of India – July 2009 to June 2011.

Qualified GATE (2009) with 89.01 percentile.

Awarded BEST POSTER by NIT Rourkela on the occasion of Research Scholar Week 2015.

Rashtrapati Scout Certificate from Honourable President of India (1999).

Permanent address: S/O-Sudhakar Dhal
At/Po-Bachhol, Via-Mashra,
Dist- Jajpur, Odisha, India,
PIN-755012
Email: jyoti84.chem@gmail.com
jyoti84_dhal@rediffmail.com